

Silicon Nano-Photonics Based Arrayed Waveguide Gratings

Shibnath Pathak

Promotoren: prof. dr. ir. W. Bogaerts, prof. dr. ir. D. Van Thourhout
Proefschrift ingediend tot het behalen van de graad van
Doctor in de Ingenieurswetenschappen: Fotonica

Vakgroep Informatietechnologie
Voorzitter: prof. dr. ir. D. De Zutter
Faculteit Ingenieurswetenschappen en Architectuur
Academiejaar 2013 - 2014



ISBN 978-90-8578-674-0
NUR 959
Wettelijk depot: D/2014/10.500/20



Universiteit Gent
Faculteit Ingenieurswetenschappen en Architectuur
Vakgroep Informatietechnologie

Silicon Nano-Photonics based Arrayed Waveguide Gratings

Arrayed Waveguide Gratings op basis van Silicium Nanofotonica

Shibnath Pathak



Proefschrift tot het bekomen van de graad van
Doctor in de Ingenieurswetenschappen:
Fotonica
Academiejaar 2013-2014



Universiteit Gent
Faculteit Ingenieurswetenschappen en Architectuur
Vakgroep Informatietechnologie

Promotoren:

Prof. Dr. Ir. Wim Bogaerts
Prof. Dr. Ir. Dries Van Thourhout

Examencommissie:

Prof. Dr. Ir. Rik Van de Walle (voorzitter)	Universiteit Gent, MMLab
Prof. Dr. Ir. Wim Bogaerts	Universiteit Gent, INTEC
Prof. Dr. Ir. Dries Van Thourhout	Universiteit Gent, INTEC
Prof. Dr. ir. Geert Van Steenberge	Universiteit Gent, CMST
Dr. Xaveer J. M. Leijtens	Technische Universiteit Eindhoven
Dr. Philippe Absil	IMEC
Dr. Ir. Pieter Dumon	Universiteit Gent, INTEC

Universiteit Gent
Faculteit Ingenieurswetenschappen en Architectuur

Vakgroep Informatietechnologie
Sint-Pietersnieuwstraat 41, B-9000 Gent, België

Tel.: +32-9-264.33.41

Fax.: +32-9-264.35.93

Acknowledgment

It is difficult to cover all the people who have directly or indirectly helped me to complete this thesis. However, I would first start with giving thanks to my supervisors Wim and Dries who trusted in my capabilities in completing the designated task. While working close to Wim during my research work I learned a lot from him; starting from 'how to design a PIC' to 'how to give a presentation'. Sharing the same big office with him I always had a '2 minutes meeting' which never ended before 15 minutes. He also gave me complete independence to take forward my research according to my plans. In one sentence he gave me everything whatever I need for my past and future research career. Although I was working close to Wim but nevertheless the valuable inputs from Dries on my research work were remarkably helpful.

A significant work in this thesis had been carried out as a part of the project HELIOS and WADIMOS. I would like to thank these projects for funding our research work. My journey started by learning python and IPKISS which would have not been accelerated without the valuable help of Manu. Thanks to Manu, he also helped me to setup my Linux PC. In the same spirit, I would like to thank Antonio who also helped me time to time during the second phase of my work.

During the second phase of my journey, we got one valuable measurement setup called "semi automatic setup". Thanks to Michael who did a great job on this aspect. For my measurement Michael not only helped me to write the measurement script but on my request several times he came to the office during the weekend. I also would like to thanks Alfonso and Pieter for all those little discussions which helped me to improve my understanding. I also like to thanks all the users of AWGs. They not only helped me to expand my research interest and motivation but their hard work influenced my publication.

I like to thank Daan, Jan, Haka, Chen, Alfonso, Hui, Samir, Aditya, Michael, Shahram, Dorian, Joroen, Adil and all others to provide a charming "quiet-environment inside the big office. I'm also thankful to the people from our lunch group. They not only called me for lunch everyday but also the discussions on the lunch table were memorable.

Special thanks to my senior Samir who helped me on my arrival to settle down in Belgium. Survival could be more difficult without his delicious chicken curry / cingri macher mali curry. Living in Ghent would be boring and lonely without my roommates Shyam and Aditya. My regards to Aditya for all those delicious dishes and discussions during the dinner.

My regards to Sarvagya, Ananth, Bendix, Utsav, Pijush, Sukumar, Shankar, Rajesh, Amit, Linghua, Khai, Martin, Andrea, Eva, Nannicha, Ashim, Peter De Heyn, Gunay for all the discussions during lunch or coffee break. I would also like to thank Bendix, Floriane and Kiya for all good time we spend during the BBQ, Party, Indian Tea evening, movie night, marriage and many more. Thanks to Amit Ghosh for all the good times we spent together.

My deepest gratitude goes to my parents. Without their endless affection and continuous support, I could not have achieved anything in my life. Also, thanks to my bother and sister for their love and supports.

Finally I would like finish by expressing my love to the beautiful and charming city of Ghent, which became my home for more than four years and it will hold a special place in my heart forever.

Thank you all, for everything.

Davis, CA, USA, January 2014

Shibnath Pathak

कर्मण्येवाधिकारस्ते मा फलेषु कदाचन ।
मा कर्मफलहेतुर्भूर्मा ते सङ्गोऽस्त्वकर्मणि ॥२- ४७॥

karmany evādhikāras te mā phalenu kadācana |
mā karmaphalahetur bhūr mā te sangostv akarmani ||2- 47||

You have a right to perform your prescribed duty,
but you are not entitled to the fruits of action.

Never consider yourself to be the cause of the
results of your activities, and never be attached
to not doing your duty.

From

Bhagavad Gita

Table of Contents

Acknowledgment	i
Nederlandstalige Samenvatting	xxiii
English summary	xxix
1 Introduction	1
1.1 Photonics	2
1.1.1 Silica-on-silicon	3
1.1.2 III-V Semiconductor materials	3
1.1.3 Lithium Niobate (LiNbO ₃)	3
1.1.4 Silicon photonics	4
1.2 Wavelength division multiplexing	5
1.3 Arrayed waveguide grating	5
1.4 Silicon AWG	7
1.5 Objective	8
1.5.1 Overview	8
References	10
2 Theory	13
2.1 Introduction	14
2.2 Optical phased array	14
2.2.1 Diffraction theory	14
2.2.2 Array factor	16
2.2.3 Example	18
2.3 Classification of AWG	20
2.3.1 AWG as a wavelength filter	20
2.3.2 AWG as an optical switch	23
2.4 Design Parameters of an AWG	24
2.4.1 Focal length	24
2.4.2 Delay Length	24
2.4.3 Diffraction order and free spectral range	25

2.4.4	Dispersion	27
2.5	Characterization	28
2.5.1	Insertion loss and non-uniformity	28
2.5.2	Crosstalk	31
2.5.3	Polarization Dependence	33
2.5.4	Temperature Dependence	34
2.6	Wavelength filter function	35
2.6.1	Wavelength router	35
2.6.2	Wavelength de/multiplexers	36
2.7	Design	38
2.7.1	Geometry of the star-coupler	38
2.7.2	Geometry of the waveguide array	39
2.7.3	Rectangular Manhattan	39
2.8	Conclusion	42
	References	43
3	Simulation	47
3.1	Introduction	48
3.2	AWG decomposition	48
3.3	IPKISS: A parametric design framework	49
3.4	Semi-analytical simulation model	52
3.4.1	Star-coupler model	53
3.4.1.1	Field profile	53
3.4.1.2	Free space propagation	54
3.4.2	Model of waveguide array	57
3.4.3	Spectral response	59
3.5	Conclusions	60
	References	61
4	Experimental demonstrations	63
4.1	Introduction	64
4.2	Fabrication of SOI integrated circuits	64
4.3	Experimental setup	65
4.3.1	Vertical coupling	66
4.3.2	Automatic vertical coupling	66
4.3.3	AWG normalization procedure	68
4.4	Design based demonstrations	69
4.4.1	Rectangular AWG	69
4.4.1.1	Design	69
4.4.1.2	Result and Discussion	70
4.4.1.3	Channel spacing mismatch	75

4.4.2	Circular AWG	77
4.4.2.1	Design	78
4.4.2.2	Results	78
4.4.3	S-shaped AWG	80
4.4.3.1	Design	80
4.4.3.2	Results	81
4.4.4	Reflection-type AWG	82
4.4.4.1	Design	82
4.4.4.2	Results	83
4.5	Application based demonstrations	83
4.5.1	De/multiplexer	83
4.5.1.1	Design	83
4.5.1.2	Result and Discussion	85
4.5.2	Router	88
4.5.2.1	Results	88
4.6	Fabrication dependence	92
4.6.1	Effect of mask discretization on waveguide width	92
4.6.1.1	Design	93
4.6.1.2	Experiment	93
4.6.2	Effect of mask discretization on waveguide length	94
4.6.2.1	Design	95
4.6.2.2	Simulation	97
4.6.2.3	Experiment	97
4.7	Polarization Diversity	100
4.7.1	Design of the 2D grating Coupler	101
4.7.2	Design of the AWG	101
4.7.3	Results	102
4.7.3.1	Analysis of the 2D grating coupler	103
4.7.3.2	Analysis of full Polarization Diversity Circuit	105
4.8	Comparison with echelle gratings	107
4.8.1	Echelle Gratings	108
4.8.2	Design	108
4.8.3	Results and Discussions	109
4.8.3.1	AWG	109
4.8.3.2	Echelle grating	110
4.9	Conclusions	113
	References	114

5	Flattened Spectral Response	117
5.1	Introduction	118
5.2	Mode overlap	119
5.3	MMI as Input Aperture	119
5.3.1	Design of MMI and AWG	121
5.3.2	Results and Discussion	124
5.3.2.1	Effect of MMI length	124
5.3.2.2	Optimization of Waveguide Array	125
5.3.2.3	Optimized Spectral Response	128
5.4	MZI as input aperture	130
5.4.1	Working Principle	132
5.4.2	Design	132
5.4.3	Simulation	134
5.5	Cascaded AWGs	135
5.5.1	Design and working Principle	137
5.5.2	Simulation	139
5.5.3	Experiment	141
5.6	Conclusions	142
	References	143
6	Electro-optic tuning of the AWG	145
6.1	Introduction	146
6.2	Optical packet switch	146
6.2.1	Design	146
6.2.1.1	Carrier-depletion based silicon modulators	147
6.2.1.2	Phased array	148
6.2.2	Simulation	149
6.2.3	Experiment	150
6.2.3.1	Modulator characteristic	150
6.2.3.2	Switch	151
6.3	Active tuning of AWG	153
6.3.1	Design	153
6.3.2	Experiment	154
6.3.2.1	Phase error correction	154
6.3.2.2	Halving the FSR	155
6.3.2.3	Spectral shift	156
6.4	Conclusion	157
	References	158

7 AWGs in other material systems	161
7.1 Introduction	162
7.2 Silicon nitride for visible wavelengths	162
7.2.1 Design	163
7.2.2 Experiment	164
7.3 Silicon for short wave infrared	165
7.3.1 Design	166
7.3.2 Experiment	167
7.4 Silicon for Mid-infrared	168
7.4.1 Design	168
7.4.2 Experiment	169
7.5 Germanium AWG for Mid-infrared	169
7.5.1 Design	170
7.5.2 Experiment	172
7.6 Conclusion	173
References	174
8 Conclusion	177
8.1 Conclusion	178
8.2 Future perspectives	180
References	183
A Design	185
A.1 Introduction	186
A.1.1 Circular manhattan	186
A.1.2 Angled waveguide with a constant bend radius	187
A.1.3 Angled waveguide with variable bend radius	188
A.2 Reflection type AWG	189
A.3 Low resolution AWG	190
A.4 Conclusions	192
References	193

List of Figures

1	Algemeen werkingsprincipe van de AWG.	xxiii
2	Gefabriceerde AWG's in silicium.	xxv
3	Simulatiemodel van de AWG. De AWG wordt opgedeeld in stukken die elke met de meest efficiënte methode worden doorgerekend.	xxvi
4	(a) Measured spectral response of 16 ×400 GHz AWG. (b) Measured flattop spectral response of 12 ×400 GHz MMI -AWG.	xxvii
5	Basic operation of an AWG.	xxix
6	Fabricated silicon AWGs.	xxx
7	AWG simulation model. The AWG is broken up in parts, where each part is simulated with the most efficient technique	xxxii
8	(a) Measured spectral response of 16 ×400 GHz AWG. (b) Measured flattop spectral response of 12 ×400 GHz MMI -AWG.	xxxiii
1.1	Fabricated silicon photonics components (a) 220 nm thick silicon waveguide cross section [16]. (b) Fiber grating coupler to couple the light from fiber to the silicon wire [17]. (c) Ring resonator. (d) Arrayed waveguide grating (AWG).	4
1.2	History of arrayed waveguide grating/ Phasar / Waveguide grating router.	6
1.3	Optical image of a fabricated silicon AWG [16].	7
2.1	Diffraction of light through an aperture.	15
2.2	(a) Arbitrary spaced linear array of isotropic point sources. (b) Equally spaced linear array of isotropic point sources.	16
2.3	Array factor of an equally spaced uniform linear array with different number of sources.	18
2.4	Far-field of an array of Gaussians with a full 1/e-width of 614 nm, spaced 2μm, for different number of apertures at λ = 1550 nm . . .	19
2.5	Far-field of an array of Gaussians with a full 1/e-width of 614 nm with 4 μm aperture spacing in the array.	20

2.6	Far-field of an array of Gaussians with a full 1/e-width of 614 nm with variation of α	21
2.7	Schematic diagram of a 16×400 GHz AWG.	22
2.8	Schematic representation of insertion loss, insertion loss non-uniformity, free spectral range(FSR), neighbour channel crosstalk, phase error crosstalk, cumulative crosstalk and passband aspect ratio.	23
2.9	The light diverges in the input star-coupler after entering from the input aperture.	25
2.10	Operational diagram of an AWG.	26
2.11	The field distribution at the image plane of a 5 channel AWG with a variation of diffraction angle.	30
2.12	Schematic diagram of the AWG with ideal delay lines and with phase error affected delay lines.	31
2.13	Schematic diagram of the AWG with ideal delay lines and with phase error affected delay lines.	32
2.14	Schematic diagram of 16 × 400GHz Polarization diversity circuit.	34
2.15	Transmission scheme of a 5 × 5 wavelength router.	35
2.16	Possible design flow for a wavelength router. Boxes are user defined parameters and Circles are calculated parameters.	36
2.17	Possible design flow for a wavelength de/multiplexers. Boxes are user defined parameters and Circles are calculated parameters.	37
2.18	(a) Geometry of the confocal-type mounting (b) Geometry of the Rowland-type mounting.	38
2.19	Geometry of rectangular manhattan waveguide paths with single waveguide width.	40
2.20	Geometry of rectangular Manhattan waveguide paths with multiple waveguide width.	41
3.1	An AWG decomposition for simulation.	49
3.2	An example of a AWG definition in IPKISS, with user defined parameters, mask layout (GDSII view) and a 2D representation of the 3D material distribution generation (virtual fabrication)	50
3.3	T-matrix approach to simulate the AWG.	52
3.4	The geometry used for CAMFR simulation and the field distribution of an aperture simulated by CAMFR.	53
3.5	The geometry used for the MEEP simulation, the refractive index distribution from the material distribution and the field distribution of the aperture simulated by MEEP.	54
3.6	Free space propagation from the central input to the central output of the star-coupler.	55

3.7	Analytically simulated field distribution of an star-coupler.	56
3.8	Free space propagation from an arbitrary input to an arbitrary output of the star-coupler.	56
3.9	Simulated transmission of an 1×16 channels star-coupler.	57
3.10	Waveguide phase error model.	58
3.11	Simulated spectral response of a 12×400 GHz MMI-AWG.	59
4.1	Overview of the fabrication process uses to fabricate the SOI based photonic device using 193 nm optical lithography.	65
4.2	The measurement setup for vertical coupling.	67
4.3	The automatic measurement setup using vertical coupling for photonics dies.	68
4.4	Normalization procedure for the AWG measurement.	69
4.5	Spectral responses of 4 channel AWGs with (a) 50 GHz (b) 100 GHz (c) 400 GHz and (d) 800 GHz channel spacing.	71
4.6	Spectral response of 8 channel AWGs with (a) 50 GHz (b) 100 GHz (c) 200 GHz and (d) 800 GHz channel spacing.	72
4.7	Spectral response of 32×200 GHz AWGs.	72
4.8	Variation of crosstalk with delay length	73
4.9	Crosstalk dependence on the design parameters.	73
4.10	Location of the four 8×400 GHz AWGs in the mask.	74
4.11	Crosstalk variation of the 8×400 GHz AWGs over the dies and within the die.	74
4.12	Deviation range Vs fitted channel spacing for (a) 12×100 GHz AWGs (b) 12×200 GHz AWGs.	75
4.13	Spectral response of 12×200 GHz AWGs using formula 1. Gray dashed lines indicates 201.9 GHz channel spacing grid.	76
4.14	Spectral response of 12×200 GHz AWGs using formula 2. Gray dashed lines indicates 201.9 GHz channel spacing grid.	76
4.15	Channel deviation for 12×100 GHz AWGs.	77
4.16	Channel deviation for 12×200 GHz AWGs.	77
4.17	optical image of the fabricated 16×400 GHz circular AWG.	78
4.18	Measured spectral response of the 16×400 GHz circular AWG.	79
4.19	Measured spectral response of the 16×200 GHz circular AWG.	79
4.20	Measured spectral response of the 16×100 GHz circular AWG.	80
4.21	Optical image of a fabricated S-shaped AWGs.	81
4.22	Measured spectral response of (a) 3×47 nm and (b) 3×40 nm S-shaped AWGs.	81
4.23	Measured spectral response of (a) 4×32 nm and (b) 3×24 nm S-shaped AWGs.	82
4.24	Optical image of a fabricated 8×200 GHz reflection type AWG.	82

4.25 Spectral response of a 8×200 GHz reflection type AWG.	83
4.26 Optical image of the fabricated AWGs.	84
4.27 Experimental spectral response of 4×100 GHz AWG with 28 waveguides used in the array.	86
4.28 Experimental spectral response of 8×250 GHz AWG with 40 waveguides used in the array.	86
4.29 Experimental spectral response of 12×400 GHz AWG with 70 waveguides used in the array.	87
4.30 (a) Insertion loss variation (b) non-uniformity variation (c) cross talk variation and (d) bandwidth variation with the variation of the number of waveguides used in the array waveguides for 4×100 GHz, 8×250 GHz and 12×400 GHz AWGs.	88
4.31 Fabricated (a) 400 GHz and (b) 200 GHz channel spaced 16 × 16 router.	89
4.32 Spectral response of 16 × 16, 400 GHz router for 1 st input.	89
4.33 Spectral response of 16 × 16, 400 GHz router for 8 th Input	90
4.34 Spectral response of 16 × 16 router of 400 GHz for all inputs	90
4.35 Spectral response of 16 × 16 router of 200 GHz for 1 st input	91
4.36 Spectral response of 16 × 16 router of 200 GHz for 8 th input	92
4.37 Spectral response of 16 × 16 router of 200 GHz for all inputs	93
4.38 Effect of mask discretization on the angled waveguides.	94
4.39 Optical image of the 8×400 GHz AWGs with 0°, 10°, 22.5° and 45° rotated layouts.	95
4.40 Spectral response of the 8×400 GHz AWGs with 0°, 10°, 22.5° and 45° rotated layouts.	96
4.41 The length deviation over the waveguides of 16 × 400 GHz AWG due to 1 nm and 5 nm grid snapping.	96
4.42 Simulated transmission spectrum of 16 × 400 GHz AWG (8th channel) for 1 nm, 5 nm and without grid snapping.	97
4.43 Experimental transmission spectrum of 16 × 200 GHz AWG using 5 nm and 1 nm grid snapping. Black line indicate the cumulative crosstalk power of the device.	98
4.44 Experimental transmission spectrum of 16 × 400 GHz AWG using 5 nm and 1 nm grid snapping. Black line indicates the cumulative crosstalk power of the device.	99
4.45 Fabricated 16× 200 GHz Polarization diversity circuit.	101
4.46 (a) Fabricated 2D grating coupler. (b) Schematic diagram of a 2D grating coupler with fiber align.	102

4.47 Spectral response of a 2D grating coupler connected to two 1D grating couplers for differently oriented input polarizations ((a) Pol-1: 90 degree, (b) Pol-2: -45 degree, c) Pol-3: 0 degree, (d) Pol-4: 45 degree oriented fiber polarizations with respect to the axis of the 2D grating).	104
4.48 Mapping of alignment tolerance for different oriented fiber polarizations ((a) Pol-1: 90 degree, (b) Pol-2: -45 degree, c) Pol-3: 0 degree, (d) Pol-4: 45 degree oriented fiber polarizations with respect to the axis of the 2D grating). (a) and (c) The solid line represents the transmission through waveguide $WG-1$. The dashed line represent the transmission through waveguide $WG-2$	105
4.49 Transmission of two 2-D grating couplers connected through waveguides. (a) Spectral response of the 2D grating for wavelength range of $1.48 \mu\text{m}$ to $1.56 \mu\text{m}$. (b) Flat passband spectral response of the 2D grating.	106
4.50 Spectral response of a 16 channels 200GHz polarization diversity wavelength de-multiplexer circuit for $Pol-1$ and $Pol-3$ polarizations.	106
4.51 (a) The output wavelength channel positions of the polarization diversity circuit for $Pol-1$, $Pol-2$, $Pol-3$, and $Pol-4$ polarizations. (b) Maximum shifted output channel. (c) Minimum shifted output channel.	107
4.52 Schematic diagram of $4 \times 20 \text{ nm}$ echelle grating.	109
4.53 Experimental result of AWGs (a) $4 \times 6.4 \text{ nm}$ (b) $8 \times 6.4 \text{ nm}$ (c) $4 \times 24 \text{ nm}$ and (d) $4 \times 32 \text{ nm}$	110
4.54 Experimental result of echelle grating (a) $4 \times 6.4 \text{ nm}$ (b) $8 \times 6.4 \text{ nm}$ (c) $4 \times 10 \text{ nm}$ and (d) $4 \times 20 \text{ nm}$	111
4.55 The estimated crosstalk mapping of (a) AWG and (b) echelle grating. (c) Estimated design of best performance de/multiplexers	112
5.1 Working principle of the AWG.	118
5.2 Spectral response profile calculated using overlap integral.	119
5.3 Schematic diagram of silicon MMI-AWG and 3D diagram of the MMI aperture used as an input aperture of the AWG.	120
5.4 Spectral response of the MMI-AWG calculated using overlap integral.	120
5.5 Working principle of the MMI-AWG for three wavelengths.	121

5.6	(a) Geometry of the MMI-aperture used in the simulations and actual design. (b)-(f) Simulated field distribution of the MMI-aperture for different widths. The black circular dots indicate, for a given MMI width, the optimal length for achieving a flat spectral response. The square dots in (d) indicate the positions 13 μm , 15 μm , 17 μm and 19 μm of the 5 μm wide MMI for which Fig. 5.8 shows the field distribution.	122
5.7	Simulated (a) field distribution of 4.0 μm , 4.5 μm , 5.0 μm , 5.5 μm and 6.0 μm wide MMI-apertures for optimal length (indicated as dot in Fig. 5.6) and (b) spectral response of the AWG using the corresponding MMI-apertures.	123
5.8	Simulated (a) field distribution at the end of the MMI for different lengths and (b) spectral response of the AWG using the corresponding MMI-apertures.	123
5.9	(a) Optical images of the fabricated 12 \times 400 GHz MMI-AWG. (b) Optical images of the fabricated MMI aperture. (c) Optical images of the fabricated waveguide array.	125
5.10	Simulated spectral response of 400 GHz AWG with variation of MMI lengths.	126
5.11	Simulation and experimental spectral response of the MMI-AWG with variation of the number of waveguides used in the waveguide array. Solid lines indicate the measurement results and dash lines indicate the simulation results.	126
5.12	(a) Passband width (passband width is normalized to the channel spacing.) vs. number of waveguides used in the waveguide array of the MMI-AWG. (b) Comparison of the aspect ratio between conventional-AWG and MMI-AWG.	127
5.13	Crosstalk vs. number of waveguides used in the waveguide array of the MMI-AWG.	128
5.14	Simulation Result of 12 \times 400 GHz MMI-AWG.	129
5.15	Measurement Result of 12 \times 400 GHz MMI-AWG.	129
5.16	1 dB, 3 dB and 10 dB bandwidth for 12 \times 400 GHz MMI-AWG. Associated non-uniformity is indicated in the graph.	130
5.17	Channel spacing variation of the 12 \times 400 GHz MMI-AWG.	131
5.18	Schematic diagram of a silicon MZI-AWG.	131
5.19	Transmission and Field distribution of the MZI.	132
5.20	Design methods of the MZI-AWG.	133
5.21	T-matrix simulation approach for the MZI-AWG.	134
5.22	Simulated spectral response of the central output channel of 9 \times 400 GHz silicon MZI-AWG.	135

5.23 Simulated spectral responses of the central output channel of 9×400 GHz silicon MZI-AWG with (a) 29 (b) 34 (c) 38 and (d) 58 waveguides in the array.	136
5.24 Simulated spectral responses of 9×400 GHz silicon MZI-AWG. . .	136
5.25 Working principle of cascaded AWG (a) AWG1 = AWG2 (b) FSR of AWG1 = channel spacing of AWG2.	137
5.26 Two methods of cascading AWGs.	139
5.27 (a) The image plane of fist AWG and the object plane of the second AWG overlap at one point. (b) The image plane of fist AWG and the object plane of the second AWG overlap by using a field lens. . . .	140
5.28 Simulation result of 7×400 GHz cascade AWG with a combination of (a) 2×200 GHz AWG, (b) 3×133 GHz, (c) 4×100 GHz (d) 2×100 GHz and 7×400 GHz.	141
5.29 Experimental result of 7×400 GHz cascade AWG.	142
6.1 Schematic diagram of a optical phase switch based on single stage modulation.	147
6.2 Schematic diagram of a interdigitated diode.	148
6.3 (a) Mask layout of the 1 × 4 silicon optical switch with 12 carrier-depletion based silicon modulators in the array (b) Enlarge portion an interdigitated diode.	149
6.4 Simulation of the 1 × 4 switch with 12 modulators in the array. . .	150
6.5 Optical power variation with (a) 1 st and (b) 6 th modulators are driven individually when all other modulators are inactive. Dots are indicating the measurement points where the solid lines are generated by the curve fitting.	151
6.6 Measured spectra of the 1 × 4 switch for (a) switching state 1 (b) switching state 2, (c) switching state 3 and (d) switching state 4. .	152
6.7 Schematic diagram of an AWG with heaters to tune the performance.	153
6.8 Heat profile of a heater on top of a silicon 450 nm wide waveguide. The image courtesy by Sarvagya Dwivedi.	154
6.9 Spectral response of the 4 × 200 GHz AWG for 2 nd output (blue line) before tuning and (red line) after tuning.	155
6.10 Spectral response of the 4 × 200 GHz AWG for 2 nd output (blue line) before tuning with the designed FSR and (red line) after tuning with half of the designed FSR.	156
6.11 Spectral response of the 4 × 200 GHz AWG for 2 nd output (blue line) before tuning by the designed FSR and (red line) after tuning with half of the designed FSR.	157
7.1 Mask layout of 12 × 2 nm Si ₃ N ₄ AWG with 60 waveguide in array. .	163

7.2	Cross-section of a fabricated Si_3N_4 waveguide. The image courtesy by Dr. A.Z. Subramanian.	164
7.3	Spectral response of the 8×2 nm Si_3N_4 AWG	164
7.4	Spectral response of the 12×1 nm Si_3N_4 AWG	165
7.5	Spectral response of the 12×0.5 nm Si_3N_4 AWG	166
7.6	Mask layout of the 6×100 GHz AWG for short wave infrared.	166
7.7	Measured spectral response of the 6×100 GHz AWG for short wave infrared.	167
7.8	Mask layout of the 6×200 GHz AWG for $3.8 \mu\text{m}$ center wavelength and mode profile of the single-mode waveguide cross sections ²	168
7.9	Measured spectral response of the 6×100 GHz AWG for short wave infrared.	169
7.10	Cross-section of a fabricated Ge waveguide. The image courtesy by Aditya Malik.	170
7.11	(a) Optical image of the fabricated 5×200 GHz Ge AWG with 36 waveguides (b) SEM image of input star-coupler. Image courtesy of Aditya Malik.	171
7.12	Spectral response of the 5×200 GHz Ge AWG (solid line) for TE polarization light (dash line) for TM polarization light.	172
A.1	Geometry of a circular manhattan waveguide paths.	186
A.2	Geometry of an angled waveguide paths with constant bend radius.	187
A.3	Geometry of an angled waveguide paths with variable bend radius.	188
A.4	Geometry of reflection type AWG with (a) rectangular manhattan and (b) angled waveguide paths.	189
A.5	MMI based reflectors (a) output looped shallowly etched MMI and (b) deep etched MMI with 45° facets.	190
A.6	Geometry of an angled waveguide paths with variable bend radius.	191

List of Tables

1.1	Comparison of AWGs for different materials	8
4.1	Design overview of the rectangular AWGs	70
4.2	Performance overview of the rectangular AWGs	71
4.3	Design overview of three AWG sets	79
4.4	Design overview of three AWG sets	85
4.5	Experimental performances overview of the 8×400 GHz AWGs with 0° , 10° , 22.5° and 45° rotated layouts	95
4.6	Comparison of AWG insertion loss (IL, center channel and outer channel) between 1nm and 5nm mask grid discretization.	100
4.7	Comparison of AWG crosstalk level (crosstalk [XT] and cumulative crosstalk [CXT]) between 1nm and 5nm mask grid discretization.	100
4.8	Comparison of size, insertion loss and crosstalk level between AWGs and Echelle gratings.	111
6.1	Performance of 1 × 4 switch at 1.52 μm wavelength.	152
8.1	State of the art of Silicon AWGs	179

List of Acronyms

A

AWG	Arrayed Waveguide Grating
AF	Array Factor

C

CMOS	Complementary Metal-Oxide-Semiconductor
CS	Channel Spacing
CXT	Cumulative Crosstalk
CWDM	Coarse Wavelength Division Multiplexing

D

DBR	Distributed Bragg reflector
DFB	Distributed Feedback
DWDM	Dense wavelength division multiplexing

F

FPR	Free Propagation Region
FSR	Free Spectral Range
FDTD	Finite Difference Time Domain

I

ICL Interband Cascade Laser

L

LAN Local Area Network

M

MAN Medium Area Network

MMI Multi Mode Interferometer

MZI Mach-Zehnder interferometer

O

OPA Optical Phased Array

OPS Optical Packet Switch

P

PDL Polarization Dependent Loss

PCG Planner Curve Grating

Q

QCL Quantum Cascade Laser

S

SOI Silicon on Insulator
SWI Short Wave Infrared

W

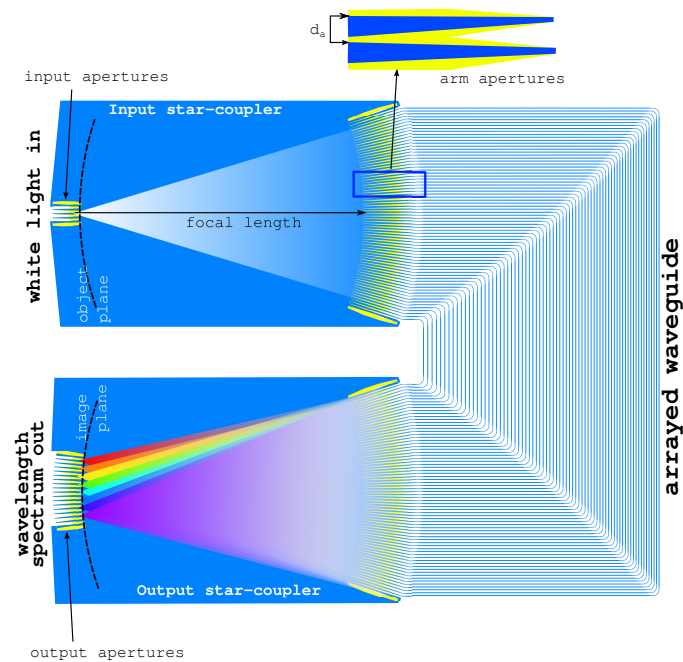
WDM Wavelength Division Multiplexing
WGR Wavelength Grating Router

Y

XT Crosstalk

Nederlandstalige Samenvatting

Optische communicatiesystemen worden ingezet voor een groeiend aantal toepassingen en diensten zoals breedbandinternet, kabeltelevisie en datatransport over kortere afstanden. De fysische drager van deze communicatienetwerken is de optische vezel, die meerdere golflengtekanalen ondersteunt via *wavelength division multiplexing* (WDM). Sinds de vroege jaren 90 zijn *Arrayed Waveguide Grating* (AWG) een van de meest gebruikte componenten in WDM systemen voor het (de)multiplexen van verschillende golflengtekanalen.



Figuur 1: Algemeen werkingsprincipe van de AWG.

AWG's zijn gebaseerd op een bundel van dispersieve optische vertragslijnen, zoals geschetst in Figuur 1. Het binnenkomende licht wordt verdeeld over de bundel in een eerste sterkoppelaar. Afhankelijk van de golflengte zal het

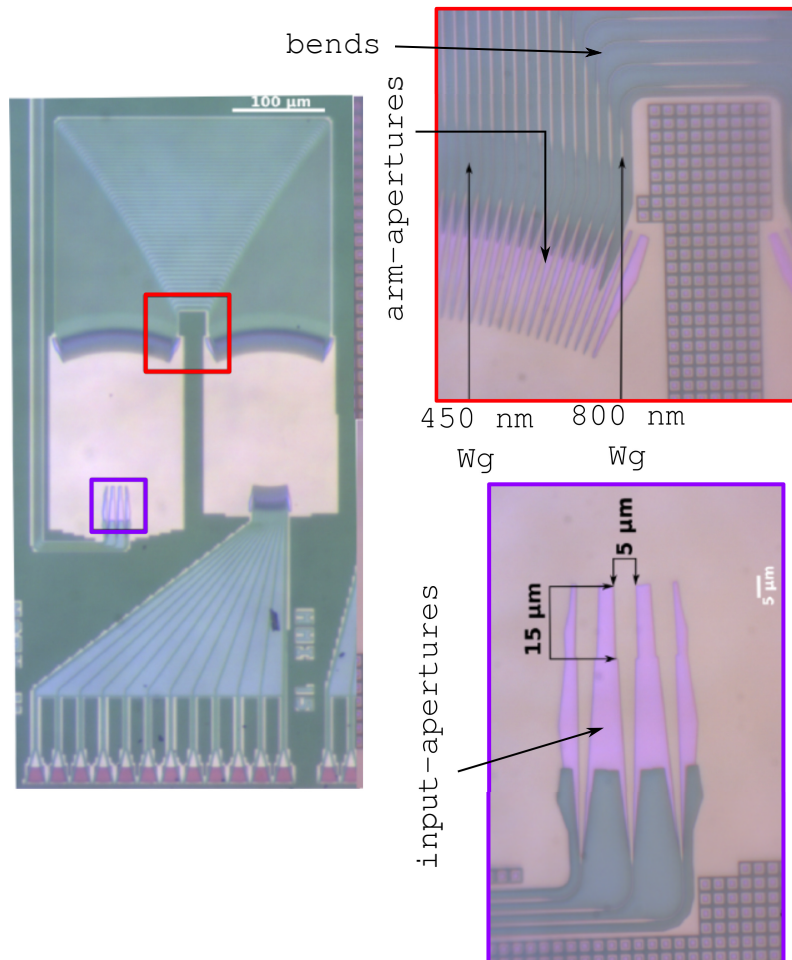
licht dan in een andere uitgang van de tweede sterkoppelaar worden geprojecteerd. Dit concept kan gerealiseerd worden in verschillende materiaalsystemen en voor verschillende golflengtegebieden. Elk materiaalplatform zal uiteraard andere mogelijkheden bieden en specifieke beperkingen opleggen voor zowel de sterkoppelaars als de golfgeleiderbundel. In materiaalsystemen met een laag indexcontrast, zoals *silica-on-silicon* of InP is een voldoende grote bochstraal nodig voor de golfgeleiders waardoor de AWG een grotere oppervlakte zal innemen. Dit is uiteraard niet bevorderlijk voor de integratie van meerdere componenten in een enkel circuit.

Wij kiezen voor een silicium-gebaseerd platform (*Silicon Photonics*). In *Silicon-on-Insulator* (SOI) is een sterk brekingsindexcontrast mogelijk waardoor golfgeleiders en bochten grootteordes compacter kunnen zijn. Daardoor kunnen in principe meer componenten in complexere circuits samengebracht worden. Bovendien laat het materiaal ook toe om CMOS technologie in te zetten voor de fabricage.

Anderzijds speelt het hoog brekingsindexcontrast ook in ons nadeel, omdat het licht in de golfgeleiders veel sneller fasefouten opstapelt. Daardoor zullen silicium golflengtefilters een grotere overspraak vertonen. Dit beperkt de mogelijke implementaties voor AWGs, in het bijzonder voor toepassingen met veel golflengtekanelen of een hoge resolutie: Daarvoor zijn immers veel en lange vertraginglijnen nodig in de golfgeleiderbundel. Een bijkomend nadeel van ons materiaalstelsel is dat het zeer polarisatiegevoelig is. Wij hebben AWG's gedemonstreerd voor een enkele polarisatie, en om polarisatie-ongevoelige circuits te realiseren hebben we het principe van polarisatie-diversiteit toegepast.

Theorie en Ontwerp

Zoals in Fig. 1 wordt getoond, bestaat een AWG uit twee sterkoppelaars en een bundel golfgeleiders met een constant lengteverschil. Het werkingsprincipe van de AWG is gebaseerd op dat van een *phased array* met identieke stralings-elementen en een constant faseverschil tussen opeenvolgende elementen. Het licht komt binnen in de eerste sterkoppelaar en diffracteert in het vlak van de chip om dan opgevangen te worden door de verschillende golfgeleiders van de bundel. Bij de propagatie door de golfgeleiderbundel zal het licht een faseverschuiving ondergaan. Het verschil in faseverschuiving tussen de opeenvolgende golfgeleiders in de bundel is constant tussen twee bundels, maar golflengteafhankelijk. Dit golflengteafhankelijke faseverschil vertaalt zich in de tweede sterkoppelaar naar een verschillende positie van het beeld: afhankelijk van de golflengte aan de input zal het licht op een andere plaats geprojecteerd worden, waar het kan opgevangen worden door een uitgangsgolfgeleider. Op



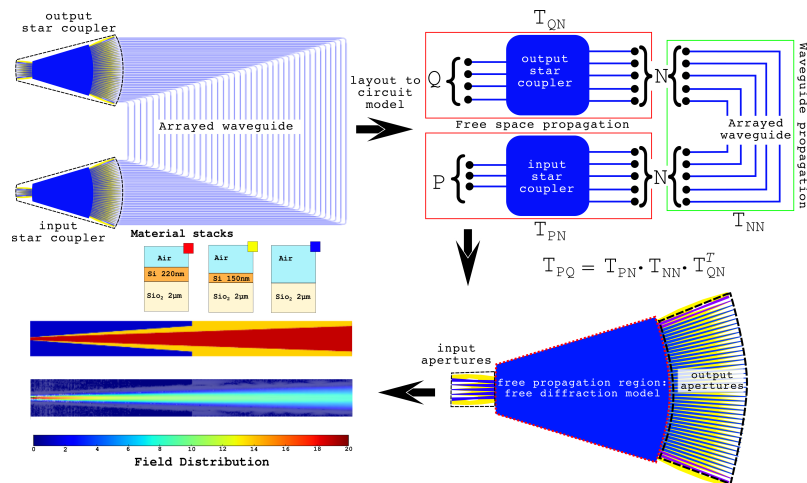
Figuur 2: Gefabriceerde AWG's in silicium.

basis van deze theorie hebben we alle formules afgeleid om AWG's te ontwerpen voor verschillende applications, zoals *(de)multiplexing* en *routing*. Uit de ontwerpparameters wordt dan de *layout* van de fabricagemaskers afgeleid. Dit hebben we gedaan voor verschillende materiaalsystemen en golflengtes, alsook verschillende geometrieën van de golfgeleiderbundel.

AWG model

Om AWG's te simuleren hebben we een semi-analytisch model ontwikkeld en dat toegevoegd aan de IPKISS ontwerpsoftware. IPKISS biedt een uitbreid-

baar parametrisch raamwerk dat eenvoudig kan herbruikt worden in verschillende technologieën. Ontwerpregels en technologiedata worden orthogonaal op de bibliotheek gedefinieerd. Ons model simuleert de transmissiematrices (T-matrix) van alle onderdelen met de meest geschikte simulatietechniek. In Figuur 3 wordt geschetst hoe de AWG eerst wordt opgedeeld in 3 stukken: de beide sterkoppelaars en de golfgeleiderbundel. De sterkoppelaars worden op hun beurt ook weer opgesplitst in de ingangs- en uitgangsaperturen en het gebied met vrije propagatie (*free propagation region* of FPR). De aperturen worden numeriek gesimuleerd op basis van eigenmode-expansie (CAMFR), en de berekende veldprofielen worden als excitatie gebruikt voor de FPR, die analytisch wordt doorgerekend op basis van 2-D Fresnel diffractie. De veldoverlap tussen het gediffracteerd licht en de uitgangsaperturen geeft dan de resulterende T-matrix van de sterkoppelaar. Het golfgeleidermodel is eenvoudig gehouden, en bestaat uit een analytische propagatie van de grondmode, rekening houdende met golflengtedispersie en stochastische fasefouten. Een matrixvermenigvuldiging geeft dan de uiteindelijke T-matrix van de volledige AWG.

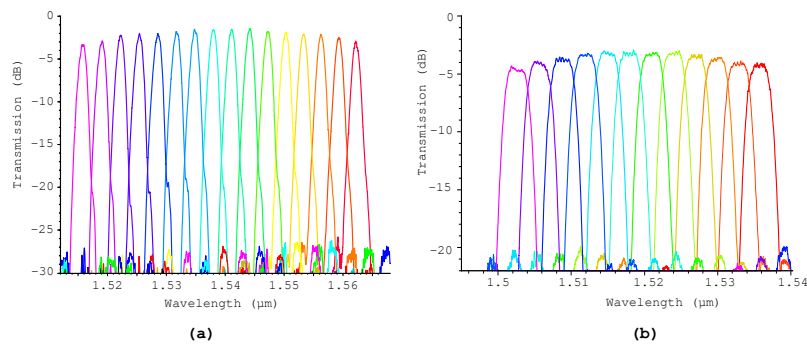


Figuur 3: Simulatiemodel van de AWG. De AWG wordt opgedeeld in stukken die elke met de meest efficiënte methode worden doorgerekend.

Experimental

We hebben AWG's ontworpen met verschillende geometrieën voor de golfgeleiderbundel. Dit bevestigde de eerdere experimenten die aantoonde dat een rechthoekige layout het voordeligst is in silicium. We fabriceerden AWGs met

4 tot 32 kanalen en 50-800 GHz kanaalspatiering. We introduceerden verbeteringen in het ontwerp, zoals monomode-multimode golfgeleiders, alsook verbeteringen in de fabricage zoals een reductie van het discretisatieraster. Hiermee demonstreerden we 16×400 GHz AWGs met een overspraak van -27dB en een transmissieverlies van slechts -1.5 dB. Dit resultaat is weergegeven in Figuur 4a. We ontwikkelden ook een S-vormige AWG voor grote kanaalspatiering, met een goede performantie bij kanaalspatieringen tussen 2000 GHz en 6000 GHz.



Figuur 4: (a) Measured spectral response of 16×400 GHz AWG. (b) Measured flattop spectral response of 12×400 GHz MMI-AWG.

De gebruikelijke spectrale respons van een AWG kanaal heeft een gaussiaans verloop, maar voor veel toepassingen is een vlakke respons wenselijk, of zelfs een vereiste. Om hieraan te voldoen wordt aan de ingangsstructuur aangepast met een multi-mode interferometer (MMI), of uitgebreid met een Mach-Zehnder interferometer (MZI) of zelfs een tweede AWG. We demonstreerden een compacte 12×400 GHz MMI-AWG met een afgevlakte respons, zoals weergegeven in Figuur 4b. Het transmissieverlies, de overspraak en de niet-uniformiteit waren respectievelijk -3.29 dB, -17.0 dB and 1.55 dB.

We toonden polarisatie-onafhankelijke multiplexering aan met behulp van *polarisation diversity*: Het binnenkomende signaal uit een optische vezel, en met een onbekende polarisatie, wordt ontbonden in twee orthogonale polarisaties die elk naar een eigen circuit worden gekoppeld. Die individuele circuits die nominaal identiek zijn verwerken het licht afzonderlijk en de resultaten worden op het einde opnieuw samengevoegd. We demonstreerden een 16×200 GHz demultiplexer met twee AWGs en 2D koppelroosters voor het splitsen van de polarisaties. Het geschatte verlies tussen de ingangs- en uitgangsvazel is -15 dB. Het on-chip verlies en de overspraak door de AWG is respectievelijk -2.6 dB en -21.5 dB. De grootste golflengteverschuiving ten gevolge van de polarisatie is slechts 0.12 nm. Het polarisatie-afhankelijk verlies varieert tussen 0.06 dB en 2.32 dB.

De toepassing van een AWG is niet beperkt tot golflengtefilters. Als we een AWG van nulde orde combineren met elektro-optische modulatoren kunnen we een optische schakelaar bouwen. One demonstratie van een 1×4 optische schakelaar heeft een transmissieverlies van -6.0 dB en een overspraakniveau van -13.6 dB.

Tenslotte toonden we de algemene inzetbaarheid van de AWG-theorie, -ontwerpmethodes en -simulatie aan door AWGs te implementeren in verschillende materiaalsystemen en voor verschillende golflengtegebieden. Door de nodige materiaalparameters en een beschrijving van het fabricageproces toe te voegen, konden we AWG's maken in siliciumnitride voor het zichtbare spectrum, silicium AWGs voor het kortegolfinfrarood bereik, en AWG's in germanium voor mid-infrarood golflengtes.

Conclusie

In dit werk voerden we een uitgebreide studie uit rond AWG's op een siliciumfotonica platform. We ontwikkelden een ontwerpprocedure en simulatiesoftware en hiermee demonstreerden we wereldklasse componenten voor golflengtemultiplexering en -routing in het gebied rond 1550 nm. We breidden dit ook uit naar andere golflengtegebieden en materiaalsystemen.

English summary

Optical communications systems are being deployed for ever more communication services, from high speed internet to telephone, cable television and short-range datacom. The backbone of this networking is the multi-wavelength optical fiber link based on wavelength division de/multiplexing (WDM). Since the early 1990s, Arrayed Waveguide Grating (AWG) based devices have been a key component in these WDM systems, allowing for demultiplexing and routing of wavelength channels.

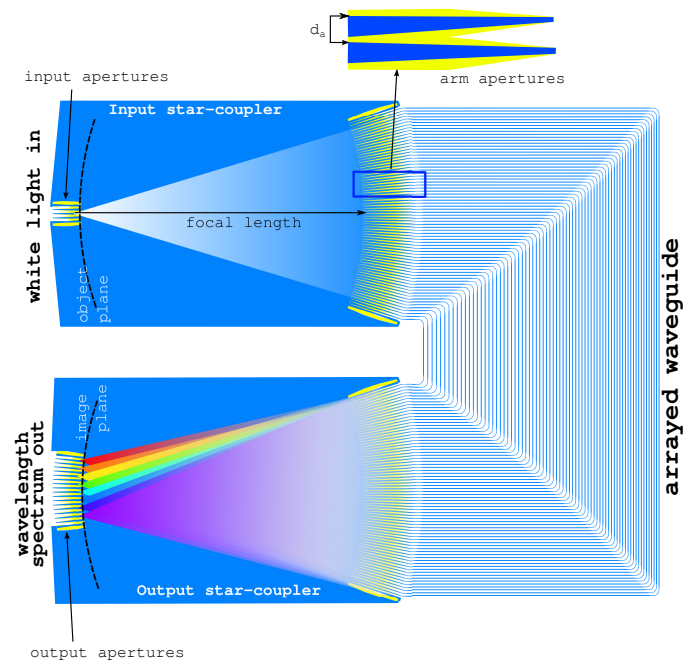


Figure 5: Basic operation of an AWG.

AWGs are based on a set of dispersive optical delay lines. This is illustrated in Figure 5. Light is distributed over the waveguides by a first star coupler, and depending on the wavelength, the light will be projected from one input to a

different output in the second star coupler. This principle can be realized in different material platforms and cover various wavelength ranges. Different platforms impose different design restrictions and opportunities for both the star couplers and the array waveguides. In low-contrast waveguides, such as silica-on-silicon and InP, bend radii will be large, resulting in relatively large devices. This is not beneficial for the integration of many additional functions on a single chip. Our platform of choice is silicon photonics. In silicon-on-insulator (SOI) the high contrast waveguides and the sharp bend radius allow to reduce the size of the device by several orders of magnitude. Therefore Si-based devices have a better potential to integrate a large number of components on a single chip. In addition, the compatibility with CMOS process technology allows the use of high-end fabrication facilities.

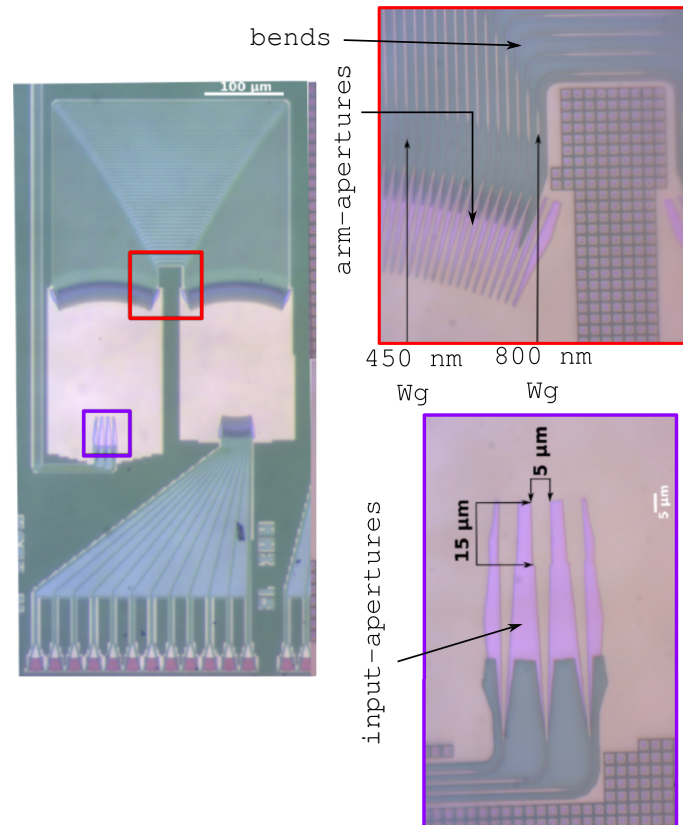


Figure 6: Fabricated silicon AWGs.

On the downside, the high refractive index contrast waveguides are very sensitive to phase errors. As a result wavelength dependent silicon devices still ex-

perience a relatively high crosstalk. This limits the implementation of the silicon AWGs challenging, especially in devices with high resolution and many channels, which require longer and more delay lines in the waveguide array. In addition to that, silicon high contrast waveguides are strongly polarization sensitive, making a polarization-insensitive circuit difficult. We demonstrated AWGs for a single polarization state, and used polarization diversity to realize a polarization independent circuit.

Theory and Design

As illustrated in Fig. 5, an AWG consists of two star-couplers and an array of waveguides with constant successive increment of length. The working principle of an AWG is based on the optical phased array, which have identical elements and constant phase difference between the successive elements. The light enters into input star-coupler and diverges. This diverging light beam is then coupled in an array of waveguides and propagates through these waveguides to a second star-coupler. During the propagation through the array waveguide the light, depending on its wavelength, accumulates a constant phase difference successive apertures in the second star-coupler. This phase difference will result in a lateral shift of the image in the second star coupler. As the phase difference is wavelength dependent the output location of the image will also be wavelength dependent, and output waveguides can be placed in the second star coupler to collect the light. Using this theory we derived all the necessary formulas to design the AWG parameters for different applications (demultiplexing and routing) and automatically generate the required mask layouts for fabrication. We did this for different materials and wavelength ranges, and different geometries of the waveguide array.

AWG model

To simulate the AWG we developed a semi-analytical model integrated with our design software (IPKISS). IPKISS is a modular framework: the components are based on parametric cells, which can be reused, modified and are portable between the technologies. Technology information then adds the default design rules and fabrication information. Our model simulates the transmission matrices (T-matrix) of all parts of the AWG using the most suitable simulation method. As shown in Figure 7, we divide the AWG in three parts: two star-couplers and the waveguide array. The star-couplers are again split up: the input and output apertures, and the free propagation region (FPR). The apertures are simulated numerically using eigenmode propagation (CAMFR), and

the calculated field-profile at the end of the aperture is used as the input for the FPR, which is solved analytically using a 2D Fresnel-diffraction scheme. Field overlaps between the diffracted fields in the FPR and the fields in the apertures is used to calculate the input-to-output transmission in the star couplers. The waveguides model is a simple propagation models based on length and incorporating dispersion and stochastic phase errors. A final T-matrix multiplication then gives the complete transmission of the AWG.

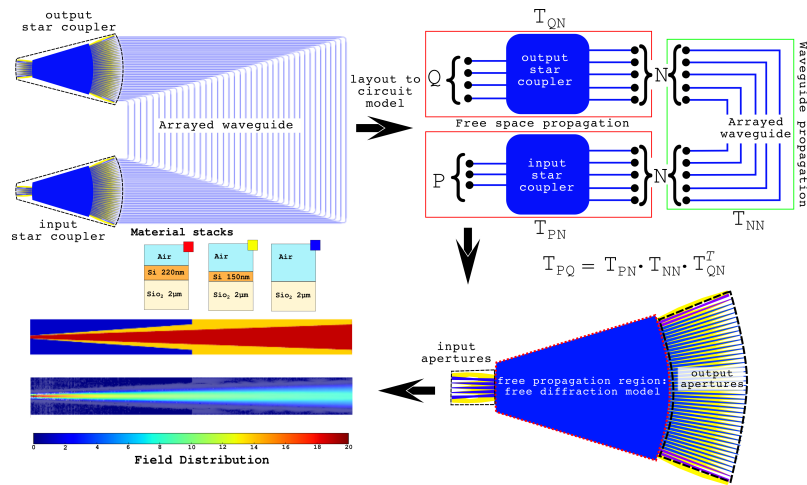


Figure 7: AWG simulation model. The AWG is broken up in parts, where each part is simulated with the most efficient technique

Experimental

We designed AWGs with different geometries of the waveguide array. With our experience based on previous tests we found that the rectangular shaped AWG is the best choice for silicon. We fabricated from 4 channels to 32 channels AWG with 50 GHz to 800 GHz channel spacing. Using design improvements like the single mode - multimode waveguide combination in the array and fabrication improvements like a smaller mask grid we demonstrated a.o. 16×400 AWGs with a crosstalk of -27 dB and the insertion loss of -1.5 dB. This particular result is shown in Fig. 8(a). We also introduced S-shaped AWGs for very large channel spacings, demonstrating decent performance for channel spacing from 2000 GHz to 6000 GHz.

The spectral response of a conventional AWG channel is Gaussian-like, but for many applications a flat spectral response is preferred, or even necessary.

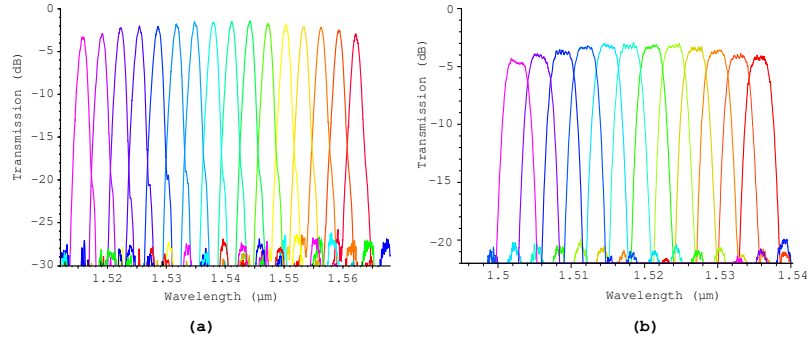


Figure 8: (a) Measured spectral response of 16×400 GHz AWG. (b) Measured flat-top spectral response of 12×400 GHz MMI-AWG.

To fulfil this requirement, the commonly used methods are using a Multi-Mode Interference Coupler (MMI) and Mach-Zehnder Interferometer (MZI) as a input of the AWG, or even a cascaded AWG. We demonstrated compact 12×400 GHz MMI-AWG with a flattened spectral response. Insertion loss, crosstalk and non-uniformity are -3.29dB, -17.0dB and 1.55dB respectively (spectral response shown in Fig. 8(b)).

Polarization independent de/multiplexing is demonstrated by using a polarization diversity scheme: incoming signals with an unknown polarization are split into two orthogonal polarizations which are then coupled separately in two identical single polarization circuits. We demonstrated 16×200 GHz polarization diversity wavelength de-multiplexer circuit using two silicon AWGs and 2D grating couplers. Estimated fiber to fiber loss is better than -15.0dB. Insertion loss and crosstalk induced by the AWGs are -2.6dB and -21.5dB, respectively. The maximum polarization dependent wavelength shift is 0.12nm. The polarization dependent loss varies between 0.06dB and 2.32dB

The concept of the AWG is not limited to wavelength filter applications. By using a zero order waveguide array and carrier depletion type modulators we demonstrated a silicon optical switch. The 1×4 switch has a measured insertion loss of -6.0 dB and crosstalk of -13.6 dB.

Finally we experimentally demonstrated the general applicability of the theory, design and simulation by designing the AWGs for different material systems and wavelength ranges. By providing an appropriate material information and a description of the fabrication process flow, we could demonstrate silicon nitride AWGs for visible wavelengths, silicon AWGs for short wave infrared and mid-infrared and germanium AWGs for mid-infrared wavelength.

Conclusion

We made an in-depth study of the potential of AWGs based on a silicon photonics platform. We developed a design procedure and a simulation tool through that demonstrated state-of-the-art devices for wavelength multiplexing and routing around 1550nm. We also extended this to other wavelength ranges and material systems.

1

Introduction

“the quantum theory of light cannot be considered satisfactory since it defines the energy of a light particle (photon) by the equation $E=hf$ containing the frequency f . Now a purely particle theory contains nothing that enables us to define a frequency; for this reason alone, therefore, we are compelled, in the case of light, to introduce the idea of a particle and that of frequency simultaneously.”

– Louis de Broglie

1.1 Photonics

The demonstration of the first semiconductor laser in 1962 [1] along with the rapid development of optical fiber form the foundations of the modern optical communication network. This development has opened a new research area, which deals with generation, transmission, modulation, amplification and detection of light. The research field has been titled photonics across the globe as it deals with photons in analogy to electronics where one deals with electrons. In short, according to the Merriam-Webster Dictionary "pho-ton-ics : a branch of physics that deals with the properties and applications of photons especially as a medium for transmitting information."

Over the last 3 decades there has been an exponential increase in the data traffic sent over global communication networks. This coupled with the fact that round the clock connectivity is a must, has pushed traditional electronics links on backfoot and has forced researchers to look in optical communication circuits on a complete system level. Thus the necessity of high speed data transfer is main driving force behind photonics. Today, computing is no longer limited by the speed of the transistors but by the short range and long range communication speed. Optical telecommunication [2] became attractive for long distance communication because of the high-performance semiconductor lasers, low-loss optical fibers and erbium-doped fiber amplifiers and the advantages of the optical fiber over metallic wires: low loss, low crosstalk, huge bandwidth. These advantages allowed optical communication to migrate from long haul backbones to the network edges, developing metropolitan area networks (MANs) [3] and campus-level local area networks (LANs) [4]. The challenge is to realize efficient and cheap optical solutions also for short distance board-to-board, chip-to-chip and intra-chip communication. To make this happen an integrated optical solution is promising. The requirement for more integrated optical solutions is pushing photonics towards more miniaturization similar as what happened with integrated electronics. As a result photonics integrated circuits (PICs) now gradually replace discrete optical components and allow to obtain multiple functionalities on a single chip.

Integrated photonics of course has its own share of drawbacks when compared with electronics. There is no single material to realize all the functionalities in photonics, unlike in electronics where the majority of the circuits are silicon based. The main reason is that silicon itself can't emit light because of its indirect bandgap. Still, efforts have been made in this direction and e.g. an optically pumped Raman silicon laser was demonstrated in 2005 [5]. But due to the optical pumping, the laser emits very little light and therefore it is thus far not promising for real life applications. At this point, a III-V materials based light source has to be integrated on a silicon photonics chip [6, 7]. Another draw-

back of photonics devices is that they have critical dimensions in the order of the wavelength. These critical dimensions are uncorrelated to the fabrication limitations. As an example, even if we improve the minimum fabricated feature size, the minimum gap required between two waveguides to avoid inter channel coupling will remain the same. Therefore also the overall device size will remain the same. Another disadvantage of photonics is that it doesn't have a basic component like electronics has the transistor.

As we discussed before integrated photonics has developed in several material systems. The most common of these are Silica-on silicon, III-V semiconductor materials, Lithium Niobate (LiNbO_3) and Silicon-on-insulator. The required condition is that the waveguide core material should have a higher index than the cladding material and both should be transparent in the operation wavelength region.

1.1.1 Silica-on-silicon

On a silicon substrate a higher doped silica is used as a core where undoped silica is used as a cladding. In general due to the doping the core has higher refractive index (in the order of 2% or lower) compare to the cladding [8, 9]. The waveguides fabricated in this low index contrast material require a large bend radius which increases the device footprint and decreases the integration density. Although this technology is very robust and mature, it is unsuitable for on-board or on-chip interconnects. Moreover, on this platform it is difficult to realize active devices.

1.1.2 III-V Semiconductor materials

GaAs and InP-based materials are used for fabricating active photonics devices. These materials are suitable for both optical and electrical functionalities due to the direct bandgap. Over the last decades these materials have not only been used for fabrication of semiconductor lasers but also for passive optical devices. This combination is the main advantage of this material platform [10]. The disadvantages are that it is expensive, has a lower-yield processing technology and lower integration density. The index contrast increases relative to silica-on-silicon but still the device size in general is bigger and hence less suitable for e.g. on-chip interconnects.

1.1.3 Lithium Niobate (LiNbO_3)

Lithium niobate is suitable for electro-optical modulation [11], acousto-optic devices and non-linear optics, but the high cost complex process makes it less suitable for large scale integration. In this material platform it is possible to

realize passive optical devices but not possible to realize the active device like laser and detectors.

1.1.4 Silicon photonics

In silicon photonics a silicon waveguide layer is used as a core on top of a buried oxide which acts as its lower cladding [12]. The refractive index of this silicon core layer and the oxide are 3.476 and 1.444 for 1500 nm wavelength, respectively. Other than the CMOS compatibility [13] this high index contrast increase the confinement of the light into the core material which makes it easier to realize smaller bend radii and guide light more efficiently [14]. A direct consequence is that the device footprint reduces significantly [15]. This makes the integration density very high. Figure 1.1 shows some silicon photonics components fabricated by using imec's CMOS pilot line process. As the light is highly confined in the core it also can result in non-linear processes.

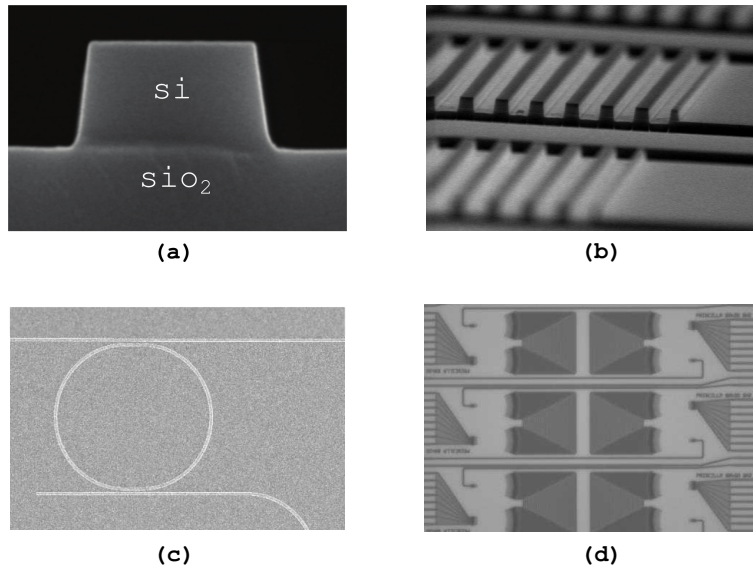


Figure 1.1: Fabricated silicon photonics components (a) 220 nm thick silicon waveguide cross section [16]. (b) Fiber grating coupler to couple the light from fiber to the silicon wire [17]. (c) Ring resonator. (d) Arrayed waveguide grating (AWG).

The main disadvantage is that the waveguides are highly sensitive to fabrication and design imperfections. Sometime the required gap for the waveguide coupling can be smaller than the minimum feature size. The sidewall roughness introduced during the waveguide etching or the thickness variations of the

wafer have significant impact on the device performance. On top of this the silicon waveguides are strongly birefringent and have significant temperature dependence.

1.2 Wavelength division multiplexing

Today optical circuits are used in all telecommunication networks. The backbone of this network is the optical fiber. To maximize the data density in this optical fiber multiple carrier wavelengths are used. This is called wavelength division multiplexing (WDM). To do that wavelength de/multiplexers are used. A multiplexer combines all the wavelength channels on a single fiber and a demultiplexer separates the wavelengths from a single fiber to the multiple wavelength channels. Therefore these WDM components are essential for the modern telecommunication network.

There are four common wavelength filters which can be used in WDM systems [16]: ring resonators, Mach-Zehnder interferometers (MZI), echelle diffraction gratings and arrayed waveguide gratings. By using single or multiple rings or MZI in a quasi periodic manner it is possible to design single channel wavelength filters. The multiple rings or MZIs are combined in order to obtain better bandwidth and roll-off. In the ring the feedback introduces very sharp channel selection, where the MZI has a simple sinusoidal filter characteristic. As the MZI doesn't introduce feedback the filter does not suffer from unwanted nonlinear effects. By using multiple such filters in parallel it is possible to design $1 \times N$ multiplexing or demultiplexing and $N \times N$ routing of many channels. However, single-component optical filters exist which are capable of multi-channel de/multiplexing. These are mainly the echelle grating and the arrayed waveguide grating (AWG). In this work, we study AWGs in silicon. A detailed comparison is given in chapter 4.

1.3 Arrayed waveguide grating

An arrayed waveguide grating (AWG) consists of two star-couplers and an array of waveguides with linearly increasing length. A star-coupler is nothing but a $1 \times N$ or $N \times N$ splitter/combiner. In 1988 Smit demonstrated first a device consisting of a parallel array of curved ridge waveguides in Al_2O_3 exploiting optical angular dispersion [18]. In the same year Dragone published the star-coupler [19]. In 1989 Smit and Vellekoop submitted a paper (published in 1991) demonstrating the phased array [20]. In this design the light is coupled to an array of circular waveguides by using slab propagation and the waveguides are terminating on an arc before reaching the points with output waveguides. This

coupling in/out to the waveguides array is similar to that used in Dragone's star-coupler. Two months later Takahashi submitted a waveguide array similar to

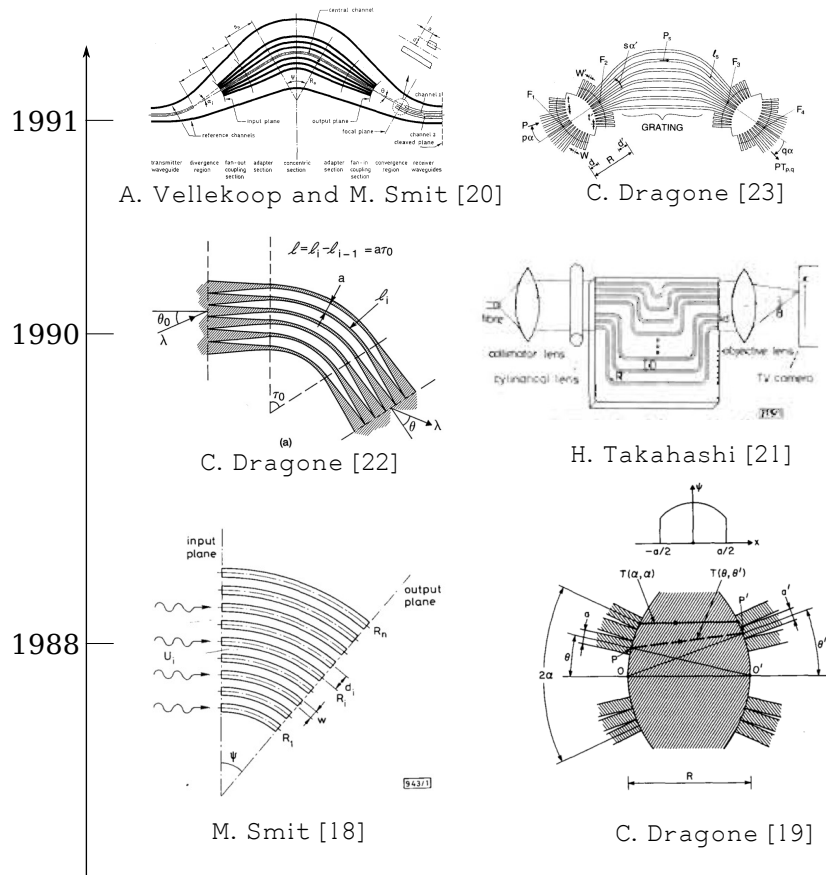


Figure 1.2: History of arrayed waveguide grating/ Phasar / Waveguide grating router.

Smit's phased array using external lenses to couple the light in and out of the chip which is similar to a free-space star-coupler [21]. One day after Takahashi's submission date, Dragone submitted the design of the waveguide grating router (WGR) [22]. In 1991 Dragone experimentally demonstrated the WGR [23].

Summarizing we can say that the AWG was developed individually by three separate groups during the early 90's. Each of these three groups gave different names to this device: Dragone's group called it the WGR (which we use for $N \times N$ de/multiplexers), Smit's group called it the PHASAR, and Takahashi's group called it the arrayed waveguide grating (AWG) (which we will use in this

work). A figure detailing this historical development ¹ is shown in Fig. 1.2.

1.4 Silicon AWG

After the first demonstrations of AWGs a lot of materials have been used to realize de/multiplexing. Table 1.1 shows an overview of the typical performance of AWGs fabricated in different material systems. More than two decades later low loss compact silicon waveguides [25] fabricated using a CMOS pilot line fabrication process were demonstrated by several groups (imec-Ghent university, Leti, IBM etc.). The tight bends and high contrast silicon waveguide allow to realize a compact AWG. But these high contrast waveguides are highly phase error sensitive for the same reason. Therefore this compact silicon AWG experienced a high crosstalk compared to those fabricated on a low index contrast material platform. Other than that the silicon AWG suffers from high polarization and temperature sensitivity. Over the years a lot of design modifications have been applied to improve the performance and also the fabrication process matured considerably. Today, and partly as a consequence of this work (see next section) the performance of silicon AWGs has reached a comparable level to that of low index contrast material platforms in terms of loss and crosstalk. A polar-

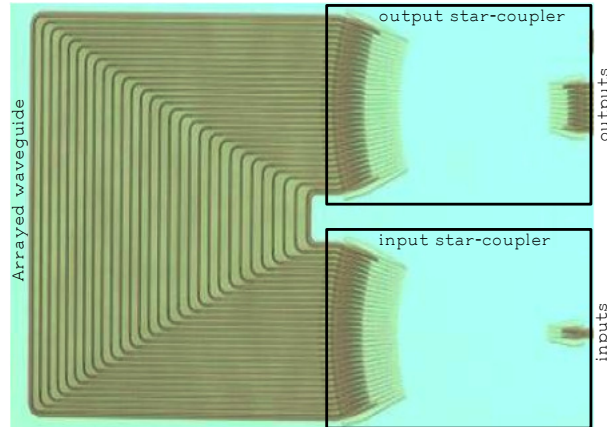


Figure 1.3: Optical image of a fabricated silicon AWG [16].

ization insensitive spectral response is achieved by using polarization diversity approach [26, 27]. The main requirement for being able to use a polarization diversity approach is to have two identical AWGs which is now possible to realize using accurate CMOS fabrication processes.

¹adapted from [24]

AWG Device Type	Channel Spacing (GHz)	Channel Number	Bend Radius (μm)	Crosstalk (dB)
Slica [28]	50	64	5000	-40
Silica [29]	25	400	2000	-25
InP [30]	10	100	500	-17
InP [31]	50	64	500	-25
Silicon [16] UGent-imec (2010)	400	8	5	-24

Table 1.1: Comparison of AWGs for different materials

The temperature dependence is still an issue. Although a lot of theoretical approaches have been proposed and demonstrated using a negative temperature coefficient based cladding but they are not suitable for a practical application as these approaches reduce the device performance significantly.

1.5 Objective

The primary goal of this work was to study arrayed waveguide gratings with WDM compatible specifications, designed and fabricated in the silicon-on-insulator platform with CMOS based wafer scale fabrication technology. The objective was to improve the performance level towards that of lower index material platforms in terms of loss and crosstalk, which would allow to use these device in optical networks. Also reaching higher resolution (lower channel spacing) and larger channel counts, as required in real optical networks, was an important objective. A further target was to demonstrate AWG devices with flattop spectral response, which have many advantages e.g. to compensate for wavelength drift in the network, fabrication inaccuracies and temperature related shifts. Above all our aim was to develop a generic design and simulation environment, practical not only for silicon based AWGs but also for other material systems and allowing to extend the application of AWGs to other applications, in other wavelength ranges.

1.5.1 Overview

In chapter 2, a review of the theory and the design of the AWG is presented. After introducing the design parameters the characteristics of the AWG are discussed. A number of different geometrical designs of the AWG are introduced. In chapter 3, an overview of the semi-analytical simulation model of the AWG is introduced. As this simulation model is integrated with the design framework IPKISS

a discussion about the integration also introduced. Experimental demonstration of the AWG is discussed in chapter 4. In this chapter the focus is on the SOI material platform with 1550 nm as a central wavelength. The experimental works described in three parts from various geometries to various applications. Fabrication dependence of the AWG also discussed in this chapter. In addition to that we discuss a polarization diversity circuit for polarization independent de/multiplexing. Finally we compare the experimental results of the AWGs with echelle gratings. In chapter 5 we discuss about the theoretical and experimental demonstration of a flattop spectral responses using MMI, MZI and an AWG as the input of the AWG. The demonstration of optical switching is discussed in chapter 6. The switching is obtained by using electro-optical phase shifters. Using the phase shifters tuning of the AWG performance is also discussed in this chapter. Collaborative works to realize the AWG in different materials for different applications are described in chapter 7. In this chapter we discuss the experimental demonstration of silicon nitride AWGs for visible wavelengths, silicon AWGs for short wave infrared and mid-infrared and germanium AWGs for mid-infrared wavelengths. Finally in chapter 8 the thesis is concluded with a discussion of future scope for this work.

References

- [1] R. N. Hall, G. E. Fenner, J. D. Kingsley, T. J. Soltys, and R. O. Carlson. *Coherent Light Emission From GaAs Junctions*. Phys. Rev. Lett., 9:366–368, Nov 1962.
- [2] R. Ramaswami. *Optical fiber communication: From transmission to networking*. Communications Magazine, IEEE, 40(5):138–147, 2002.
- [3] K.C. Laudon and K. Laudon. *Management Information Systems: Managing the Digital Firm (13th Edition)*. Prentice Hall, 2013.
- [4] R.M. Metcalfe, D.R. Boggs, C.P. Thacker, and B.W. Lampson. *Multipoint data communication system with collision detection*, December 13 1977. US Patent 4,063,220.
- [5] H. Park, A. Fang, S.Kodama, and J. Bowers. *Hybrid silicon evanescent laser fabricated with a silicon waveguide and III-V offset quantum wells*. Opt. Express, 13(23):9460–9464, Nov 2005.
- [6] S. Keyvaninia, S. Verstuyft, S. Pathak, F. Lelarge, G.-H. Duan, D. Bordel, J.-M. Fedeli, T. De Vries, B. Smalbrugge, E. J. Geluk, J. Bolk, M. Smit, G. Roelkens, and D. Van Thourhout. *III-V-on-silicon multi-frequency lasers*. Opt. Express, 21(11):13675–13683, Jun 2013.
- [7] M. Sugo, H. Mori, Y. Itoh, Y. Sakai, and M. Tachikawa. *1.5 um-Long-Wavelength Multiple Quantum Well Laser on a Si Substrate*. Japanese Journal of Applied Physics, 30:3876–3878, 1991.
- [8] S. Suzuki, Y. Yanagisawa, M. Hibino, and K. Oda. *High-density integrated planar lightwave circuits using SiO₂-GeO₂ waveguides with a high refractive index difference*. Lightwave Technology, Journal of, 12(5):790–796, 1994.
- [9] A. Himeno, K. Kato, and T. Miya. *Silica-based planar lightwave circuits*. Selected Topics in Quantum Electronics, IEEE Journal of, 4(6):913–924, 1998.
- [10] J. H. D. Besten, R. G. Broeke, M. V. Geemert, J.J.M. Binsma, F. Heinrichsdorff, and T. V. Dongen. *An Integrated 4 Laser on InP*. Photonics Technology Letters, IEEE, 15(3):368–370, 2003.
- [11] E.L. Wooten, K.M. Kissa, A. Yi-Yan, E.J. Murphy, D.A. Lafaw, P.F. Hallemeier, D. Maack, D.V. Attanasio, D.J. Fritz, G.J. McBrien, and D.E. Bossi. *A review of lithium niobate modulators for fiber-optic communications systems*. Selected Topics in Quantum Electronics, IEEE Journal of, 6(1):69–82, Jan 2000.

-
- [12] R. A. Soref, J. Schmidtchen, and K. Petermann. *Large single-mode rib waveguides in GeSi-Si and Si-on-SiO₂*. *Quantum Electronics, IEEE Journal of*, 27(8):1971–1974, Aug 1991.
- [13] W. Bogaerts. *Nanophotonic Waveguides and Photonic Crystals in Silicon-on-Insulator*. PhD thesis, Ghent University, 2004.
- [14] W. Bogaerts and S.K. Selvaraja. *Compact Single-Mode Silicon Hybrid Rib/Strip Waveguide With Adiabatic Bends*. *Photonics Journal, IEEE*, 3(3):422–432, 2011.
- [15] P. Dumon. *Ultra-Compact Integrated Optical Filters in Silicon-on-insulator by Means of Wafer-Scale Technology*. PhD thesis, Ghent University, 2007.
- [16] W. Bogaerts, S.K. Selvaraja, P. Dumon, J. Brouckaert, K. De Vos, D. Van Thourhout, and R. Baets. *Silicon-on-Insulator Spectral Filters Fabricated With CMOS Technology*. *IEEE Journal of Selected Topics in Quantum Electronics*, 16(1):33–44, 2010.
- [17] D. Vermeulen, S. Selvaraja, P. Verheyen, G. Lepage, W. Bogaerts, P. Absil, D. Van Thourhout, and G. Roelkens. *High-efficiency fiber-to-chip grating couplers realized using an advanced CMOS-compatible Silicon-On-Insulator platform*. *Opt. Express*, 18(17):18278–18283, Aug 2010.
- [18] M.K. Smit. *New focusing and dispersive planar component based on an optical phased array*. *Electronics Letters*, 24(7):385–386, Mar 1988.
- [19] C. Dragone. *Efficient NxN star coupler based on Fourier optics*. *Electronics Letters*, 24(15):942–944, Jul 1988.
- [20] A.R. Vellekoop and M.K. Smit. *Four-channel integrated-optic wavelength demultiplexer with weak polarization dependence*. *Lightwave Technology, Journal of*, 9(3):310–314, 1991.
- [21] H. Takahashi, S. Suzuki, K. Kato, and I. Nishi. *Arrayed-waveguide grating for wavelength division multi/demultiplexer with nanometre resolution*. *Electronics Letters*, 26(2):87–88, Jan 1990.
- [22] C. Dragone. *Optimum design of a planar array of tapered waveguides*. *Journal of the Optical Society of America A*, 7(11):2081, 1990.
- [23] C. Dragone, C.A. Edwards, and R.C. Kistler. *Integrated optics NxN multiplexer on silicon*. *Photonics Technology Letters, IEEE*, 3(10):896–899, Oct 1991.
- [24] C. R. Doerr. *Planar Lightwave Devices for WDM, in Optical Fiber Telecommunications*, volume 4. Academic Press, ISBN 0-12-395172-0, 2002.

- [25] W. Bogaerts, R. Baets, P. Dumon, V. Wiaux, S. Beckx, D. Taillaert, B. Luyssaert, J. Van Campenhout, P. Bienstman, and D. Van Thourhout. *Nanophotonic waveguides in silicon-on-insulator fabricated with CMOS technology*. Lightwave Technology, Journal of, 23(1):401–412, 2005.
- [26] W. Bogaerts, D. Taillaert, P. Dumon, D. Van Thourhout, R. Baets, and E. Pluk. *A polarization-diversity wavelength duplexer circuit in silicon-on-insulator photonic wires*. Optics express, 15(4):1567–78, Feb 2007.
- [27] S. Pathak, M. Vanslembrouck, P. Dumon, D. Van Thourhout, and W. Bogaerts. *Compact SOI-based polarization diversity wavelength demultiplexer circuit using two symmetric AWGs*. Opt. Express, 20(26):B493–B500, Dec 2012.
- [28] K. Okamoto. *Progress and technical challenge for planar waveguide devices: silica and silicon waveguides*. Laser & Photonics Reviews, 6(1):14–23, 2012.
- [29] Y. Hida, Y. Hibino, T. Kitoh, Y. Inoue, M. Itoh, T. Shibata, A. Sugita, and A. Himeno. *400-channel 25-GHz spacing arrayed-waveguide grating covering a full range of C- and L-bands*. In Optical Fiber Communication Conference and International Conference on Quantum Information, page WB2, 2001.
- [30] F.M. Soares, N.K. Fontaine, R.P. Scott, J-H Baek, X. Zhou, T. Su, S. Cheung, Y. Wang, C. Junesand, S. Lourdudoss, K.Y. Liou, R.A. Hamm, W. Wang, B. Patel, L. A. Gruezke, W.T. Tsang, J.P. Heritage, and S.J.B. Yoo. *Monolithic InP 100-Channel x 10-GHz Device for Optical Arbitrary Waveform Generation*. Photonics Journal, IEEE, 3(6):975–985, Dec 2011.
- [31] M. Kohtoku, H. Sanjoh, S. Oku, Y. Kadota, Y. Yoshikuni, and Y. Shibata. *InP-based 64-channel arrayed waveguide grating with 50 GHz channel spacing and up to -20 dB crosstalk*. Electronics Letters, 33(21):1786–1787, Oct 1997.

2

Theory of arrayed waveguide gratings

“Whether you can observe a thing or not depends on the theory which you use.
It is the theory which decides what can be observed.”

– Albert Einstein

2.1 Introduction

In a microwave system a large antenna can be replaced by many small antennas without degrading the performance. Such an array has many advantages over a single large antenna. To scan a large antenna, the entire antenna has to be moved, whereby the scanning speed is limited by the mechanical movement of the antenna. In an antenna array, the beam can be scanned, without moving the antennas. It is only necessary to change the phase of the signals arriving at each antenna of the array. The speed of this phase scan depends on the electronics which control the phase of the antenna. Such a phase controlled array is called a "phased array". Microwave phased arrays have many applications in radar. The concept of the microwave phased array can be used also in the optical domain which is famous as optical phased array (OPA) [1].

Although the concept is the same the optical phased array have its own challenges: as the wavelength of light is small the spacing between the antennas of the array becomes critical. Also the phase control of these antennas is different compared to that of RF signals. Today OPAs are used for beam steering [2], beam focusing, shaping and wavefront sensing. An important addition to this application list is that of optical wavelength filtering using arrayed waveguide gratings (AWG). To understand the operation of an AWG, we first discuss the general case of OPAs. After that we will zoom in on the theory of the AWG, which can be considered as a special design of the general OPAs.

2.2 Optical phased array

The radiation pattern of an optical phased array is determined by the shape, amplitude and phase of the individual apertures of the array and their position and orientation. The calculation is simplified considering each of these apertures as an isotropic point source. The far-field pattern of the array, with the individual apertures taken as isotropic point sources, is called the array factor [3]. The array factor is a very important parameter for an OPA with identical apertures as the final far-field radiation pattern will be easily obtained by multiplying the far-field pattern of the individual aperture with the array factor. Therefore first we discuss the far-field of a single radiating aperture, which is calculated using the scalar diffraction theory. After that the array factor is calculated for the linear array configuration, which is the case relevant for the AWG design.

2.2.1 Diffraction theory

Given that the propagation of light remains in plane in integrated photonics circuits, we can limit ourselves mostly to a 2D description and to 2D diffraction

theory.

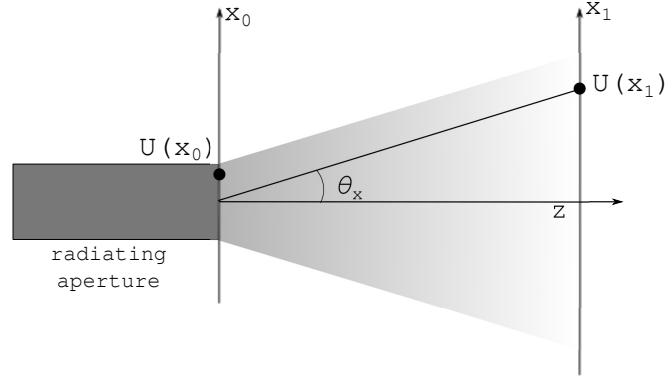


Figure 2.1: Diffraction of light through an aperture.

The diffraction pattern of an aperture supporting a scalar field U at the x_0 axis towards the x_1 axis at a distance z (see Fig. 2.1) can be obtained from the Fresnel diffraction integral [4]:

$$U(x_1) = \frac{j e^{-jkz} e^{-jkx_1^2/2z}}{\lambda z} \int_{-\infty}^{+\infty} U(x_0) e^{-jkx_0^2/2z} e^{-j2\pi x_1 x_0/\lambda z} dx_0 \quad (2.1)$$

When the distance z is large ($z \gg k(x_0^2)_{max}/2$) the quadratic phase term can be neglected and Eq. 2.1 will simplify to:

$$U(x_1) = \frac{j e^{-jkz} e^{-jkx_1^2/2z}}{\lambda z} \int_{-\infty}^{+\infty} U(x_0) e^{-j2\pi x_1 x_0/\lambda z} dx_0 \quad (2.2)$$

This shows that the field at the x_1 axis is the Fourier transform of the field at the x_0 axis, when the spatial frequencies are defined as $f_x = -x_1/\lambda z$. This region is called the far field of the aperture and we are operating in the so-called Fraunhofer diffraction regime.

The fundamental mode of an integrated waveguide can be approximated by a Gaussian function. Let's consider a Gaussian aperture, and calculate its radiation pattern analytically using Eq. 2.2. The Gaussian field at x_0 axis can be written as

$$U(x_0) = e^{-x_0^2/w^2} \quad (2.3)$$

where w is the half $1/e$ width of the Gaussian field. The radiation pattern at the x_1 axis has again a Gaussian shape, which can be derived by inserting Eq. 2.3 into Eq. 2.2:

$$U(x_1) = \frac{j\pi^{1/2} e^{-jkz} e^{-jkx_1^2/2z}}{\lambda z} w^2 e^{-(\pi w x_1/\lambda z)^2} \quad (2.4)$$

The far field can then be normalized by the radiation field at $x_1=0$.

$$U_N(x_1) = \frac{U(x_1)}{U_0} = e^{-jkx_1^2/2z} e^{-(\pi wx_1/\lambda z)^2} \quad (2.5)$$

2.2.2 Array factor

Fig. 2.2(a) shows the fundamental configuration of the linear array, where each of the apertures is replaced by an isotropic point source to calculate the array factor (AF). An isotropic point source is a hypothetical, lossless source occupying a point in space and radiating to all directions uniformly. The radiation field of an isotropic point source in a spherical coordinate system is given by

$$I_0 = \frac{e^{-jkr}}{4\pi r} \quad (2.6)$$

The far-field radiation pattern is obtained from the angular dependence (i.e. at constant r) of the radiation field [3]; therefore the pattern of a point source i.e. the array factor (AF) is constant and given by:

$$AF = I_0 \quad (2.7)$$

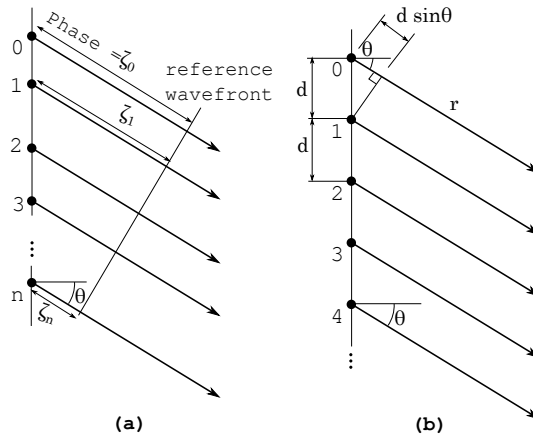


Figure 2.2: (a) Arbitrary spaced linear array of isotropic point sources. (b) Equally spaced linear array of isotropic point sources.

The radiation pattern of the array shown in Fig. 2.2(a) can be calculated by taking the sum of all the response of the isotropic point sources at the reference wavefront. Then the array factor of the array shown in Fig. 2.2(a) is

$$AF = I_0 e^{j\zeta_0} + I_1 e^{j\zeta_1} + I_2 e^{j\zeta_2} + I_3 e^{j\zeta_3} + \dots \quad (2.8)$$

Where ζ_0, ζ_1, \dots are the phases of the outgoing plane waves with respect to the reference wavefront due to the point sources at locations designated as 0, 1, \dots . The terms I_0, I_1, \dots contain the amplitude and phase variation of the corresponding point source. This is very general expression of the array factor and can be applied for any linear array configuration.

In the AWG the apertures are uniformly spaced similar to the array configuration shown in Fig. 2.2(b). The gap between two successive point sources is constant and equal to d . Let's assume the phase of the zeroth point source is zero ($\zeta_0 = 0$). Therefore the phase of the first point source relative to the zeroth point source is $\zeta_1 = kd \sin \theta$. This process continues and Eq. 2.8 becomes

$$\text{AF} = I_0 + I_1 e^{jkd \sin \theta} + I_2 e^{jk2d \sin \theta} + \dots = \sum_{n=0}^{N-1} I_n e^{jkn d \sin \theta} \quad (2.9)$$

We consider the array has N point sources. If we consider the point sources in the array have a linear phase progression i.e the phase difference (α) between two adjacent sources is constant then the radiation field of the n^{th} source will be

$$I_n = A_n e^{jn\alpha} \quad (2.10)$$

Then Eq. 2.9 becomes

$$\text{AF} = \sum_{n=0}^{N-1} A_n e^{jn(kd \sin \theta + \alpha)} \quad (2.11)$$

we can define $kd \sin \theta + \alpha = \psi$ to simplify the discussion. Then

$$\text{AF} = \sum_{n=0}^{N-1} A_n e^{jn\psi} \quad (2.12)$$

The above equation can be further simplified by considering the sources of the array have equal amplitude (A_0). Then

$$\text{AF} = A_0 \sum_{n=0}^{N-1} e^{jn\psi} \quad (2.13)$$

Mathematically the above equation can be further simplified to

$$\text{AF} = A_0 e^{j(N-1)\psi/2} \frac{\sin(N\psi/2)}{\sin(\psi/2)} \quad (2.14)$$

The phase factor ($e^{j(N-1)\psi/2}$) is not important unless the array is interacting with another source. As we are interested in the amplitude distribution of the radiation field we can modify Eq. 2.14 to

$$|\text{AF}| = A_0 \frac{\sin(N\psi/2)}{\sin(\psi/2)} \quad (2.15)$$

Now we normalize the array factor by its maximum value, to find:

$$|f(\psi)| = \frac{|AF|}{|AF|_{\psi=0}} = \frac{\sin(N\psi/2)}{N \sin(\psi/2)} \quad (2.16)$$

This is the normalized array factor for a linear array with N sources having equal amplitude. Fig. 2.3 shows the variation of the array factor with ψ for 2, 3, 5 and 10 apertures in the array. The array factor is periodic in 2π therefore the

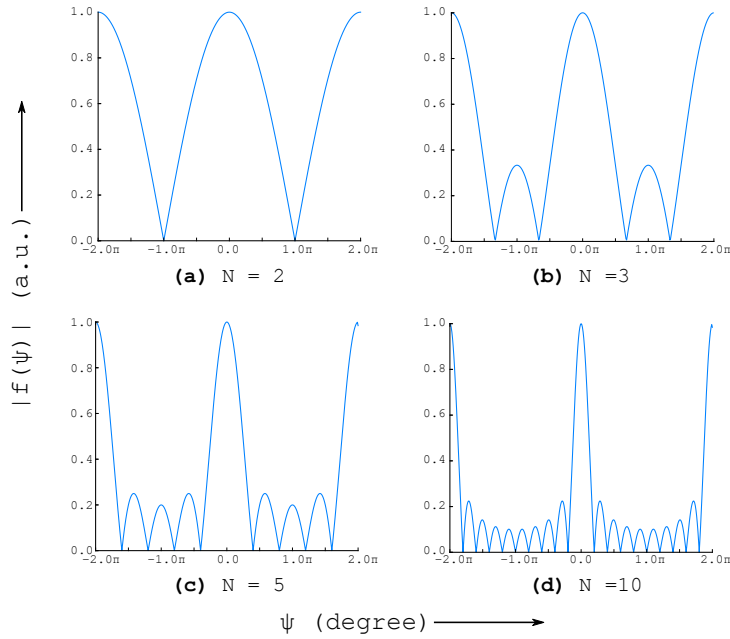


Figure 2.3: Array factor of an equally spaced uniform linear array with different number of sources.

below discussion is focused on the -2π to 2π region. For $N \geq 3$ the array factor has main lobes and side lobes. As N increases the number of side lobes also increases to $N - 2$. The width of the side lobe is $2\pi/N$ and the width of the main lobe is $4\pi/N$. So the main lobe will be narrower for larger N . The peak power of the side lobe also decreases with increasing N .

2.2.3 Example

The fundamental mode of an integrated photonics waveguide can be approximated by a Gaussian function. For a more practical example we chose a Gaussian field with a full $1/e$ -width of 614 nm (corresponding to the TE fundamental mode width of an 800 nm wide SOI at 1550 nm wavelength)

The far-field intensity as calculated from Eq. 2.5 and 2.16 can be written as

$$|I| = \left| e^{-(\pi w \sin \theta / \lambda)^2} \frac{\sin[\frac{N}{2}(\frac{2\pi d}{\lambda} \sin \theta + \alpha)]}{N \sin[\frac{1}{2}(\frac{2\pi d}{\lambda} \sin \theta + \alpha)]} \right|^2 \quad (2.17)$$

where the half 1/e-width w is $0.614/2 \mu\text{m}$ and the wavelength λ is $1.55 \mu\text{m}$.

As a first example the spacing between two successive source points d is chosen to be $2 \mu\text{m}$ and the number of apertures N varies from 1 to 15. The constant phase difference between two successive apertures α is set to zero. Fig.

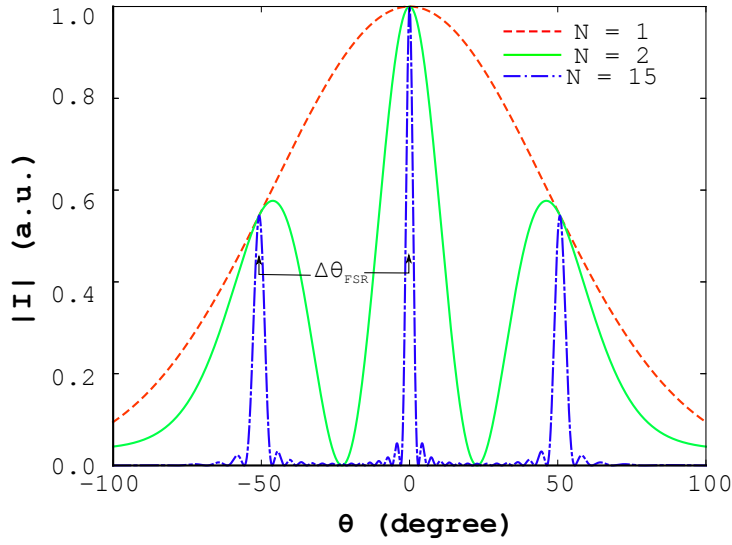


Figure 2.4: Far-field of an array of Gaussians with a full 1/e-width of 614 nm , spaced $2 \mu\text{m}$, for different number of apertures at $\lambda = 1550 \text{ nm}$

2.4 shows the far-field for 1, 2, 15 apertures in the array. From the discussion on the array factor it was clear that as we increases the number of apertures the main lobes will be narrower. From Fig. 2.3 we can see that the main lobe is periodic with 2π angle i.e. $\psi (=kd \sin \theta)$ equal to 2π . Using this the angular gap between the two peaks which is also known as angular free spectral range ($\Delta\theta_{\text{FSR}}$) can be calculated as

$$\Delta\theta_{\text{FSR}} = \sin^{-1}(2\pi/kd) \approx \lambda/d \quad (2.18)$$

For the second example we fixed the number of apertures N to 15 and increased the spacing between two successive apertures d from $2 \mu\text{m}$ to $4 \mu\text{m}$. The far-field pattern of this configuration is shown in Fig. 2.5. Now we can compare the far-field from Fig. 2.4 and 2.5 with $2 \mu\text{m}$ and $4 \mu\text{m}$ aperture spacing respectively.

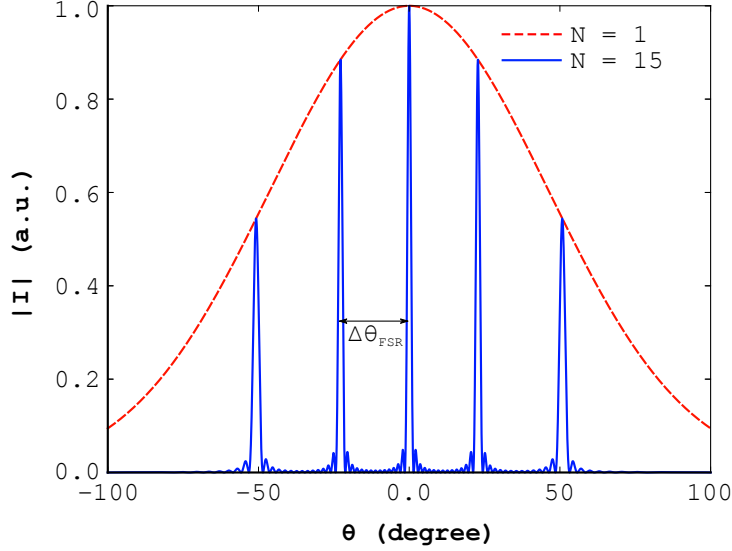


Figure 2.5: Far-field of an array of Gaussians with a full $1/e$ -width of 614 nm with $4 \mu\text{m}$ aperture spacing in the array.

As we double the spacing not only the main lobes became narrower the $\Delta\theta_{\text{FSR}}$ also reduced by half.

As a third example we varied the phase difference (α) between two successive apertures where N and d are fixed to 15 and $2 \mu\text{m}$ respectively. Figure 2.6 shows the far-field patterns for α varying from -0.2π to π . The far-field pattern moves along the θ axis with the variation of α . This forms the basis of an OPA based optical filters, where different wavelength accumulate different phase after propagating through a fixed length waveguide.

2.3 Classification of AWG

An arrayed waveguide grating (AWG) consists of two star-couplers and an array of waveguides as shown in Fig 2.7. At the input side the star-coupler works as a splitter and at the output side it is a combiner. Depending on the design of the waveguide in the array it is possible to obtain various functionalities. But here we mainly focus on the AWG as a wavelength filter and optical switch.

2.3.1 AWG as a wavelength filter

When the AWG is used as a wavelength filter, the waveguides in the array increases linearly in length, which introduce a liner progression of phase. The op-

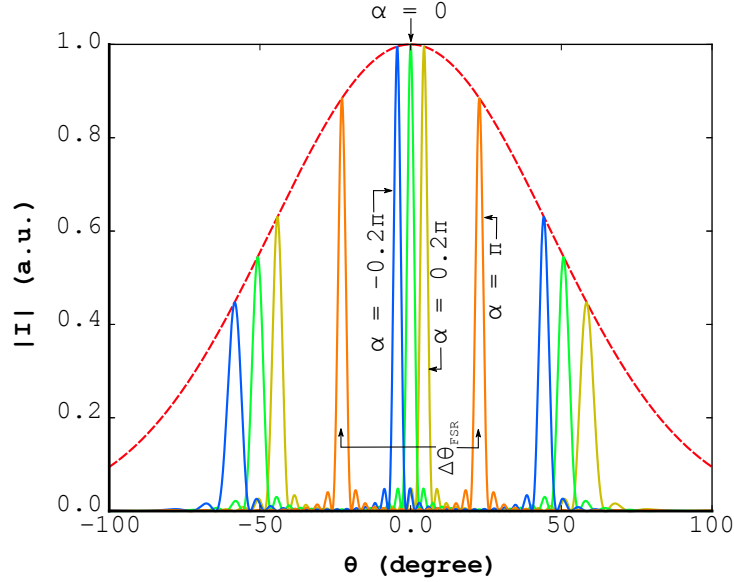


Figure 2.6: Far-field of an array of Gaussians with a full $1/e$ -width of 614 nm with variation of α .

eration principle of the AWG as a wavelength filter is described as follows. A light beam exiting from a waveguide aperture enters into the input star-coupler and diffracts. This expanding light beam is then distributed over an array of waveguides and propagates through these waveguides to the output star-coupler. The optical path length difference between two successive waveguides in the array is constant. Therefore, for the center wavelength, the field distribution at the entrance of the waveguide array will be reproduced at its exit aperture. In a perfect system a perfect image of the object plane can then be formed and the field distribution in the image plane will have the same amplitude and phase as the field distribution of the object plane [5]. Obviously, the imaging is never perfect because one uses a finite number of waveguides in the array and the array has a finite numerical aperture.

The phase difference in the waveguide array varies with wavelength because of their length difference and the wavelength dependence of the propagation constant. This phase delay will induce a tilt in the phase fronts in the output star-coupler and introduce a lateral shift of the image field profile. The spectral response of the AWG will therefore be determined by the overlap of this shifted field profile with the mode profile of the different output waveguide apertures located in the image plane. In conventional AWGs the geometry of the aperture at the input (object plane) and output (image plane) is identical: this results

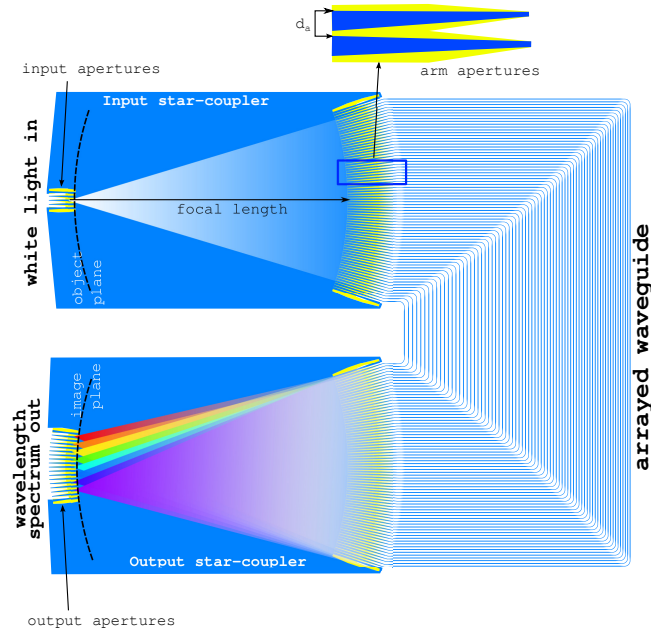


Figure 2.7: Schematic diagram of a 16×400 GHz AWG.

in a maximal overlap when the shifted image is perfectly aligned with one of the output apertures (i.e. at a given wavelength). However, the coupled output power rapidly drops with a small image shift (i.e. a small wavelength shift) as shown in Fig. 2.8.

We can correlate the working principle of the AWG wavelength filter with the third case discussed in section 2.2.3, where the phase difference α is wavelength dependent. Therefore the different wavelengths will introduce different α and as shown in Fig. 2.6 there will be shift in a far-field pattern.

Fig. 2.8 gives a the schematic representation of the spectral response of an AWG indicating the important characteristics (insertion loss, insertion loss non-uniformity, free spectral range(FSR) [5], neighbour channel crosstalk, phase error crosstalk, cumulative crosstalk and passband aspect ratio [6]) of the response. These parameters will be used in the following discussion to describe the performance of the AWG. Usually the crosstalk of an AWG is characterized by the single channel crosstalk floor which is the crosstalk floor measured with one active input channel. Under operational conditions when all the input channels are active, the crosstalk of all channels (which is further referred to as the cumulative crosstalk) will be added linearly, which results in a much higher effective crosstalk. In Fig. 2.8 the conventional crosstalk and the cumulative crosstalk of the center channel are indicated: the conventional crosstalk

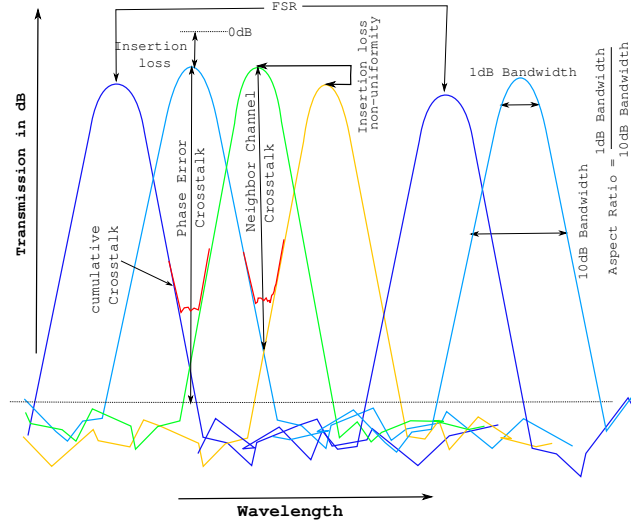


Figure 2.8: Schematic representation of insertion loss, insertion loss non-uniformity, free spectral range (FSR), neighbour channel crosstalk, phase error crosstalk, cumulative crosstalk and passband aspect ratio.

is defined by the difference between the crosstalk floor and the peak power of the channel. We define the cumulative crosstalk as the difference between the peak power in the channel and the cumulative power coupled to the other channels, added up over the wavelength band of the channel. The cumulative crosstalk has two major contributions: at the edges of the wavelength band it is dominated by the slope of the nearest neighbor channel (further referred to as neighboring channel contributed crosstalk) and the center part which is mainly caused by phase errors (further referred to as phase error contributed cumulative crosstalk).

2.3.2 AWG as an optical switch

When the AWG used as an optical switch, all waveguides in the array are set at the same length. Therefore all the wavelengths entering from an input will end up in the same output. A wavelength independent phase shift can be applied by using electro-optical phase shifters to move the light from one output to the other. These phase shifters should be capable to introduce a phase between 0 and 2π . The details will be discussed in chapter 6.

2.4 Design Parameters of an AWG

In this section we will discuss the essential design parameters of an AWG: focal length, delay length, free spectral range (FSR), dispersion, order. These parameters are interdependent on each other, being related through effective index and group index, which makes the design procedure of an AWG complex. The design becomes easier if we assign a value for some of these parameters and then derive the rest. Let's start the calculation by assigning the following parameters: input and output aperture width (d_o), arm aperture pitch (d_a), channel spacing (CS), number of waveguides in the array (N_{arms}) and number of wavelength channels (N_{out}). The input and output aperture widths are considered to be identical. The input/output and arm apertures are shown in Fig. 2.7 and 2.9. The channel spacing is the wavelength separation between the adjacent output channels. It is often expressed in the frequency domain (GHz). As the parameters are interdependent one can always start by assigning other set of parameters and calculate back these parameters.

2.4.1 Focal length

The focal length (R_a) is an important parameter for the star-coupler as it governs the distribution of the light from the input aperture in the input star coupler and the refocusing of light from the output star coupler in the output apertures. The width of the divergent light depends on the diffraction angle (θ_{da}) of the input aperture and distance traveled by the light in the free space region. It is desirable that this divergent light completely couples into the waveguide array to minimize the loss. So the focal length of the star-coupler can be defined as the distance traveled by divergent light to couple completely into the waveguide array (shown in Fig. 2.9). Therefore for a fixed input aperture width, arm aperture pitch and number of waveguides the focal length of the star-coupler should be:

$$R_a = \frac{d_a \cdot N_{arms}}{\theta_{da}}, \quad (2.19)$$

The focal length needs to be determined accurately as a wrong focal length will increase the insertion loss of the device: an overestimated focal length will increase the loss because the device will get bigger, whereas underestimated focal length will also increase the loss due to the sides of the star-coupler. The diffraction angle (θ_{da}) of the input aperture can be determined analytically using Fresnel's diffraction method or by using a BPM and a FDTD simulator.

2.4.2 Delay Length

The delay length (ΔL) is the length difference between two successive waveguides in the array. The delay length can be derived from the diffraction equa-

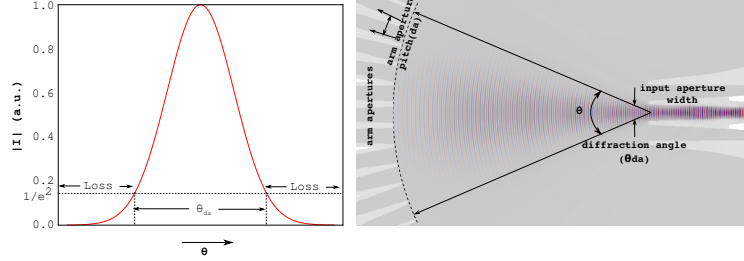


Figure 2.9: The light diverges in the input star-coupler after entering from the input aperture.

tion of the AWG. As shown in Fig. 2.10 let's consider a light beam entering from point P_1 in the input star-coupler and propagating through the two adjacent waveguides A_1A_2 and B_1B_2 , which are the $(i-1)^{th}$ and i^{th} waveguides. After passing through the waveguides these two light beams meet at point P_2 in the output star-coupler. For a light beam of wavelength λ the path difference of these two light beams $P_1A_1A_2P_2$ and $P_1B_1B_2P_2$ will be equal to an integer multiple of 2π to create a constructive interference at P_2 . Therefore the grating equation can be written as

$$\beta_{slab}d_a \sin\theta_1 + \beta_{wg}\Delta L - \beta_{slab}d_a \sin\theta = 2\pi m \quad (2.20)$$

where β_{wg} and β_{slab} are the propagation constants of the waveguide mode and the slab mode for the wavelength of λ , θ_1 and θ are the angles of the input (P_1) and output (P_2) with the center axis of the star-couplers (as shown in Fig. 2.10) and m is the order of the phased array. Eq. 2.20 can be further simplified by replacing the propagation constants with the effective index.

$$n_{slab}d_a \sin\theta_1 + n_{wg}\Delta L - n_{slab}d_a \sin\theta = m\lambda \quad (2.21)$$

where n_{slab} and n_{wg} are the effective indexes of the slab and the waveguide mode. The center wavelength λ_c is the wavelength for which this condition occurs of the center at the output plane. Since θ_1 and θ equal zero for the center wavelength, the grating equation (2.21) to determine the delay length simplifies to

$$\Delta L = m \cdot \frac{\lambda_c}{n_{wg}(\lambda_c)}, \quad (2.22)$$

where $n_{wg}(\lambda_c)$ is the effective index of the waveguide at the center wavelength.

2.4.3 Diffraction order and free spectral range

The free spectral range(FSR) is the difference between the two wavelengths from two adjacent orders overlapping in the same output channel. In terms of phase

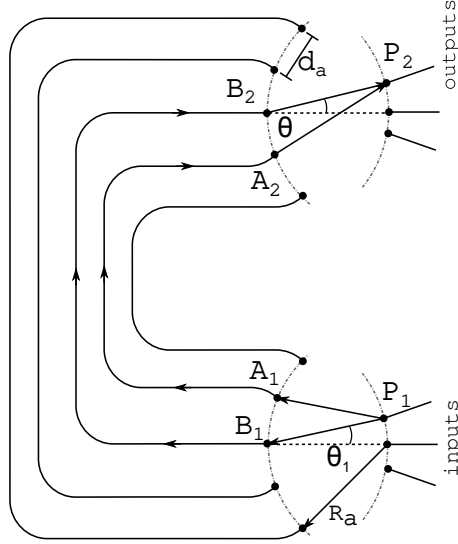


Figure 2.10: Operational diagram of an AWG.

the FSR is the difference between the two wavelengths for which the phase difference ($\Delta\phi$) between two successive waveguides become 2π which returns the light back into the same position of the image plane. If we consider λ_m the wavelength of m order overlap to with the wavelength λ_{m+1} of the order $m+1$ then the phase difference between them should be 2π , which makes a relation between the two orders :

$$\left(\frac{n_{wg}(\lambda_{m+1})}{\lambda_{m+1}} - \frac{n_{wg}(\lambda_m)}{\lambda_m}\right) \cdot \Delta L = 1 \quad (2.23)$$

This equation can be further simplified by applying a first order approximation to the effective index:

$$n_{wg}(\lambda_{m+1}) = n_{wg}(\lambda_m) - \frac{dn}{d\lambda} \lambda_{FSR} \quad (2.24)$$

Now Eq. 2.23 for the center wavelength (λ_c) of the m th order is

$$n_{g,wg} \cdot \frac{v_{FSR}}{c} \cdot \Delta L = 1 \quad (2.25)$$

Where $n_{g,wg}$ is the group index of the waveguide and v_{FSR} is the free spectral range in the frequency domain. The expression for the group index is

$$n_{g,wg} = n_{wg}(\lambda_c) - \lambda_c \frac{dn_{wg}}{d\lambda} \quad (2.26)$$

As we can see from Eq. 2.25 the delay length is inversely proportional to the FSR therefore the size of the AWG will increase as we decrease the FSR. By

substituting the delay length in Eq. 2.25 we get a relation between the order and the FSR.

$$m = \frac{n_{wg}(\lambda_c) \cdot \nu_c}{n_{g,wg} \cdot \nu_{FSR}} \quad (2.27)$$

The relation between the FSR in the wavelength domain (λ_{FSR}) and frequency domain (ν_{FSR}) can be written as:

$$\frac{\lambda_{FSR}}{\lambda_c} = \frac{\nu_{FSR}}{\nu_c} \quad (2.28)$$

Now by substituting the ν_{FSR} from Eq. 2.28 in Eq. 2.25 we get a relation between the delay length and the FSR in the wavelength domain.

$$\Delta L = \frac{\lambda_c^2}{n_{g,wg} \lambda_{FSR}} \quad (2.29)$$

From the above equation we can see that as the delay length is inversely proportional to the group index of the waveguide the use of high contrast waveguides will reduce the AWG size significantly compared to low index contrast waveguides.

2.4.4 Dispersion

The dispersion of an AWG can be defined by two ways: the lateral dispersion (D), which is the lateral displacement (ds) of the focal spot per unit frequency (dν) in the image plane and the angular dispersion, which is the angular displacement (dθ) of the focal spot per unit frequency (dν) in the output star-coupler. The relation between these two is

$$D = \frac{ds}{d\nu} = R_a \cdot \frac{d\theta}{d\nu} \quad (2.30)$$

The dispersion angle (θ) of a wavelength λ can be derived from the grating equation (see Eq. 2.20) by considering that the light enters from the center input channel at the input star-coupler i.e. $\theta_1 = 0$.

$$\sin\theta = \frac{n_{wg}(\lambda) \cdot \Delta L - m \cdot \lambda}{n_{slab}(\lambda) \cdot d_a}, \quad (2.31)$$

Now if we replace the delay length ΔL in equation 2.31 the expression for θ becomes

$$\sin\theta = m \cdot \frac{n_{wg}(\lambda) \cdot \lambda_c - n_{wg}(\lambda_c) \cdot \lambda}{n_{wg}(\lambda_c) \cdot n_{slab}(\lambda) \cdot d_a} \quad (2.32)$$

This equation gives a clear picture of how the wavelength is mapped over the image plane. θ will be zero for $\lambda = \lambda_c$, θ will be positive for $\lambda < \lambda_c$ and θ will

be negative for $\lambda > \lambda_c$. Therefore in Fig. 2.7 the red light indicates the longer wavelength side and the blue light indicates the shorter wavelength side.

The angular dispersion is obtained by differentiating Eq. 2.32. In the vicinity of $\sin\theta = \theta$ the result is

$$\frac{d\theta}{dv} = -\frac{m\lambda_c^2 n_{g,wg}}{n_{slab} n_{wg}(\lambda_c) d_a c} \quad (2.33)$$

where c is the light velocity and $n_{g,wg}$ is the group index of the waveguide (Eq. 2.26).

To calculate the position of the output aperture for a given wavelength in the image plane we can either use Eq. 2.32 or 2.33. The first approach using Eq. 2.32 will give more accurate dispersion as the calculation takes into account the index variation of the slab waveguide with wavelength. But this equation also requires a highly accurate waveguide effective index model. The second approach is much more relaxed in terms of effective index mismatch as it depends on the group index of the waveguide. But the draw back is that the effective index of the slab is considered as a constant with wavelength. This assumption can hold only for the narrow wavelength band devices close to the centre wavelength. For the device working over a broad wavelength band the first approach will be more accurate compared to the second.

The expression of angular dispersion (Eq. 2.33) can be used to find out the angular gap between two adjacent orders i.e. the angular free spectral range. The equation will be

$$\Delta\theta_{FSR} = \frac{d\theta}{dv} \cdot v_{FSR} = -\frac{m\lambda_c^2 n_{g,wg} v_{FSR}}{n_{slab} n_{wg}(\lambda_c) d_a c} \quad (2.34)$$

The above equation can be modified further by inserting the order as defined from Eq. 2.27. Therefore the result is

$$\Delta\theta_{FSR} = -\frac{\lambda_c}{n_{slab} d_a} \quad (2.35)$$

This is the same equation which we discussed in Eq. 2.18.

2.5 Characterization

2.5.1 Insertion loss and non-uniformity

The Insertion loss of an AWG is the result of various loss mechanisms:

- Propagation loss from the waveguides and the slabs
- The bend losses

- Reflections from the gap between two successive arm apertures
- Defocussing at the output waveguides
- Mismatch between the imaged field and the mode-profile of the output waveguides
- Coupling loss in the waveguide array etc.

The propagation loss of the waveguides and the slab can be reduced by improving the side wall roughness of the waveguide and making the waveguides wider. By reducing wafer thickness variations the defocusing at the output waveguides can be improved. The bend loss is already very small compared to that in low index contrast waveguides. For silicon-on-insulator the bend loss can be reduced significantly by using adiabatic bends [7]. The reflections from the gap between two successive arm apertures is the most significant contribution to the loss. To reduce this loss a wide shallowly etched aperture is used, followed by a long adiabatic taper to connect with the single mode waveguide [8]. But the adiabatic taper needs to be sufficiently long such that light propagating in the waveguide array makes a smooth transition to the free-space region in the star-couplers. These losses contribute significantly in real life AWGs due to the finite resolution of the lithography process. But in ideal conditions the loss of a particular wavelength will be determined by the imaging which decides how much light couples into the other orders. Let's consider an AWG with an arm aperture pitch d_a and N the number of waveguides (which will control the focal length R_a) of the input star-coupler and the output star-coupler). From the discussion in section 2.2.3 we can derive the field distribution at the image plane of the AWG which is shown in Fig. 2.11. The maximum power of the center wavelength will be in the order m along the center axis. A fraction of light will couple into adjacent orders depending on the far field of the individual arm aperture. This fraction of light is the reason behind the loss in the center channel. Other wavelengths as the light follows the far-field envelop of the individual arm aperture, will experience higher loss compared to the central wavelength. This difference in loss is known as the channel non-uniformity loss.

The insertion loss of the AWG will decrease if we increase the number of waveguides in the array (N). This will decrease the line width of the main lobes and will increase power. But this will not change the percentage of the power coupled into the other orders compared to the central order. So this will improve the overall loss but the non-uniformity loss will remain the same.

Now we can consider a situation where we decrease the arm aperture pitch d_a . This can be done in two ways: either decreasing the spacing between the apertures or decreasing the aperture width. First if we decrease the spacing between the apertures $\Delta\theta_{\text{FSR}}$ will increase. As a consequence the percentage of the

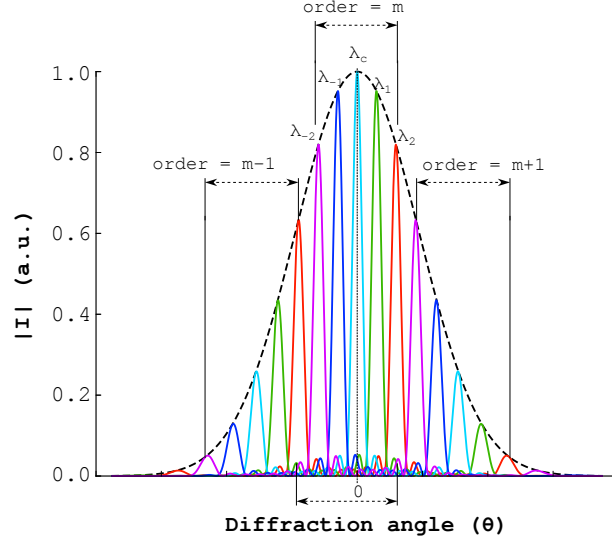


Figure 2.11: The field distribution at the image plane of a 5 channel AWG with a variation of diffraction angle.

power coupled into the other order compared to the central order will decrease, which will improve the overall loss of the device. Second if we decrease the arm aperture width in order to decrease the arm aperture pitch, both the $\Delta\theta_{\text{FSR}}$ and the far-field envelop will increase but not at the same magnitude. This will decide the percentage of the power coupled into the other orders. The diffraction angle of a wavelength will be the same if we keep m/d_a constant in Eq. 2.32. As the wider far-field decreases the roll off of the transfer characteristic, the non-uniformity loss for the other wavelengths will be improved significantly.

From Fig. 2.11 we can see that for the side channels (let's consider the wavelength channel λ_2 indicated by a red line) the AWG is creating two images at both sides of the central axis: one at the dispersion angle θ for the central order (m) and another at dispersion angle $\theta + \Delta\theta_{cs}$ for the adjacent order ($m - 1$ for wavelength channel λ_2). This occurs when the FSR is equal to the product of the number of output channels and the channel spacing. Therefore for a side channel the power will be divided into these two images. For a large FSR we can consider $\theta + \Delta\theta_{cs}$ equal to θ i.e. the AWG will create two equal intense images at both sides of the central axis. Therefore the side channels will experience at least 3 dB loss for large FSR cyclic AWGs. So the non-uniformity in loss between the central channel to the outer-most channel will be maximum 3 dB. This non-uniformity loss is low for a small FSR cyclic AWG and an AWG with a large FSR where the FSR is greater than the product of the number of output channels and

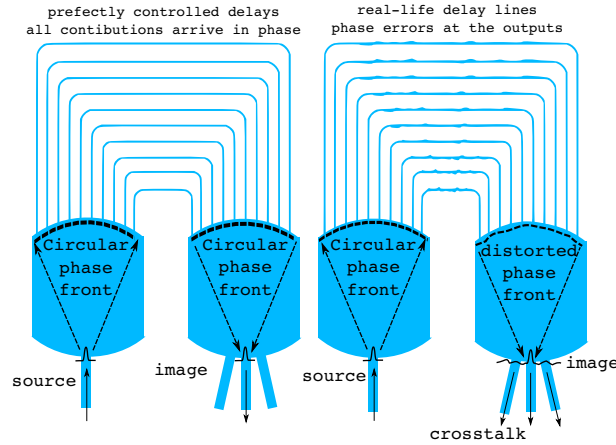


Figure 2.12: Schematic diagram of the AWG with ideal delay lines and with phase error affected delay lines.

the channel spacing.

2.5.2 Crosstalk

Crosstalk can be defined as the difference between the desired and undesired light received by a channel. The crosstalk of an AWG can be classified into two categories based on the origin: neighbouring channel contributed crosstalk (due to the shape of the neighbouring channels which come to the center of a channel) and phase error contributed crosstalk (due to the phase error accumulated by the AWG) as shown in Fig. 2.8. The neighbouring channel contributed crosstalk depends on the channel bandwidth, which can be decreased by increasing the number of waveguides used in the array [9]. The phase error contributed crosstalk is the combined effect of many mechanisms: accumulating phase errors along the delay lines, reflections, defocusing in the star-couplers, and cross-coupling in the array. It is not straightforward to separate the contributions of each of these mechanisms, although past experiments have already significantly reduced the contribution of some of these effects. E.g. the effect of reflections were reduced by using double-etched apertures [8].

The key contributor to crosstalk in the AWGs remain the phase errors that are accumulated along the delay lines [8]. When the distributed light in the waveguides recombines in the output star-coupler, phase errors will translate in ripples in the optical phase front as shown in Fig. 2.12. These ripples will induce sidelobes in the image at the output waveguides, resulting in optical power coupled to the wrong outputs. We can separate these phase errors into two categories: deterministic and stochastic errors. In the latter category we find side-

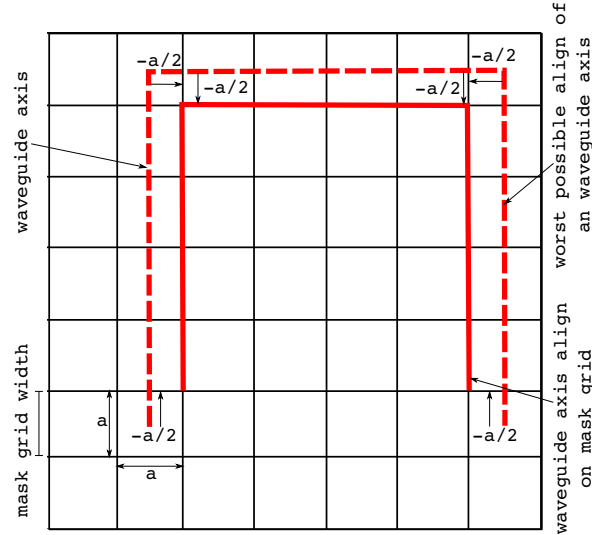


Figure 2.13: Schematic diagram of the AWG with ideal delay lines and with phase error affected delay lines.

wall roughness and line width/thickness variations as key causes. The high contrast waveguides are inherently much more sensitive to phase errors due to the sidewall roughness compared to the low index contrast waveguides. As a result silicon AWGs have higher crosstalk compared to the lower index contrast InP and Silica AWGs. Sidewall roughness and line width/thickness variations are the fabrication imperfections which can be partly reduced by engineering the design of the AWG: Using wider waveguides in the delay sections can alleviate the impact of these effects [8]. But the wider waveguide can support higher order modes, which is also not desirable as higher order modes will also contribute to the phase error. This problem can be solved by ensuring only the ground mode is excited using a smooth adiabatic transition from the single mode waveguide to the wider waveguide. Mask discretization on the other hand result in deterministic errors [6].

As the common design of our AWGs uses rectangular ‘Manhattan’ waveguide paths [8] where the bend sections are identical for all delay lines, we first looked at the effect of the mask grid on the straight delay sections of the AWG. The effect is illustrated in Fig. 2.13. The path for the delay line is calculated along 3 sides of a rectangle (taking into account the length of the bends). During that calculation, the coordinates of the sides are calculated to high precision. However, during subsequent export to a GDSII mask file, the waveguides are snapped to a fixed grid. While the grid snapping in the mask design is fairly

random (a rounding error depending on the calculated delay length), it is a deterministic process: two identically designed AWGs will experience the same phase error contributions from grid snapping. As the length deviation is not constant over the array quasi-random phase errors will be introduced, which will increase the crosstalk of the device.

2.5.3 Polarization Dependence

Polarization dependence of an AWG depends on the polarization dependence of the waveguide array. If the propagation constant of the waveguide is the same for the fundamental TE and TM mode then the AWG will be polarization independent. But birefringent waveguides which have different propagation constant for the fundamental TE and TM mode, will experience a shift in the spectral responses of the AWG for TE and TM mode. This is known as the polarization dispersion. The polarization dispersion is higher for high index contrast waveguides compared to low index contrast waveguides.

To solve this polarization dependence several concepts have been developed in different material platforms. An elegant method applied in silica-based devices is to use a half-wave plate in the middle of the waveguide array. The method can also be used in a high contrast AWG using a waveguide polarization rotator [10]. Light polarized along a certain axis will be converted in to the orthogonal polarization by the polarization rotator in the waveguide array after traveling half of the distance. Therefore, in the second half of the waveguide array the TE polarized light will be traveling as TM polarized light and vice-versa. Therefore the TE and TM polarized light will experience the same phase change irrespective of the polarization dependence of the waveguides.

Another method to solve the polarization dependence of the AWG is by making a perfectly square waveguide surrounded by the same cladding on all sides. This waveguide will become polarization independent as the index contrast will be the same along the vertical and lateral direction. It is also possible to have a polarization independent waveguide by choosing the top and side cladding such a way that both polarizations feel the same effective index along the vertical and lateral directions. However this will require a very specific waveguide geometry and is also difficult to implement for an AWG which uses a waveguide array with a combination of single mode and wider waveguides (to reduce the phase error).

Because polarization-independent waveguides in a high-contrast material platform (e.g. SOI) are difficult to fabricate, the commonly accepted approach to achieve a polarization independent circuit is the polarization diversity scheme [11, 12]: incoming signals with unknown polarization are split into two orthogonal polarizations which are then coupled separately in two identi-

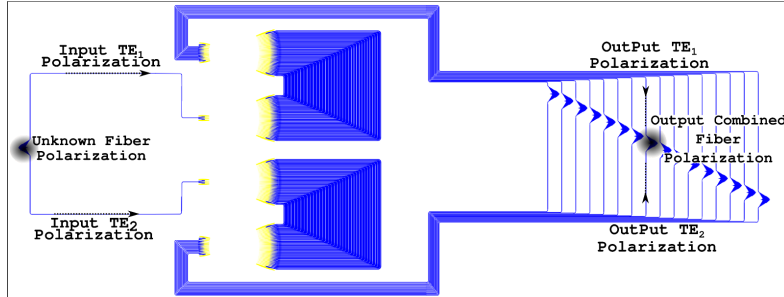


Figure 2.14: Schematic diagram of $16 \times 400\text{GHz}$ Polarization diversity circuit.

cal single-polarization circuits as shown in Fig. 2.14. The key challenge for this scheme to work is to realize two completely identical circuits, requiring a highly accurate fabrication process or active tuning or trimming. In some cases, the polarization diversity circuit with two AWGs can be replaced by a single AWG used in both directions [13]. But this is not always possible and introduces additional loss and back reflection in the fiber. The details of the measurement results for a polarization independent device as show in Fig. 2.14 is discussed in chapter 4.

2.5.4 Temperature Dependence

Temperature dependence is a major issue for wavelength dependent passive devices. As silicon is highly sensitive to the temperature, the silicon AWG inherently becomes temperature sensitive. For high index contrast waveguides based AWGs this dependence is higher compared to the low index contrast AWGs. The main effect of temperature change on the performance of an AWG is wavelength shifting. As a result, the output channels will no longer receive the desired wavelengths. For SOI based AWGs the temperature dependence is around $0.1 \text{ nm}/^\circ\text{C}$. So for $30\text{-}40^\circ\text{C}$ temperature change, the corresponding wavelength shift is a few nanometers, which is large enough to detune the target wavelength for de/multiplexer application.

To solve this temperature dependence several concepts can be used. The temperature sensitivity can be reduced by using a polymer cladding which have a negative temperature coefficient i.e. the effective index will decrease as we increase the temperature which will balance the positive effective index change of the core material [14]. With a combination of the narrow and wide waveguides one can achieve temperature insensitive spectral response. But the required length of the waveguides will be very large compare to the normal design, which will increase the device size as well as the loss [15, 16]. The device size can be improved by using the waveguide array with combination of the slotted wave-

guides. The transition between slot and ridge waveguide is lossy which will increase also the device loss [17]. In this context it is necessary to look for a new techniques, which required further work in future.

2.6 Wavelength filter function

The design of an AWG be classified in two categories based on its application: a wavelength router or a wavelength de/multiplexer. In this section we will discuss the details of these two designs.

2.6.1 Wavelength router

The first wavelength routers were demonstrated by Dragone [18, 19] in 1991, which have N inputs and outputs. Such a device has FSR equal to the number of channels multiplied by the channel spacing, which will rotate the input wavelengths along the outputs in a cyclic way. Due to this cyclic behavior the wavelength routers are also known as cyclic AWGs. Fig. 2.15 shows the wavelength

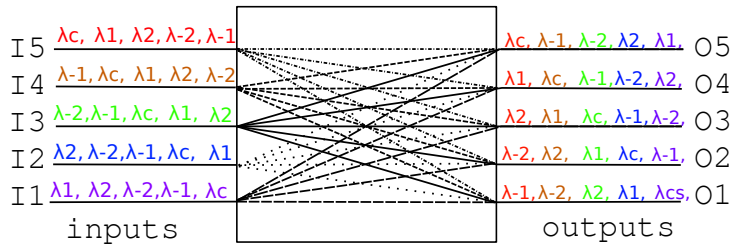


Figure 2.15: Transmission scheme of a 5×5 wavelength router.

response of a 5×5 wavelength router. From the figure we can see that when light enters from the central input channel, the center wavelength (λ_c) will go to the central output channel and when we change the input channel the wavelength response at the output channels rotate shift in cyclic manner. The first and last output channel will experience approximately 3 dB excess loss compared to the center output channel as discussed in section 2.5.1. Due to reciprocity the spectral response of an output channel will also experience approximately the same excess loss of 3 dB for the first and last input channels compared to the center input channel. For the example shown in Fig. 2.15 the combination of I1 to O1, O5 and I5 to O1, O5 the spectral response will experience more loss compare to any other input-output combinations [20].

The design procedure is illustrated in Fig. 2.16. The fundamental step of this design flow is that the central wavelength is modified to get an integer value of

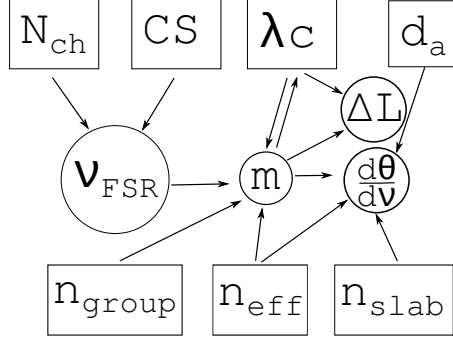


Figure 2.16: Possible design flow for a wavelength router. Boxes are user defined parameters and Circles are calculated parameters.

the order. This modified central wavelength will be used to calculate the delay length (ΔL) and the angular dispersion ($d\theta/dv$). The second possible design flow of the wavelength router is to modify the FSR from the rounded order instead of the central wavelength which will change the channel spacing of the device. The detail experimental work for the silicon AWG router is discussed in chapter 4.

2.6.2 Wavelength de/multiplexers

For a de/multiplexer the FSR should be equal or larger than the number of channels multiplied by the channel spacing. A possible design procedure is given in Fig. 2.17. The main aim of this design flow is to keep the device size small while optimizing the performance [9]. From Eq. 2.29 we can see that the delay length (ΔL) of the AWG sets its FSR. By using Eq. 2.27 we can modify the expression of the angular dispersion (Eq. 2.33)

$$\frac{d\theta}{dv} = -\frac{\lambda_c}{n_{slab}d_a v_{FSR}} \quad (2.36)$$

Now the dispersion from Eq. 2.30 can be modified by using Eq. 2.36.

$$D = -\frac{R_a \lambda_c}{n_{slab} d_a v_{FSR}} \quad (2.37)$$

If we increase the FSR the dispersion will decrease and there will be a physical overlap in the output apertures. This can be avoidable either by increasing the focal length (R_a) or decreasing the arm aperture pitch d_a . The first option, increasing R_a , results in a significantly increased device size and associated with that a larger propagation loss, a stronger defocussing effect [21] and increased phase errors, all of which are undesirable. On the other hand, if we increase the

FSR by decreasing d_a the total device size remains the same: given that the total acceptance angle θ_{acc} of the array remains the same this option means that we have to increase the number of waveguides ($\theta_{acc} = N \times d_a$) but as the FSR scales inversely proportional to ΔL the maximum waveguide length remains the same.

Decreasing the arm aperture pitch has significant impact on the performance of the AWG. The propagation loss and the imaging quality of the array are the main factors contributing to the insertion loss of the device. Given that the average length of the delay lines remains unchanged, the total propagation loss will not increase.

Furthermore, as per the discussion in section 2.5.1 for a fixed number of channels, the increasing FSR will decrease the roll-off of the transfer characteristic for the outer channels, resulting in a smaller non-uniformity between the inner and outer channels. The bandwidth of the individual wavelength channels on the other hand will remain constant as the channel spacing, the dispersion in the object plane (D) and the width of the input and output apertures are kept fixed with the variation of the arm aperture pitch and the FSR. This also implies that the neighbouring channel crosstalk will remain unchanged for the larger FSR devices. Also the effect on the crosstalk floor due to phase errors in the waveguide array will be small as the average length of the waveguides remains unaltered.

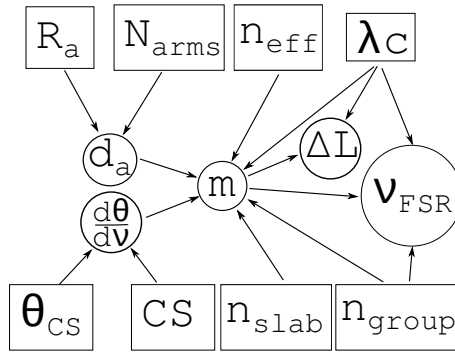


Figure 2.17: Possible design flow for a wavelength de/multiplexers. Boxes are user defined parameters and Circles are calculated parameters.

The main limitation to further increase the number of waveguides and the FSR is the decreasing spacing between the waveguides in the array itself. The reduced distance can introduce coupling between the waveguides, possibly resulting in additional phase errors. Another limitation is that the smaller width will increase the scattering loss of the arm aperture.

2.7 Design

From the previous discussion it is clear that high contrast silicon AWGs may suffer from high insertion loss and phase errors (resulting in high crosstalk). In general these problems are not determined by the design but by fabrication imperfections [22]. The effects of fabrication imperfections on the performance of a silicon AWG can be reduced by engineering the design of the AWG [6, 8, 9, 23]. Therefore in this section we are looking for different designs of the AWGs and their respective implications, advantages and disadvantages. We begin by looking at various geometrical parameters and then discuss about some variations in the AWG design.

2.7.1 Geometry of the star-coupler

A star-coupler is a collection of waveguide apertures with proper positioning around a free space region. Based on the mounting of the waveguide apertures the star-coupler can be classified into two categories: confocal and Rowland type mounting. As shown in Fig. 2.18 (a) and (b) the arm apertures and the input/output apertures are placed along the grating line and the focal line respectively. For the confocal mounting (shown in Fig. 2.18 (a)) the grating line and

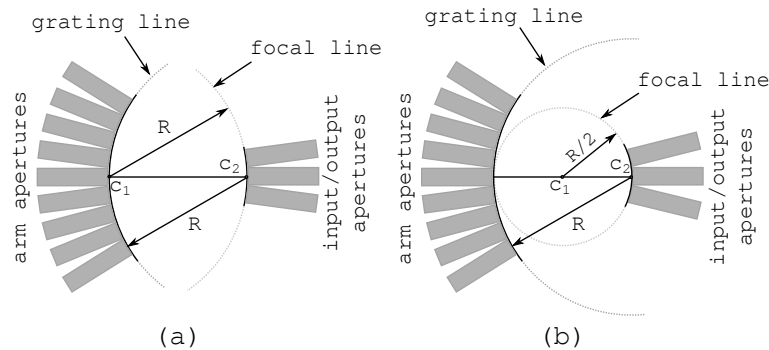


Figure 2.18: (a) Geometry of the confocal-type mounting (b) Geometry of the Rowland-type mounting.

the focal line are the perimeters of two circles where the radius of both circles is equal to the focal length of the star-coupler (R). The centers of these two circles c_2 and c_1 are at a distance R apart from each other. For the Rowland mounting shown in Fig. 2.18 (b) the radius of the grating line remains the same but the radius of the focal line is half of the focal length ($R/2$) and the distance between c_1 and c_2 also is $R/2$. Using Rowland mounting the second order aberrations (defocus) and the third order aberrations (coma) can be avoided [24]. However the

very first AWG with optimized star-coupler [18] and numerous AWGs after that are designed with the confocal configuration [6, 8, 9, 23]. This is because AWGs are mainly designed for a relatively small number of input/output apertures (i.e. θ_{io} is small) and a large number of waveguides (i.e. R is large) for which the difference in positions calculated by the confocal and Rowland mounting becomes negligible. However if many inputs/outputs channel are desired, Rowland mounting will result in a device free of aberrations as described above.

To design a star-coupler we need to calculate the position of these apertures accurately for both mountings. We can find out the position of the apertures on a circle by knowing the angle between the central axis and the aperture axis. If the angle of the aperture is θ from the circle equation the position of the aperture will be

$$x = R \cos \theta + x_c \quad (2.38)$$

and

$$y = R \sin \theta + y_c \quad (2.39)$$

where (x_c, y_c) is the center and R is the radius of the circle. If we consider that c_2 (center of the grating line) is the origin, the position of the grating aperture at an angle of θ_g will be $(R \cos \theta_g, R \sin \theta_g)$ for both the confocal and the Rowland mounting. As c_2 is the origin the coordinates of c_1 are $(-R, 0)$ and $(-R/2, 0)$ for the confocal and the Rowland mounting, respectively. If the angle of an input/output aperture is θ_{io} the position of the aperture will be $(R \cos \theta_{io} - R, R \sin \theta_{io})$ for the confocal mounting and $(\frac{R}{2} \cos \theta_{io} - \frac{R}{2}, \frac{R}{2} \sin \theta_{io})$ for the Rowland mounting.

2.7.2 Geometry of the waveguide array

The waveguide array section is an essential part of the AWG as it controls the channel spacing, FSR, bandwidth, crosstalk etc. The optimized design of the waveguide array changes depending on parameters such as its material system, minimum bend radius, application, fabrication limitation etc. In the next section we will discuss rectangularly shaped waveguide arrays, which have been implemented in IPKISS. Several other shapes of waveguide arrays also discussed in appendix A.

2.7.3 Rectangular Manhattan

As discussed in chapter 4 the rectangular Manhattan waveguide path is the best choice for the high contrast silicon AWG [6, 8, 9, 23]. In rectangular delay line the straight waveguide sections are laid along the x and y direction connected by equal radius bends. As x and y is also the direction of the mask grid line the width of the straight waveguides will be unaffected by the mask discretization. Let's consider two aperture end points P_1 and P_2 of the input and output

star-couplers respectively. The distance between P_1 and P_2 is L along the x axis. These two points need to be connected with a waveguide of length equal to l as shown in Fig. 2.19. The two apertures are creating an angle of θ and $\pi - \theta$ at the points P_1 and P_2 with the positive x axis. As shown in Fig. 2.19 the delay line equation will be

$$l_1 + l_2 + l_3 + l_4 + l_5 + l_6 + l_7 + l_8 = l \quad (2.40)$$

From Fig. 2.19 it can be seen that the waveguide path is symmetric on both side of the line AB. Therefore Eq. 2.40 reduces to

$$r\pi/2 - r\theta + l_2 + l_4 = l/2 \quad (2.41)$$

As the bend radius (r) is kept constant for all delay lines, lengths l_3 and l_6 are the same for all the delay lines. l_1 and l_8 vary with the angle of the star-coupler's output aperture. l_4 and l_5 depend on the distance between P_1 and P_2 . But l_2 and l_7 are free to be adjusted in the delay line to keep the waveguide array condition (delay length (ΔL) is constant) fulfilled. Before we proceed let's find out

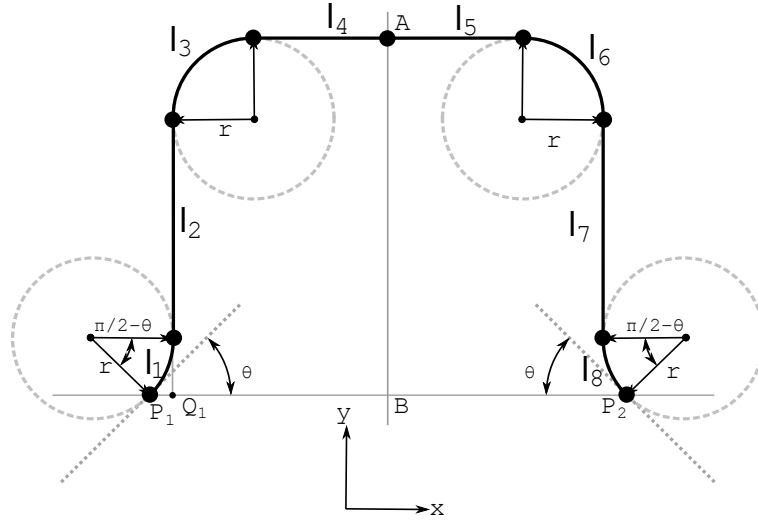


Figure 2.19: Geometry of rectangular manhattan waveguide paths with single waveguide width.

the distance between P_1 and Q_1 .

$$P_1Q_1 = r(1 - \sin\theta) \quad (2.42)$$

To connect P_1 and P_2 with a rectangular Manhattan path the following criterium should be fulfilled.

$$L \geq 2r(1 - \sin\theta) + 2r \quad (2.43)$$

and

$$l - 2\pi r + 2r\theta \geq L - 2r(1 - \sin\theta) - 2r \quad (2.44)$$

Normally the waveguides used in the delay line are kept at single mode width to avoid phase errors related to excitation of higher order modes in the waveguide. But the single mode waveguides are more sensitive to the sidewall roughness i.e. they become more sensitive to the phase error. To reduce this phase error sensitivity an adiabatic taper is used to increase from single to multi mode waveguide width in the array. This adiabatic tapering makes sure that only the fundamental mode is excited in the broad waveguide. This reduces the phase errors significantly as the mode is confined very well in the waveguide and doesn't feel the side walls. To keep the footprint of the AWG small the bends are kept single mode. In Fig. 2.20 the four bends, l_1 , l_3 , l_6 and l_8 are made with the waveguide at single mode width and the straight sections l_2 , l_4 , l_5 and l_7 are made with a waveguide at multi-mode width. As the effective index of the single mode waveguide and the multi-mode waveguide is different, in order to keep the waveguide array condition (delay length (ΔL) is constant) fulfilled, the total length of the single mode waveguides needs to be equal in every delay lines. As sections l_3 and l_6 are the same for all delay lines but l_1 and l_8 depend

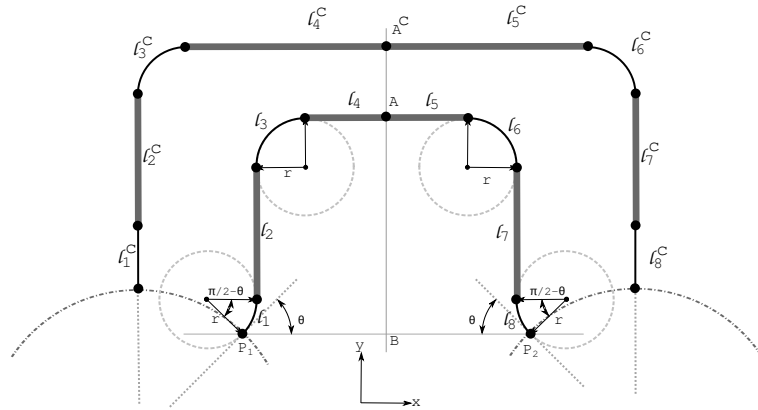


Figure 2.20: Geometry of rectangular Manhattan waveguide paths with multiple waveguide width.

on the angle of the apertures, which is equal to $2r(\pi/2 - \theta)$. Therefore l_1 and l_8 are balanced for all the delay lines by using section of single mode straight waveguides. The length of these bends will be maximum for the side output apertures and minimum for the central output aperture of the star-coupler. If we consider θ_{min} is the angle of the side output aperture the straight section required to balance the single mode waveguide length of an arbitrary delay lines is equal to $2r(\theta - \theta_{min})$. As shown in Fig. 2.19 l_1^c and l_8^c are the required straight

section for the central delay line, which is equal to $r(\pi/2 - \theta_{min})$. In reality the effective index of the bend waveguide can be different from that of the straight waveguide. Therefore the single mode waveguide length of an arbitrary delay line should be modified to $2r(\theta - \theta_{min})(n_{wg,bends}/n_{wg})$.

An experimental demonstration of the rectangularly shaped AWGs is discussed in chapter 4.

2.8 Conclusion

Starting from the general theory of the phased array we built up a theory of the AWG used as a wavelength filter. The brief discussion about the optical phased array helps to understand the loss mechanisms of the AWG. I also discussed the crosstalk, polarization and temperature dependence of the AWG. In terms of application we suggested two different approaches for de/multiplexing and router design. Finally we briefly discussed about the design procedure of the star-coupler and the waveguide array for rectangularly shaped AWG. The design procedure of the other geometries are discussed in Appendix 1.

References

- [1] P.F. McManamon, T.A. Dorschner, D.L. Corkum, L.J. Friedman, D.S. Hobbs, M. Holz, S. Liberman, H.Q. Nguyen, D.P. Resler, R.C. Sharp, and E.A. Watson. *Optical phased array technology*. Proceedings of the IEEE, 84(2):268–298, Feb 1996.
- [2] K. Van Acoleyen. *Nanophotonic Beamsteering Elements Using Silicon Technology for Wireless Optical Applications*. PhD thesis, Ghent University, 2012.
- [3] W. L. Stutzman and G. A. Thiele. *Antenna Theory and Design*. WILEY, 1998.
- [4] J. Goodman. *Introduction to Fourier Optics*. Roberts and Company Publishers, 2004.
- [5] M.K. Smit and C. van Dam. *PHASAR-based WDM-devices: Principles, design and applications*. Selected Topics in Quantum Electronics, IEEE Journal of, 2(2):236–250, Jun 1996.
- [6] S. Pathak, M. Vanslebrouck, P. Dumon, D. Van Thourhout, and W. Bogaerts. *Optimized Silicon AWG With Flattened Spectral Response Using an MMI Aperture*. Lightwave Technology, Journal of, 31(1):87–93, Jan 2013.
- [7] W. Bogaerts and S.K. Selvaraja. *Compact Single-Mode Silicon Hybrid Rib/Strip Waveguide With Adiabatic Bends*. Photonics Journal, IEEE, 3(3):422–432, 2011.
- [8] W. Bogaerts, S.K. Selvaraja, P. Dumon, J. Brouckaert, K. De Vos, D. Van Thourhout, and R. Baets. *Silicon-on-Insulator Spectral Filters Fabricated With CMOS Technology*. IEEE Journal of Selected Topics in Quantum Electronics, 16(1):33–44, 2010.
- [9] S. Pathak, D. Van Thourhout, and W. Bogaerts. *Design trade-offs for silicon-on-insulator-based AWGs for (de)multiplexer applications*. Opt. Lett., 38(16), Aug 2013.
- [10] M. Aamer, A.M. Gutierrez, A. Brimont, D. Vermeulen, G. Roelkens, J.M. Fedeli, A. Hakansson, and P. Sanchis. *CMOS Compatible Silicon-on-Insulator Polarization Rotator Based on Symmetry Breaking of the Waveguide Cross Section*. IEEE Photonics Technology Letters, 24(22):2031–2034, 2012.
- [11] C.R. Doerr, M. Zirngibl, C.H. Joyner, L.W. Stulz, and H.M. Presby. *Polarization diversity waveguide grating receiver with integrated optical preamplifiers*. Photonics Technology Letters, IEEE, 9(1):85–87, Jan 1997.

- [12] T. Barwicz, M. R. Watts, P. T. Popovic, M. A. and Rakich, L. Socci, F. X. Kartner, E. P. Ippen, and H. I. Smith. *Polarization-transparent microphotonic devices in the strong confinement limit*. Nature Photonics, 1(1):57–60, Jan 2007.
- [13] W. Bogaerts, D. Taillaert, P. Dumon, D. Van Thourhout, R. Baets, and E. Pluk. *A polarization-diversity wavelength duplexer circuit in silicon-on-insulator photonic wires*. Optics express, 15(4):1567–78, Feb 2007.
- [14] L. Wang, W. Bogaerts, P. Dumon, S. K. Selvaraja, J. Teng, S. Pathak, X. Han, J. Wang, X. Jian, M. Zhao, R. Baets, and G. Morthier. *Athermal arrayed waveguide gratings in silicon-on-insulator by overlaying a polymer cladding on narrowed arrayed waveguides*. Applied Optics, 51(9):1251–1256, Mar 2012.
- [15] M. Uenuma and T. Motooka. *Design of a temperature-independent Arrayed Waveguide Grating on SOI Substrates*. In 4th IEEE International Conference on Group IV Photonics, pages 1–3, 2007.
- [16] M. Uenuma and T. Motooka. *Temperature-independent silicon waveguide optical filter*. Opt. Lett., 34(5):599–601, Mar 2009.
- [17] H. Huang, S.T. Ho, D. Huang, Y. Tu, and W. Liu. *Design of temperature-independent arrayed waveguide gratings based on the combination of multiple types of waveguide*. Applied optics, 49(16):3025–3034, 2010.
- [18] C. Dragone. *An NxN optical multiplexer using a planar arrangement of two star couplers*. Photonics Technology Letters, IEEE, 3(9):812–815, Sept 1991.
- [19] C. Dragone, C.A. Edwards, and R.C. Kistler. *Integrated optics NxN multiplexer on silicon*. Photonics Technology Letters, IEEE, 3(10):896–899, Oct 1991.
- [20] S. Pathak, M. Vanslebrouck, P. Dumon, D. Van Thourhout, and W. Bogaerts. *Compact 16x16 channels routers based on silicon-on-insulator AWGs*. In 16th Annual symposium of the IEEE Photonics Benelux Chapter, pages 101–104. IEEE Photonics Society, 2011.
- [21] A. Klekamp and R. Munzner. *Calculation of imaging errors of AWG*. Light-wave Technology, Journal of, 21(9):1978–1986, Sept 2003.
- [22] C. Dragone. *Crosstalk caused by fabrication errors in a generalised Mach-Zehnder interferometer*. Electronics Letters, 33(15):1326–1327, 1997.

-
- [23] S. Pathak, M. Vanslembrouck, P. Dumon, D. Van Thourhout, and W. Bogaerts. *Compact SOI-based polarization diversity wavelength demultiplexer circuit using two symmetric AWGs*. *Opt. Express*, 20(26):B493–B500, Dec 2012.
- [24] R. Marz and C. Cremer. *On the theory of planar spectrographs*. *Lightwave Technology, Journal of*, 10(12):2017–2022, Dec 1992.

3

Simulation model of arrayed waveguide gratings

"Scientific models have all these connotations. They are representations of states, objects, and events. They are idealized in the sense that they are less complicated than reality and hence easier to use for research purposes. These models are easier to manipulate and "carry" than the real thing. The simplicity of models, compared with reality, lies in the fact that only the relevant properties of reality are represented."

– Russell L. Ackoff

3.1 Introduction

An appropriate simulation model is required for photonics components to predict the behaviour of the components or to validate complex photonics circuits. Today a lot of simulation tools are available for photonics devices: beam propagation method (BPM), eigenmode solver, finite-difference time-domain (FDTD) etc. But an AWG is too large to practically simulate with these simulators. Therefore the complete simulation model of an AWG requires the individual simulations of several photonic components. This is equivalent to the circuit model of an electronic system where individual electronic components (e.g. transistors, amplifiers, delay clocks) are connected with each other. In electronics all the simulation models are abstract and usually do not contain any physical simulation.

A hybrid simulation model is built for the AWG where all components are simulated individually by suitable physical simulators and finally a circuit model generates simulation results of the whole device by combining the results of all the physical simulations. Therefore we will start our discussion with decomposing the AWG. The decomposition become easier as the simulation tool is integrated with our design software (IPKISS), which is based on parametric cell. Before we proceed to the details of the semi-analytical model we give a look to our design software IPKISS in order to understand the advantages of the integration between IPKISS and the AWG model. Finally we discuss about the most suitable simulators for each of these building blocks of the AWG to obtain the simulated spectral response.

3.2 AWG decomposition

The AWG is one of the most complicated passive components in the integrated photonics. For simulation we will decompose the AWG as shown in Fig. 3.1. An AWG consists of two star-couplers and an array of waveguides. The two star-couplers used in the AWG are not always the same. But same simulation method can be applied for both the star-couplers. The array of waveguide is a collection of waveguides with successive increment of length which can be simulated by a single waveguide simulator which simulate one waveguide at time and periodically build up the simulation result of the array. Therefore if we decompose the AWG the fundamental blocks will be a star-coupler and a waveguide.

A star-coupler consist of the slab region, the input and the output waveguide aperture. The input and output waveguide apertures have not necessarily the same specifications, but can be simulated using the same simulator. The slab will be simulated for one source and one receiving point by using the input and output aperture's vectors. Therefore the if we decompose the star-coupler the

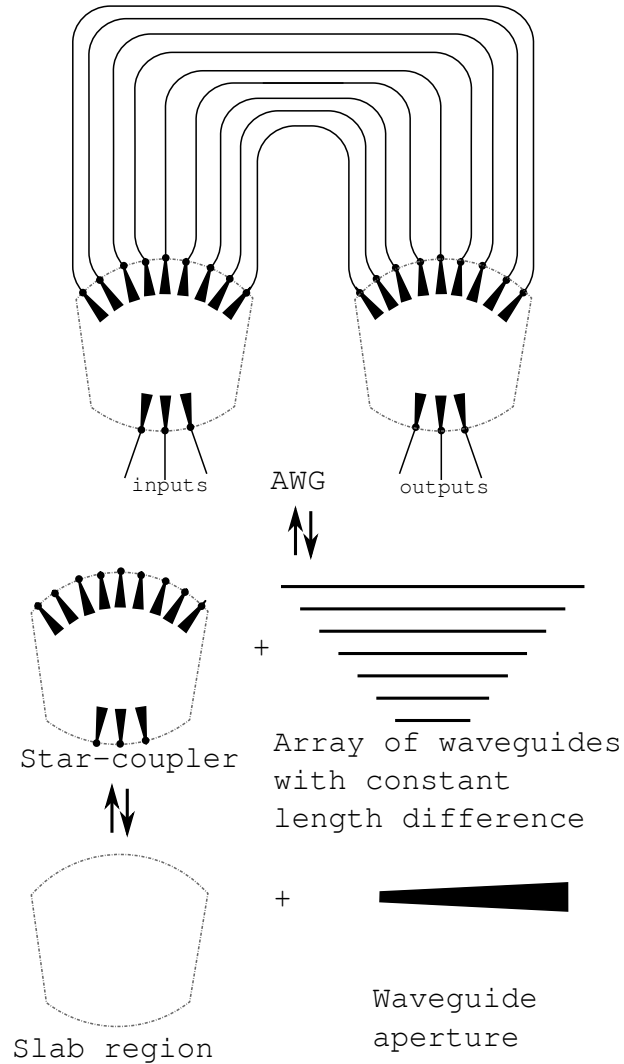


Figure 3.1: An AWG decomposition for simulation.

fundamental block will be a waveguide aperture and a slab region. The details of this individual simulations are described in section 3.4.

3.3 IPKISS: A parametric design framework

IPKISS ([1]) is a photonic design framework developed at Ghent University and imec [2–4]. Its origin dates back to 2001 when research in silicon photonics ex-

posed the needs for tools to generate complex waveguide circuit layouts in a parametric way (e.g. to generate designs with parameter sweeps on some circuit elements). At that point, the decision was made to implement this tool as a scripting framework in Python [5], because of the flexibility and readability of the language and the availability of many high-performance scientific libraries. With IPKISS, the photonics research group has generated hundreds of designs of silicon photonic integrated circuits, and a large library of parametric building blocks was constructed, together with the layer settings to generate complex GDSII files. Since then, IPKISS has evolved from a flexible GDSII generator to a broader component-oriented design framework.

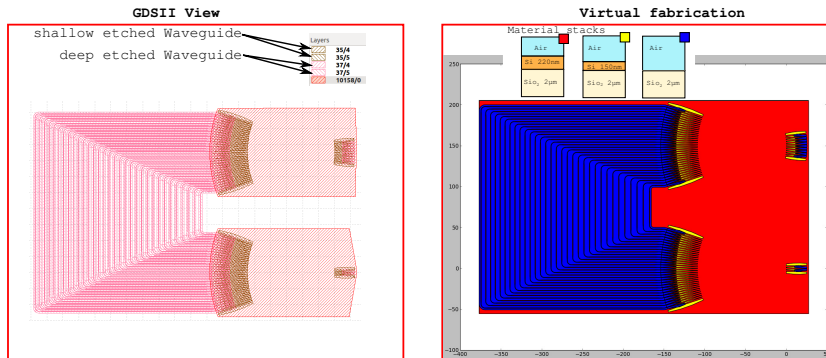


Figure 3.2: An example of a AWG definition in IPKISS, with user defined parameters, mask layout (GDSII view) and a 2D representation of the 3D material distribution generation (virtual fabrication)

The main advantage of IPKISS is that it allows users to define parametric building blocks. A building block can be either atomic or hierarchical. The atomic building blocks are stand alone blocks having no children. The hier-

archical building blocks contain other 'child' building blocks and connect them together into a (sub)circuit. Both the atomic and hierarchical building blocks are treated in the same way. Different representations (views) are added to visualize these building blocks. Mask layout is only one of those. Other such views include input-output ports, interconnectivity matrix (or netlist), 3D geometry, and interfaces to simulation tools for physical and circuit simulation. IPKISS itself does not perform simulations, but the python scripting framework makes it easy to interface IPKISS to our AWG model.

IPKISS itself manages the interaction between the views and the associated tools. As an example, the interaction between different views of an AWG in IPKISS is illustrated in Fig. 3.2. In this example, we need to define a mask layout for this AWG, consisting of a set of polygons on the correct layers, such that the component can be fabricated with lithography. The definition of these layers is stored in a technology file, which contains the specifics of the fabrication technology. Based on this mask layout, IPKISS can now generate other views. If the technology file specifies a fabrication process, IPKISS can apply the virtual fabrication flow to the mask layout, which results in a 3D distribution of materials showing the effect of fabrication on each polygon. This built-in virtual fabrication engine generates an approximate geometry of material stacks. The 3-D geometry can be used directly to define the simulation volume for a physical simulation. If the user has also specified input and output ports, the simulation volume could be supplied with the necessary excitation sources and monitors at the inputs and outputs.

As per the discussion in section 3.2 on a lower hierarchical level an AWG consists of two fundamental building blocks: waveguides and waveguide apertures. Shallowly etched apertures (details of the shallow etched aperture are discussed in chapter 4) are used to design the AWG. IPKISS places the shallowly etched aperture repeatably in the appropriate positions calculated from the design procedure of the AWG. If we consider a star-coupler has P inputs and N outputs IPKISS will also provide P and N input and output ports respectively. A set of waveguides will be used to connect the output ports of the first star-coupler to the second. The length of the waveguides is calculated by the design procedure of the AWG, which is also (the algorithm described in chapter 2) implemented in the python environment to avoid unwanted errors. By using user defined and predefined parameters the theoretical model calculates all the necessary design parameters like position and orientation of the input and output apertures of the star-couplers, length of the waveguides etc.. These design parameters are used by IPKISS to create the mask layout. The semi-analytical simulation model of the AWG also uses these design parameters and the 2D materials geometries, which are generated by IPKISS.

3.4 Semi-analytical simulation model

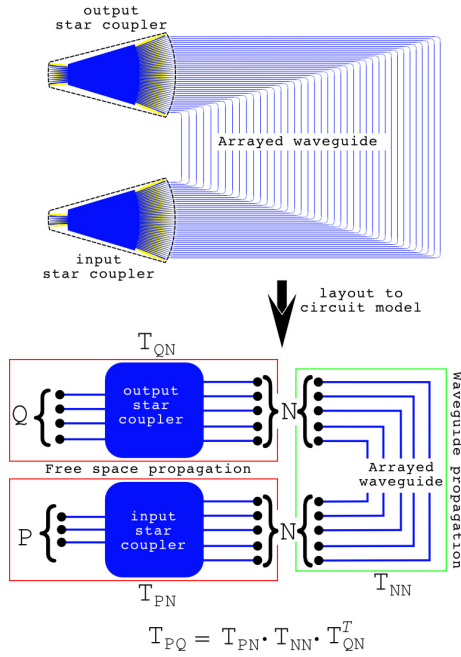


Figure 3.3: T-matrix approach to simulate the AWG.

IPKISS provides the 2D material geometry of the AWG which can be used by an FDTD simulator (like meep [6]) to simulate the AWG. Due to the large physical size of the AWG the calculation times of the FDTD simulation will be very high. Therefore we intend to find an alternative fast simulation method [7, 8] with a high accuracy. To reduce the complexity we introduced a simple unidirectional circuit level simulator, where we calculate the transmission matrices (further referred as T-matrix) of the star-couplers and the waveguide array separately and later we combine them together to get the T-matrix of the AWG [9].

Let's consider an AWG with P input channels, Q output channels and N arms as shown in Fig. 3.3. Then the T-matrix of the input star coupler is T_{PN} , the T-matrix of the output star coupler is T_{QN} and the T-matrix of the waveguide array is T_{NN} . So the overall T-matrix (T_{PQ}) of the AWG is calculated as

$$T_{PQ} = T_{PN} \cdot T_{NN} \cdot T_{QN}^T \quad (3.1)$$

3.4.1 Star-coupler model

In an AWG the most complex and difficult part to simulate is the star-coupler. For the star coupler we developed a hybrid analytical simulation model. As shown in Fig. 3.2 the star-couplers are again split in three parts: the input apertures, the output apertures and the free space region. We used different approaches to simulate the waveguide apertures and the free space region [10].

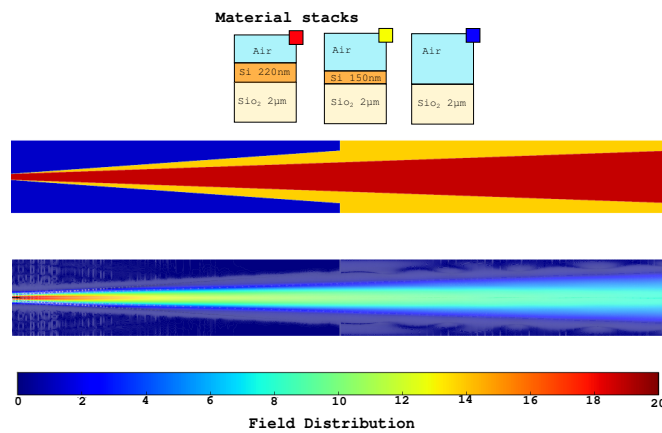


Figure 3.4: The geometry used for CAMFR simulation and the field distribution of an aperture simulated by CAMFR.

3.4.1.1 Field profile

The field profile at the junction between the input / output aperture and the slab region is necessary for the analytical model of the free space propagation. To obtain the field profile, the apertures are simulated numerically using eigenmode propagation (CAMFR [11]). CAMFR is a python scripting based eigenmode and propagation solver. The 2D material geometry created by IPKISS can be used by CAMFR. The accuracy is increased and time is saved by reusing the geometry from the mask layout for the simulation. Therefore in IPKISS CAMFR is integrated as simulation engine. Figure 3.4 shows the geometry used for the CAMFR simulation and the simulated field distribution of the aperture. CAMFR launches the field from the left hand side of the material and the field profile at the right hand side of the material is used for further simulation in the free propagation region of the star-coupler. Alternatively, we can use 2D or 3D FDTD (MEEP) to simulate the aperture as shown in Fig. 3.5.

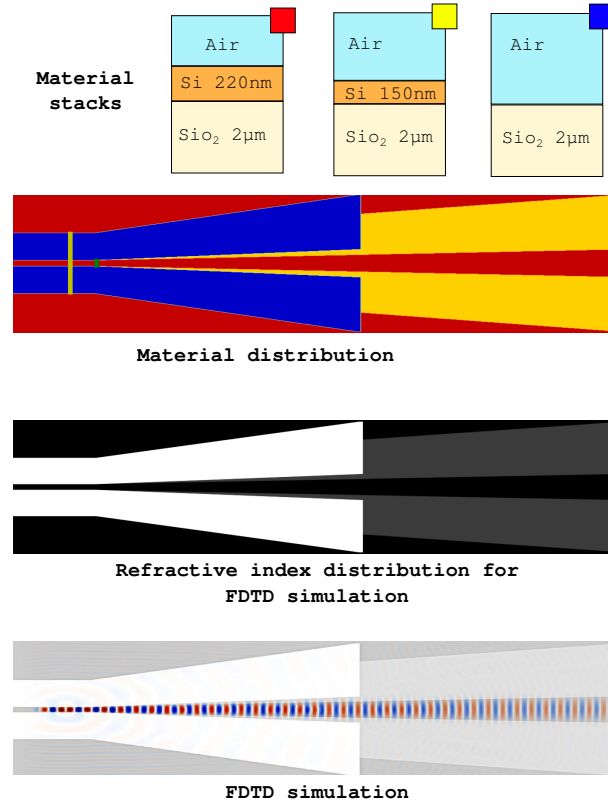


Figure 3.5: The geometry used for the MEEP simulation, the refractive index distribution from the material distribution and the field distribution of the aperture simulated by MEEP.

3.4.1.2 Free space propagation

The calculated field-profile is used to simulate the free-space propagation region [10], which is solved analytically using a 2D Fresnel-diffraction scheme [12]. This analytical solution is implemented in python [13]. In this python script, the field profile of the aperture is a 1D matrix. The total number of elements in this 1D matrix equals the total number of points considered along the width of the aperture. These number of points will decide the required simulation time. Let's consider the aperture width is along the x direction and the width step is dx . The number of elements of the field profile matrix and the width step (dx) for both the input and output aperture should be equal.

Let's consider u_{in} and u_{out} are the unnormalized field profile of the input

and output aperture. The power normalized field profile will be

$$f_{\text{in}}(x) = \frac{u_{\text{in}}(x)}{\sqrt{\int_{-\infty}^{+\infty} |u_{\text{in}}(x)|^2 dx}} \quad (3.2)$$

$$f_{\text{out}}(x) = \frac{u_{\text{out}}(x)}{\sqrt{\int_{-\infty}^{+\infty} |u_{\text{out}}(x)|^2 dx}} \quad (3.3)$$

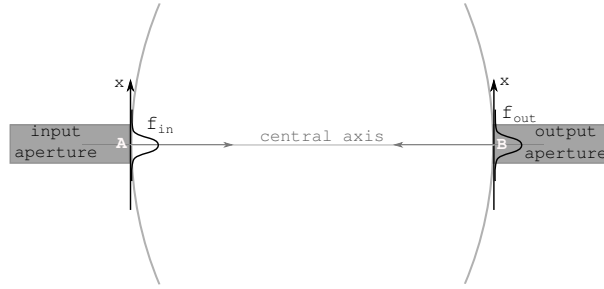


Figure 3.6: Free space propagation from the central input to the central output of the star-coupler.

To start with a simple situation let's consider the light is propagating from the central input aperture to the central output aperture as shown in Fig. 3.6. The field f_{in} is broken up into a sum of plane waves by taking the Fourier transform (F) [12].

$$F\{f_{\text{in}}(x)\} = \int_{-\infty}^{+\infty} f_{\text{in}}(x) \exp(jxk_x) dx \quad (3.4)$$

Where k_x is the spatial wavenumber. These plain waves are propagating from point A to point B. If the distance between A and B is considered to be AB the equation of the plane waves at point B will be

$$F'(k_x) = F\{f_{\text{in}}(x)\} \exp(j\sqrt{k^2 - k_x^2}|AB|) \quad (3.5)$$

where k is the propagation constant of the slab waveguide. k is defined as

$$k = \frac{2\pi n_{\text{slab}}}{\lambda_0}. \quad (3.6)$$

where λ_0 is the wavelength of the light and n_{slab} is the effective index of the slab waveguide. Now by converting these plane waves ($F'(k_x)$) back into the spatial domain we obtain the field at point B. If the inverse Fourier transform is denoted as F^{-1} , the field at point B can be written as

$$F''(x) = F^{-1}[F\{f_{\text{in}}(x)\} \exp(j\sqrt{k^2 - k_x^2}|AB|)] \quad (3.7)$$

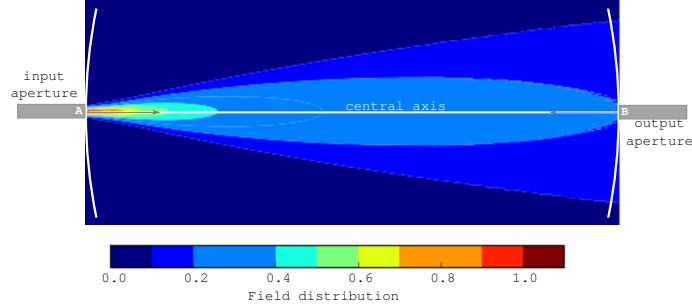


Figure 3.7: Analytically simulated field distribution of a star-coupler.

Fig. 3.7 shows the field distribution ($F''(x)$) over the space between A and B. The transmission (T) from the input aperture to the output aperture is obtained by calculating the scalar overlap integral between $F''(x)$ and $f_{\text{out}}(x)$. Therefore T will be

$$T = \int_{-\infty}^{+\infty} f_{\text{out}}^*(x) F^{-1} [F\{f_{\text{in}}(x)\} \exp(j\sqrt{k^2 - k_x^2}|AB|)] dx \quad (3.8)$$

Now this equation (Eq. 3.8) is modified for arbitrary placed input and output apertures. Let's consider the input and output aperture are positioned at angle θ_{in} and θ_{out} with respect to the central axis respectively as shown in Fig. 3.8. The line connecting point A to B has an angle θ_{AB} with respect to the central

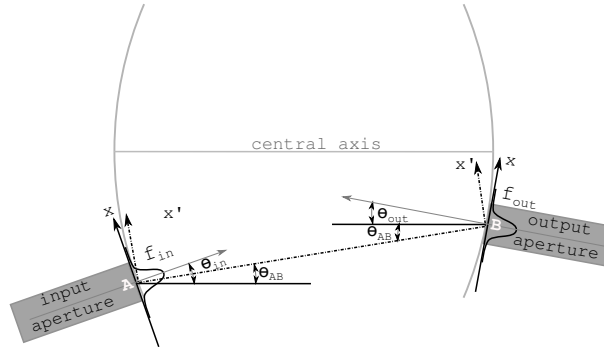


Figure 3.8: Free space propagation from an arbitrary input to an arbitrary output of the star-coupler.

axis. The equation (Eq. 3.8) will remain valid if we just replace the field f_{in} and f_{out} with the modified fields along the propagation line AB. The modified input and output field orthogonal to the propagation line AB can be denoted as

$$f'_{\text{in}}(x) = f_{\text{in}}(x) \exp[jkx(\theta_{\text{in}} - \theta_{\text{AB}})] \quad (3.9)$$

$$f'_{\text{out}}(x) = f_{\text{out}}(x) \exp[jkx(\theta_{\text{out}} + \theta_{\text{AB}})] \quad (3.10)$$

In the algorithm the integration of Eq 3.8 is replaced by summation and all multiplications are the matrix multiplications as the field is represented by a 1D matrix [14]. The python-numpy [15] library is used for the Fourier transform (*fft*) and inverse Fourier transform (*ifft*). Finally by using this transmission equation (Eq 3.8) repeatedly we can build the T-matrix of a star coupler with multiple inputs and outputs. Fig. 3.9 shows the transmission of an 1×16 star-

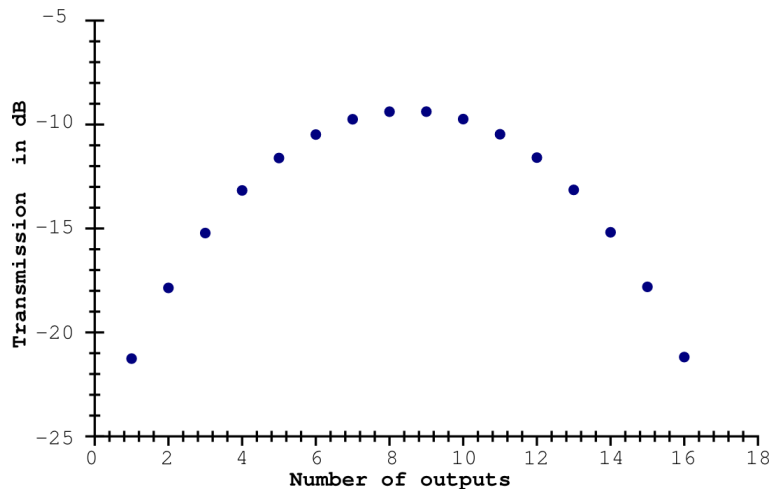


Figure 3.9: Simulated transmission of an 1×16 channels star-coupler.

coupler. From Fig. 3.9 we can see that the central channels contain a lot of power compared to the side channels. The single mode waveguide width increases adiabatically to the width of the aperture at the junction with the slab region as it moves toward the slab to keep the single mode condition unchanged. The width of the aperture at the junction with the slab region decreases adiabatically to the single mode waveguide width as it moves away from the slab, which will introduce very minimum coupling. Each aperture also has a similar aperture on both sides which introduces similar coupling for each individual aperture. Therefore this coupling between apertures can be neglected in the phase calculation of the AWGs.

3.4.2 Model of waveguide array

The outputs of the two star-couplers are connected by a waveguide array. These single mode waveguides are well separated in the array to avoid coupling between the waveguides. Therefore in our simulation the coupling between two

successive apertures is not taken into account. This makes the simulation model simpler. The transmission of the waveguide can be written as

$$T = \exp\left\{j \cdot \frac{2\pi n_{eff}(\lambda_0)L}{\lambda_0}\right\} \quad (3.11)$$

where n_{eff} is the effective index of the waveguide, L is the length of the waveguide used for the mask design, λ_0 is the operating wavelength. In general the waveguides used to connect the two star-couplers have multiple of bends. These bends have different losses and phase contributions compared to the straight waveguides. In the silicon AWG design we use an equal number of bends with constant bend radius in every waveguide of the array, which cancels out the phase variation of the bends from the phase difference between two successive waveguides. Therefore there is no need to introduce the effect of the bends in Eq. 3.11. Equation 3.11 is modified further to introduce waveguide loss and phase errors.

$$T = \exp\left\{\frac{j2\pi n_{eff}L}{\lambda} - \alpha_{loss}L + j\sigma_{phase}(\lambda) \cdot L^{\frac{1}{2}}\right\} \quad (3.12)$$

where α_{loss} is introduced to take into account the propagation loss and the last term is used to simulate phase errors due to small variations in waveguide width. α_{loss} is calculated from the waveguide loss measurement. To quantify

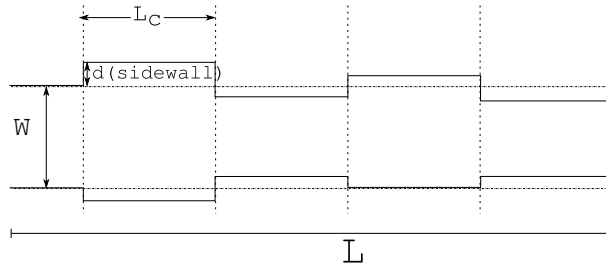


Figure 3.10: Waveguide phase error model.

the phase error we assumed the variations on each sidewall to be stationary and uncorrelated for both sidewalls [16]. But along a sidewall the variation can be considered highly correlated within a correlation length. Thus, the phase error deviation can be described as

$$\sigma_{phase}(\lambda) = \left\{L_c \cdot \left(\frac{\delta\beta(\lambda)}{\delta\omega}\right)^2 \cdot \sigma_{d(sidewall)}^2\right\}^{\frac{1}{2}} \quad (3.13)$$

where L_c is the correlation length along which the sidewall approximately keeps a constant lateral position as shown in Fig. 3.10, $\frac{\delta\beta(\lambda)}{\delta\omega}$ is the variation of propagation constant with the variation of the waveguide width for the operating

wavelength λ , and $\sigma_{d(\text{sidewall})}^2$ is the variance of the waveguide width deviation. This will introduce an additional phase factor in the transmission of the waveguides depending on the length of the waveguide. As the distribution of the sidewall roughness over a waveguide is random, we used Monte Carlo methods to estimate the phase error variation by running the simulation for 100 samples.

In the python script, if the AWG has N waveguides the waveguide model will create an $N \times N$ matrix. Since we neglect the waveguide coupling the $N \times N$ matrix will be a diagonal matrix.

3.4.3 Spectral response

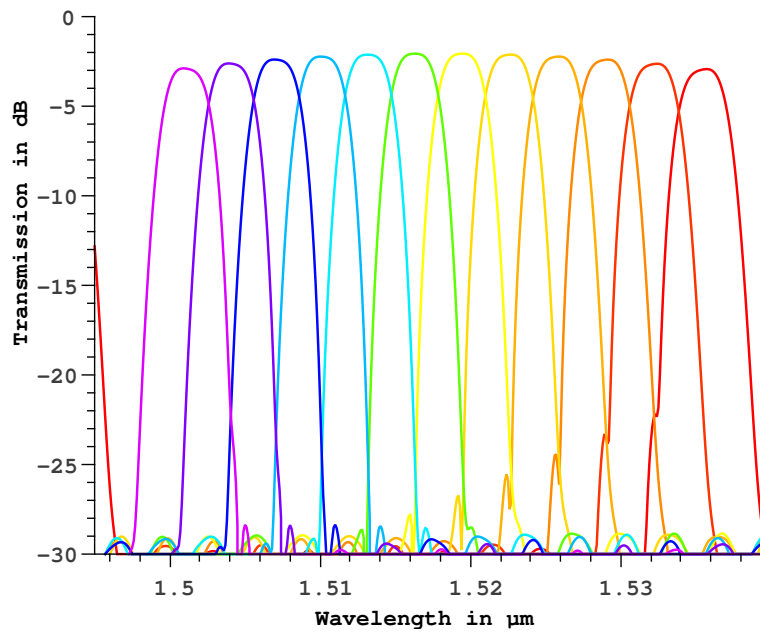


Figure 3.11: Simulated spectral response of a 12×400 GHz MMI-AWG.

Finally by multiplying all the transmission matrices we can obtain the spectral response of the AWG. As an example Fig. 3.11 shows simulated result of a 12×400 GHz MMI-AWG with flat spectral response. Details of this work is described in chapter 5 where we demonstrate that these simulation results agree closely with the experimental results [17, 18].

3.5 Conclusions

We developed a semi-analytical simulation model for the AWG. The simulation results are very much comparable with experimental results (see chapter 4), which also increases the reliability of the model. The simulation time required by the model is low as the core of the simulation is carried out analytically. This helps designing AWGs with appropriate parameters for different applications. This model can be used in a complex circuit, where the AWG is just one of the components of the circuit. The model only considers 2D geometries which makes it not completely accurate. The phase error model is based on a simple stochastic assumption which makes it also not fully accurate. To make the waveguide model more accurate coupling between two successive waveguide needs to be introduced in the model. In the future the model can be further modified by introducing a bidirectional S-matrix instead of a unidirectional T-matrix. This can also then support the reflection of AWG. Finally the analytical slab simulator can be used for other components like echelle gratings.

References

- [1] *IPKISS*. <http://www.ipkiss.be>.
- [2] W. Bogaerts, P. Dumon, E. Lambert, M. Fiers, S. Pathak, and A. Ribeiro. *IP-KISS: A parametric design and simulation framework for silicon photonics*. In 9th IEEE International Conference Group IV Photonics, pages 30–32, August 2012.
- [3] W. Bogaerts, Y. Li, S. Pathak, A. Ruocco, M. Fiers, A. Ribeiro, E. Lambert, and P. Dumon. *Integrated design for integrated photonics: from the physical to the circuit level and back*. In Proc. SPIE 8781, Integrated Optics: Physics and Simulations (invited), pages 878102–878102–11, 2013.
- [4] M. Fiers, E. Lambert, S. Pathak, B. Maes, P. Bienstman, W. Bogaerts, and P. Dumon. *Improving the design cycle for nanophotonic components*. Journal of Computational Science, 4(5):313–324, 2013.
- [5] *Python Programming Language*. <http://www.python.org/>.
- [6] *MIT Electromagnetic Equation Propagation (MEEP)*. <https://launchpad.net/python-meep>, <http://ab-initio.mit.edu/meep/>.
- [7] P. Munoz, D. Pastor, and J. Capmany. *Modeling and design of arrayed waveguide gratings*. Lightwave Technology, Journal of, 20(4):661–674, Apr 2002.
- [8] E. Kleijn, M.K. Smit, and X.J.M. Leijtens. *New Analytical Arrayed Waveguide Grating Model*. Lightwave Technology, Journal of, 31(20):3309–3314, 2013.
- [9] S. Pathak, W. Bogaerts, E. Lambert, P. Dumon, and D. Van Thourhout. *Integrated Design and Simulation Tools for Silicon Photonic Arrayed Waveguide Gratings*. In IEEE Photonics Benelux Chapter, pages 41–44, November 2010.
- [10] C. R. Doerr. *Planar Lightwave Devices for WDM, in Optical Fiber Telecommunications*, volume 4. Academic Press, ISBN 0-12-395172-0, 2002.
- [11] *CAvity Modelling FRamework (CAMFR)*. <http://camfr.sourceforge.net>.
- [12] J. Goodman. *Introduction to Fourier Optics*. Roberts and Company Publishers, 2004.
- [13] P. Dumon. *Ultra-Compact Integrated Optical Filters in Silicon-on-insulator by Means of Wafer-Scale Technology*. PhD thesis, Ghent University, 2007.

- [14] S. Trester. *Computer-simulated Fresnel diffraction using the Fourier transform*. Computing in Science Engineering, 1(5):77–83, Sep 1999.
- [15] *Numpy*. <http://www.numpy.org/>.
- [16] T. Goh, S. Suzuki, and A. Sugita. *Estimation of waveguide phase error in silica-based waveguides*. Lightwave Technology, Journal of, 15(11):2107–2113, Nov 1997.
- [17] S. Pathak, E. Lambert, P. Dumon, D. Van Thourhout, and W. Bogaerts. *Compact SOI-based AWG with flattened spectral response using a MMI*. In 8th IEEE International Conference Group IV Photonics, pages 45–47, 2011.
- [18] S. Pathak, M. Vanslebrouck, P. Dumon, D. Van Thourhout, and W. Bogaerts. *Optimized Silicon AWG With Flattened Spectral Response Using an MMI Aperture*. Lightwave Technology, Journal of, 31(1):87–93, Jan 2013.

4

Experimental demonstrations

"Every experiment destroys some of the knowledge of the system which was obtained by previous experiments."

– Werner Heisenberg

4.1 Introduction

In this chapter we will discuss experimental results of AWGs fabricated in the SOI material system, which are designed and fabricated based on the theoretical knowledge we gained in the previous chapters and its implementation in our simulation framework. The experimental work is discussed in three parts. First we demonstrate differently shaped AWGs (rectangularly, circularly, S-shaped and reflection type). The second classification is based on application: the de/multiplexers and routers. In third section, we study the accuracy of fabrication based on the mask discretization. In addition to this we discuss the polarization diversity circuit for polarization independent de/multiplexing. Finally we conclude the experimental work by comparing the experimental results of the AWGs with another widely used de/multiplexer in silicon the echelle grating.

4.2 Fabrication of SOI integrated circuits

Microelectronics fabrication technology has become one of the most advanced manufacturing technologies in the past 50 years. The drive to get more functionalities and density of CMOS (complementary metal-oxide semiconductor) circuits requires development of state of the art patterning tools. The primary goal of a CMOS pilot line (such as the one we are using in imec) is to increase the device density with high repeatability. Similar fabrication technology can be used for Si photonics for the realization of SOI waveguide circuits with high density on a wafer.

Figure 4.1 shows the overview of the fabrication process used to fabricate SOI photonic wire waveguides using 193 nm optical lithography¹. The process starts with a commercially available 200 mm SOI wafer which has 220 nm thick silicon guiding layer on top of a 2 μm buried oxide layer. In the first step, the wafer is coated with an anti-reflection coating and photoresist. The anti-reflection coating can be used either on top or at the bottom of the photoresist. The photoresist alone is not sufficient for reliable patterning because when a wafer coated with only photoresist is illuminated, the light is reflected from the substrate generating a standing wave pattern in the photoresist which introduces a variation in line width. With an optimum thickness of the anti-reflection coating it is possible to suppress this reflection. Using simulations and experiments S. K. Selvaraja obtained 330 nm and 77 nm as optimal thickness of the photoresist and the anti-reflection coating respectively [1]. After applying these coatings the wafer is briefly baked to evaporate the solvents. The resist coated wafers are then exposed with the image of the mask using a 193 nm ArF laser in a scanner. The intensity of the illuminated light available on the

¹this work was part of the PhD research of Dr.Shankar Kumar Selvaraja.

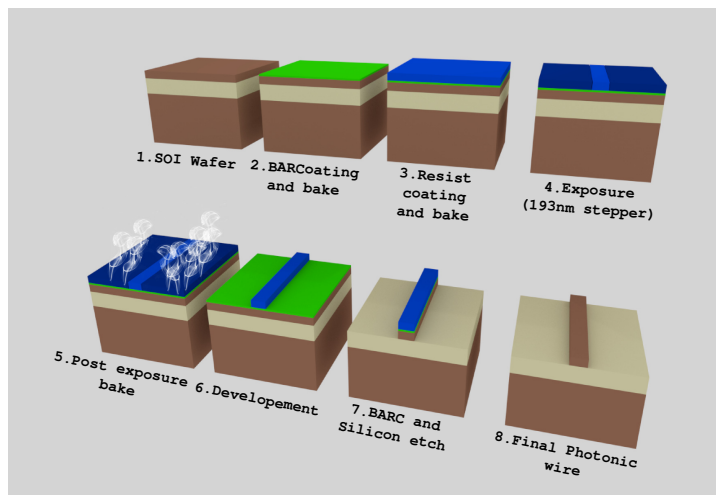


Figure 4.1: Overview of the fabrication process used to fabricate the SOI based photonic device using 193 nm optical lithography.

surface of the photoresist (also called exposure dose) defines the sidewall angle and the line width of the developed photoresist. A low dose can introduce a partial removal of photoresist or increased line width whereas a high dose reduces the line width. The photons create precursors which trigger a chemical change in the resist during post-exposure baking. The exposed areas are then removed with a selective solvent in a process called development. After the lithography the structures, which are patterned in the photoresist are ready for dry etching. In our process we have etching recipes optimized for 220 nm deep etch and 70 nm shallow etch. More details of the etching process are discussed in [1]. A proper etching recipe is required to achieve low sidewall roughness. The sidewall roughness contributes to the loss and phase error of the waveguides. As high contrast waveguides are more sensitive to the sidewall roughness, the delay lines of the AWG can accumulate large phase errors, and finally the phase errors will reflect as a high crosstalk. As our AWGs are made out of deep and shallowly etched waveguides two separate patterning steps are needed.

4.3 Experimental setup

To characterize the optical properties of the AWGs, we measure the transmission of light through the AWG as a function of wavelength. For this purpose various light sources and photodetectors are available at the Photonics Research Group. To carry out the characterization, the light needs to couple from the

fiber to the SOI waveguide and vice versa. A common coupling method¹ is using a fiber grating coupler. The vertical coupling has a lot of advantages over other coupling methods e.g. the fiber grating couplers can have a high coupling efficiency (up to 70 % in silicon [2]), good alignment tolerances, enable a compact device size and require no post-processing.

4.3.1 Vertical coupling

Figure 4.2 shows the measurement setup for vertical coupling. The light from a tunable laser is coupled into the waveguide by positioning the fiber vertically over the fiber coupler. In general the high contrast silicon waveguides are strongly birefringent but depending on its design, a common 1-D fiber grating coupler couples either the TE or the TM polarization into the waveguide. Mostly light with TE polarization is used, as this is the ground mode of a standard sub-micron wire waveguide. Since the grating coupler couples light with only a selected polarization and rejects the other polarization, it is important to have the light at the output of the fiber with the desired polarization. To achieve this, a polarization controller is used in between the laser and input fiber grating coupler. Similar to the incoupling another grating coupler is used to couple the light back into the output fiber, which is connected directly to the power meter. Both the laser and the power meter are controlled by the computer through a GPIB interface. To avoid back reflection the design of the fiber grating coupler is intentionally optimized such that the fibers are tilted 10° with respect to the vertical axis [3] at maximum efficiency.

We align the fibers with respect to the grating using X-Y-Z movable stages by a two step alignment method: crude alignment and active alignment. The crude alignment is obtained by monitoring the relative position of the fiber and the shadow captured by the microscope camera. In this way when both input and output fibers are aligned the fibers are aligned further by using active alignment which is done by maximizing the power received from the output fiber.

In general the grating coupler has a bandwidth of a few tens of nanometer. Another limitation of the fiber grating is the wavelength dependent coupling efficiency which require a complex measurement method to normalize the AWG spectrum (discuss in section 4.3.3).

4.3.2 Automatic vertical coupling

The vertical measurement setup can be upgraded to a more advanced, highly accurate automatic setup by using motion controlled X-Y-Z movable stages for the fibers and sample. Such a setup is available in the group for both photonics

¹other coupling methods are described in the PhD thesis of Dr. Wim Bogaerts.

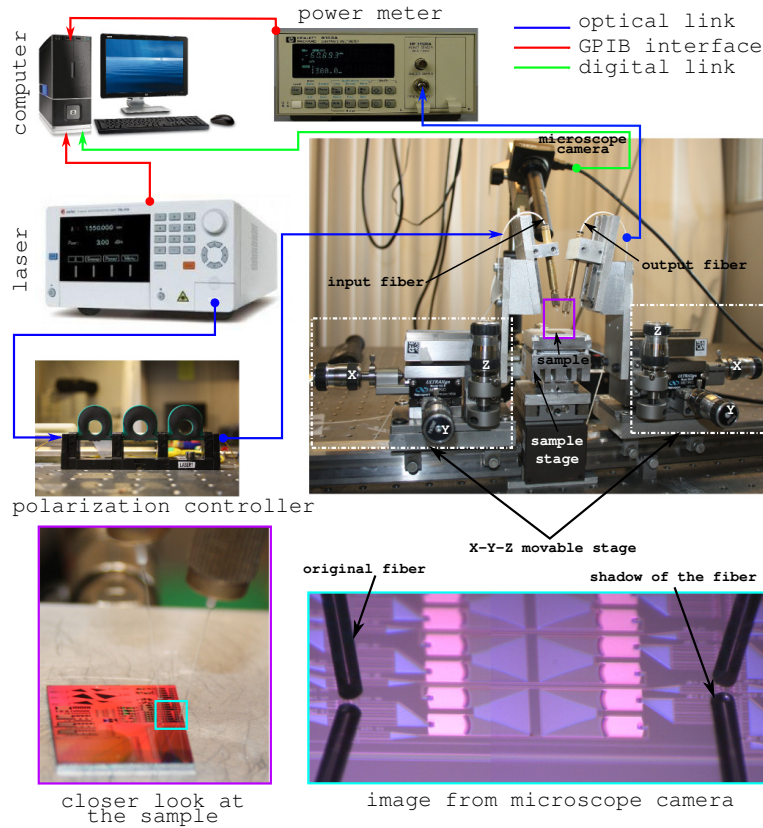


Figure 4.2: The measurement setup for vertical coupling.

dies and wafers. The main difference between these two setups is that the die scale setup has a sample stage which is capable of only unidirectional movement whereas the wafer scale measurement setup has a wafer stage which is capable of not only X-Y-Z movement but also rotations. The automatic measurement setup for die scale measurements shown in Fig. 4.3. The combination of a motion controller and the X-Y-Z stages allows aligning the fibers with an accuracy of $0.01\mu\text{m}$ in X, Y, Z directions.

The measurement starts with a manual alignment on the reference structure by applying the same two alignment methods as discussed in the previous section: crude alignment and active alignment. The relative positions between the reference structure and the desired devices are generated by using the ports information provided by IPKISS (discussed in chapter 3) during designing of the mask layout. These relative positions help the motion controller to move the fibers to the correct fiber grating couplers. At this position, with the help of the

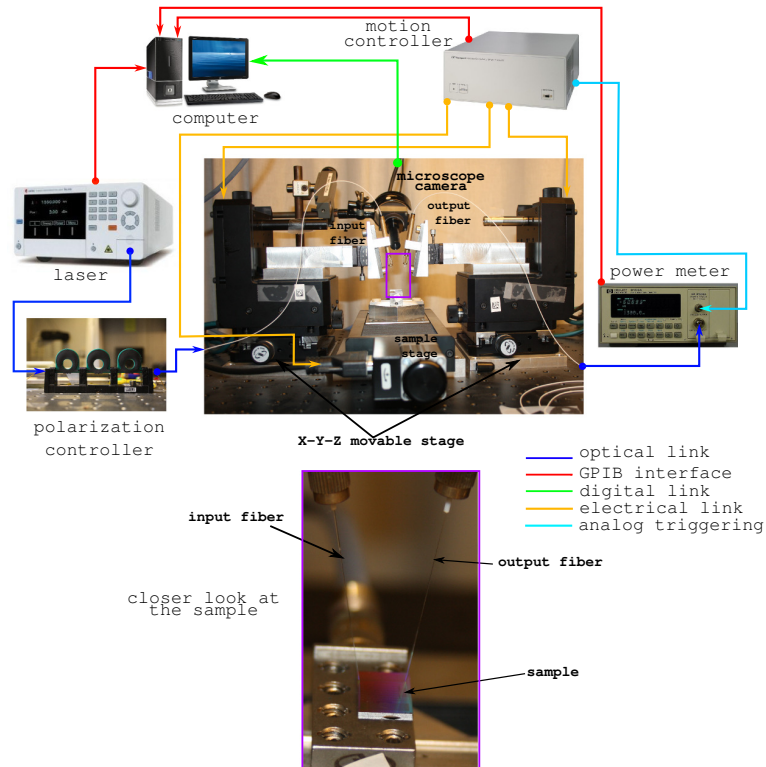


Figure 4.3: The automatic measurement setup using vertical coupling for photonic dies.

external triggering of the power meter the motion controller aligns the fibers at the maximum coupling positions by moving the fibers in X and Y direction simultaneously. The coupling is not optimized by moving the fibers in Z direction as this can result a collision with the sample. The relative positions are further optimized for small rotations of the sample during placement of the sample on the sample stage. This setup not only measures accurately and efficiently but it also saves a lot of human labor.

4.3.3 AWG normalization procedure

The main limitation of the fiber grating is the wavelength dependent coupling efficiency. This has to be taken into account when measuring demultiplexer devices: when aligning each output at the peak wavelength of the channel, the transmission of the on-chip device will be overestimated after normalization. We compensate for this by optimizing the measurement procedure as shown

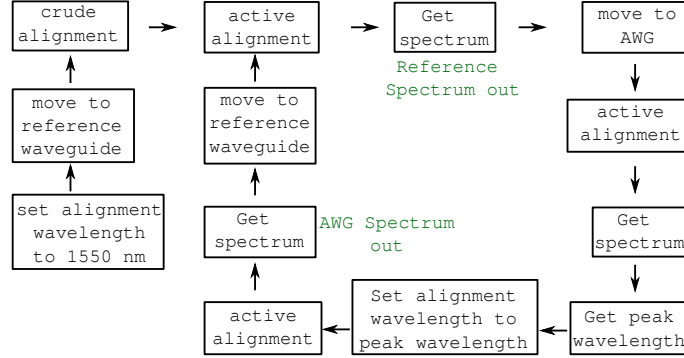


Figure 4.4: Normalization procedure for the AWG measurement.

in Fig. 4.4. To normalize the AWG spectrum from the fiber grating coupler we used a reference structure (in general it is straight waveguide) next to the AWG design using the same grating coupler. We start our measurement by aligning our fibers with the reference structure when the laser is set to the central wavelength 1550 nm. After taking the spectrum of the reference by sweeping the laser wavelength the fibers are moved to the AWG and take the spectrum to get the peak wavelengths. These peak wavelengths are used to align the fiber to get the spectrum. Finally each of these responses are normalized from the corresponding reference responses which are also measured by aligning the fiber to the reference waveguide for all those peak wavelengths.

4.4 Design based demonstrations

In chapter 2 we already discussed that not all possible designs are suitable for a given material platform. In this section we describe rectangularly, circularly, S-shaped and reflection type AWGs.

4.4.1 Rectangular AWG

In the high contrast silicon platform the best performances are achieved by the rectangularly shaped AWGs with a combination of multi-mode and single-mode waveguides. The rectangularly shape makes the device more fabrication tolerant compared to other shapes.

4.4.1.1 Design

We designed AWG's with different channel counts and channel spacings. The FSR of the AWGs is equal to the product of the channel spacing and the number

of wavelength channels, where the wavelength channels contain two dummy channels at the side in addition to the desired channels count. In silicon we designed AWGs from 50 GHz to 800 GHz channel spacing with a variation of 4 to 32 wavelength channels. The design details of different fabricated AWGs are shown in Table 4.1

Channels	Spacing [GHz]	Waveguides	Area [μm^2]	FSR [GHz]	ΔL [μm]
4	50	24	3100×243	6×50	261.82
4	100	24	1595×243	6×100	130.62
4	200	24	847×243	6×200	65.6
4	400	24	278×243	6×400	32.8
4	800	24	470×243	6×800	16.11
8	50	40	3170×308	10×50	157.1
8	100	40	1635×308	10×100	78.26
8	200	40	870×308	10×200	39.13
8	400	40	490×308	10×400	19.56
8	800	40	300×307	10×800	9.78
16	200	72	920×446	18×200	21.87
16	400	72	530×435	18×400	10.93
32	200	136	490×307	34×200	11.5

Table 4.1: Design overview of the rectangular AWGs

4.4.1.2 Result and Discussion

Figure 4.5 and 4.6 show the measured spectral response of 4 and 8 channel AWGs with the channel spacing varying from 50 GHz to 800 GHz. The measured spectral response of the 16 channel AWGs are shown in section 4.6.2 (Fig. 4.43 and 4.44 for 200 GHz and 400 GHz respectively). From the spectral responses and the performance table 4.2 we can conclude that as we increase the channel spacing with a constant channel count, the device performance improves significantly. The insertion loss improves from -3.5 dB to -1.3 dB as the channel spacing increases from 100 GHz to 800 GHz for a 4 channel AWG. The crosstalk also improves from -10 dB to -26.3 dB for an increase of channel spacing from 100 GHz to 800 GHz in a 4 channel AWG. The 8 channel AWGs also shows similar improvements. The FSR is linearly dependent on the channel spacing for this set of designs as shown Table 4.1.

As the FSR increases with an increasing channel spacing for a constant channel count i.e. the delay length decreases for the same increment of the channel spacing, the device becomes smaller and collects less phase errors. This

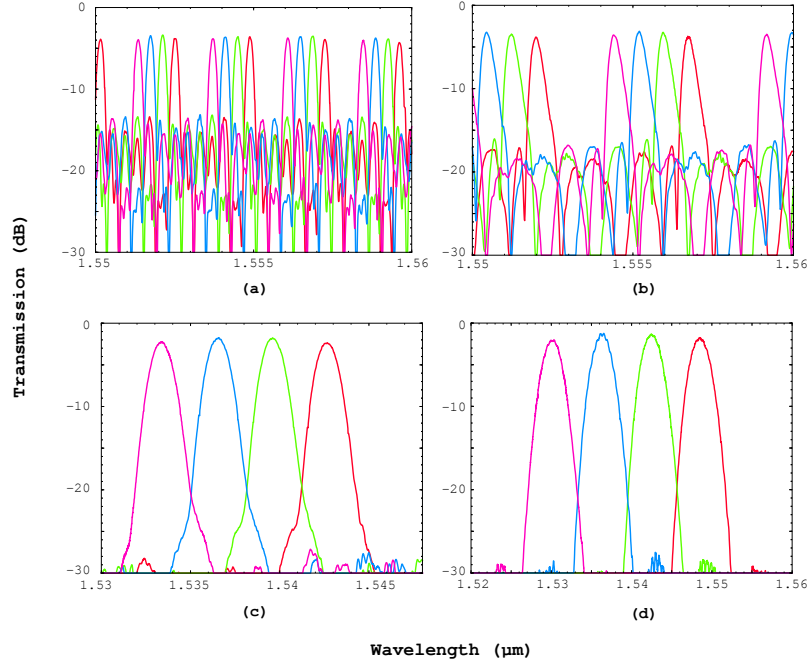


Figure 4.5: Spectral responses of 4 channel AWGs with (a) 50 GHz (b) 100 GHz (c) 400 GHz and (d) 800 GHz channel spacing.

Channels	Spacing [GHz]	Insertion loss [dB]	Side channel loss [dB]	Crosstalk [dB]
4	50	-3.5	-4	-10
4	100	-3.1	-3.8	-13
4	200	-1.7	-2.6	-23
4	400	-1.8	-2.2	-27
4	800	-1.3	-2.2	-26.3
8	50	-2.9	-4.1	-11.2
8	100	-2	-3.5	-21
8	200	-1.9	-3.1	-23.6
8	400	-1.3	-2.7	-26
8	800	1.8	-3.5	-27
16	200	-2	-3.7	-22.5
16	400	-1.5	-3.5	-26
32	200	-2.1	-4.3	-15.5

Table 4.2: Performance overview of the rectangular AWGs

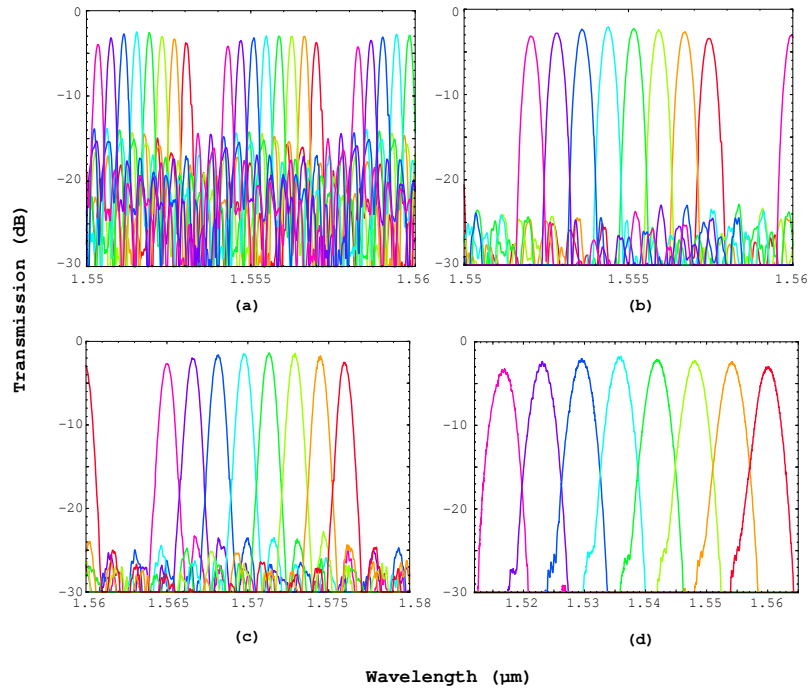


Figure 4.6: Spectral response of 8 channel AWGs with (a) 50 GHz (b) 100 GHz (c) 200 GHz and (d) 800 GHz channel spacing.

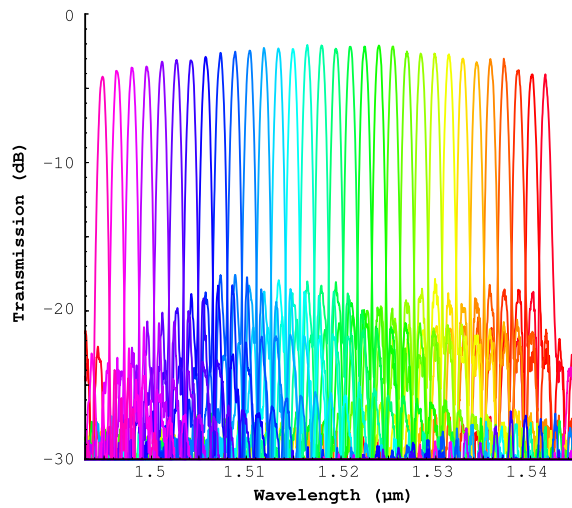


Figure 4.7: Spectral response of 32×200 GHz AWGs.

situation can be understood from Fig. 4.8, which shows the variation of the crosstalk with delay length. From this figure it is clear that the crosstalk increases with an increment of delay length. Now if we concentrate on the variations of the crosstalk with the number of channels in Fig. 4.8 we can see that for the same delay length the crosstalk gets worse with increasing number of channels. For a constant delay length an increase of the number of wavelength

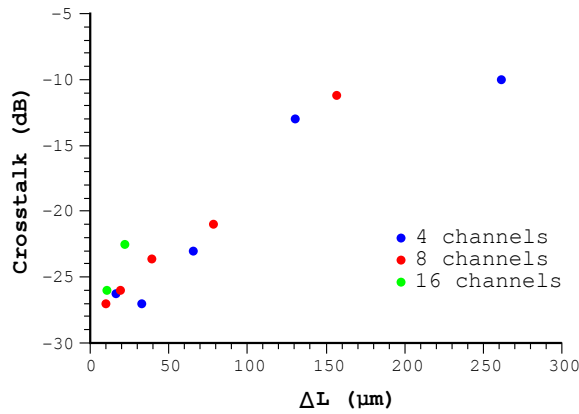


Figure 4.8: Variation of crosstalk with delay length

channels increases the number of waveguides in the array as shown in Table 4.1. As the number of waveguides increased the device size increases simultaneously, which will also increase the phase error. This crosstalk dependence is

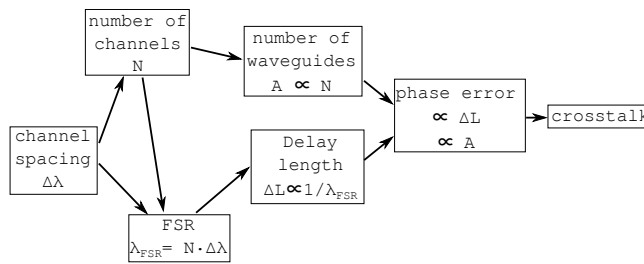


Figure 4.9: Crosstalk dependence on the design parameters.

shown in Fig. 4.9. Due to the rectangularly shaped waveguide array the lower delay length will decrease the gap between two successive waveguides which will increase the waveguide coupling and as a consequence the crosstalk will increase.

The results shown in Table 4.2 are the best measured performance of the AWGs. But the performance of the AWG varies between die to die and wafer to

wafer. To characterize the performance variation between the dies and within the dies we used four 8×400 GHz AWGs, located at different locations in a die as shown in Fig. 4.10.

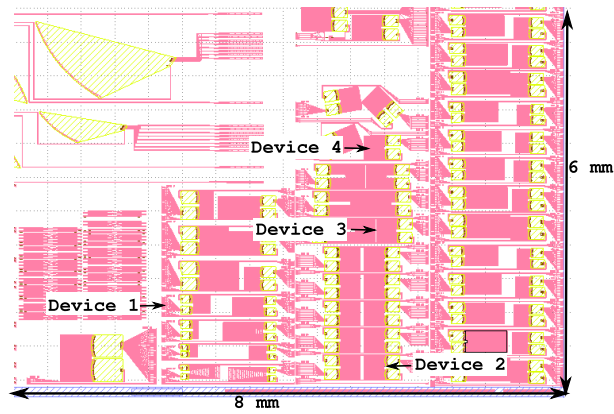


Figure 4.10: Location of the four 8×400 GHz AWGs in the mask.

Fig. 4.11 shows the measured crosstalk of the 8×400 GHz AWGs for different dies. The crosstalk is not only varying for different dies but is also varying within a die. The crosstalk is measured within the range of -23.5 dB to -16 dB. From Fig. 4.11 it shows that the center of the wafer has uniform crosstalk variation.

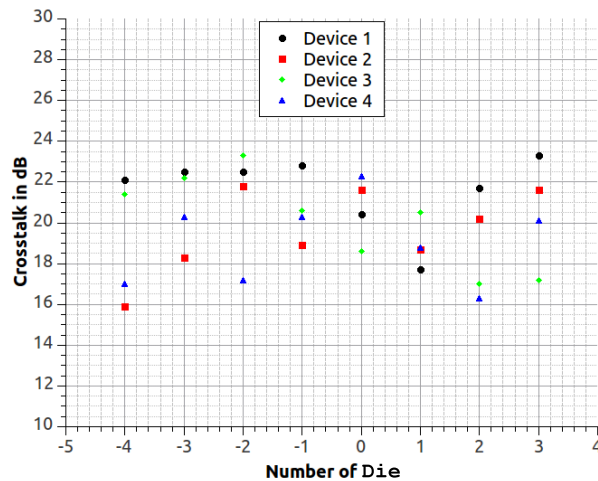


Figure 4.11: Crosstalk variation of the 8×400 GHz AWGs over the dies and within the die.

4.4.1.3 Channel spacing mismatch

The performance of the silicon AWG is highly depend on the fabrication. Due to the line width / thickness variation and the dispersion mismatch it is difficult to obtain desirable channel spacing. In chapter 2 section 2.4.4 we described two formulas to calculate the position of the output apertures. First

$$\sin\theta = m \cdot \frac{n_{wg}(\lambda) \cdot \lambda_c - n_{wg}(\lambda_c) \cdot \lambda}{n_{wg}(\lambda_c) \cdot n_{slab}(\lambda) \cdot d_a} \quad (4.1)$$

and second

$$\frac{d\theta}{dv} = - \frac{m\lambda_c^2 n_{g,wg}}{n_{slab} n_{wg}(\lambda_c) d_a c} \quad (4.2)$$

To demonstrate the channels spacing mismatch compared to desire channel spacing we designed two identical AWGs for 12×100 GHz and 12×200 GHz. The position of output channels are designed one with Eq. 4.1 and another with Eq. 4.2 for both the AWGs.

To characterize the channel spacing mismatch first we found that the optimized channel spacing which is calculated as the fitted channel spacing for which the deviation range is minimum. The channel spacing deviation is the gap between the measured channel position and the desire channel position. Figure 4.12 shows that for 100 and 200 GHz AWGs the optimized channel spac-

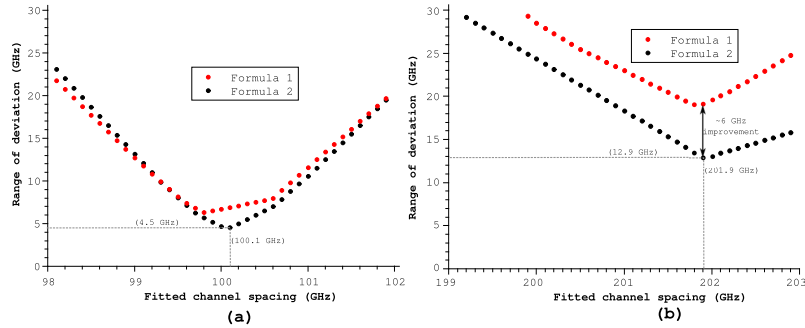


Figure 4.12: Deviation range Vs fitted channel spacing for (a) 12×100 GHz AWGs (b) 12×200 GHz AWGs.

ing are 100.1 and 201.9 GHz respectively using the second formula. The minimum deviation range for 100 and 200 GHz AWGs are 4.5 and 12.9 GHz respectively.

Figure 4.13 and 4.14 show the measured spectral responses of 12×200 GHz AWGs using first and second formulas respectively. Figure 4.15 and 4.16 show the channel deviation for 100 GHz and 200 GHz AWGs. As the FSR of 100 GHz AWG is smaller than the 200 GHz AWG and the effective index mismatch within

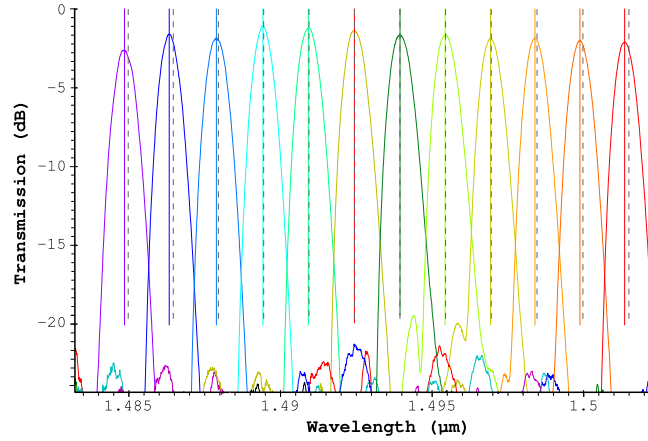


Figure 4.13: Spectral response of 12×200 GHz AWGs using formula 1. Gray dashed lines indicates 201.9 GHz channel spacing grid.

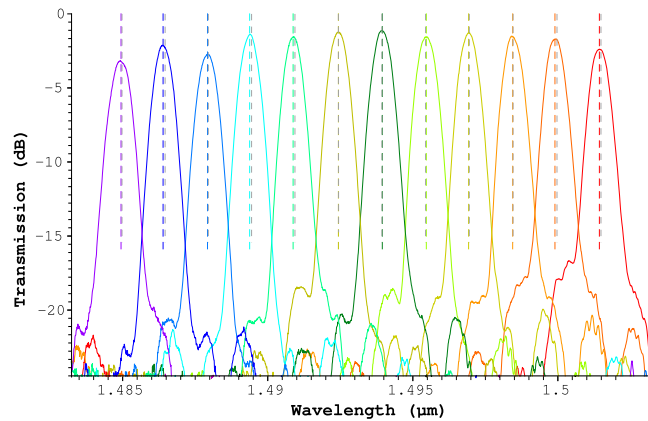


Figure 4.14: Spectral response of 12×200 GHz AWGs using formula 2. Gray dashed lines indicates 201.9 GHz channel spacing grid.

a small wavelength range is small, the channel deviation for 100 GHz AWG is smaller. For smaller FSR both the formulas have almost the same deviation but for larger FSR the second formula has less deviation. This can be explained by the fact that second formula is much more tolerant from the effective index deviation. From Fig. 4.16 we can see that the channel spacing deviation for second formula is random and needs a very accurate dispersion model to improve it further.

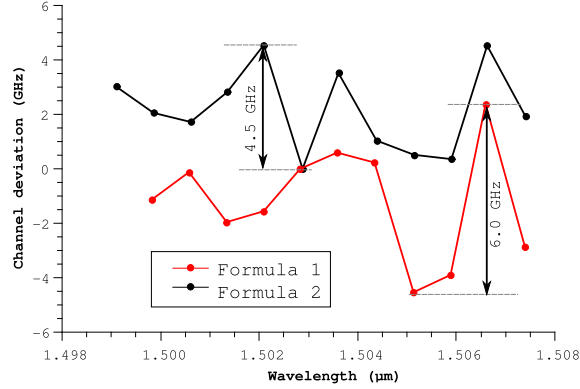


Figure 4.15: Channel deviation for 12×100 GHz AWGs.

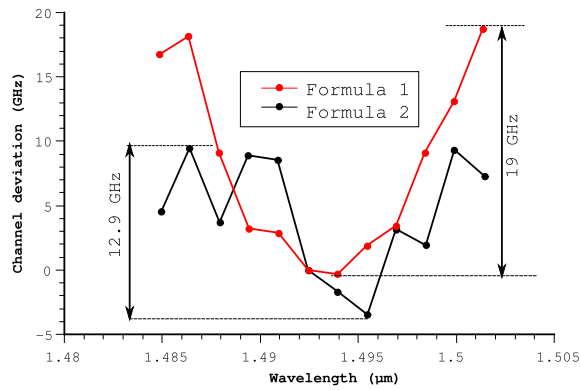


Figure 4.16: Channel deviation for 12×200 GHz AWGs.

4.4.2 Circular AWG

As we discussed in chapter 2 the circularly shaped AWG is one of the best choices for a low index contrast platform where the bend radius is large. In the rectangularly shaped design the multi-mode waveguide tapers to a single mode waveguide for the bends, which keeps the bend radius small. The circularly shaped design requires having a large bend and therefore the delay lines can be made completely out of multi-mode waveguides. To avoid wavefront distortion and crosstalk due to multimode interference these multi mode waveguides are tapered to a single mode waveguide at the star-couplers.

4.4.2.1 Design

To demonstrate circularly shaped AWG in silicon we designed three 16 channel devices with 400, 200 and 100 GHz channel spacing. Figure 4.17 shows the optical image of the fabricated 16×400 GHz AWG. All the AWGs have 90 waveguides in the array and the waveguides are 800 nm wide. Although the bend radius is large the device size remains similar to that of the rectangularly shaped AWG. The footprint of the 400, 200 and 100 GHz devices are 475×325 , 775×325 and $1365 \times 325 \mu\text{m}^2$ respectively. Figure 4.17 shows the optical image of the fabri-

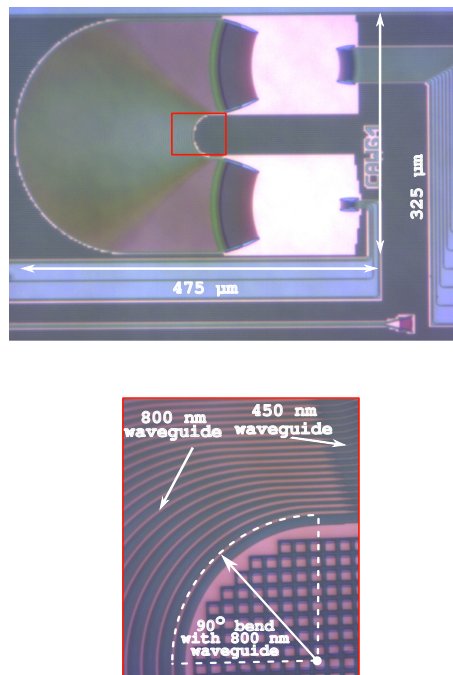


Figure 4.17: optical image of the fabricated 16×400 GHz circular AWG.

cated 16×400 GHz AWGs and a closer look into the waveguide array which is created with a combination of 450 nm and 800 nm waveguides.

4.4.2.2 Results

Figure 4.18, 4.19 and 4.20 shows the measured spectral response of circularly shaped AWG with 400, 200 and 100 GHz channel spacing respectively. The detailed performances of the devices is given in Table 4.3.

Similar to the rectangular AWG as we decrease the FSR the delay lines become longer and accumulate more phase errors. As a consequence the perfor-

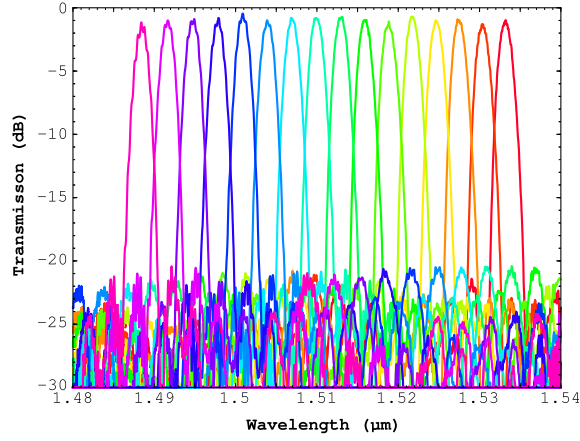


Figure 4.18: Measured spectral response of the 16×400 GHz circular AWG.

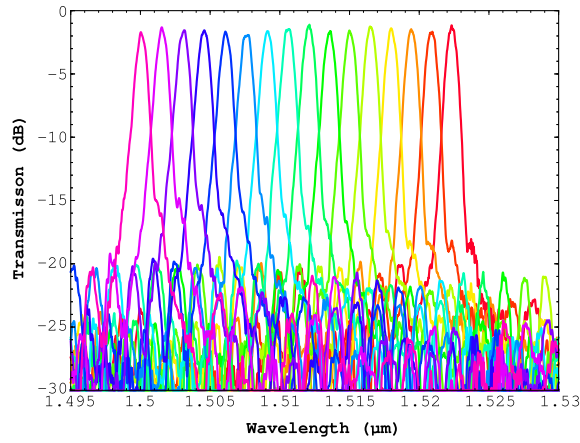


Figure 4.19: Measured spectral response of the 16×200 GHz circular AWG.

Channels	Channel spacing [GHz]	Insertion loss [dB]	Crosstalk [dB]
16	400	-0.75	-20
16	200	-1.3	-16
16	100	-1.9	-13.5

Table 4.3: Design overview of three AWG sets

mance decreases as we decrease the channel spacing. The best performance is achieved for the 400 GHz device with -0.75 dB loss and -20 dB crosstalk. The

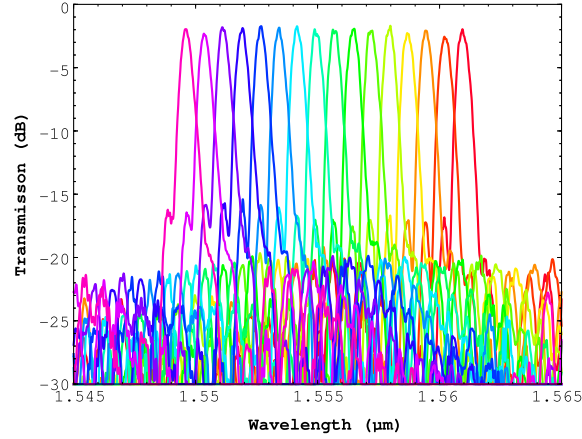


Figure 4.20: Measured spectral response of the 16×100 GHz circular AWG.

circularly shaped AWGs have larger crosstalk compared to the rectangularly shaped AWG. Although both the devices have equally long delay lines the circular shaped delay lines will accumulate more phase error due to the mask grid discretization effect on the bends (discussed in section 4.6.1), the effective index mismatch between the straight and the bend waveguides. This is the first generation device and there is a lot of rooms for the improvement of the performance: use of adiabatic bends can improve the performance.

4.4.3 S-shaped AWG

In chapter 2 we discussed the limitations of the rectangularly shaped AWG (when the FSR or channel spacing becomes too large, waveguides in the rectangular array will come too close together) and proposed an S-shaped AWG as an alternative layout for larger FSR/channel spacing. In this section we will discuss the design and the experimental results of the fabricated S-shaped AWGs in SOI.

4.4.3.1 Design

We designed four different S-shaped AWGs with 24 nm, 32 nm, 40 nm and 47 nm channel spacing. The devices with 24 nm and 32 nm spacing have 4 wavelength channels with 16 waveguides in the array. Twelve waveguides are used for the 40 nm and 47 nm channel spacing devices with 3 wavelength channels. Due to the S-shaped routing the shortest waveguide of the S-shaped AWG is large compared to the rectangularly shaped AWG even though the delay length is small, which makes the device bigger. The 4×22 nm S-shaped AWG is $305 \times 260 \mu\text{m}^2$.

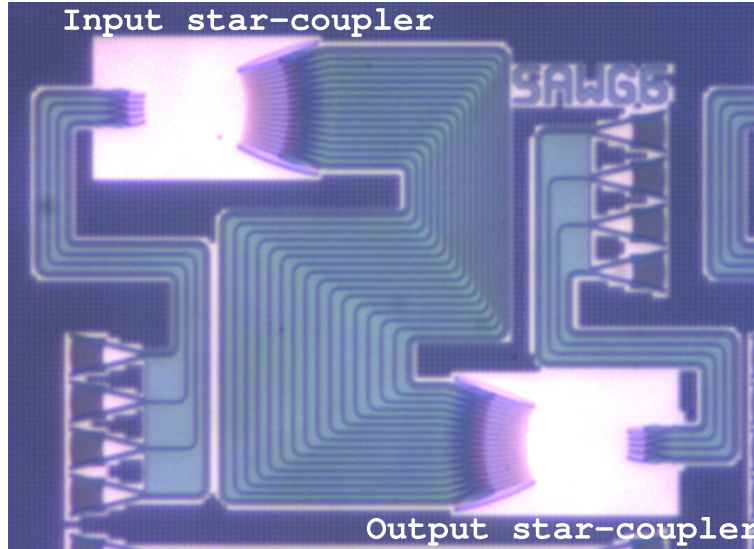


Figure 4.21: Optical image of a fabricated S-shaped AWGs.

4.4.3.2 Results

Figures 4.22 and 4.23 show the spectral response of the 3×47 nm, 3×40 nm, 4×32 nm and 4×24 nm S-shaped AWGs. The devices with large channel spacing have smaller delay length and hence have better performance: the insertion loss is -1.7 dB and the crosstalk is -22 dB. As we decrease the channel spacing from 47 nm to 40 nm the performance degrades: the insertion loss becomes -1.8 dB and the crosstalk becomes -20.5 dB. The 4×24 nm S-shaped AWG has a measured in-

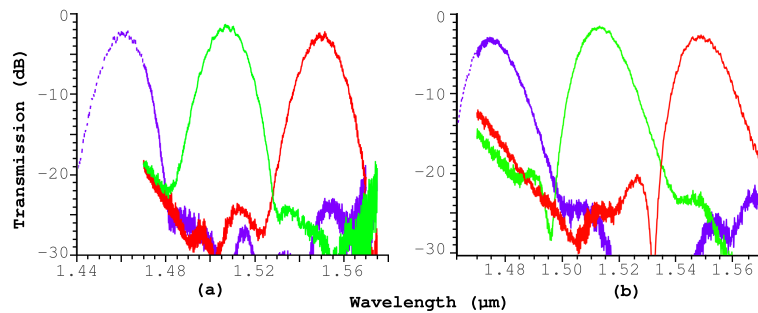


Figure 4.22: Measured spectral response of (a) 3×47 nm and (b) 3×40 nm S-shaped AWGs.

sertion loss of -1.7 dB and -20.6 dB crosstalk. The measured insertion loss and the crosstalk are -2.0 dB and -19.0 dB respectively for the 4×32 nm S-shaped

AWG. The S-shaped delay lines have a higher impact on the length deviation due to the mask discretization. The spectral responses have a higher noise floor at the lower and higher wavelengths due to the grating coupler. These are the

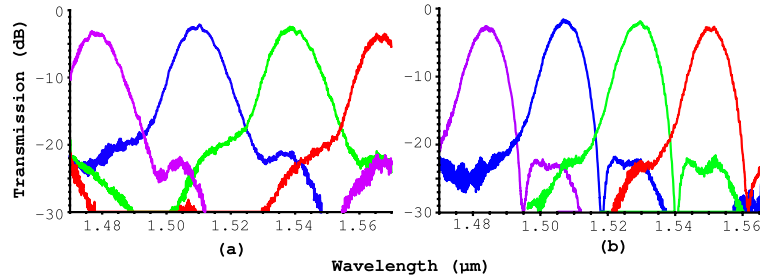


Figure 4.23: Measured spectral response of (a) 4×32 nm and (b) 3×24 nm S-shaped AWGs.

first generation devices, which need further optimization for improving the performance.

4.4.4 Reflection-type AWG

The first generation reflection type AWG used distributed Bragg reflectors (DBR). The design of the DBR is critical as its performance is highly fabrication dependent.

4.4.4.1 Design

We designed a 8×200 GHz reflection type AWG with 34 waveguides in the array. The footprint reduces significantly as we need to use only one star-coupler and half of the delay lines, resulting the footprint of the 8×200 GHz device is $828 \times 180 \mu\text{m}^2$. The reflectors consist of first-order distributed Bragg reflectors (DBR) with four deeply etched trenches of 70 nm width and 340 nm pitch

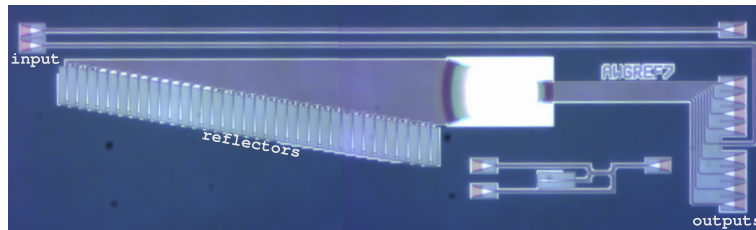


Figure 4.24: Optical image of a fabricated 8×200 GHz reflection type AWG.

Figure 4.24 shows the optical image of the fabricated device.

4.4.4.2 Results

Figure 4.25 shows the measured spectral response of the reflection type AWG. The measured insertion loss of the device is -7.5 dB and the crosstalk is -18.0 dB. As the AWG is illuminated from the center channel, this channel is missing from the measured spectral response. The device has very high loss and crosstalk because of the DBR.

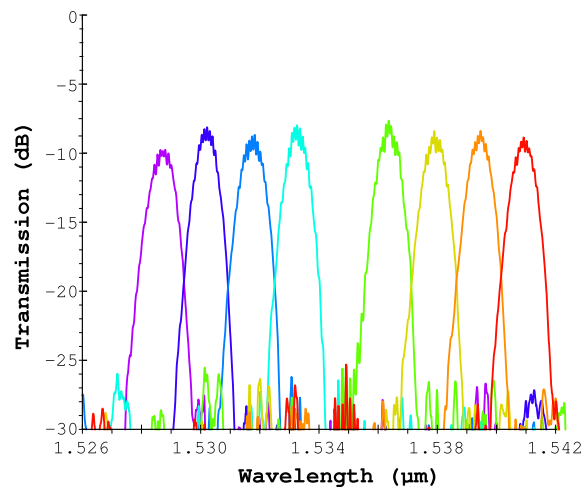


Figure 4.25: Spectral response of a 8×200 GHz reflection type AWG.

4.5 Application based demonstrations

In this section we will discuss de/multiplexer (FSR is larger than the product of number of channel and channel spacing) and wavelength router (FSR is equal to the product of number of channel and channel spacing).

4.5.1 De/multiplexer

4.5.1.1 Design

We designed three sets of AWGs for three different channel spacings. Each of these three sets (4×100 GHz, 8×250 GHz and 12×400 GHz) of AWGs have four variations of the number of waveguides used in the array waveguides and at the same time we also changed the FSR (see chapter 2). See [4, 5] for design details of the SOI AWGs. The focal length of the star couplers was kept constant for each of those sets of AWG designs at $80 \mu\text{m}$, $100 \mu\text{m}$ and $120 \mu\text{m}$ respectively. Table 4.4

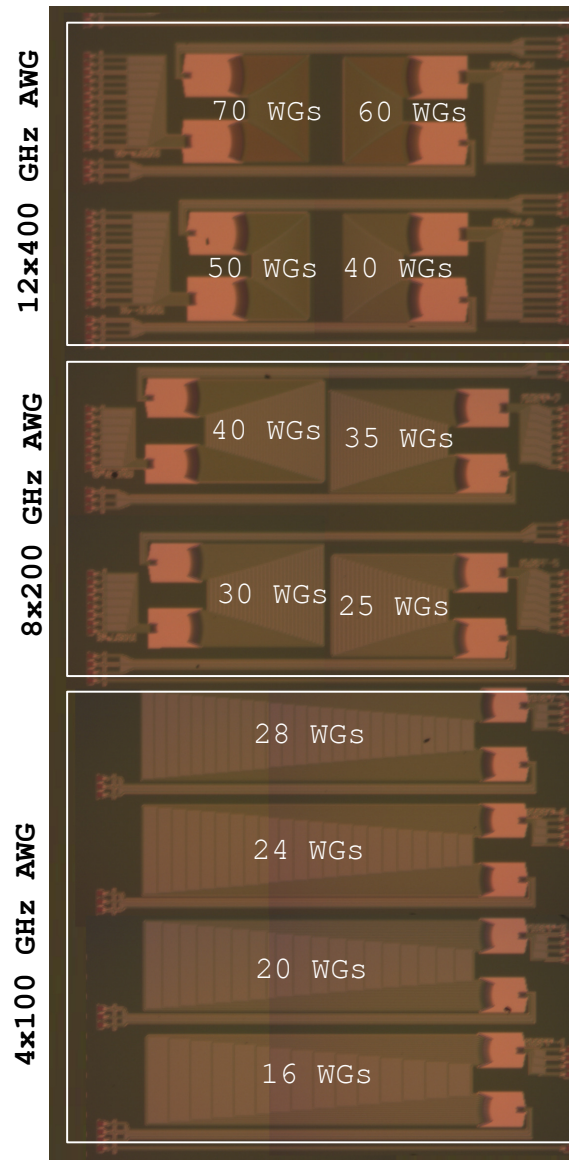


Figure 4.26: Optical image of the fabricated AWGs.

gives further design details for each of the fabricated devices. Fig. 4.26 shows optical microscope image of the fabricated AWGs.

Sets (size)	Wave- guides	Arm aperture width(μm)	Order	Delay length(μm)	FSR (nm)
4 \times 100 GHz (1180 \times 285 μm^2)	16	3.49	254	146.15	4.3
	20	2.75	230	116.81	5.3
	24	2.26	169	97.25	6.4
	28	1.91	145	83.44	7.5
8 \times 250 GHz (540 \times 320 μm^2)	25	2.75	65	37.4	16.8
	30	2.26	54	31.07	20.2
	35	1.91	47	27.05	23.2
	40	1.65	41	23.59	26.6
12 \times 400 GHz (380 \times 330 μm^2)	40	2.01	26	14.96	42.0
	50	1.57	20	11.51	54.6
	60	1.28	17	9.78	64.2
	70	1.07	15	8.63	72.8

Table 4.4: Design overview of three AWG sets

4.5.1.2 Result and Discussion

Figures 4.27, 4.28 and 4.29 show the measured spectral response of the 4 \times 100 GHz, 8 \times 250 GHz and 12 \times 400 GHz AWGs using 28, 40 and 70 waveguides in the array respectively. The measured FSR for these devices was 6.9nm, 24.8nm and 69.8nm respectively. It is immediately obvious that the loss and the crosstalk improves considerably when the AWG channel spacing is increased. As we can see from Fig. 4.27, 4.28 and 4.29 the shape of the individual AWG channel is slightly asymmetric but similar for all the channels of the device. This asymmetry could be due to minor phase variations in the waveguides or due to the fabrication errors in the input/output apertures of the AWGs.

Insertion loss and non-uniformity Figure 4.30(a) shows how the insertion loss changes with the variation of the number of waveguides used in the waveguide array. As already mentioned above, the insertion loss improves when going from 100GHz to 200GHz and then 400GHz channel spacing, which is related to the decrease in device size and associated propagation loss. Within one device group the insertion loss improves when the number of waveguides is increased, as predicted in section 2. Further improvement is restricted by the width of the shallowly etched arm apertures to avoid high loss due to the reflection. Figure 4.30(b) shows the non-uniformity in the insertion loss between the center channel and the outer channel as function of the number of waveguides in the array. As expected from the reasoning in the previous paragraph the uniformity improves with increasing FSR.

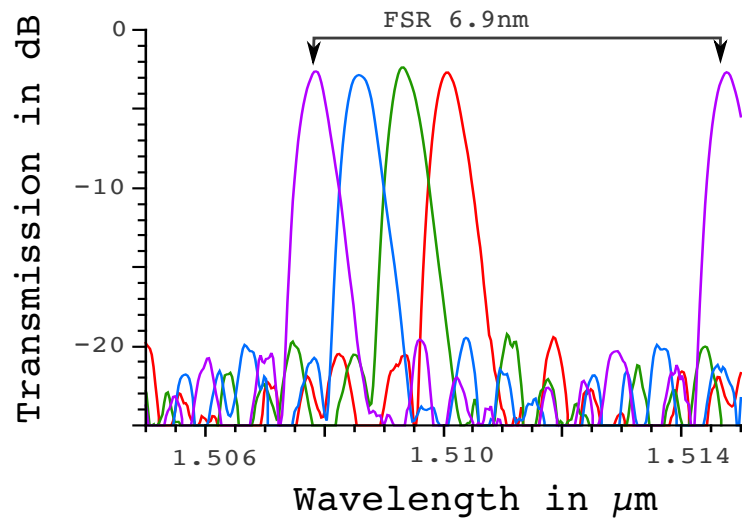


Figure 4.27: Experimental spectral response of 4 \times 100 GHz AWG with 28 waveguides used in the array.

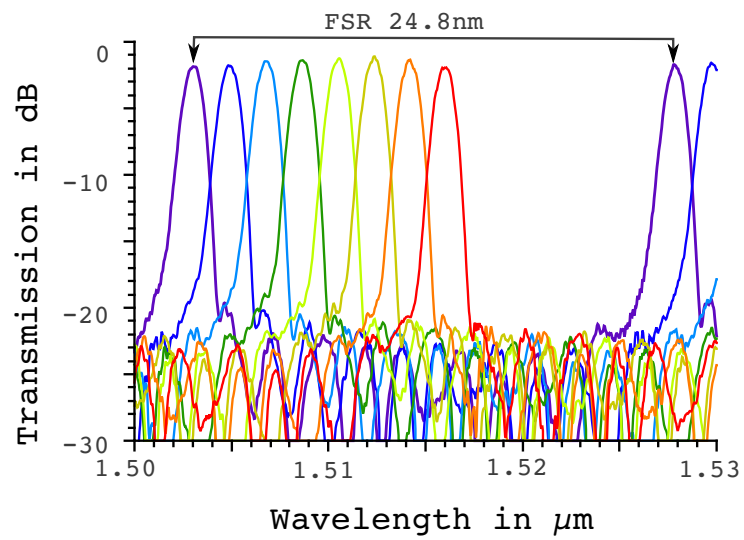


Figure 4.28: Experimental spectral response of 8 \times 250 GHz AWG with 40 waveguides used in the array.

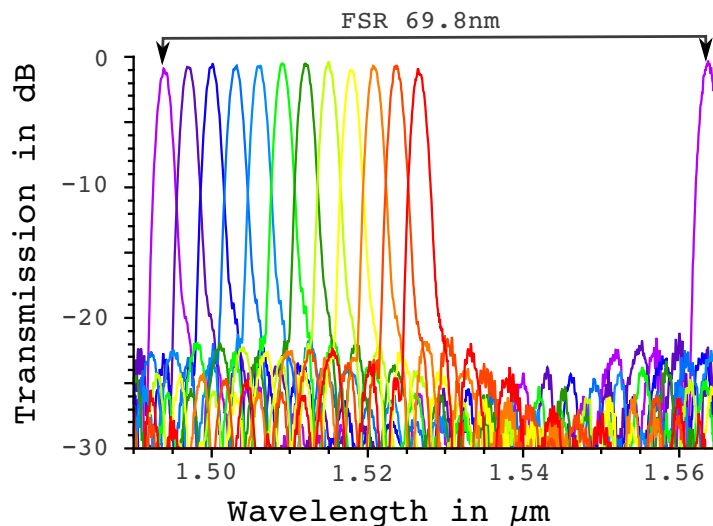


Figure 4.29: Experimental spectral response of 12×400 GHz AWG with 70 waveguides used in the array.

Crosstalk Figure 4.30(c) shows how the crosstalk level changes with the number of waveguides used in the array. The crosstalk level is defined by taking the difference (in dB) between the crosstalk floor and the center channel loss and as can be seen from Fig. 4.30(c) the crosstalk improves considerably when increasing the channel spacing. This improvement originates both from an improved center channel loss for the larger channel spacing devices and from an improving crosstalk floor. Within one device group (with fixed channel spacing) the crosstalk level increases when increasing the number of waveguides within the array. In this case the crosstalk floor remains nearly constant between devices but the central channel loss improves significantly. The random sidewall roughness of the waveguide introduces sidelobes, which leads to unequal crosstalk variation compared to the center channel loss. It is expected that the overall sidewall roughness of the waveguide will be better for a dense waveguide array due to a more uniform etch profile during the fabrication process. It is expected that further increasing the number of waveguides will not improve the performance given that in that case the waveguides in the array start to couple, introducing a new crosstalk source.

Bandwidth Within a group of devices we expect the bandwidth to be constant as the channel spacing and the star coupler size were fixed (as discussed in chapter 2). But from Fig. 4.30(d) we can see some small variation in the 3 dB

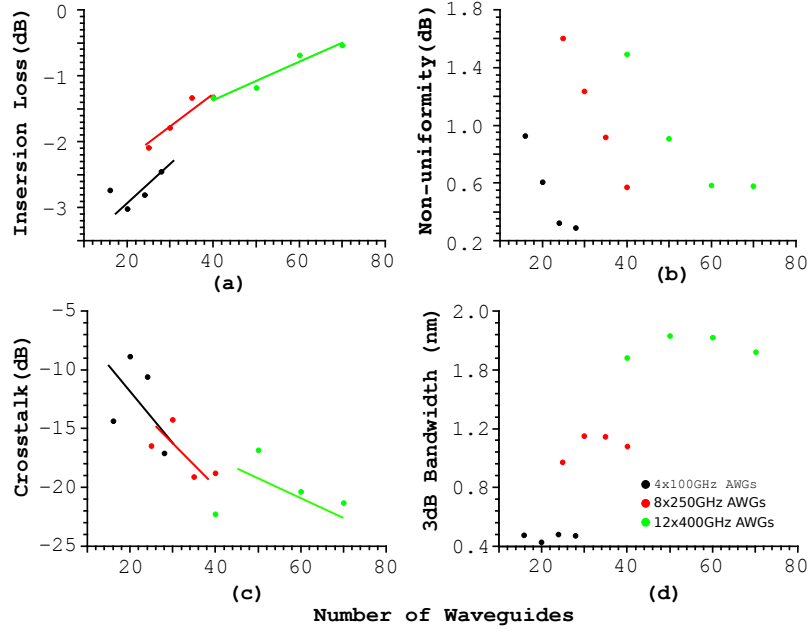


Figure 4.30: (a) Insertion loss variation (b) non-uniformity variation (c) cross talk variation and (d) bandwidth variation with the variation of the number of waveguides used in the array waveguides for 4×100 GHz, 8×250 GHz and 12×400 GHz AWGs.

bandwidth. A possible explanation can be the random shape changes of a wavelength channel due to variations in the line widths and local wafer thickness. Alternatively it could be due to a ripple in the transfer characteristics caused by parasitic reflections at the fiber couplers introducing uncertainty in the exact shape of the AWG transfer function.

4.5.2 Router

We designed 16×16 router for two different channel spacings: 200 and 400 GHz. See chapter 2 for design details of the SOI AWGs. The 200 and 400 GHz fabricated devices have a footprint of $475 \times 330 \mu\text{m}^2$. The fabricated devices are shown in the Fig. 4.31 The devices are also normalized from grating coupler.

4.5.2.1 Results

Figures 4.32 and 4.33 show the spectral responses of the 16×16 , 400 GHz router for the 1st and the 8th input channel respectively. The loss of the center output channel for the 1st input is -5.0 dB which is 2 dB higher than the loss of the

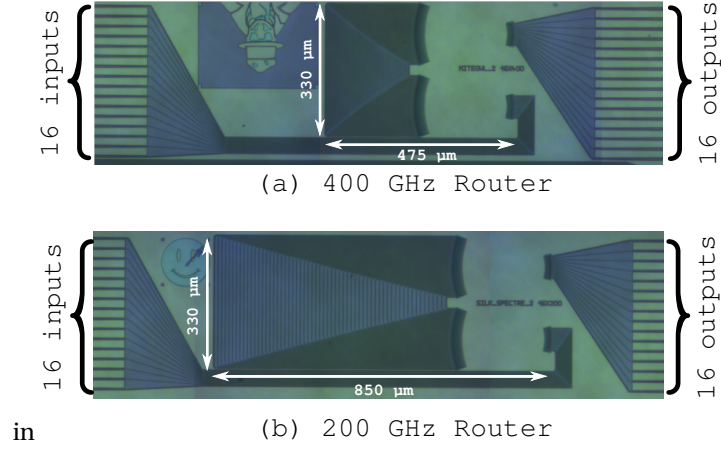


Figure 4.31: Fabricated (a) 400 GHz and (b) 200 GHz channel spaced 16×16 router.

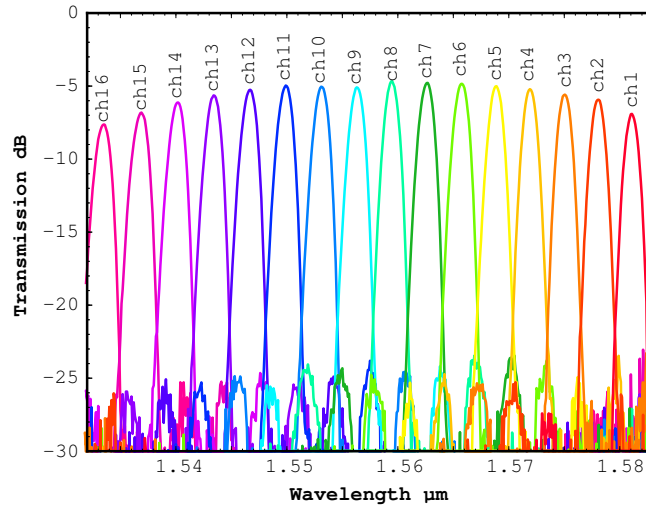


Figure 4.32: Spectral response of 16×16 , 400 GHz router for 1^{st} input.

same channel for the 8^{th} input. The 1^{st} input is more lossy compared to the 8^{th} input because of the same reason that the side output channels experience 3 dB extra loss compared to the center input channel as discussed in the chapter 2. The combination of the side input and side channel will experience up to 6 dB extra loss compared to the combination of the center input and center output channel for a $N \times N$ router. The measured non-uniformity of I16-O1 channels and I8-O8 channels is 4.6 dB. The crosstalk of the 1^{st} and 8^{th} input are -19 and

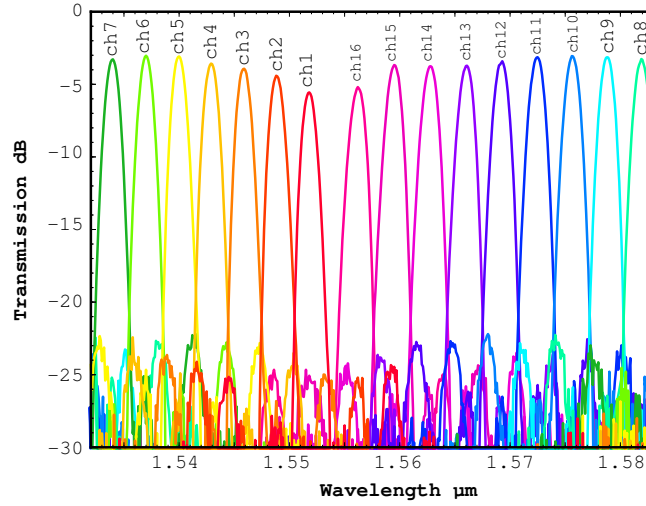


Figure 4.33: Spectral response of 16 × 16, 400 GHz router for 8th Input

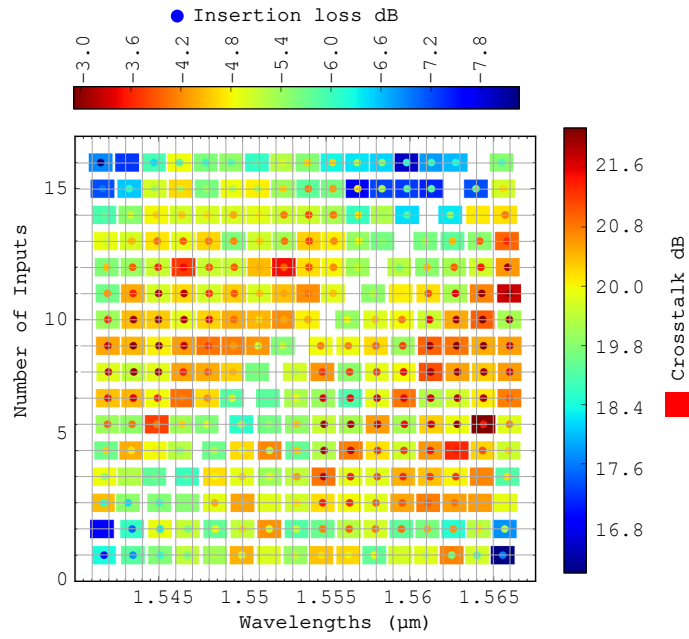


Figure 4.34: Spectral response of 16 × 16 router of 400 GHz for all inputs

-20 dB respectively.

Figure 4.34 shows the entire spectral response of the 16 × 16, 400 GHz router. The position of the rectangles and the circles indicates the position of the output

channels for the different input channels. The color of the rectangle indicates the crosstalk and the color of the circle indicates the insertion loss of the corresponding channels. Ideally all points should be perfectly aligned on the 16×16 matrix but for this device the matrix is diagonally shifted towards higher wavelengths. This imperfect cyclic behavior can be explained by the mismatch between the dispersion used in the design and the actual waveguide. The amount of imperfection is dependent on the wavelength: for lower wavelengths the imperfection is low whereas for higher wavelengths the imperfection is large. From the loss distribution matrix we can conclude that the center input-output combinations provides low loss wavelength channels and the side input-output combination experiences high loss. The fabricated 200 GHz router shows simi-

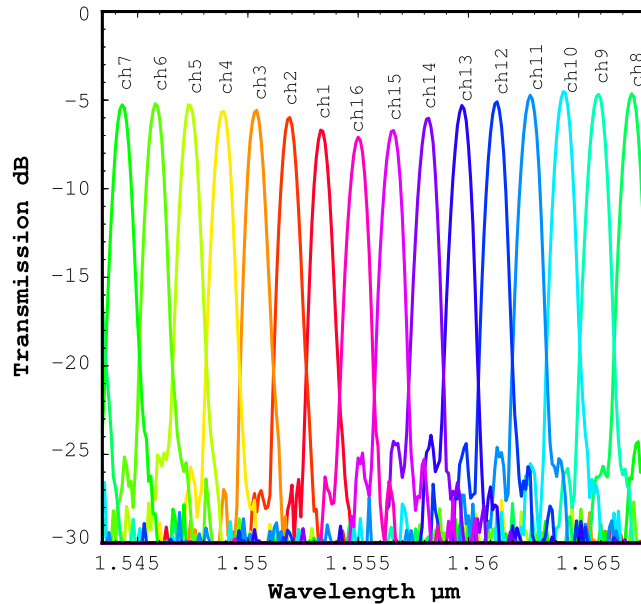


Figure 4.35: Spectral response of 16×16 router of 200 GHz for 1st input

lar performances compared to the 400 GHz router in terms of loss and crosstalk. Figure 4.35 and 4.36 shows the spectral response of the 16×16 , 200 GHz router for the 1st and the 8th input respectively. The loss of the center output channel for the 8th input is -2.8 dB which is 1.8 dB better than the loss of the same channel for the 1st input. The crosstalk of the 1st and 8th input are -19 and -20 dB respectively.

Figure 4.37 shows the entire spectral response of the 16×16 , 200 GHz Router. With comparison to the 400 GHz router the 200 GHz router has less loss but due to a large delay length the channel crosstalk is higher. The 16×16 matrix of input/output channel combinations shows small misalignments. An

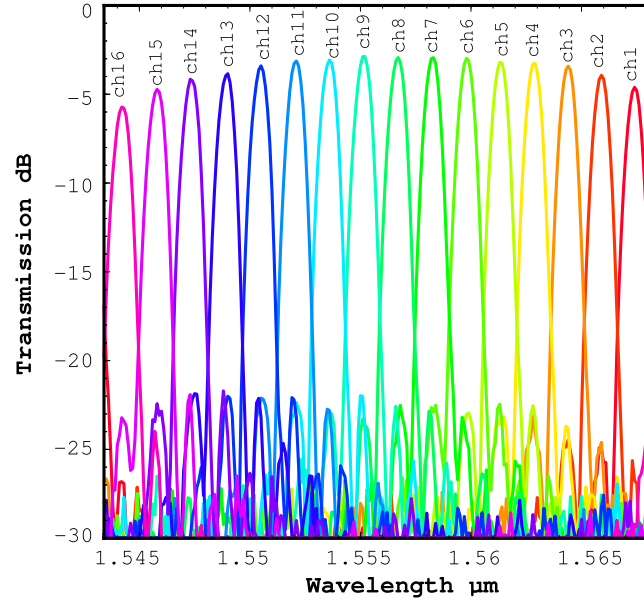


Figure 4.36: Spectral response of 16×16 router of 200 GHz for 8^{th} input

imperfect cyclic behavior is observed for longer wavelengths.

The 200 GHz device shows a better agreement with design compared to the 400 GHz due to the fact that 400 GHz has larger wavelength range which makes the device more sensitive to the imperfection of the dispersion model. Both devices have room for improvement. However in order to obtain a perfect cyclic behavior the dispersion model needs to be optimized to exclude any systematic fabrication imperfection.

4.6 Fabrication dependence

In chapter 2, we described the effect of mask discretization on the performance of the AWGs. Depending on the design, mask discretization has a significant effect on the width and the length of the waveguides. Therefore in this section we will experimentally verify its effect on the performance of the AWGs.

4.6.1 Effect of mask discretization on waveguide width

The mask discretization will not have any effect on the waveguide width if the waveguides are aligned with the mask grid axis and the waveguide width is an integer multiple of the mask grid width. The silicon AWGs are made out of 450 nm and 800 nm wide waveguides and the mask grid is 5 nm. Therefore mask

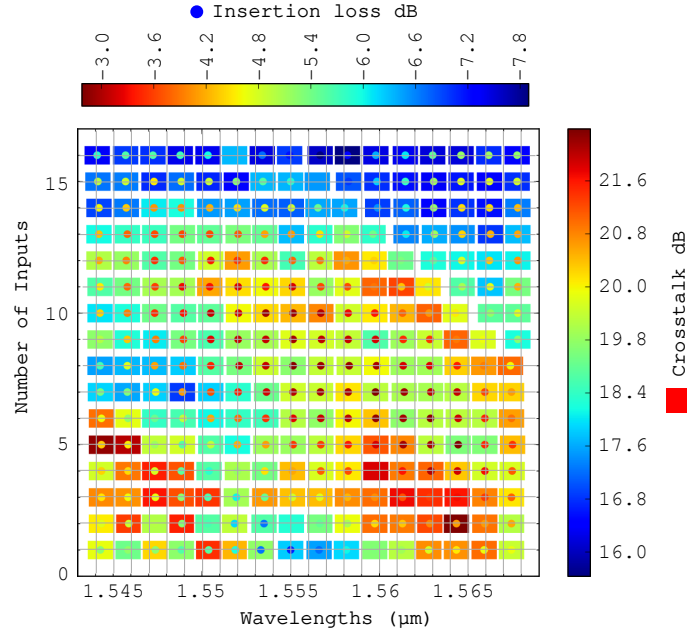


Figure 4.37: Spectral response of 16×16 router of 200 GHz for all inputs

discretization will not influence the straight waveguide width if it is aligned with the mask grid axis. For bends and angled waveguides the mask discretization will increase the influence of phase errors due to line width variations as shown in Fig. 4.38. This is one of the reasons why the best performance in the high contrast silicon is achieved by the rectangularly shaped AWGs.

4.6.1.1 Design

To illustrate this we use four identical 8×400 GHz AWGs with different rotations on the mask. The AWGs are placed at an angle of 0° , 10° , 22.5° and 45° with respect to the horizontal mask grid as shown in Fig. 4.39. With 5 nm mask grid discretization the waveguides will be affected by the additional line width variation depending on the angle of rotation. It is very obvious that as the line width variation increases the loss of the waveguides and the phase errors will increase.

4.6.1.2 Experiment

Figure 4.40 shows the spectral response of the 8×400 GHz AWGs with 0° , 10° , 22.5° and 45° rotated layouts. It is expected and proven from the spectral response of the AWG that the 0° orientation is the best working angle: the inser-

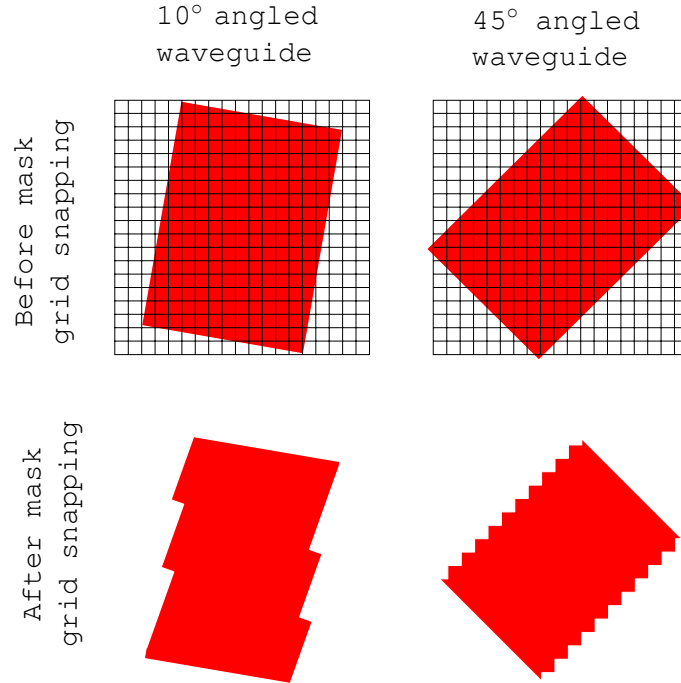


Figure 4.38: Effect of mask discretization on the angled waveguides.

tion loss and crosstalk of the AWG is -2.5 dB and -19 dB respectively. The loss and crosstalk increased as we rotated the AWG at 45° angle. At 45° angle the mask discretization is introducing a symmetric zig-zag stepping in the width along the length, which increases the insertion loss to -5.5 dB and increases the crosstalk to -10 dB. The situation becomes even worse for a 22.5° angle, as the symmetric stepping breaks are introduced more like random phase errors which increased the loss to -7.0 dB and the crosstalk to -5 dB. Due to the arbitrary stepping on the 10° angled waveguides the spectral response of the AWG becomes worst: the loss and crosstalk is -7.5 dB and -3 dB respectively.

4.6.2 Effect of mask discretization on waveguide length

When the waveguide is aligned with the mask grid axis and the width/length of the waveguide is integer multiply of the mask grid width, the mask discretization [6] does not affect the width/length. The width of the waveguide used in the array are integer multiple of the mask grid width but the length is not. Therefore the mask discretization has a significant effect on the length. In this section we discuss the effect of this length variation on the performance of the AWGs.

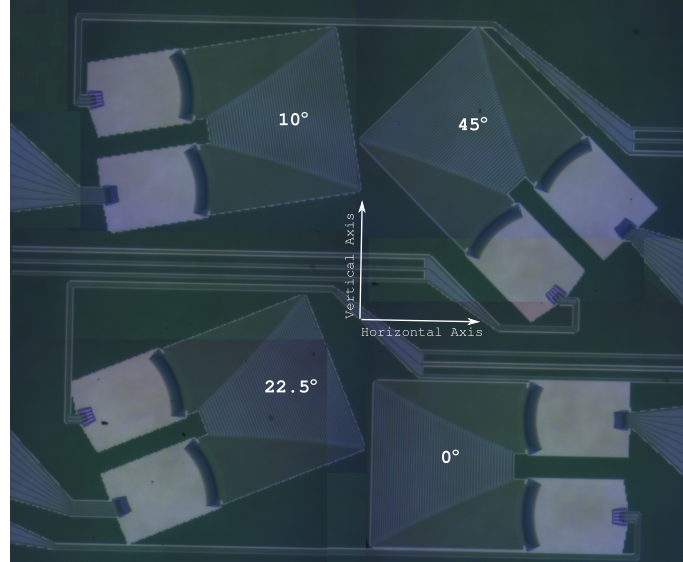


Figure 4.39: Optical image of the 8×400 GHz AWGs with 0°, 10°, 22.5° and 45° rotated layouts.

Rotation (degree)	Loss (dB)	crosstalk (dB)
0	-2.5	-19
10	-7.5	-3
22.5	-7	-5
45	-5.5	-10

Table 4.5: Experimental performances overview of the 8×400 GHz AWGs with 0°, 10°, 22.5° and 45° rotated layouts

4.6.2.1 Design

We used the same design to generate two sets of AWGs on the same mask with 1 nm and 5 nm grid snapping. Independent of the channel spacing, for the same number of wavelength channels we used the same number of waveguides: 24, 40 and 72 waveguides for 4, 8 and 16 channel AWGs respectively. For an equal number of wavelength channels and an equal number of waveguides the delay length of the 200 GHz device will be twice the delay length of the 400 GHz device. This will increase the influence of phase errors due to the sidewall roughness. But crosstalk floor due to the grid snapping will be nearly similar.

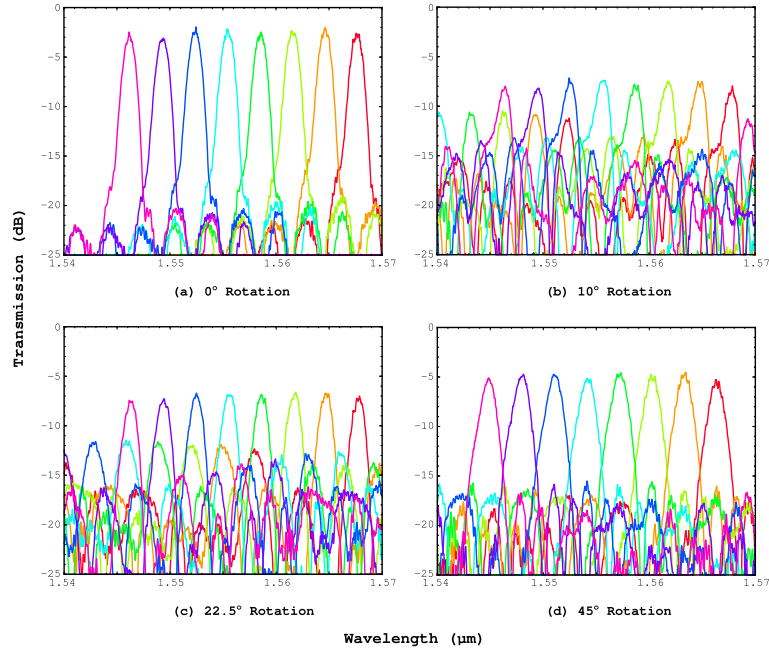


Figure 4.40: Spectral response of the 8×400 GHz AWGs with 0° , 10° , 22.5° and 45° rotated layouts.

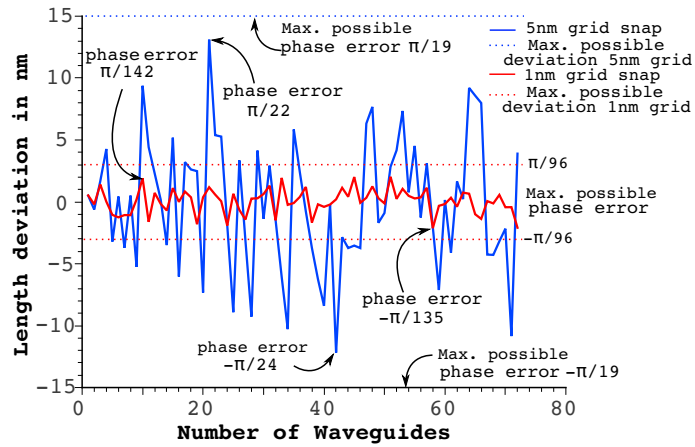


Figure 4.41: The length deviation over the waveguides of 16×400 GHz AWG due to 1 nm and 5 nm grid snapping.

4.6.2.2 Simulation

The AWGs were simulated using our semi-analytical simulator described in chapter 3. As we want to illustrate the effect on the crosstalk due to the phase errors introduced by the grid snapping we didn't include any stochastic phase error due to sidewall roughness in the simulation. In IPKISS (see chapter 3) it is possible to get the waveguide length information before and after grid snapping. Figure 4.42 shows the simulated spectral response of the 8th channel of

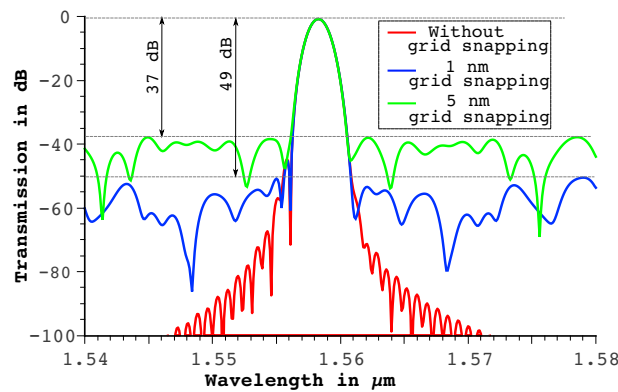


Figure 4.42: Simulated transmission spectrum of 16×400 GHz AWG (8th channel) for 1 nm, 5 nm and without grid snapping.

the 16×400 GHz AWG without grid snapping, and for 1 nm and 5 nm snapping. The simulation indicates, as expected, that the insertion loss will not be affected significantly while the crosstalk floor will increase due to the coarser mask grid. In the simulation we can see that the crosstalk is improved by 12 dB as we change the grid from 5 nm to 1 nm.

4.6.2.3 Experiment

Fig. 4.43 and 4.44 show the measured spectral response of 16×200 GHz and 16×400 GHz AWGs using 5 nm and 1 nm grid snapping. For the 16×400 GHz AWGs the crosstalk floor drops from -21 dB (for the 5 nm grid) to -26 dB (for the 1 nm grid) [7]. For the 16×200 GHz AWGs the crosstalk floor drops from -19.8 dB (for the 5 nm grid) to -22.5 dB (for the 1 nm grid). We see that the crosstalk is substantially higher than for the simulated AWGs, because other crosstalk mechanisms are still present, mainly the phase error contribution of the sidewall roughness, which is also the reason behind the smaller improvement for the 200 GHz device as the delay length is double that of the 400 GHz AWGs: $21.86 \mu\text{m}$ for 16×200 GHz vs. $10.93 \mu\text{m}$ for 16×400 GHz AWGs.

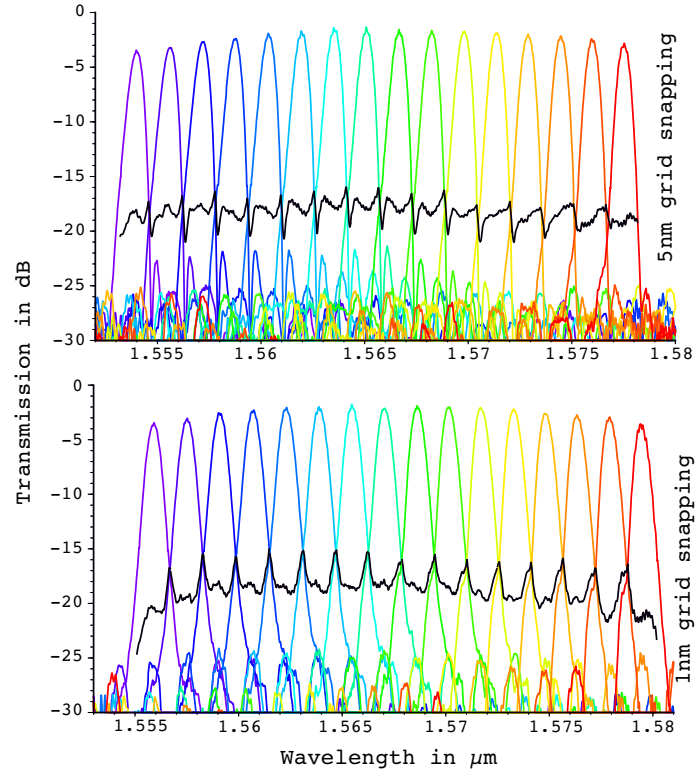


Figure 4.43: Experimental transmission spectrum of 16×200 GHz AWG using 5 nm and 1 nm grid snapping. Black line indicate the cumulative crosstalk power of the device.

The cumulative crosstalk is -17 dB and -22 dB for 400 GHz AWGs using the 5 nm and 1 nm grid, respectively. For 200 GHz AWGs the cumulative crosstalk improves from -15 dB for the 5 nm grid to -17 dB for the 1 nm grid. Fig. 4.43 and Fig. 4.44 show that for the 5 nm grid devices the neighboring channel contributed cumulative crosstalk is almost equal to the phase error contributed cumulative crosstalk as the channel overlap is minimal. For the 1 nm grid the neighboring channel contributed cumulative crosstalk is dominating due to the reduction of the discretization induced phase errors. This neighboring channel contributed cumulative crosstalk can be improved further by increasing the number of waveguides used in the array (see chapter 5).

Other AWGs, with different channel counts, show similar improvements as listed in table 4.6 and 4.7. From table 4.7 we can see that with a fixed number of output channels, when we decrease the channel spacing, the improvement of the crosstalk reduces because of the longer delay line length. The situation

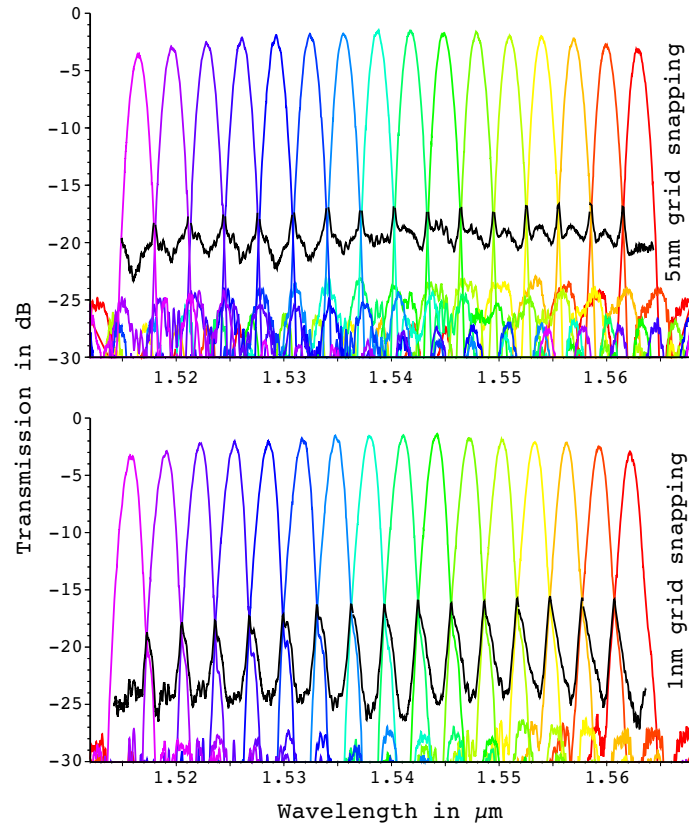


Figure 4.44: Experimental transmission spectrum of 16×400 GHz AWG using 5 nm and 1 nm grid snapping. Black line indicates the cumulative crosstalk power of the device.

is much more complex when the channel spacing is fixed and the number of output channels is increasing: the delay length will be shorter but the number of waveguides will increase, which will increase the size of the AWG. Therefore, depending on the number of waveguides used in the array, the improvement of the crosstalk varies with the number of output channels. Ideally the insertion loss of an AWG should be independent of the grid discretization but in table 4.6 we can see some variation in the insertion loss. This can be explained by the normalization with slightly different fabricated grating couplers or thickness and width variation of the waveguides over the wafer, which also leads to a wavelength shift of the full spectrum as we can see from Fig. 4.43 and Fig. 4.44.

Channels	Spacing	Area [μm^2]	IL 5nm [dB]	IL 1nm [dB]
4	200	845×243	-1.9→-2.3	-1.7→-2.6
4	400	468×237	-2.2→-2.5	-1.8→-2.2
8	200	873×308	-1.5→-2.7	-1.9→-3.1
8	400	490×307	-2.3→-3.7	-1.3→-2.7
16	200	920×446	-1.6→-3.6	-2.0→-3.7
16	400	530×435	-1.5→-3.5	-1.5→-3.5

Table 4.6: Comparison of AWG insertion loss (IL, center channel and outer channel) between 1nm and 5nm mask grid discretization.

Channels	Spacing	XT 5nm [dB]	XT 1nm [dB]	Δ XT [dB]	CXT 5nm [dB]	CXT 1nm [dB]	Δ CXT [dB]	FSR [nm]
4	200	-18.3	-23	4.7	-16.3	-20.5	4.2	9.5
4	400	-21.6	-27	5.4	-20.3	-24.7	4.4	19
8	200	-20.5	-23.6	3.1	-17.8	-19.0	1.2	15.8
8	400	-20	-26	6.0	-17	-21.5	4.5	32
16	200	-19.8	-22.5	2.7	-15	-17	2.0	29
16	400	-21	-26	5.0	-17	-22	5.0	54

Table 4.7: Comparison of AWG crosstalk level (crosstalk [XT] and cumulative crosstalk [CXT]) between 1nm and 5nm mask grid discretization.

4.7 Polarization Diversity

In chapter 2 we discussed about the polarization dependence of the AWGs. We also stated some of the possible solutions. One of the solutions is using a polarization diversity scheme. In this section we will discuss about the design and experimental demonstration of a SOI-based polarization diversity wavelength de-multiplexer circuit using two symmetric AWGs and a compact 2-D grating coupler, which is used to couple the unknown fiber polarization into two separate waveguides by splitting the light in two orthogonal polarizations. The schematic diagram of a 16×400 GHz polarization diversity circuit is shown in Fig. 4.45



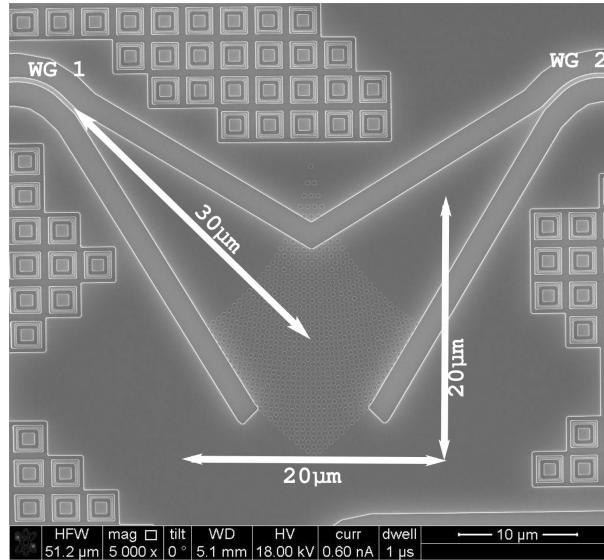
Figure 4.45: Fabricated 16×200 GHz Polarization diversity circuit.

4.7.1 Design of the 2D grating Coupler

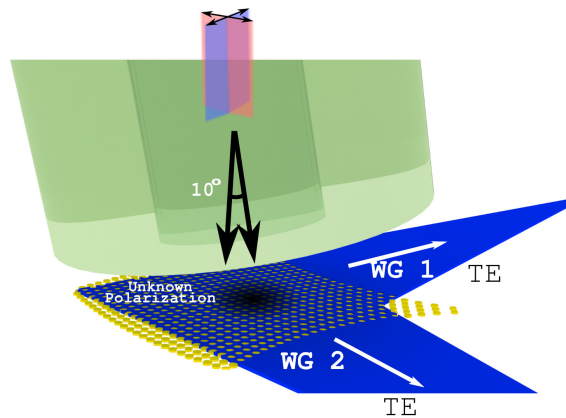
As discussed in section 4.3 a typical 1-D fiber grating coupler can couple either TE or TM polarized light into the waveguide. But a 2-D fiber grating coupler can couple any fiber polarization by splitting them into the TE modes of two orthogonally oriented waveguides [8]. Vice versa, the 2-D grating coupler can couple the light back into the fiber by combining the two TE modes into orthogonal fiber modes. This splitter/combiner functionality of 2-D grating couplers allows us to drive two identical circuits separately to achieve polarization independent operation in a polarization diversity scheme. Figure 4.46(a) shows a SEM-picture and a schematic diagram of a 2-D focusing grating coupler. The use of the 2-D focusing grating coupler [9] reduces the taper length of the access waveguide compared to the standard 2-D grating coupler [8]. As shown in Fig. 4.46(b) the fiber is placed quasi vertically over the grating with a 10° tilt to avoid coupling to the backward propagating mode and reflections back into the fiber. The 2-D grating couplers are fabricated using a double etch process. The grating holes are etched 70 nm into a 220 nm thick silicon slab while the access waveguides are defined by etching 220 nm deep trenches. The diameter of the grating holes is 390 nm and the pitch of the grating is 610 nm. The grating lines are curved to focus the coupled light directly into a 500 nm wide wire waveguide within a distance of only $30 \mu\text{m}$. This eliminates the need for a separate taper.

4.7.2 Design of the AWG

In chapter 4 we gave a detailed overview of the design of silicon AWGs. We used the same design method to design two 16 channels AWGs with 72 waveguides in the waveguide array as the basis of our polarization diversity circuit. The channel spacing is 200 GHz (1.6 nm). The size of a single 16×200 GHz AWG is $365 \times 650 \mu\text{m}^2$.



(a)



(b)

Figure 4.46: (a) Fabricated 2D grating coupler. (b) Schematic diagram of a 2D grating coupler with fiber align.

4.7.3 Results

To measure the polarization diversity circuit the automatic measurement (see section 4.3) is modified by replacing the fiber based polarization controller with an electronics polarization controller (HP8169A). We use a known 1-D TE grat-

ing coupler to calibrate the fiber polarization.

4.7.3.1 Analysis of the 2D grating coupler

To analyze the performance of the 2D grating coupler we designed a test circuit where 2D grating couplers are directly connected with two 1D grating couplers which only couple the TE polarization of the waveguide. We excited the 2D grating coupler with four differently oriented fiber polarizations (90, -45, 0 and 45 degree with respect to the axis of the 2D grating, respectively denoted as $Pol-1$, $Pol-2$, $Pol-3$, and $Pol-4$ in Fig. 4.47) and measured the spectral response from two waveguides connected to the 2D coupler and terminated with 1D TE grating couplers (which are denoted as $WG-1$ and $WG-2$ in Fig. 4.47). Figure 4.47 shows that when the 2D grating coupler is excited by the 90 or 0 degree oriented polarization ($Pol-1$ and $Pol-3$) the power is divided equally into both waveguides ($WG-1$ and $WG-2$). To the contrary, when the polarization is oriented along the -45 or 45 direction, the light predominantly couples towards respectively $WG-1$ and $WG-2$ as we can see in Fig. 4.47(b) and 4.47(d). Figure 4.47 also shows that the transmission is wavelength dependent, which is related to the wavelength dependent coupling efficiency of the 1D and 2D grating couplers.

Using our automatic setup, we mapped the tolerance towards fiber misalignments of the 2-D grating coupler. The input fiber was scanned over the grating coupler in a 2-D pattern, while the output fiber was fixed at its original position above the 1D grating couplers connected to respectively $WG-1$ and $WG-2$. The center between the two positions obtained by optimizing the transmission through respectively $WG-1$ and $WG-2$ with the input polarization oriented along $Pol-3$ was taken as the origin (0, 0) for plotting Fig. 4.48. The mapping was carried out for a wavelength of $1.55 \mu\text{m}$. From Fig. 4.48 we can observe that an equal amount of power is coupled to $WG-1$ and $WG-2$ for the polarization oriented along $Pol-1$ and $Pol-3$, when shifting their maximum transmission position towards the respective waveguides. For polarization $Pol-2$ and $Pol-4$ the maximum transmission position shifts towards the waveguide $WG-1$ and $WG-2$, respectively. The offset between the optimal position of $WG-1$ and $WG-2$ is less than a micrometer and similarly, the offset between the maximum transmission positions for polarization $Pol-2$ and $Pol-4$ is less than half a micrometer. These offsets in optimal coupling positions are the main source of the polarization dependent loss (PDL) in this circuit. It is also possible to optimize the alignment of the fiber for maximum overlap of the spectrum to reduce the PDL. But this will introduce an additional insertion loss. From Fig. 4.48 we can also observe that the power drops by 2 dB if the fiber moves $4\mu\text{m}$ away from the center. The PDL of the 2D grating coupler can be further improved by using a π phase-shifter in one of the waveguides [10].

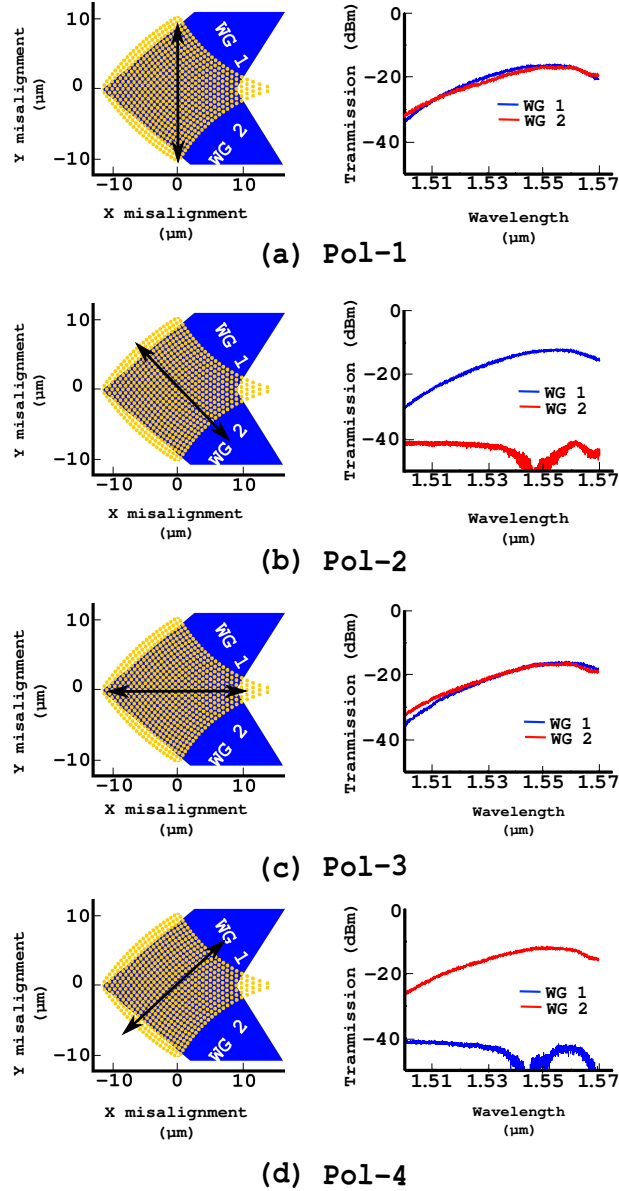


Figure 4.47: Spectral response of a 2D grating coupler connected to two 1D grating couplers for differently oriented input polarizations ((a) Pol-1: 90 degree, (b) Pol-2: -45 degree, (c) Pol-3: 0 degree, (d) Pol-4: 45 degree oriented fiber polarizations with respect to the axis of the 2D grating).

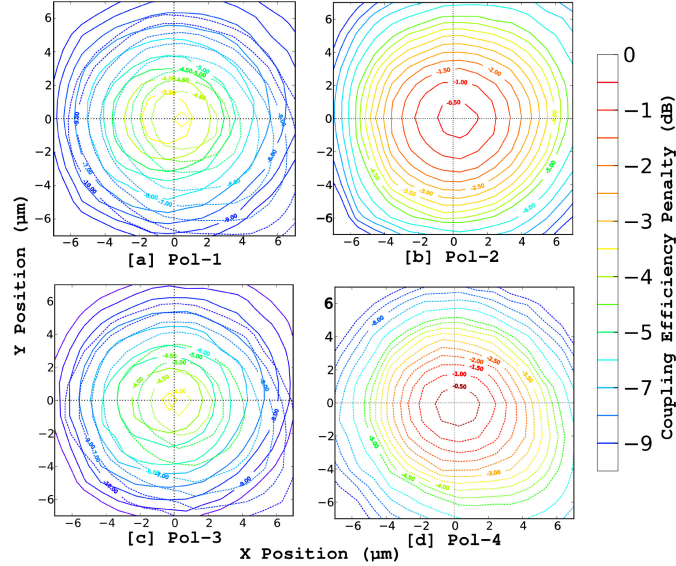


Figure 4.48: Mapping of alignment tolerance for different oriented fiber polarizations ((a) Pol-1: 90 degree, (b) Pol-2: -45 degree, (c) Pol-3: 0 degree, (d) Pol-4: 45 degree oriented fiber polarizations with respect to the axis of the 2D grating). (a) and (c) The solid line represents the transmission through waveguide WG – 1. The dashed line represent the transmission through waveguide WG – 2.

To evaluate the wavelength dependent transmission for light polarized along *Pol – 1* and *Pol – 3* we use a reference circuit where two 2D grating couplers are connected with two waveguides of equal length. We optimize the alignment of both fibers for the *Pol – 1* polarization and measure the spectral response for both the *Pol – 1* and *Pol – 3* polarizations. The results are shown in Fig. 4.49(a). Both spectra are shifted with respect to each other. This illustrates very well how the polarization dependent loss will be wavelength dependent. Fig. 4.49(b) shows the wavelength range where the spectral response of the 2D grating becomes nearly flat. In this range, the wavelength variation of the PDL is minimal compared to the rest of the spectrum. The measured PDL of the 2-D grating coupler is 1.1 dB at the wavelength of $1.52 \mu\text{m}$ where we measure the highest coupling efficiency.

4.7.3.2 Analysis of full Polarization Diversity Circuit

Figure 4.50 shows the spectral response of a 16 channel (200GHz channel spacing) polarization diversity wavelength de-multiplexer circuit for *Pol – 1* and

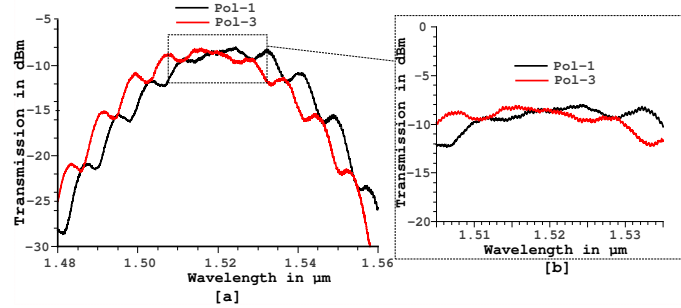


Figure 4.49: Transmission of two 2-D grating couplers connected through waveguides. (a) Spectral response of the 2D grating for wavelength range of $1.48 \mu\text{m}$ to $1.56 \mu\text{m}$. (b) Flat passband spectral response of the 2D grating.

Pol – 3 polarizations. The center channel experiences an on-chip insertion loss of -2.6 dB [11] contributed by the AWGs. The estimated loss introduced by the two 2D grating couplers (one at input and other at the output) is 12 dB . The crosstalk of the circuit is -21.5 dB [11]. The output channels are well aligned in terms of polarization-dependent wavelength shift. From Fig. 4.50 we can observe the power is well matched for channels 7, 8, 9, 13, 14 and 15 as the channels are laid on the overlapped wavelength region of the 2D grating couplers, shown in Fig. 4.49(b). The other channels experience power deviations

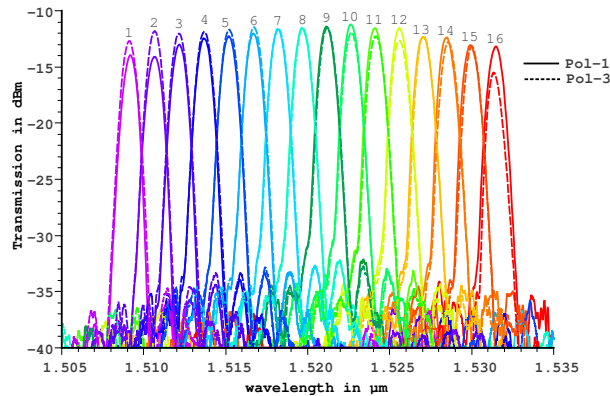


Figure 4.50: Spectral response of a 16 channels 200GHz polarization diversity wavelength de-multiplexer circuit for *Pol* – 1 and *Pol* – 3 polarizations.

due to the 2D grating coupler. The polarization-dependent loss is measured to

be between 0.06 dB (channel 8) and 2.32 dB (channel 16) in the best respectively worst case.

The mismatch between the two fabricated AWGs induces a polarization-dependent wavelength shift, but it is very low, as can be seen in Fig. 4.50. Fig.

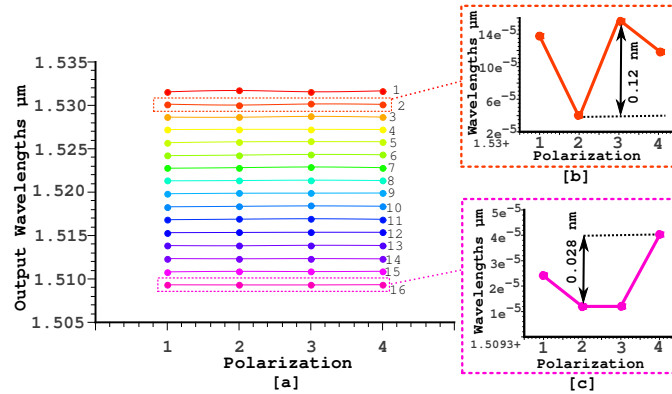


Figure 4.51: (a) The output wavelength channel positions of the polarization diversity circuit for Pol-1, Pol-2, Pol-3, and Pol-4 polarizations. (b) Maximum shifted output channel. (c) Minimum shifted output channel.

ure 4.51(a) plots the position of all 16 channels for the four polarization states considered. The polarization-dependent wavelength shift is measured to be between 0.12 nm and 0.028 nm in the worst respectively best case, as shown in Fig. 4.51(b) and 4.51(c).

4.8 Comparison with echelle gratings

Another commonly used component for WDM is the echelle grating (sometimes called planar concave grating or PCG), which was also demonstrated in various material systems, including silica-on-silicon [12–14], InP [15–17], silicon-on-insulator [18, 19], germanium-on-silicon [20, 21] etc. Just like the AWG it is based on multi-path interference of light, but the implementation of the delays between the paths is different: in an AWG the different paths are individual waveguides arranged in an array, while in an echelle grating the light travels freely through a *slab* medium and is reflected by a series of facets. Before we proceed to the experimental comparison we discuss the working principle of echelle gratings.

4.8.1 Echelle Gratings

The working principle of the echelle grating is similar to the AWG in the sense that in both devices, multipath interference with a set of equally spaced delay lengths is used. However, the delays are now implemented in the free propagation region itself, using reflective facets. This means the same slab area is used for diffraction and refocusing. While this is a more efficient use of space it puts restrictions on the positioning of the input and output waveguides.

As with the AWG, the optical group delay length between facets determines the FSR. In silicon, the slab waveguide has significantly lowered dispersion, and thus a lower group index. This means that the physical delay length needs to be larger than in an AWG to obtain the same FSR. This causes an echelle grating to grow faster in footprint than a comparable AWG when many facets are needed. However, for a large FSR and few channels, an echelle grating can be extremely compact. Moreover, it does not suffer from layout restrictions for very short delays, making it very suitable to realize CWDM (de)multiplexers with a few, widely spaced channels.

As with an AWG, crosstalk in an echelle grating can be result from imperfect imaging of the refocused light. The errors in the image can originate from two sources: phase errors in the delay path, and imperfect reflection and scattering by the facets. The phase errors in an echelle gratings are accumulated in the slab, and the variations in optical path length can be attributed to thickness variations. As the thickness changes typically occur on longer length scales and are not as stochastic in nature as linewidth variations in waveguides, the phase errors do not necessarily follow the same \sqrt{L} rule as with AWGs. Instead, larger echelle gratings will suffer disproportionately from crosstalk compared to AWGs.

As for the role of the grating facets, this is an inherent problem of the design of echelle gratings, combined with technology limitations: the grating facets will always suffer from corner effects which will cause undirected scattering light. The smaller the facets, the larger the effect of these corners. Using larger facets alleviates this issue, but will increase the size of the device, and increase the length of delay paths.

4.8.2 Design

For comparison we used an 4×6.4 nm and 8×6.4 nm rectangularly shaped AWG. As we introduced the S-shaped AWG as an alternative layout for larger FSR/channel spacing we designed also 4×24 nm 4×32 nm S-shaped AWGs. The footprint of S-shaped AWGs is larger than the rectangular-shaped AWGs: the size of the 4×6.4 nm box-shaped AWG is $275 \times 245 \mu\text{m}^2$ while the size of the 4×24 nm S-shaped AWG is $305 \times 260 \mu\text{m}^2$.

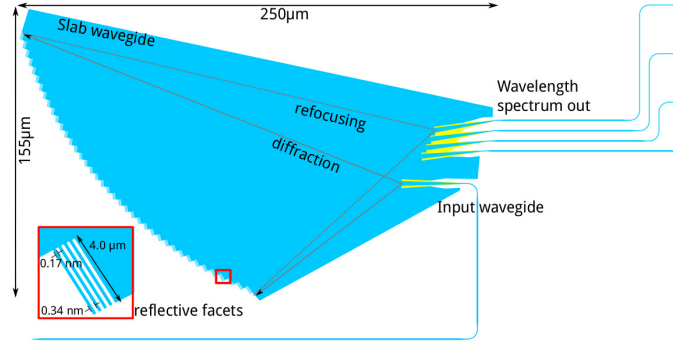


Figure 4.52: Schematic diagram of 4×20 nm echelle grating.

The design of the echelle gratings is based on a Rowland geometry and the design procedure is detailed in [19]. Similar to the AWG design the input and output apertures are shallowly etched to reduce reflections. As shown in Fig. 4.52 the reflectors consist of first-order distributed Bragg reflectors (DBR) with four deeply etched trenches of 70 nm width and 340 nm pitch. Figure 4.52 shows the schematic diagram of a 4×20 nm echelle grating; the footprint is $250 \times 155 \mu\text{m}^2$. The device size increases rapidly as we decrease the channel spacing/FSR: the size of the 4×6.4 nm echelle grating is $275 \times 245 \mu\text{m}^2$.

4.8.3 Results and Discussions

To characterize the echelle grating we also used 1D curved grating coupler to couple in/out the light and the measurement was performed using the automatic measurement set-up.

4.8.3.1 AWG

The 4×6.4 nm box-shaped AWG has a measured insertion loss of -1.53 dB and -27 dB crosstalk. If we keep the channel spacing constant, but increase the number of channels, the FSR will go up, the delay length will go down, but the number of arms needs to go up (more channels within an FSR). Overall, this does not significantly increase the device footprint. As the average delay line length has not changed significantly either, the impact on the crosstalk is negligible. The insertion loss and the crosstalk are -1.86 dB and -27.3 dB for the 8×6.4 nm box-shaped AWG.

If we keep the number of channels constant (4) but increase the channel spacing (and thus the FSR as well), we need to change the shape of the AWG to an S-shape. The much longer delay lines incur a penalty: the 4×24 nm box-

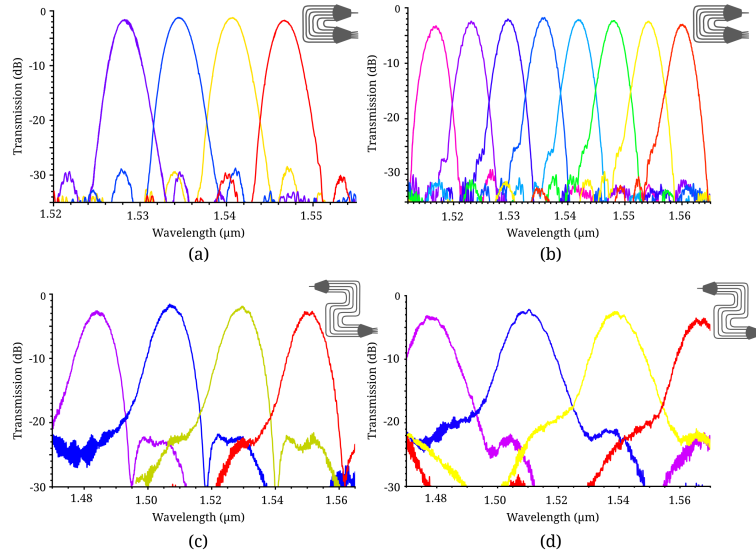


Figure 4.53: Experimental result of AWGs (a) 4×6.4 nm (b) 8×6.4 nm (c) 4×24 nm and (d) 4×32 nm.

shaped AWG has a measured insertion loss of -1.7 dB and -20.6 dB crosstalk. The performance of a 4×32 nm S-shaped AWG is even worse: the measured insertion loss is -2.0 dB and the crosstalk is -19.0 dB. In Fig. 4.53 we can see the measured transmission spectrum of the AWGs.

4.8.3.2 Echelle grating

The 4×6.4 nm echelle grating has a measured insertion loss of -1.43 dB and a crosstalk of -18.7 dB. This is significantly worse than the AWG with the same specifications. The channel spacing is small for an echelle grating, and it needs a very large slab region which can induce too large phase errors. This improves when we increase the channel spacing (and thus the FSR): the crosstalk of the 4×10 nm echelle grating drops to -24.0dB, and the insertion is -1.6 dB. Further incrementing the channel spacing will make the echelle grating more sensitive to the size of the grating teeth and their positioning. For the 4×20 nm echelle grating the crosstalk is -23.0 dB and the insertion loss increases to -2.2 dB. The transmission spectra of the echelle gratings are shown in the Fig. 4.54. The dotted lines in the 4.54 are indicating an accidentally damaged output channel or a spectrum outside the range of the tunable laser used for characterization.

Based on this experimental demonstration and with the help of simulation we tried to estimate the crosstalk of the AWG and echelle grating as function of

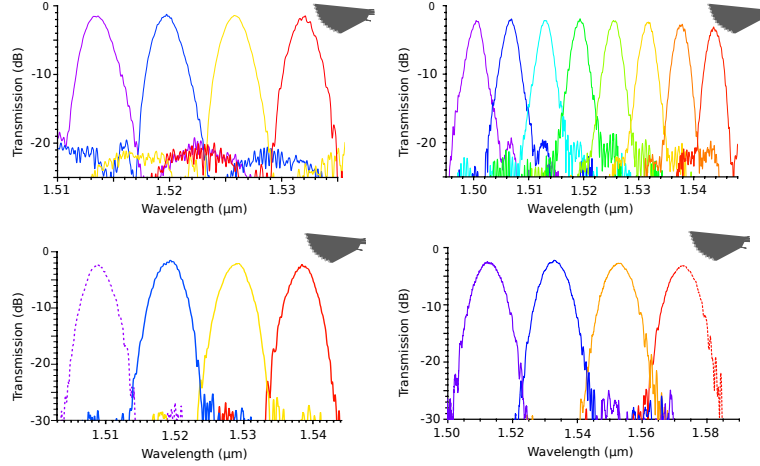


Figure 4.54: Experimental result of echelle grating (a) 4×6.4 nm (b) 8×6.4 nm (c) 4×10 nm and (d) 4×20 nm.

Device Type	Area μm^2	Channels	Spacings (nm)	Waveguides / grating facets	Loss (dB)	XT (dB)	FSR (nm)
Box-AWG	275×245	4	6.4	24	-1.53	27.1	38
Box-AWG	310×305	8	6.4	40	-1.86	27.3	64
S-AWG	305×260	4	24	16	-1.68	20.6	88
S-AWG	305×260	4	32	16	-2.1	19.1	144
PCG	700×420	4	6.4	70	-1.43	18.7	70
PCG	700×385	8	6.4	90	-1.55	19.7	100
PCG	450×220	4	10	60	-1.57	24.2	120
PCG	250×155	4	20	40	-2.2	23.3	120

Table 4.8: Comparison of size, insertion loss and crosstalk level between AWGs and Echelle gratings.

the channel spacing and number of wavelength channels. Figure 4.55 (a) and (b) show the estimated crosstalk for AWG and echelle grating. Figure 4.55 (c) shows the expected best working regions for each type of device. As shown in Fig. 4.55(a) the crosstalk of the AWG will improve with increasing number of wavelength channels for a constant channel spacing assuming that the phase error originates from the waveguide array only. But for S-shaped AWGs the crosstalk increases due to the increasing length of the smallest delay line. The black line indicating the border between the rectangular and S-shaped AWG. For the echelle gratings, as the FSR increases (either by increasing the number of wavelength channels or when increasing the channel spacings) the crosstalk

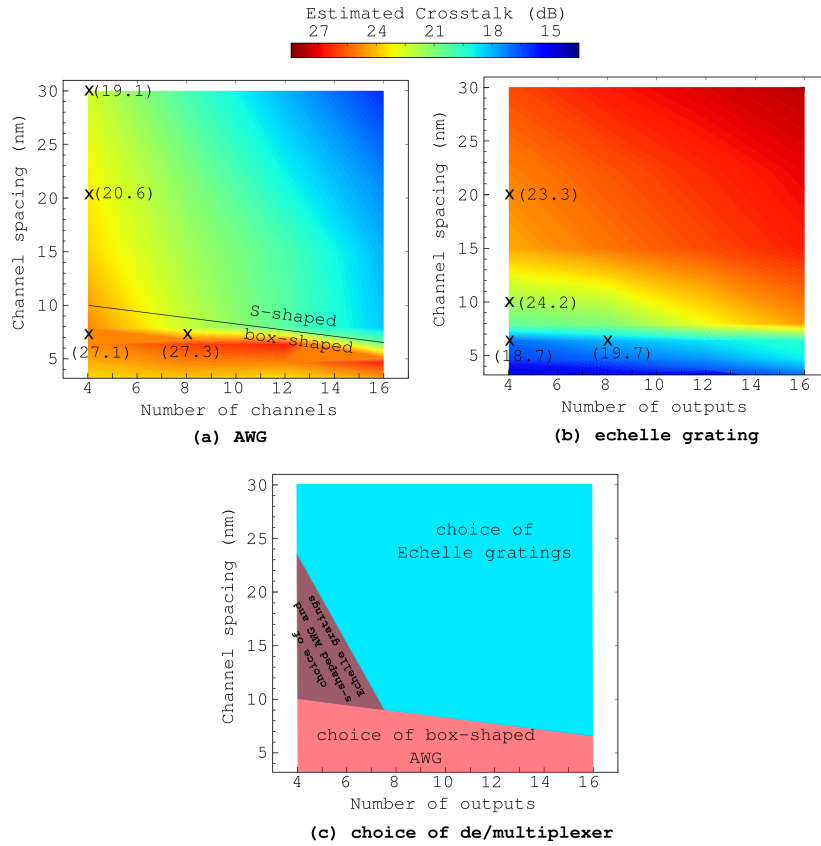


Figure 4.55: The estimated crosstalk mapping of (a) AWG and (b) echelle grating. (c) Estimated design of best performance de/multiplexers

decreases. From Fig 4.55 (c) it is clear that if the de/multiplexer design is possible by using the box-shaped AWG the performance will be the best i.e. high resolution de/multiplexing. For the low resolution de/multiplexing echelle grating is the best choice. The S-shaped AWG is the alternative choice for the low resolution de/multiplexing with smaller number of wavelength channels. Although by looking at the active tuning capability of the AWG (both rectangularly and S-shaped) it can be the potential device for all range of low resolution de/multiplexing.

4.9 Conclusions

We demonstrated rectangularly, circularly, S-shaped and reflection type AWGs in silicon with a variation of channel spacing from 50 GHz (0.35 nm) to 6000 GHz (43 nm). The best performance is achieved by the rectangularly shaped AWG. We experimentally demonstrate the AWG for de/multiplexing and wavelength router applications. We minimized the polarization dependent loss by using a polarization diversity circuit. We compared the performance of two grating based wavelength de/multiplexers in silicon: arrayed waveguide gratings and echelle gratings. The echelle gratings are the best choice for low resolution (CWDM) de/multiplexer applications. For high resolution de/multiplexer applications AWGs are a better choice. For larger channel spacings AWGs suffer from layout restrictions, which can be overcome by using an S-shaped geometry at the cost of performance.

References

- [1] S. K. Selvaraja. *Wafer-Scale Fabrication Technology for Silicon Photonic Integrated Circuits*. PhD thesis, Ghent University, 2011.
- [2] D. Vermeulen, S. Selvaraja, P. Verheyen, G. Lepage, W. Bogaerts, P. Absil, D. Van Thourhout, and G. Roelkens. *High-efficiency fiber-to-chip grating couplers realized using an advanced CMOS-compatible Silicon-On-Insulator platform*. *Opt. Express*, 18(17):18278–18283, Aug 2010.
- [3] D. Taillaert, F. Van Laere, M. Ayre, W. Bogaerts, D. Van Thourhout, P. Bienstman, and R. Baets. *Grating Couplers for Coupling between Optical Fibers and Nanophotonic Waveguides*. *Japanese Journal of Applied Physics*, 45(8A):6071–6077, 2006.
- [4] W. Bogaerts, S.K. Selvaraja, P. Dumon, J. Brouckaert, K. De Vos, D. Van Thourhout, and R. Baets. *Silicon-on-Insulator Spectral Filters Fabricated With CMOS Technology*. *IEEE Journal of Selected Topics in Quantum Electronics*, 16(1):33–44, 2010.
- [5] S. Pathak, D. Van Thourhout, and W. Bogaerts. *Design trade-offs for silicon-on-insulator-based AWGs for (de)multiplexer applications*. *Opt. Lett.*, 38(16), Aug 2013.
- [6] S. Day, J. P. Stagg, D. Moule, S. J. Clements, C. Rogers, S. Ojha, T. Clapp, J. Brook, and J. Morley. *The elimination of sidelobes in the arrayed waveguide WDM*. In *Integrated Photonics Research*, page IMC5, 1996.
- [7] S. Pathak, M. Vanslambrouck, P. Dumon, D. Van Thourhout, and W. Bogaerts. *Effect of mask grid on SOI arrayed waveguide grating performance*. In *10th IEEE Int. Conf. Group IV Photonics*, 2013.
- [8] D. Taillaert, H. Chong, P.I. Borel, L.H. Frandsen, R.M. De La Rue, and R. Baets. *A compact two-dimensional grating coupler used as a polarization splitter*. *Photonics Technology Letters, IEEE*, 15(9):1249–1251, Sept 2003.
- [9] F. Van Laere, W. Bogaerts, P. Dumon, G. Roelkens, D. Van Thourhout, and R. Baets. *Focusing Polarization Diversity Grating Couplers in Silicon-on-Insulator*. *Lightwave Technology, Journal of*, 27(5):612–618, March 2009.
- [10] R. Halir, D. Vermeulen, and G. Roelkens. *Reducing Polarization-Dependent Loss of Silicon-on-Insulator Fiber to Chip Grating Couplers*. *IEEE Photonics Technology Letters*, 22(6):389–391, 2010.

- [11] S. Pathak, M. Vanslembrouck, P. Dumon, D. Van Thourhout, and W. Bogaerts. *Compact SOI-based polarization diversity wavelength demultiplexer circuit using two symmetric AWGs*. Opt. Express, 20(26):B493–B500, Dec 2012.
- [12] R. Adar, C.H. Henry, C. Dragone, R.C. Kistler, and M.A. Milbrodt. *Broadband array multiplexers made with silica waveguides on silicon*. Lightwave Technology, Journal of, 11(2):212–219, Feb 1993.
- [13] Y. Inoue, A. Himeno, K. Moriwaki, and M. Kawachi. *Silica-based arrayed-waveguide grating circuit as optical splitter/router*. Electronics Letters, 31(9):726–727, Apr 1995.
- [14] S. Janz, A. Balakrishnan, S. Charbonneau, P. Cheben, M. Cloutier, A. Delaigè, K. Dossou, L. Erickson, M. Gao, P.A. Krug, B. Lamontagne, M. Packirisamy, M. Pearson, and D.X. Xu. *Planar waveguide echelle gratings in silica-on-silicon*. Photonics Technology Letters, IEEE, 16(2):503–505, 2004.
- [15] H. Bissessur, F. Gaborit, B. Martin, P. Pagnod-Rossiaux, J.L. Peyre, and M. Renaud. *16 channel phased array wavelength demultiplexer on InP with low polarization sensitivity*. Electronics Letters, 30(4):336–337, February 1994.
- [16] M. Zirngibl, C. Dragone, and C.H. Joyner. *Demonstration of a 15x15 arrayed waveguide multiplexer on InP*. Photonics Technology Letters, IEEE, 4(11):1250–1253, Nov 1992.
- [17] J.J. He, B. Lamontagne, A. Delage, L. Erickson, M. Davies, and E.S. Koteles. *Monolithic integrated wavelength demultiplexer based on a waveguide Rowland circle grating in InGaAsP/InP*. Lightwave Technology, Journal of, 16(4):631–638, 1998.
- [18] J. Brouckaert, W. Bogaerts, S. Selvaraja, P. Dumon, R. Baets, and D. Van Thourhout. *Planar concave grating demultiplexer with high reflective Bragg reflector facets*. IEEE Photonics Technology Letters, 20(4):309–311, 2008.
- [19] J. Brouckaert, W. Bogaerts, P. Dumon, D. Van Thourhout, and R. Baets. *Planar concave grating demultiplexer fabricated on a nanophotonic silicon-on-insulator platform*. Journal of Lightwave Technology, 25(5):1269–1275, 2007.
- [20] A. Malik, M. Muneeb, S. Pathak, Y. Shimura, J. Van Campenhout, R. Loo, and G. Roelkens. *Germanium-on-Silicon Mid-Infrared Arrayed Waveguide*

Grating Multiplexers. Photonics Technology Letters, IEEE, 25(18):1805–1808, 2013.

- [21] A. Malik, M. Muneeb, Y. Shimura, J. Van Campenhout, and G. Roelkens. *Germanium-on-silicon mid-infrared waveguides and Mach-Zehnder interferometers*. In IEEE Photonics Conference, 2013.

5

Flattened Spectral Response

5.1 Introduction

In previous chapters, we had a look into the design and performance of conventional AWGs. These AWGs had a conventional transmission i.e. the spectral response at each output is Gaussian-like. A main application of the AWGs is (de)multiplexing action in an optical networking system. The Gaussian response doesn't offer a lot of tolerance in such a system. A small spectral misalignment will introduce a high penalty in transmission. The active devices (such as lasers, LEDs) and also the AWG are highly temperature/fabrication dependent, which makes it difficult to design the device such that the peak of the channel and active device coincide. A very simple method to improve this is to generate a flattop spectral response in the AWG. The flattop spectral response will ensure that even if the active device is emitting at a slightly off wavelength or the AWG has fabrication imperfections, the transmission will not suffer. Various spectral response methods have been proposed: a Multi-Mode Interference Coupler (MMI) integrated with an AWG as an input aperture [1, 2], a Mach-Zehnder Interferometer (MZI) used as input aperture [3–5] and cascaded AWGs [6]. All these techniques have their own advantages and disadvantages. In

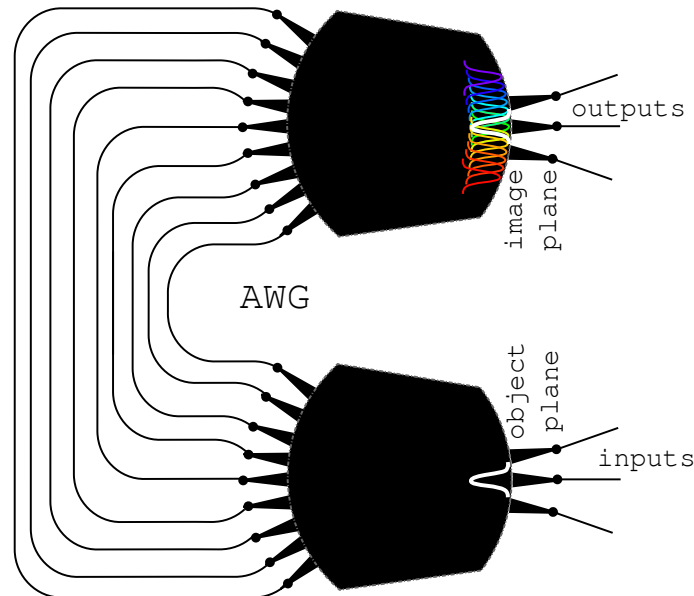


Figure 5.1: Working principle of the AWG.

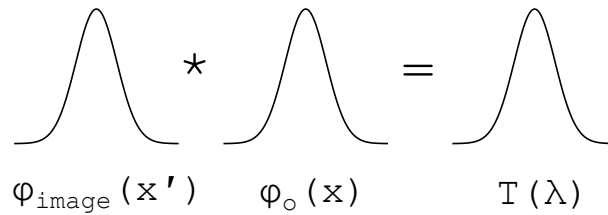
this chapter we will discuss the design methods, simulation and experimental results developed and obtained for all these three methods for the silicon-on-insulator platform.

5.2 Mode overlap

In chapter 2 we describe the working principle of the AWG. But to get a flattop spectral response we need to understand the mode overlap in the AWG. We can recall the working principle of the AWG as shown in Fig.5.1. The field profile of the input aperture at the object plane will create the same field profile (ideally) for all wavelengths at the image plane with a shift along the image plane. These field profiles at the image plane will overlap with the mode profile of the output aperture in order to determine the spectral response of the AWG. This working principle is illustrated in Fig. 5.2. The spectral response of the AWG can be written as

$$T(\lambda) = \int \phi_{image}(x')\phi_o(x)dx \quad (5.1)$$

where $\phi_{image}(x')$ is the 1:1 image field of the input field profile; $\phi_o(x)$ is the output aperture field profile. x' is a wavelength (λ) dependent coordinate which allows the field profile to move along the image plane as the wavelength changes.



$$\phi_{image}(x') \star \phi_o(x) = T(\lambda)$$

Figure 5.2: Spectral response profile calculated using overlap integral.

From Eq. 5.1 it is clear there are three parameters which influence the shape of the spectral response of the AWG: the field profiles of the input and output aperture and the wavelength dependence of the imaged field profile. A flattop spectral response can be obtained by changing one of these.

5.3 MMI as Input Aperture

A flat spectral response can be achieved by using an MMI as an input aperture of the AWG as shown in Fig. 5.3. This approach was first proposed by Soole *etal.* for InP-based AWGs [1]. Later MMI-AWG have been demonstrated for different material platforms [1, 2, 7, 8]. The operation principle of an MMI-AWG is described as follows. At the object plane of the AWG the MMI aperture will generate a wider twofold field profile with its precise shape depending on the length, width and taper width of the MMI (as shown in Fig 5.3). This two fold field profile generated by the MMI is not very wavelength dependent. Therefore

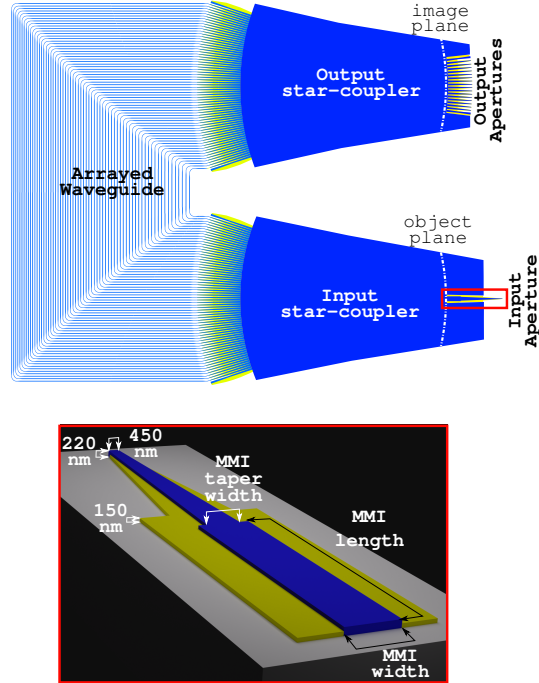


Figure 5.3: Schematic diagram of silicon MMI-AWG and 3D diagram of the MMI aperture used as an input aperture of the AWG.

in Eq. 5.1 the $\phi_{image}(x')$ will be replaced by the two fold image field profile. The output aperture field profile ($\phi_o(x)$) and the wavelength dependent dispersion will remain the same. This situation is illustrated in Fig. 5.4. By plotting the

$$\begin{array}{c}
 \text{[Graph of } \phi_{image}(x') \text{]} * \text{ [Graph of } \phi_o(x) \text{]} = \text{ [Graph of } T(\lambda) \text{]} \\
 \phi_{image}(x') \quad \phi_o(x) \quad T(\lambda)
 \end{array}$$

Figure 5.4: Spectral response of the MMI-AWG calculated using overlap integral.

spectral response for three wavelengths, Fig. 5.5 further illustrates how a flat-field response is formed in an MMI-AWG.

The design of the MMI is very critical to obtain the flattop spectral response. The major design parameters are: MMI width, MMI length, taper width, taper

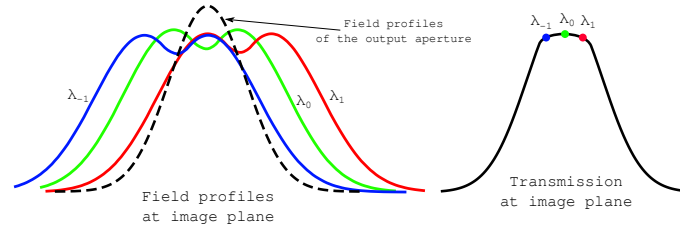


Figure 5.5: Working principle of the MMI-AWG for three wavelengths.

length and taper position. With careful optimization of these parameters, we can produce a perfect two fold field at the object plane which will produce a flattened spectral response. Note that the MMI-AWG intrinsically has a somewhat higher loss than a conventional AWG because of shape mismatch in the image plane of the AWG and the fact that the power in the image is now spread over a wider area to obtain a flat-top wavelength response.

5.3.1 Design of MMI and AWG

All devices were designed to be fabricated on the imec 200 mm pilot line SOI platform. Similar to the other silicon AWG designs, a shallow etch process was used for defining all star coupler apertures, including the MMIs, to reduce reflections at the transitions. The output apertures are $2\ \mu\text{m}$ wide and are connected to a $450\ \text{nm}$ wide photonic wire through a $25\ \mu\text{m}$ long adiabatic taper. The input apertures of the MMI-AWGs consist of a $42\ \mu\text{m}$ long taper having a width of $4\ \mu\text{m}$ coupled to an MMI with length and width varied as discussed below. Both the MMI and the taper are shallowly etched.

As discussed above, by placing an MMI at the input of the AWG we can tailor the image of the input field for an optimized overall response. The MMI aperture needs to be about twice as broad as the output aperture to be able to create an image which is sufficiently flat. For narrower MMIs, the profile will be too narrow and for broader MMIs, the profile will have a significant dip in the middle. It also depends strongly on the dispersion of the waveguide array, i.e. the lateral shift of the spot as function of the wavelength. Figure 5.6 shows the simulated field distribution for $4.0\ \mu\text{m}$, $4.5\ \mu\text{m}$, $5.0\ \mu\text{m}$, $5.5\ \mu\text{m}$ and $6.0\ \mu\text{m}$ wide and up-to $25.0\ \mu\text{m}$ long MMIs. The black circular dots in the figure indicate the optimal length to achieve a flat spectral response. The simulation method is explained in chapter 3. When used in an AWG the MMI should interface at this point with the FPR. A line scan of the field profile at these positions is shown in Fig. 5.7 (as a function of width) and in Fig. 5.8 (as a function of length). From this figure it is obvious that the overlap of the output waveguide field profile (dash-dot line) with the input field profile of the $4.0\ \mu\text{m}$ wide MMI-aperture will

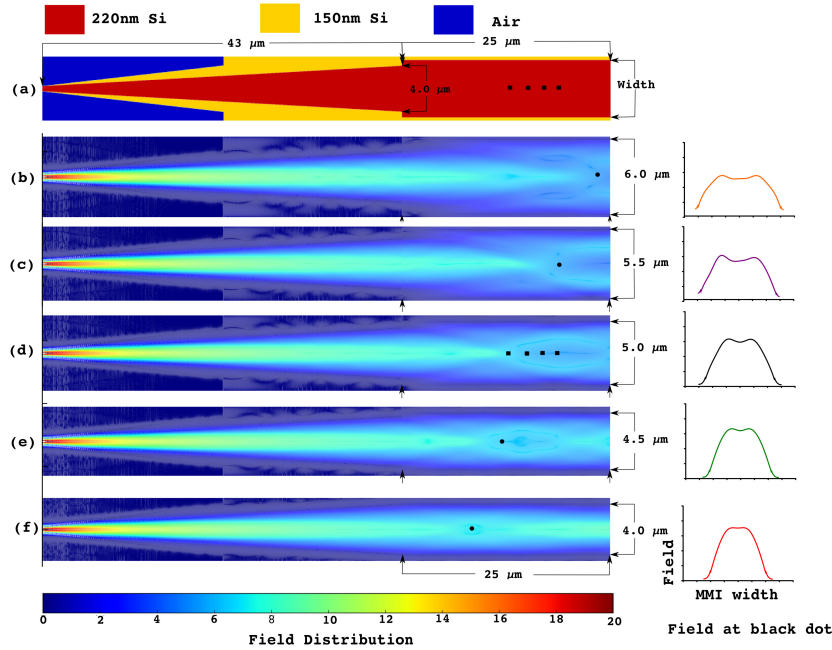


Figure 5.6: (a) Geometry of the MMI-aperture used in the simulations and actual design. (b)-(f) Simulated field distribution of the MMI-aperture for different widths. The black circular dots indicate, for a given MMI width, the optimal length for achieving a flat spectral response. The square dots in (d) indicate the positions 13 μm , 15 μm , 17 μm and 19 μm of the 5 μm wide MMI for which Fig. 5.8 shows the field distribution.

produce the lowest loss but will have a spectral response with narrower, more rounded top. The 4.5 μm and 5.0 μm wide MMI-apertures (close to twice the width of the output aperture) are the best compromise for achieving a low loss and flat spectral response. The loss will increase significantly for further increments in width.

The flatness of the spectral response depends on the length of the MMI-aperture as well. To illustrate this we use a 5.0 μm wide MMI-aperture. Figure 5.6(d) shows the field as it propagates through the 5.0 μm wide and 25.0 μm long MMI-aperture. In Fig. 5.8 we can see how the field distribution changes from a Gaussian-like to a twofold image with a center dip, by varying the length of the MMI from 13 μm to 19 μm (the width of the MMI in this example was fixed to 5 μm). At a certain point along the length of the MMI, we get a field profile with a flat region in the center. The overlap of this flat image field and the mode in

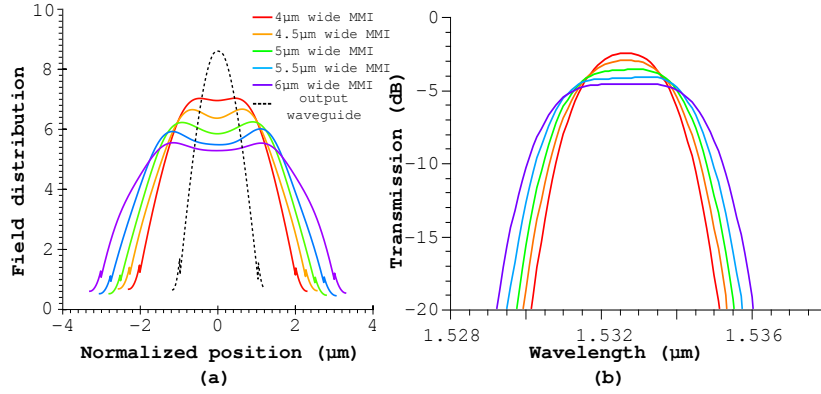


Figure 5.7: Simulated (a) field distribution of 4.0 μm , 4.5 μm , 5.0 μm , 5.5 μm and 6.0 μm wide MMI-apertures for optimal length (indicated as dot in Fig. 5.6) and (b) spectral response of the AWG using the corresponding MMI-apertures.

the image plane will produce a flattened spectral response. The width of the flat

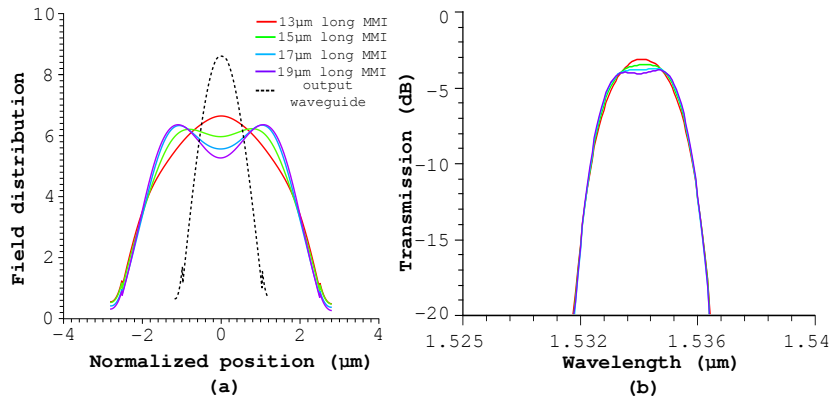


Figure 5.8: Simulated (a) field distribution at the end of the MMI for different lengths and (b) spectral response of the AWG using the corresponding MMI-apertures.

region in the spectral response depends on the width of the input field at the entrance of the first free propagation region from the MMI-aperture.

Also the number of waveguides in the dispersive array will strongly influence the transfer characteristics of the device. The required acceptance angle of the array is determined by the apertures used at the input and output planes of the star couplers. Hence, if we increase the number of waveguides in the array, we will also have to increase the focal length of the FPR. This in turn, for a given

shift in wavelength, will increase the lateral shift in the image plane. Also, the increase in number of waveguides itself will improve the image sharpness and the neighboring channel crosstalk will be lower. On the other hand as we discussed in chapter 4 a higher number of waveguides will introduce more phase errors, resulting in a larger overall crosstalk floor. A good compromise for the number of waveguides to keep both the steepness of the pass band and the crosstalk floor within limits is to use between 2.5 and 4 times the number of wavelength channels in one FSR. However, the passband aspect ratio [8] is largely independent of the number of waveguides, but almost fully determined by the overlap of the image with the output aperture mode. To map the influence of the number of waveguides, we designed AWGs with 44, 47, 50, 53 and 56 waveguides.

5.3.2 Results and Discussion

To characterize the device, grating couplers are integrated with the input and output channels of the AWGs. These have a coupling efficiency with standard single mode fiber of nearly 30% [9]. To eliminate the effect of the grating coupler from the AWGs spectral response we subtract the transmission of the AWG from the transmission of a reference waveguide having identical grating couplers. In this section first we separately describe the effect of the MMI length and the effect of the number of waveguides used in the waveguide array on the AWG spectral response. Next we discuss the characterization of the MMI-AWG optimized based on the previous results. Figure 5.9 shows an example of a fabricated MMI-AWGs.

5.3.2.1 Effect of MMI length

The simulated and experimental spectral response of MMI-AWGs with four different MMI lengths (13 μm , 15 μm , 17 μm and 19 μm) is shown in Fig. 5.10. The width of the MMIs was equal to 5 μm in each case. We observe that there is a significant qualitative correspondence: the 13 μm MMI results in a Gaussian-like response, 15 μm MMI results in a flattop response, 17 μm MMI results in a small dip and 19 μm MMI results in a large dip at the center of the response. The experimental results for the 17 μm and 19 μm MMI-AWG show a higher center dip than the simulated response, most probably to be explained by a small mismatch in MMI width, waveguide thickness or choice of refractive index used in the simulation. From these results we can conclude that a 15 μm long and 5 μm wide MMI is suitable for achieving a flat-spectral response.

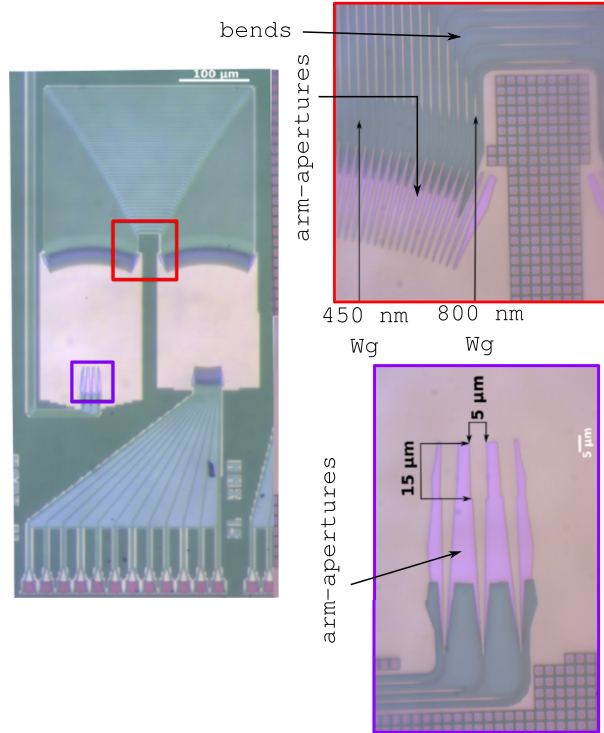


Figure 5.9: (a) Optical images of the fabricated 12×400 GHz MMI-AWG. (b) Optical images of the fabricated MMI aperture. (c) Optical images of the fabricated waveguide array.

5.3.2.2 Optimization of Waveguide Array

The most complex part of the AWG to optimize is the waveguide array. The optical path length difference between two successive waveguides of the array is constant over the array (see chapter 2) and depends on the design parameters (e.g. the desired free spectral range). A key variable is also the number of waveguides to be used in the array, which influences the steepness of the pass band and the crosstalk floor. As discussed above, a good compromise for the number of waveguides is to use between 2.5 and 4 times the number of wavelength channels in one FSR. To map the influence of the number of waveguides, we designed 12×400 GHz AWGs with 44, 47, 50, 53 and 56 waveguides in the array, whereby an MMI-aperture of $5 \mu\text{m}$ wide and $15 \mu\text{m}$ long was used as the input for the first star coupler. Figure 5.11 shows the simulated and experimental spectral response for these devices. Both in the simulated and the experimental results we observe that the pass band width increases as the number of wave-

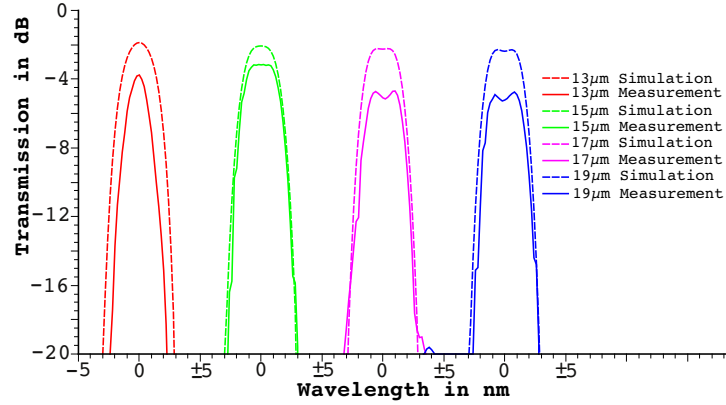


Figure 5.10: Simulated spectral response of 400 GHz AWG with variation of MMI lengths.

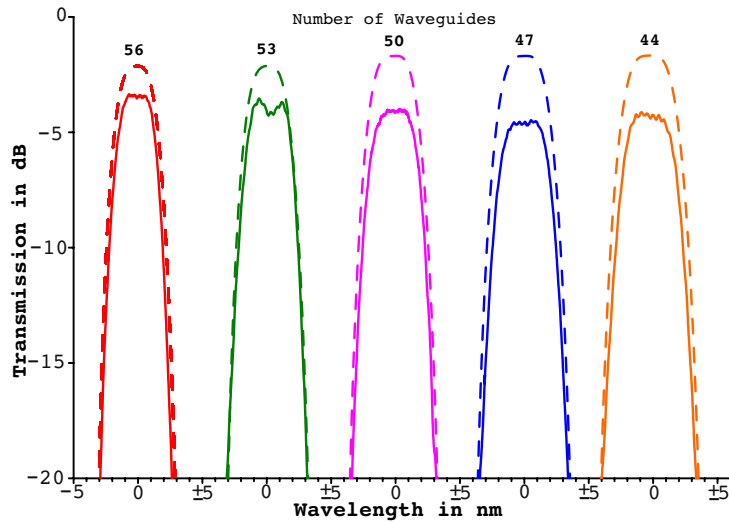


Figure 5.11: Simulation and experimental spectral response of the MMI-AWG with variation of the number of waveguides used in the waveguide array. Solid lines indicate the measurement results and dash lines indicate the simulation results.

guides decreases, but that the flatness of the response is not affected.

Bandwidth and Aspect Ratio The simulated and experimental 1 dB and 10 dB normalized passband widths of AWGs with increasing number of array waveguide are shown in Fig. 5.12(a). The 1 dB and 10 dB normalized passband

width decreases with an increasing number of waveguides in the array, both for conventional and for MMI-AWGs. For the MMI-AWG the experimental result matches the simulation results very well. In Fig. 5.12(b) we can see that the as-

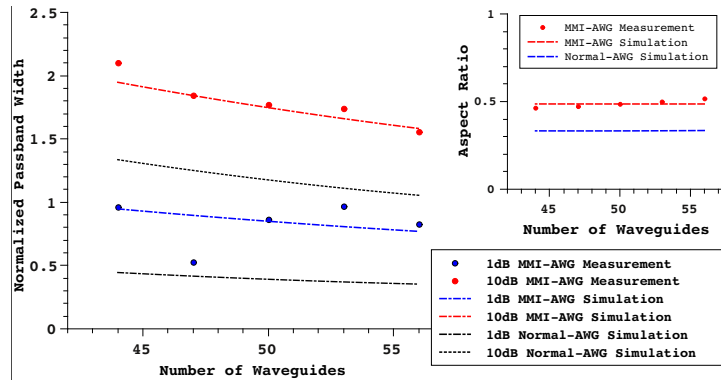


Figure 5.12: (a) Passband width (passband width is normalized to the channel spacing.) vs. number of waveguides used in the waveguide array of the MMI-AWG. (b) Comparison of the aspect ratio between conventional-AWG and MMI-AWG.

pect ratio of the conventional AWGs is much lower than that of the MMI-AWGs: simulated values for the aspect ratio of conventional AWGs and MMI-AWGs are 0.33 and 0.49 respectively. These values are nearly independent of the number of waveguides in the array.

Crosstalk The crosstalk is mainly dependent on the number of waveguides used in the waveguide array. From Fig. 5.12 (a) we can observe that with 44 waveguides in the array the 1 dB bandwidth is nearly equal to the channel spacing of the AWG (i.e. normalized passband width equal to one), implying that the neighboring channel crosstalk will be high. For a higher number of waveguides the neighboring channel crosstalk decreases. Figure 5.13 shows that the experimental neighboring channel crosstalk follows the same trend as the simulated results. As the number of waveguides increases the effect of phase errors also increase. The phase errors are mostly dependent on the side wall roughness and thickness variations of the waveguides in the waveguide array. In Fig. 5.13 we can observe that for lower numbers of waveguides in the AWG, the effect of phase errors decreases. For 56 waveguides the neighboring channel crosstalk and the crosstalk floor are at the same level. When further increasing the number of waveguides, the neighboring channel crosstalk will decrease below the crosstalk floor. In Fig. 5.13 we can also observe that the experimental phase errors do not match the simulated phase errors. The reason behind this dis-

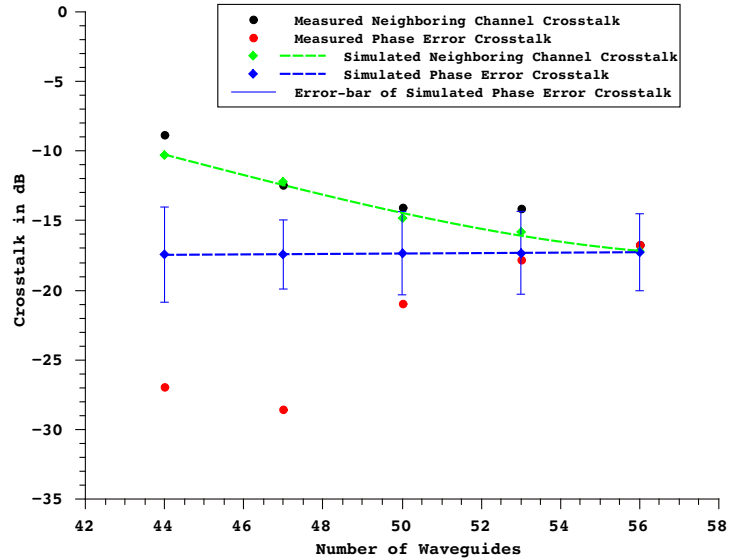


Figure 5.13: Crosstalk vs. number of waveguides used in the waveguide array of the MMI-AWG.

crepancy is in the phase error model, which is based on a one-dimensional approximation while in reality the thickness variation and the inclined sidewall of the waveguide have an important impact on the phase errors and the phase errors between waveguides might be correlated.

5.3.2.3 Optimized Spectral Response

From the previous results we can conclude that the 12×400 GHz MMI-AWG with 56 waveguides and a $15 \mu\text{m}$ long and $5 \mu\text{m}$ wide MMI as the input aperture presents a good compromise in achieving a flat response with minimal loss and good crosstalk level. Using our AWG model (see chapter 3) we simulate this device now in more detail. Figure 5.14 shows that the device is expected to exhibit a central channel loss of -2.07 dB, an insertion loss non-uniformity of 0.8 dB and a crosstalk level of -19.5 dB [7, 8], which is defined by the neighboring channels. Experimentally we find (Fig. 5.15) a central channel loss of -3.29 dB, an insertion loss non-uniformity of 1.55 dB and a crosstalk of -17.0 dB [7, 8], which is defined by the phase error level. In both simulation and experiment we see that not all channels have a perfect flat-top response, but are slightly asymmetric: the left side channels have left side increments and the right side channels have right side increments. This is an effect of imaging aberrations for the outer channels [10]. As expected the MMI-AWG also has a somewhat higher

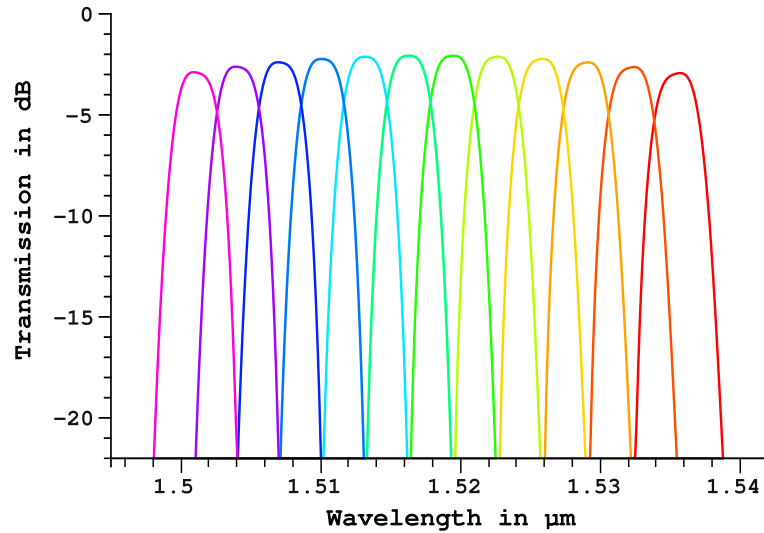


Figure 5.14: Simulation Result of 12×400 GHz MMI-AWG.

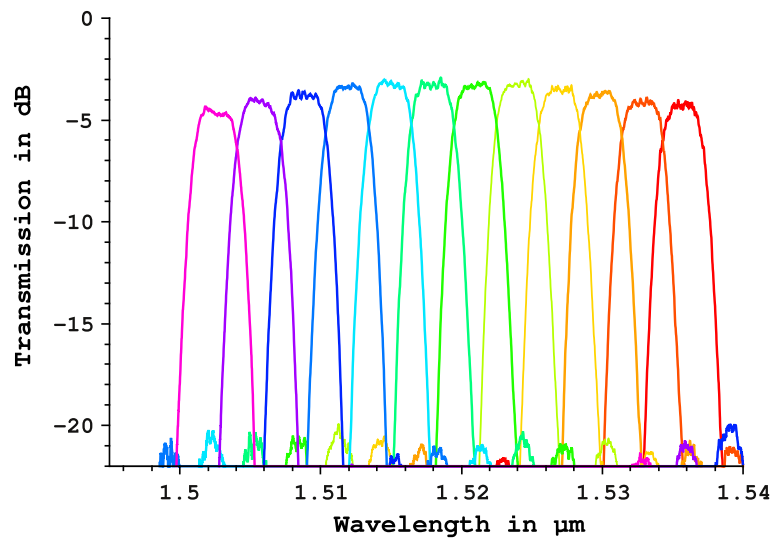


Figure 5.15: Measurement Result of 12×400 GHz MMI-AWG.

loss than a conventional AWG with the same design parameters because of the shape mismatch in the image plane of the AWG and the fact that the power in the image is now spread over a wider area to obtain a flat-top wavelength response. The difference in center channel loss between simulation and experimental result is due to the waveguide propagation loss, the slab propagation

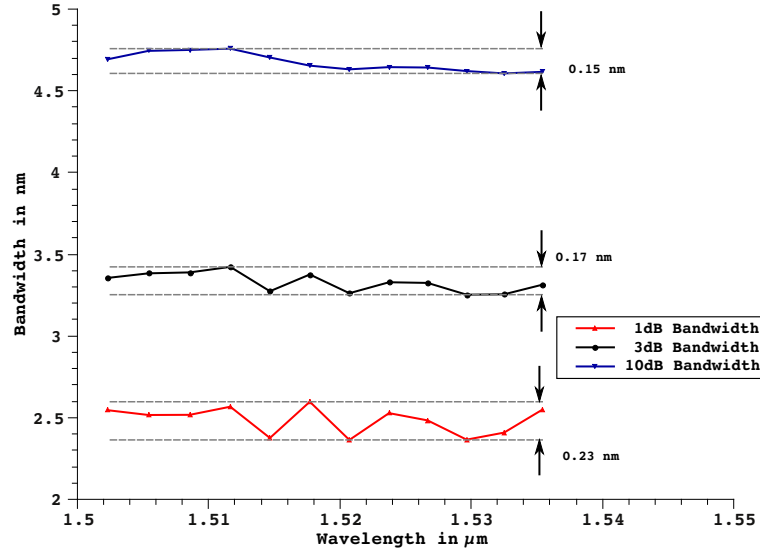


Figure 5.16: 1 dB, 3 dB and 10 dB bandwidth for 12×400 GHz MMI-AWG. Associated non-uniformity is indicated in the graph.

loss and the diffraction angle of the aperture mismatch between the designed and the fabricated AWGs. The dispersion mismatch and the aperture field profile mismatch between the designed and the fabricated waveguide is the reason behind the mismatch of insertion loss non-uniformity. One of the main concerns for this type of device is the non-uniformity of bandwidth and channel spacing over the different channels due to the dispersion mismatch between the designed and the fabricated waveguide.

We observe that for this device (shown in Fig. 5.16) the non-uniformity of the 1 dB, 3 dB and 10 dB bandwidths is 0.23 nm, 0.17 nm and 0.15 nm respectively. Figure 5.17 shows that the channel spacing decreases as the wavelength increases although the device was designed for a constant channel spacing of 400 GHz taking into account first-order dispersion. The deviation between experimental results and design value can be explained by the mismatch in the dispersion relation and waveguide thickness used in our model compared to the actually fabricated waveguide. The average channel spacing obtained from Fig. 5.17 is 391 GHz.

5.4 MZI as input aperture

The flattop spectral response obtained by using an MMI aperture as the input is inherently lossy due to the mode profile mismatch between the input MMI

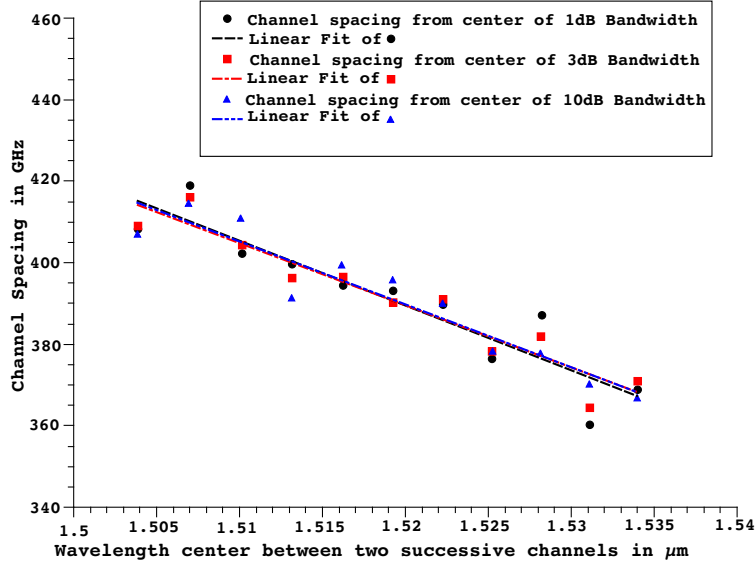


Figure 5.17: Channel spacing variation of the 12x400 GHz MMI-AWG.

aperture and output aperture. This situation can be improved by using a Mach-Zehnder Interferometer (MZI) as the input [3–5, 11]. With a MZI the input field at the object plane will be wavelength dependent and the field overlap with the output field at the image plane will be better. Figure 5.18 shows the schematic diagram of a silicon MZI-AWG.

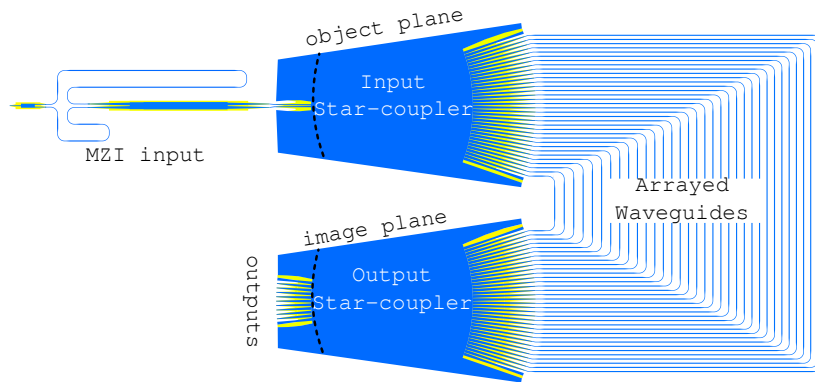


Figure 5.18: Schematic diagram of a silicon MZI-AWG.

5.4.1 Working Principle

The unbalanced MZI is connected to the AWG as shown in Fig. 5.18. The MZI and the AWG is designed such a way that for each wavelength channel the spot movement versus wavelength at the MZI-AWG interface is synchronized. The synchronization can be established by equating the FSR of the MZI and the channel spacing of the AWG and both the MZI and the AWG must have the same curvature. The spot movement versus wavelength is further illustrated in Fig. 5.19. For the wavelength λ_0 there is a no clear 'spot' at the interface of the MZI-AWG. Therefore one can consider the 'center of mass' of the optical power distribution of the MZI is moving continuously between the two states with wavelength variation. This will be imaged by the AWG at the output waveguide and the synchronization with the MZI will make the center of mass of the image stationary at the output waveguides of the AWG, which will create the flattop passband. The synchronization between the MZI and the AWG can be further

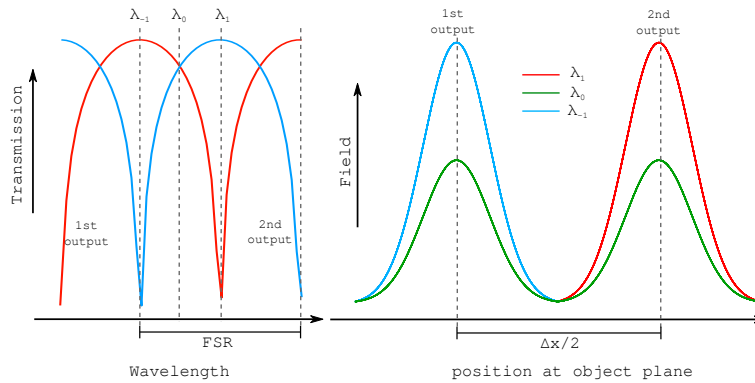


Figure 5.19: Transmission and Field distribution of the MZI.

illustrated from the spectrum overlap as shown in Fig. 5.22, which shows a simulated spectral response of an 9×400 GHz MZI-AWG (we will discuss about the simulation method in the next section). The flattop spectral response also depends on the individual passband shape of the AWG.

5.4.2 Design

The MZI used consists of two MMIs and two delay lines. The first MMI (further referred to as the splitter MMI) splits the light equally into the two delay lines and after propagating through these delay lines the light will be combined into the second MMI (further refer to as the combiner MMI). The delay length is calculated from the FSR in a similar way as for the AWG (see chapter 2). We can connect the MZI and the AWG in two different ways as shown in Fig. 5.20. The

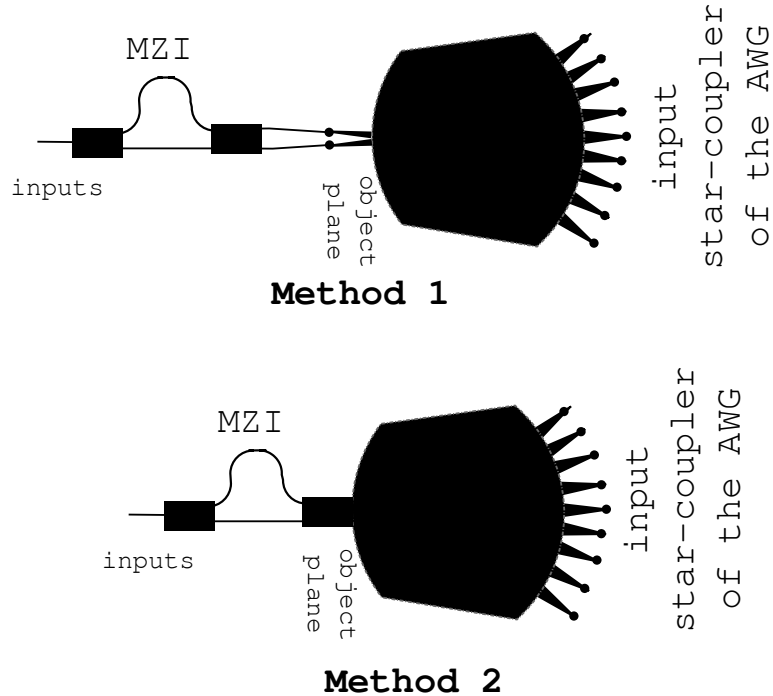


Figure 5.20: Design methods of the MZI-AWG.

first method is to connect a 1×2 MZI to the two inputs of the AWG [3–5]. Let's consider the lateral dispersion per channel spacing of the AWG is Δx . Therefore the lateral displacement of these two input apertures of the AWG should be $\Delta x/2$. If Δx is equal to the sum of the output aperture widths and the gap between the apertures (limited by the fabrication) the input apertures will physically overlap with each other. This can be solved either by reducing the width of the input apertures or by increasing the lateral dispersion of the AWG. The mismatch between the input and output apertures will increase the insertion loss of the device. On the other hand a large lateral dispersion will affect the flatness of the spectral response.

As shown in Fig. 5.20 in a second method the combiner MMI is directly used as the input aperture of the AWG [11]. The length and width of the combiner MMI are adjusted in such a way that the separation between the two constructive interference images at the interface of the combiner MMI and the input star-coupler becomes $\Delta x/2$. Although it is not very straight forward to design the combiner MMI but the design is not limited by the input aperture spacing (which is determined by the fabrication process) and also have a smaller footprint.

5.4.3 Simulation

To simulate the MZI-AWG we can use the same T-matrix approach which we already described in chapter 3. Let's consider that the number of outputs of the MZI-AWG is N then the T-matrix of the AWG will be $T_{\text{awg}}_{2 \times N}$ and of the MZI will be $T_{\text{mzi}}_{1 \times 2}$ as shown in Fig. 5.21. Matrix multiplication of these two

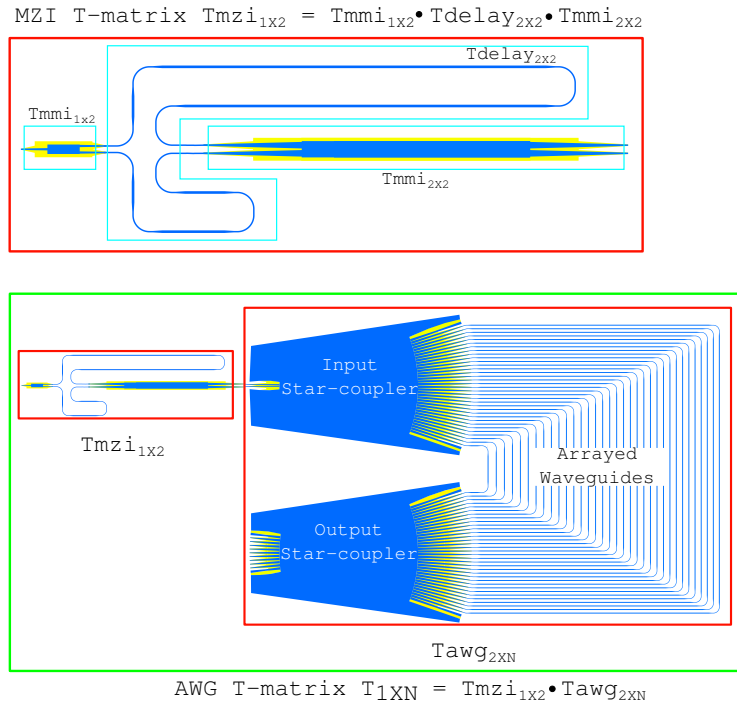


Figure 5.21: T-matrix simulation approach for the MZI-AWG.

T-matrices will give the transmission of the whole MZI-AWG. The T-matrix of the MZI can further be broken into three parts: splitter MMI ($T_{\text{mmi}}_{1 \times 2}$), delay lengths ($T_{\text{delay}}_{2 \times 2}$) and combiner MMI ($T_{\text{mmi}}_{2 \times 2}$). As shown in Fig. 5.21 the matrix multiplication of these three T-matrices will give the transmission of the MZI. With our simulator we simulate a 9×400 GHz silicon MZI-AWG. The FSR of the MZI which equals the channel spacing of the AWG is 400 GHz. The output aperture width is $2 \mu\text{m}$ while the input aperture is chosen to be $0.9 \mu\text{m}$. The AWG has 29 waveguides in the array. The spectral response of the MZI-AWG (shown in Fig. 5.22) is the resultant of the spectral response of the MZI and the spectral responses of the AWG for individually active inputs. The shape of the spectral response of the MZI-AWG is very much controlled by the shape of these individual spectral responses of the AWG. As the shapes of the spectrum produced

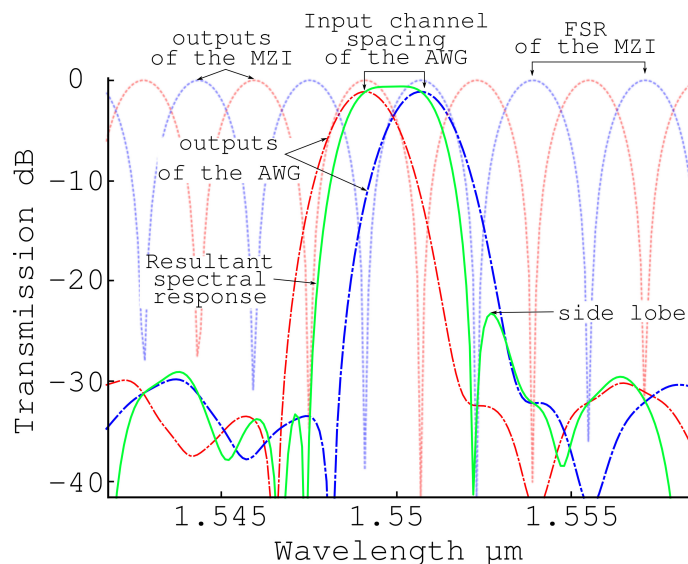


Figure 5.22: Simulated spectral response of the central output channel of 9×400 GHz silicon MZI-AWG.

by the MZI and the AWG are different from each other, the spectral response of the MZI-AWG will contain some side lobe as shown in Fig 5.22. These side lobes can be removed by decreasing the bandwidth of the AWGs wavelength channel. The bandwidth of the AWG can be reduced by increasing the number of waveguides used in the array as shown in Fig. 5.23. When we increase the number of waveguides from 29 to 34 the bandwidth of the individual spectral response of the AWG decreases, resulting in a reduction of the side lobes but also in the appearance of a central dip in the spectral response. Fig. 5.24 shows the spectral response of the 9×400 GHz silicon MZI-AWG. To achieve perfect flatness and low crosstalk the spectral responses of the AWG and the MZI should be perfectly aligned in the wavelength domain which is difficult to obtain if we move away from the central order. Therefore as we can see from Fig. 5.24 the central channels are flat where the side channels are distorted towards one side. This situation will become worse in real life devices as the mismatch will be higher due to fabrication imperfections.

5.5 Cascaded AWGs

The flattop spectral response obtained by using an MMI-AWG or an MZI-AWG depends a lot on the fabrication process. The two biggest problems in the SOI fabrication process are line width variations and wafer thickness variations. In

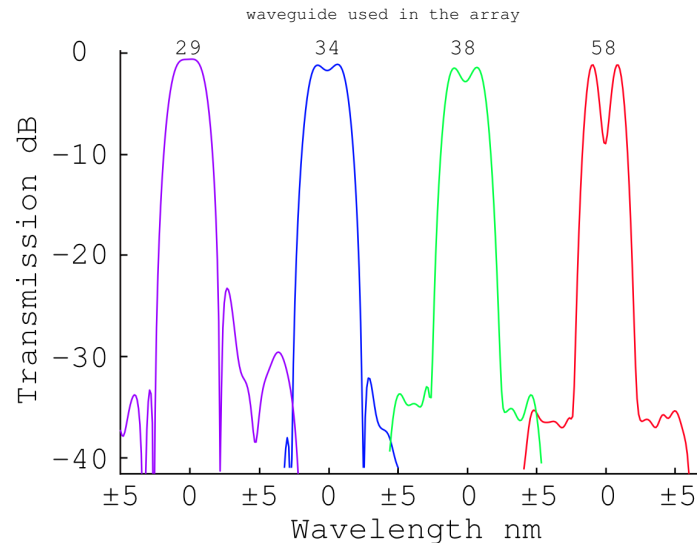


Figure 5.23: Simulated spectral responses of the central output channel of 9×400 GHz silicon MZI-AWG with (a) 29 (b) 34 (c) 38 and (d) 58 waveguides in the array.

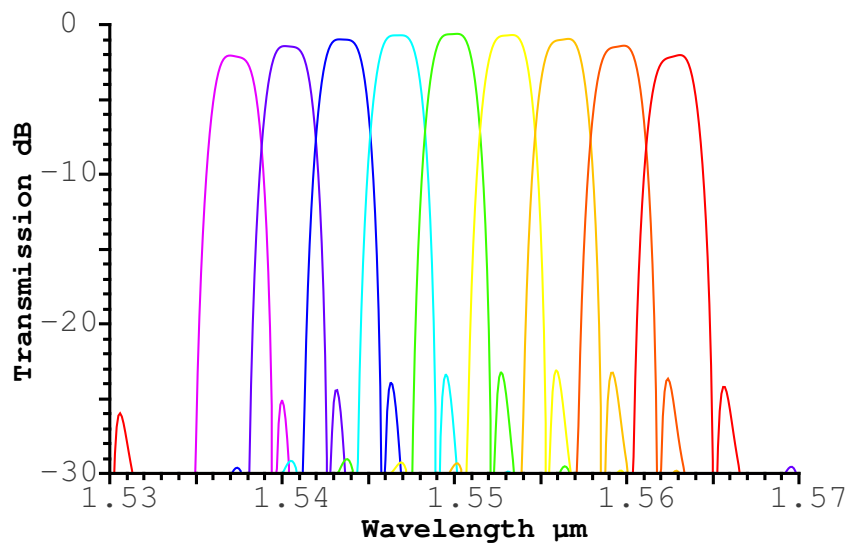


Figure 5.24: Simulated spectral responses of 9×400 GHz silicon MZI-AWG.

general these variations are random in nature and very difficult to predict and to include in device simulations. This fabrication dependency leads to an uncer-

tainty in achieving a flattop spectral response. However solutions which nullify this uncertainty do exist. One solution could be the cascading of two AWGs. Since both AWGs will be fabricated close to each other, both will experience similar kinds of fabrication conditions [6]. A major drawback of using this approach is that since both AWGs contribute to the loss, the insertion loss of the overall device will be higher.

5.5.1 Design and working Principle

An AWG works both as a multiplexer and demultiplexer. As shown in Fig. 5.25(a) when the two identical AWGs are connected the demultiplexed wavelengths of the first AWG are combined back to a single waveguide by the second AWG. Now

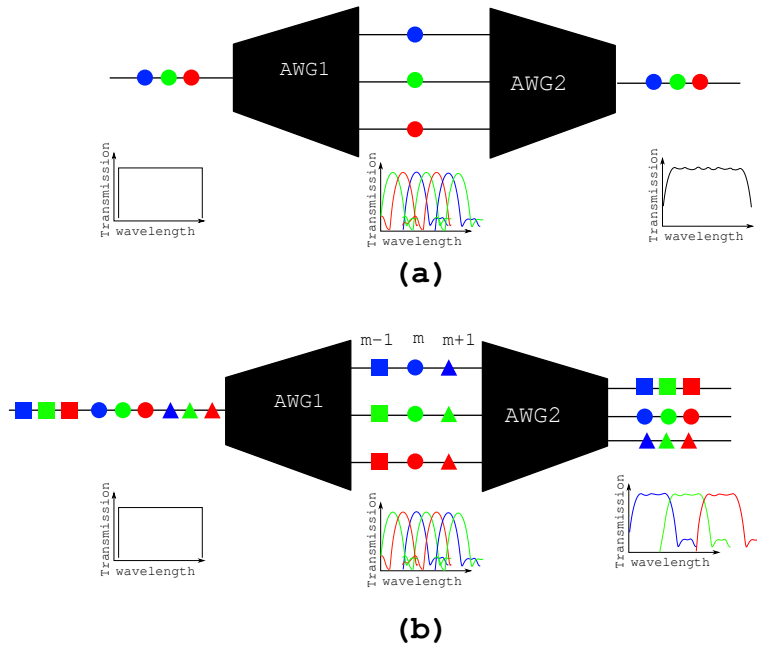


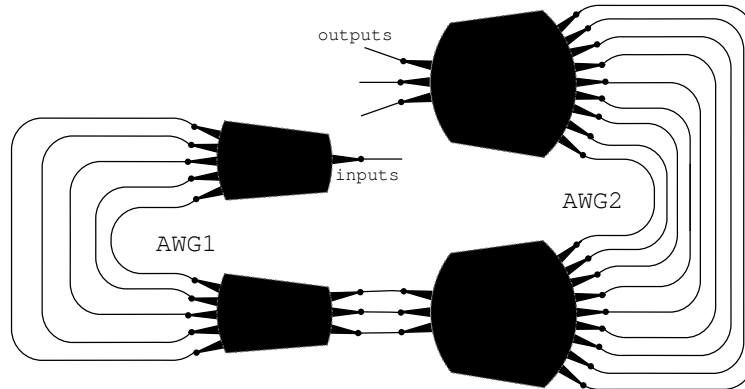
Figure 5.25: Working principle of cascaded AWG (a) $AWG1 = AWG2$ (b) FSR of $AWG1 =$ channel spacing of $AWG2$.

if we makes the FSR of the first AWG equal to the channel spacing of the second AWG, only the wavelengths within one FSR of the first AWG will be combined to one output waveguide of the second AWG as shown in Fig. 5.25 (b). The wavelengths of the order m of the first AWG combine to the centre output of the second AWG and for adjacent orders $m-1$ and $m+1$ the wavelengths are combined to the adjacent outputs of the second AWG. In order to achieve this functionality another criteria is that the input star-coupler of the second AWG needs to

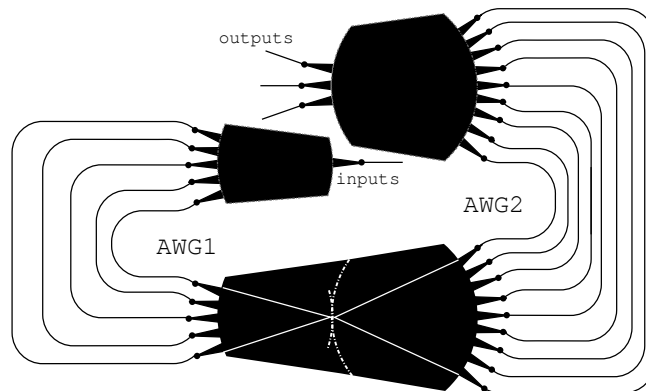
have the same channel spacing as the first AWG. This can be implemented in two ways (shown in Fig. 5.26): In the first method the first AWG is connected to the second AWG using equal length waveguides. In the second method the same slab is used for the output star-coupler of the first AWG and the input star-coupler of the second AWG.

Both methods have some limitations related to the high contrast silicon platform. As the side channels of an AWG will experience 3 dB extra loss compared to the center channel and the resultant shape is the combine effect of all the output channels of the first AWG, the flatness of the resultant spectral response will be improved as we increase the number of output channels of the first AWG. But for SOI a small channel spacing AWG is difficult to fabricate as the phase error will increase the device crosstalk significantly. Up to now we have been able to demonstrate minimum 100 GHz channel spaced AWGs. This is imposing a restriction on the design i.e. for a 400 GHz flattop AWG we can have the first AWG with maximum 4 outputs. To keep the loss minimal we use the same input and output star couplers but for second AWG as the input star-coupler channel spacing is lower than the output star-coupler, the input star-coupler will be different from the output star-coupler to avoid physical overlap. This problem will not arise for the second method. But the non-uniformity loss of the side channel will be higher in the combined star-coupler method which will disturb the flatness of the resultant spectral response.

The performance of the device using the common star-coupler method will be very much dependent on this common star-coupler. For the central wavelength the light coming from the first AWG will merge at a point along the center axis of the star-coupler with the focal point of the input star-coupler of the second AWG and maximum power will transfer from the first AWG to the second AWG. This situation is shown in Fig. 5.27 (a). For other wavelengths the light will experience a high loss depending on the gap between the image plane of the first AWG and the object plane of the second AWG. As a result spectral response will be distorted and no longer have a flattop. This situation can be improved by introducing a field lens [12] between the image plane of the first AWG and the object plane of the second AWG as shown in Fig. 5.27 (b). A in-plane field lens can be achieved by shallowly etching the lensing area. The propagation direction of the light coming out from the output star-coupler of the first AWG will be directed by the lens to cover all the waveguides in the second AWG. This will minimize the loss of the side wavelengths, which will improve the flatness of the resultant spectral response. The flatness will be improved further by decreasing the lateral dispersion of the output star-coupler of the first AWG.



Method 1: waveguide connection



Method 2: star-coupler connection

Figure 5.26: Two methods of cascading AWGs.

5.5.2 Simulation

We simulate a 7×400 GHz cascaded AWG using method 1 illustrated in Fig. 5.26. As we described earlier, the shape of the spectral response depends on the number of output channels of the first AWG, which in turn depends on the channel spacing of the first AWG. Let's consider three different designs for the first AWGs while the second AWG remains 7×400 GHz: 2×200 GHz, 3×133 GHz and 4×100 GHz AWGs. Let's first look at the device where 2×200 GHz AWG is connected to the two inputs of the 7×400 GHz AWG. The spectral response of the device is shown in Fig. 5.28 (a). This device is similar to the MZI-AWG with only one dif-

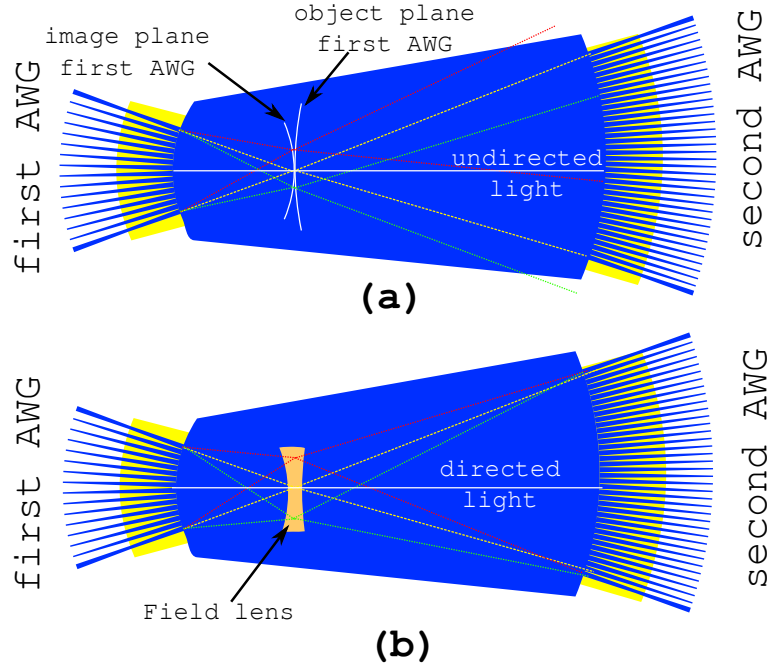


Figure 5.27: (a) The image plane of first AWG and the object plane of the second AWG overlap at one point. (b) The image plane of first AWG and the object plane of the second AWG overlap by using a field lens.

ference: the bandwidth of the first AWG is controllable irrespective of its channel spacing while for an MZI it is difficult to change the bandwidth. Therefore the cascaded AWG will not suffer from the side lobes.

As we keep the channel spacing of the final spectral response constant and increase the number of outputs of the first AWG from two to three, the channel spacing will become 133 GHz. The spectral response of the device is shown in Fig. 5.28 (b). Among these three output channels of the first AWG the central output channel will have higher power compared to the side two channels which creates an increment in the central part of the resultant spectral response. This situation can be improved as we increase the number of output channels of the first AWG to four. As we can see from Fig. 5.28 (c) the flatness of the spectral response has improved but is still not completely flat. The reason is that the center two channels of the first AWG have more power than the side two channels, which reduces the flatness. The flatness can be improved with a cost of half bandwidth as we connect only the center two output channels of the first AWG to the second AWG. The spectral response for this case is shown in Fig. 5.28 (d). Although the flatness get disturb due to the increment number of output

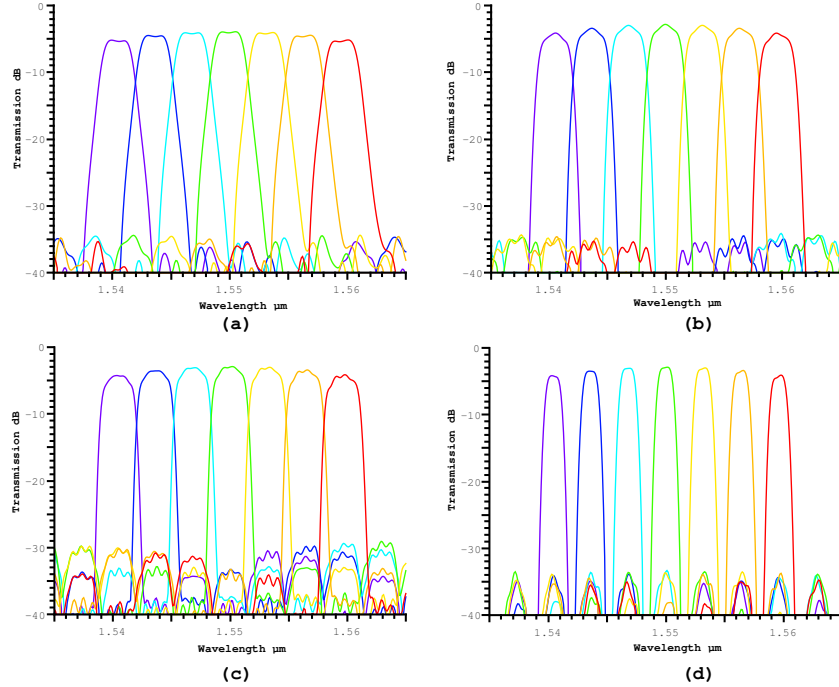


Figure 5.28: Simulation result of 7×400 GHz cascade AWG with a combination of (a) 2×200 GHz AWG, (b) 3×133 GHz, (c) 4×100 GHz (d) 2×100 GHz and 7×400 GHz.

waveguide of the first AWG the roll-off (aspect ratio) improves significantly.

5.5.3 Experiment

As a demonstration we designed a 7×400 GHz cascaded AWG using the common star-coupler method. The common star-coupler of the first and second AWG is designed with a center point overlap. The spectral response of the 7×400 GHz cascade AWG is shown in Fig. 5.29. The shape of the wavelength channel is well predicted as per the discussion in section 5.5.1. The insertion loss of the device is -6.4 dB and the crosstalk is -20 dB. The device size is $1050 \times 430 \mu\text{m}^2$. This first generation of the cascaded AWG needs further optimization to achieve a low loss flattop AWG.

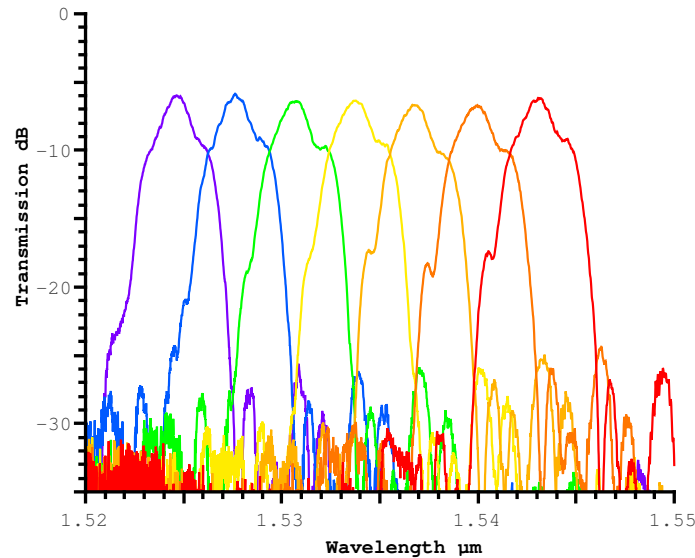


Figure 5.29: Experimental result of 7×400 GHz cascade AWG.

5.6 Conclusions

We discussed three different methods to obtain a flattop spectral response. Experimentally a compact 12-channel flat-top MMI-AWG on silicon-on-insulator (SOI) was presented. The device size is $560 \times 350 \mu\text{m}^2$. The experimental results match well with the simulation results. The effect of the MMI length on the spectral response of the AWG is demonstrated in detail both through simulation and by experimental results. The aspect ratio of the channel response of the MMI-AWGs is considerably improved compared to that of a conventional AWG. The neighboring channel crosstalk depends on the number of waveguides and also matches well with the simulation. For MZI-AWGs and cascaded AWGs we proposed a design for the silicon platform. These designs show promising results in simulations and need to be demonstrated experimentally. These methods are also applicable for the echelle gratings to get flattop spectral response.

References

- [1] J. B. D. Soole, M.R. Amersfoort, H.P. LeBlanc, N. C. Andreadakis, A. Rajhel, C. Caneau, R. Bhat, M.A. Koza, C. Youtsey, and I. Adesida. *Use of multimode interference couplers to broaden the passband of wavelength-dispersive integrated WDM filters*. Photonics Technology Letters, IEEE, 8(10):1340–1342, Oct 1996.
- [2] D. Dai, W. Mei, and S. He. *Using a tapered MMI to flatten the passband of an AWG*. Optics Communications, 219(16):233–239, 2003.
- [3] T. Shibata, S. Kamei, T. Kitoh, T. Tanaka, and M. Kohtoku. *Compact and low insertion loss (1.0 dB) Mach-Zehnder interferometer-synchronized arrayed-waveguide grating multiplexer with flat-top frequency response*. Opt. Express, 16(21):16546–16551, Oct 2008.
- [4] S. Kamei, T. Kitoh, T. Goh, A. Mori, and H. Takahashi. *Low-loss, wide and low-ripple passband arrayed-waveguide grating with tandem MZI-synchronized configuration*. In 35th European Conference on Optical Communication, volume 2009, pages 1–2. IEEE, 2009.
- [5] C.R. Doerr, L.W. Stulz, R. Pafchek, and S. Shunk. *Compact and low-loss manner of waveguide grating router passband flattening and demonstration in a 64-channel blocker/multiplexer*. IEEE Photonics Technology Letters, 14(1):56–58, 2002.
- [6] G.H.B. Thompson, R. Epworth, C. Rogers, S. Day, and S. Ojha. *An Original Low-Loss and Pass-Band Flattened SiO₂ on Si Planar Wavelength Demultiplexer*. In Optical Fiber Communication Conference and Exhibit, pages 76–77, 1998.
- [7] S. Pathak, E. Lambert, P. Dumon, D. Van Thourhout, and W. Bogaerts. *Compact SOI-based AWG with flattened spectral response using a MMI*. In 8th IEEE International Conference Group IV Photonics, pages 45–47, 2011.
- [8] S. Pathak, M. Vanslambrouck, P. Dumon, D. Van Thourhout, and W. Bogaerts. *Optimized Silicon AWG With Flattened Spectral Response Using an MMI Aperture*. Lightwave Technology, Journal of, 31(1):87–93, Jan 2013.
- [9] F. Van Laere, T. Claes, J. Schrauwen, W. Scheerlinck, S. and Bogaerts, D. Tailaert, L. O’Faolain, D. Van Thourhout, and R. Baets. *Compact focusing grating couplers for silicon-on-insulator integrated circuits*. IEEE Photonics Technology Letters, 19(23):1919–1921, 2007.
- [10] A. Klekamp and R. Munzner. *Calculation of imaging errors of AWG*. Lightwave Technology, Journal of, 21(9):1978–1986, Sept 2003.

-
- [11] H. F. Bulthuis. *Passband flattening of a phasar*. US Patent 6,289,147, 2001.
 - [12] K. Van Acoleyen and R. Baets. *Compact lens-assisted focusing tapers fabricated on silicon-on-insulator*. In Group IV Photonics (GFP), 2011 8th IEEE International Conference on, pages 157–159, Sept 2011.

6

Electro-optic and thermal tuning

"Before the effect one believes in different causes than one does after the effect."

– Friedrich Nietzsche

6.1 Introduction

In previous chapters we have focused on the design, simulation and measurement of AWGs as pure passive components i.e. the variation in the effective index of the waveguide is only as determined by the waveguide geometry. Since we already discussed that mismatch between fabrication and design can introduce extra errors, it would be useful to have some post fabrication control over the effective index. One obvious way of changing the effective index of a mode traveling inside a waveguide is by changing the temperature which results in a shift of the refractive index of the material. This can be done by fabricating a heater using metal lines on top of a waveguide. Alternatively, electro-optic modulators can also change the phase of the light. These modulators are fabricated by doping the semiconductor material. These active components allow us to expand the applications of AWGs and also improve their performance. In this chapter we will first demonstrate optical switching using modulators and AWGs, and second we will tune an AWG using heaters to improve its performance.

6.2 Optical packet switch

Power and cost inefficient electrical switching is one of the biggest limitations in optical communication networks. A possible solution is Optical Packet Switching (OPS) which has the potential of a fast reconfiguration time and a broad optical bandwidth. Various types of integrated switch designs have been demonstrated on various material systems based on different schemes: The broadcast and select scheme [1, 2], the cascaded arrangements schemes [3, 4] and single stage modulation scheme [5–8]. Under the first two switching schemes, excellent switching properties such as fast response time, large extinction ratio, and low loss are demonstrated. But using these two methods, it is difficult to realize large channel count integrated switches as the optical loss and the crosstalk increase rapidly with increasing channel count. Optical switching with a single stage modulation scheme is most likely the best choice for a large channel integrated switch [6]. This scheme typically has lower loss, lower power consumption and smaller footprint with increasing channel count compared to the other two methods [6].

6.2.1 Design

One method of designing a single modulation stage optical switch [6] is using an AWG as shown in Fig. 6.1. An array of equal-length waveguides is used to create a zero-order grating. To achieve switching the waveguides include phase modulators. The total device size and loss are largely dominated by the phase

modulators.

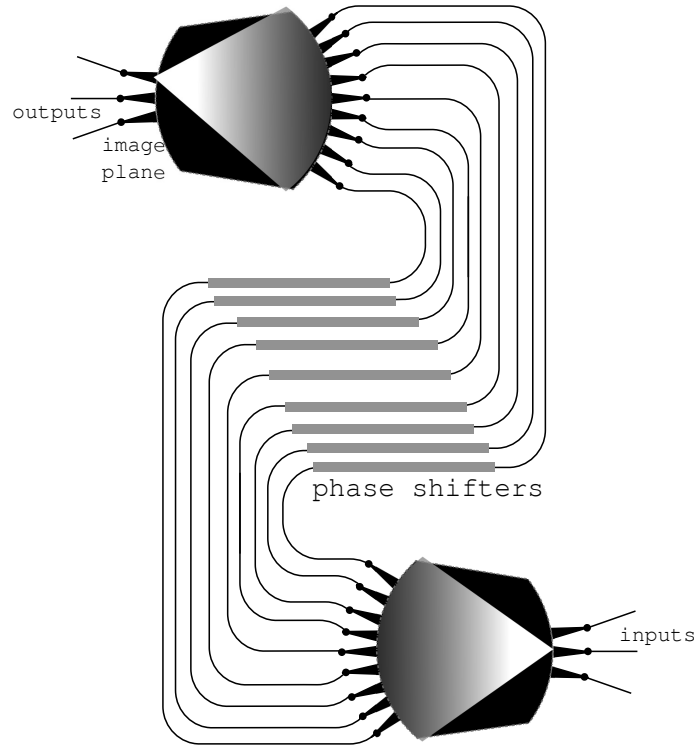


Figure 6.1: Schematic diagram of an optical phase switch based on single stage modulation.

6.2.1.1 Carrier-depletion based silicon modulators

The requirements for the phase modulator in the optical switch are a phase modulation from 0 to 2π , low optical loss and high operation speed. In silicon the carrier-depletion based modulator is the most used solution due to its CMOS compatibility, fabrication simplicity, and high speed modulation [9]. The waveguide contains a pn -junction, allowing to modulate the refractive index by applying a voltage. The performance of a typical phase shifter is defined by its modulation efficiency $V_\pi L_\pi$, the propagation loss, and the capacitance and the series resistance of the diode. The $V_\pi L_\pi$ is the required length of modulator to get a π phase change for unit voltage change. This modulation efficiency of a pn doped phase shifter is determined by the overlap of the optical mode with the space-charge region of the diode. The speed of the modulator depends on the depletion capacitance of the diode. The propagation loss is determined by

the overlap between free carriers and the optical mode. Therefore, the doping pattern and concentration are the critical parameters for a modulator in order to achieve optimized performance.

We had a choice between two types of carrier-depletion based modulators: lateral and interdigitated diode on a 500 nm wide shallowly etched waveguide. The lateral diode has p -type and n -type sections on the sides of the waveguide while the interdigitated diode consists of alternative sections of opposite polarities along the light propagation direction as shown in Fig. 6.2. Based on the comparison between these two diodes which is described by Hui Yu et al. [10] the interdigitated diode was selected. The modulation efficiency of the diode

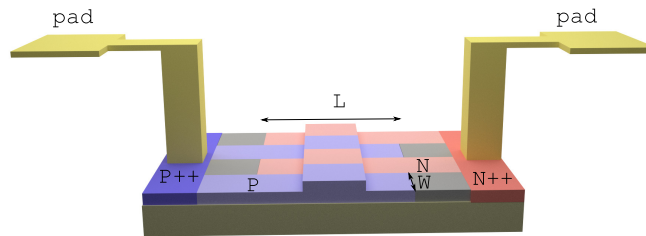


Figure 6.2: Schematic diagram of a interdigitated diode.

depends on the width W of interdigitated implantation windows and the overlap length L between two adjacent windows as show in Fig. 6.2. An optimal performance is achieved with an overlap length L of $1.6 \mu\text{m}$ and a width of 300 nm , with a doping concentration of $2 \times 10^{18} \text{ cm}^{-3}$

The diode reaches its breakdown at -9 volt reverse bias. Therefore we need to choose the modulator length in such a way that we get at least 2π phase change within the voltage limit and low optical loss. Taking into account the fabrication imperfection we used 3.2 mm long modulators. The estimated insertion loss of the modulator is -6 dB.

6.2.1.2 Phased array

A zeroth order AWG requires a S-shaped waveguide array design. As shown in Fig. 6.1 the center sections of the S-shaped waveguides are replaced by equal length modulators. Other than the modulators the waveguides are made out of 450 nm and 800 nm wide waveguides. The optical path length between the waveguides is balanced individually for the 450 nm and 800 nm wide waveguides.

We designed a 1×4 silicon optical switch with 12 carrier-depletion based silicon modulators in the array. We used two dummy output channels. $2 \mu\text{m}$ wide apertures are used at the interface between the star-coupler and the waveguide

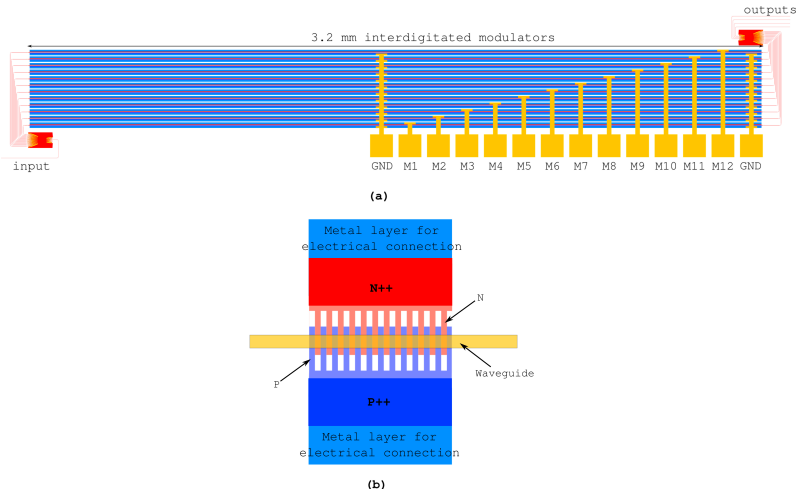


Figure 6.3: (a) Mask layout of the 1×4 silicon optical switch with 12 carrier-depletion based silicon modulators in the array (b) Enlarge portion of an interdigitated diode.

array. Following the AWG theory discussed in chapter 2 we need many waveguides in the array in order to get a sharp image at the output. But in this case we are limited by the measurement capability of our Lab. We can drive up to 16 modulators with a constant voltage (details of measurement setup in Section 6.2.3). We used only 12 modulators, which will increase the neighbor channel crosstalk. The high neighbor channel crosstalk translates in smaller extinction in the switch. One can increase the extinction by using more modulators in the array.

6.2.2 Simulation

In chapter 3 we discussed the simulation of an AWG. To adopt this simulation for modulator based AWGs, we added a variable phase for modulators in the transmission equation of the waveguide (described in section 2.3.2 waveguide array model) to the phase term used for the waveguide length. As all the waveguides are equally long the spectral response will be almost wavelength independent. To find the transmission variation with respect to the phase introduced by the modulators we run a loop of simulations while the phase is varying from -2π to 2π .

Figure 6.4 shows the simulation result of the 1×4 switch when the wavelength is fixed to $1.55 \mu\text{m}$. In the simulation we consider only the waveguide loss. The simulation shows four operation states where one channel get maxi-

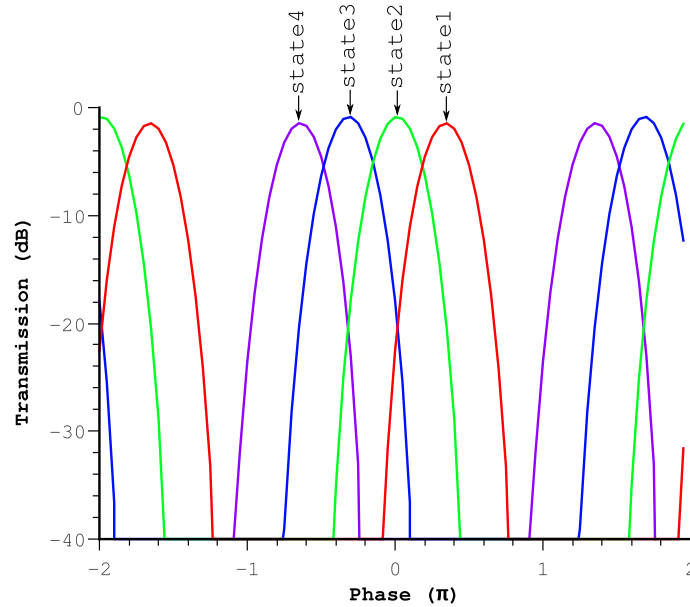


Figure 6.4: Simulation of the 1×4 switch with 12 modulators in the array.

imum power while the other three get minimum power. The difference between this power is noted as extinction of the switch. The simulation shows that for state 2 and 3 the corresponding channel experiences -0.9 dB loss and for the other two states (state 1 and 4) the loss increases to -1.5 dB. The reason behind this non-uniformity is the same as for the AWG as discussed in chapter 2. The simulated extinction of the device is -18 dB. In the simulation we didn't take into account the unwanted amplitude modulation of the real life phase modulators.

6.2.3 Experiment

To characterize this device we used our traditional fiber grating coupler method to couple the light in and out. An array of 20 probes with $125 \mu\text{m}$ spacing is used to drive the 12 modulators. As shown in Fig. 6.3 the first and last pads are used for common grounds. These probes are driven by a NI-PXI analog output card which is connected to a PXI chassis. The analog output card contains 16 voltage and 16 current sources which have a limitation of $\pm 10 \text{ V}$ and up-to 20 mA.

6.2.3.1 Modulator characteristic

The modulators are characterized by driving them individually when the input and output fiber is fixed. The optical power will be influenced with a variation

of the phase induced by the modulator. The intensity of these power variations is dependent on the amount of power propagating through the corresponding modulator. As the far field of a Gaussian like mode-profile is again Gaussian-like, the star-coupler will distribute the light among the modulators in such a way that the center modulators will receive more power than the side modulators. Therefore the central modulator will have more influence on the output optical power.

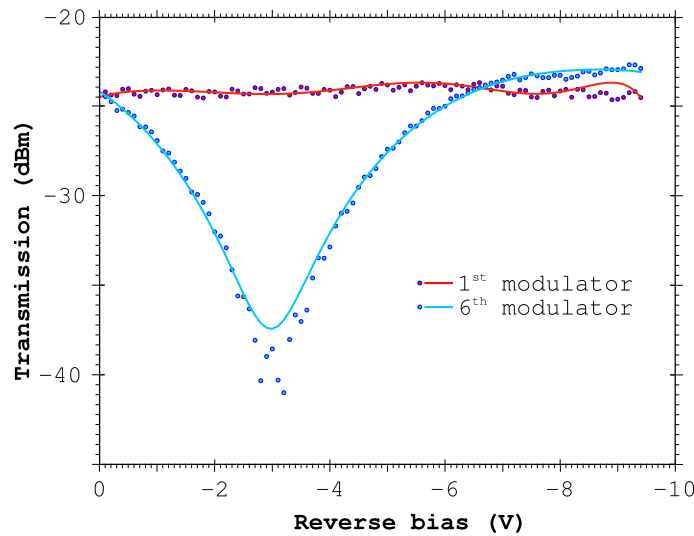


Figure 6.5: Optical power variation with (a) 1st and (b) 6th modulators are driven individually when all other modulators are inactive. Dots are indicating the measurement points where the solid lines are generated by the curve fitting.

Fig. 6.5 shows that indeed the voltage changes on the 6th modulator have more impact than those on the 1st modulator. From the output optical power variation with respect to the reverse bias voltage for the 6th modulator we can conclude that the 3.2 mm long modulator is capable of producing a 2π phase shift. Due to fabrication imperfection all modulators in the switch will be slightly different from each other.

6.2.3.2 Switch

The switching states of a switch can be measured by using two methods: by calibrating all the modulators and by optimizing every modulators for each switch state. But an accurate calibration of the modulator is not possible as the phase change with reverse bias is not linear. The calibration will be more inaccurate

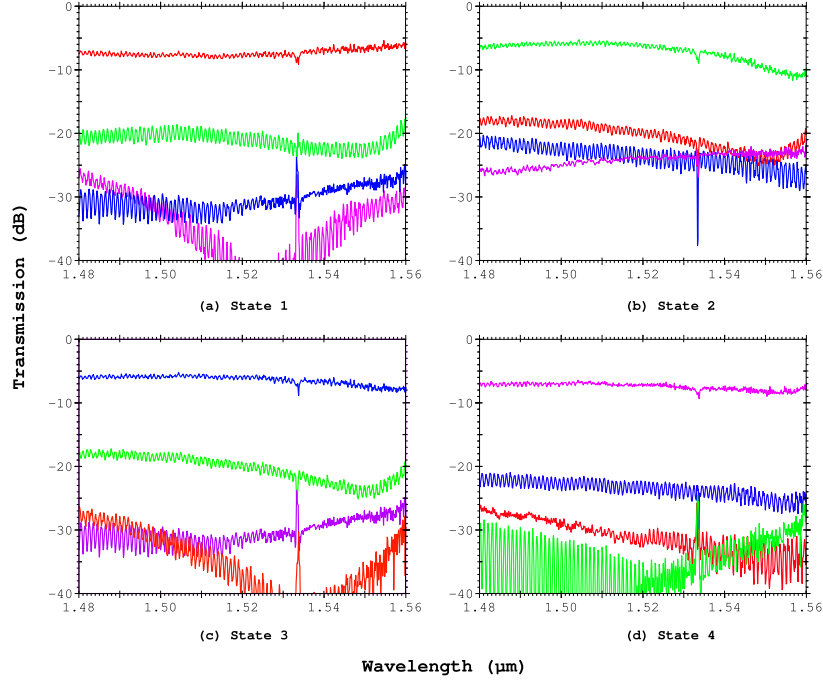


Figure 6.6: Measured spectra of the 1×4 switch for (a) switching state 1 (b) switching state 2, (c) switching state 3 and (d) switching state 4.

for the outer arms as its contain lower optical power. The second method is much more accurate as the every modulators are optimized to determine the switching states.

Figure 6.6 shows the four switching states of the 1×4 switch as determined using the second method. The detailed performance of this switch for the wavelength $1.52 \mu\text{m}$ is given in Table 6.1

Switching states	Channel Loss (dB)	Extinction (dB)
1	-7.7	13
2	- 6.2	13.5
3	-6.0	13.6
4	- 7.2	16

Table 6.1: Performance of 1×4 switch at $1.52 \mu\text{m}$ wavelength.

The measurement results show a good agreement with simulations. The loss in the switch is introduced by the modulators and the extinction is limited by the number of modulators used in the array. Typically a fraction of light will be

reflected from the junction between the doped and undoped waveguide. This reflection causes a fluctuation in the spectral response which become the dominant effect when the channel received minimal power. This interface can be optimized for lower reflection. Further, from Fig. 6.5 we see that to obtain a phase change of 2π , the modulators have to be driven very close to their breakdown. Also this might cause additional reflections.

The switching speed depends on the modulation speed of the diode. This interdigitated diode has been shown to supports 10 Gbit/s modulation. A high speed low loss modulator will increase the performance of the switch.

6.3 Active tuning of AWG

The performance of an AWG is very much dependent on its fabrication. A very small phase change in the device results in a large crosstalk. This fabrication dependent phase error can be improved by using active tuning. An option for lossless tuning is using heaters on top of waveguides. But tuning with heaters suffers from other disadvantages like thermal crosstalk and efficiency of the heaters is depended on surrounding temperatures and applied power.

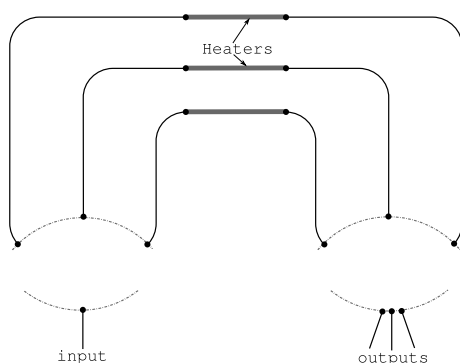


Figure 6.7: Schematic diagram of an AWG with heaters to tune the performance.

Figure 6.7 shows the schematic diagram of an AWG which has an array of equal length heaters on top of the waveguide array.

6.3.1 Design

We designed a 4×200 GHz AWG with 14 waveguides in the array for thermal tuning. A $2.4 \mu\text{m}$ wide shallowly etched aperture is used in the interface between the waveguide array and star-coupler. As an input/output a $2.0 \mu\text{m}$ wide

shallowly etched aperture is used. To reduce the number of waveguides we used a wider waveguide aperture for the AWG. The number of waveguides is limited by the number of heaters we can drive individually using our measurement facility.

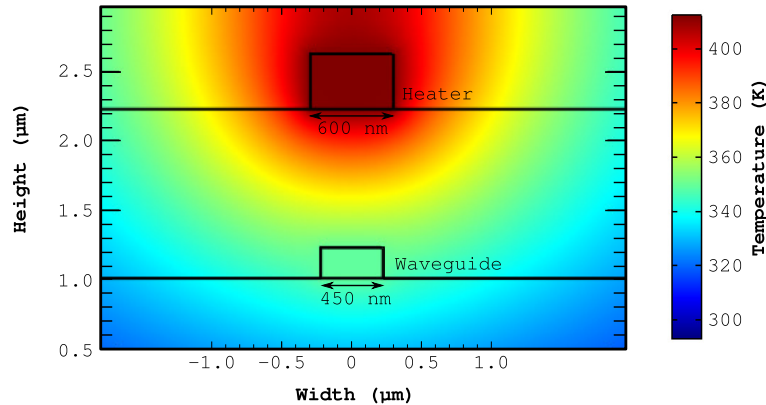


Figure 6.8: Heat profile of a heater on top of a silicon 450 nm wide waveguide. The image courtesy by Sarvagya Dwivedi.

A 400 nm thick 600 nm wide tungsten heater is fabricated on top of silicon oxide [11]. A 1 μm thick silicon oxide is used between the waveguide and heater such that the mode in silicon doesn't feel the heater and hence no light is absorbed as shown in Fig. 6.8. 75 μm long heaters are used to tune the AWG.

6.3.2 Experiment

We used the same measurement setup which was used to test the optical packet switch, described in section 6.2.3. As we have 14 waveguides in the array we also have 14 heaters to drive. The average measured resistance of the heater was 80 ohms.

6.3.2.1 Phase error correction

We first tuned up all the waveguides with equal voltages and then optimize each heater to optimize the phase errors. In Fig. 6.9 shows the spectral response of a 4×200 GHz AWG for the 2nd output varying before and after tuning. The measured loss of the channel is -2.3 dB. The side lobes can be reduced by 2 dB by tuning the waveguides. In general the silicon AWGs arm have a phase error in the order of $\pi/20$ [12, 13]. In order to correct such a small amount of error a high resolution voltage source is required. Another problem is the thermal

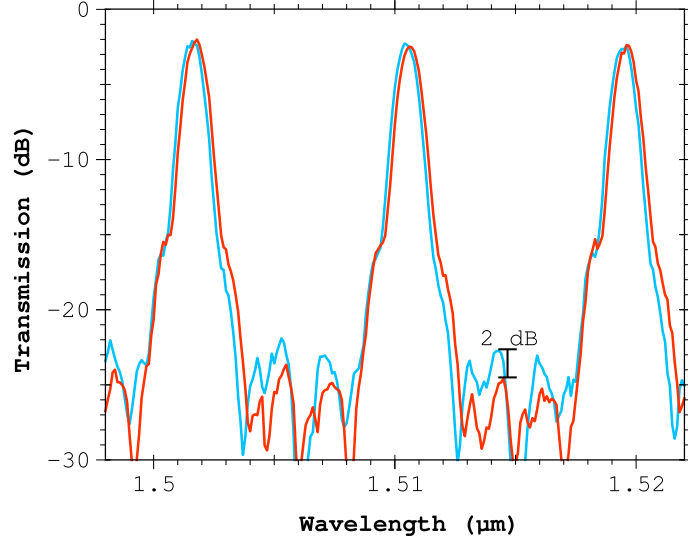


Figure 6.9: Spectral response of the 4×200 GHz AWG for 2^{nd} output (blue line) before tuning and (red line) after tuning.

crosstalk introduced by the heaters but the advantage is that they induce very little optical loss.

6.3.2.2 Halving the FSR

By tuning the odd positioned waveguides (1^{st} , 3^{rd} , 5^{th} etc.) we can reduce the FSR by half. When the reduced phase of the two successive odd and even waveguide (1^{st} - 2^{nd} , 3^{rd} - 4^{th} etc.) becomes equal these two waveguides will act as a single waveguide but with an odd symmetry mode. Before tuning the optical path length of the waveguide array can be written as

$$L_1 - L_2 = L_2 - L_3 = L_3 - L_4 = \dots = \Delta L \quad (6.1)$$

After tuning the modified equation will be

$$L'_1 - L'_2 = L'_2 - L'_3 = L'_3 - L'_4 = \dots = \Delta L' \quad (6.2)$$

where the relation between Eq. 6.1 and 6.2

$$\begin{aligned} L'_1 &= L_1 = L_2 \\ L'_2 &= L_3 = L_4 \\ &\dots \end{aligned} \quad (6.3)$$

Therefore the modified delay length will be doubled and the FSR will be reduced by half.

$$\Delta L' = 2\Delta L \quad (6.4)$$

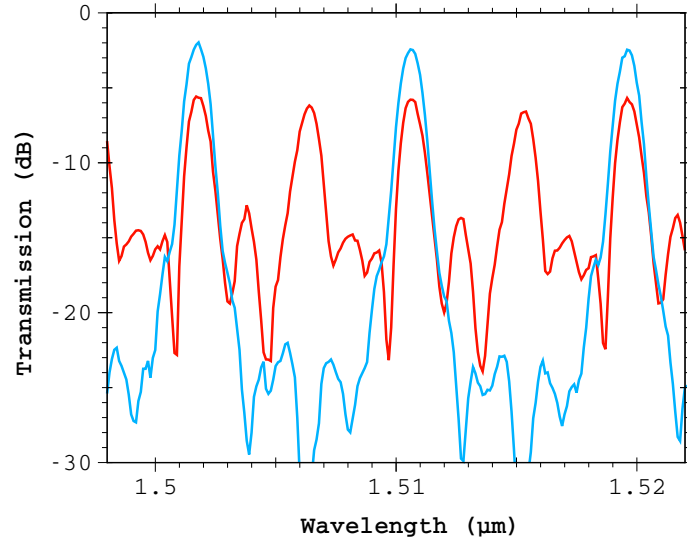


Figure 6.10: Spectral response of the 4×200 GHz AWG for 2^{nd} output (blue line) before tuning with the designed FSR and (red line) after tuning with half of the designed FSR.

Figure 6.10 shows that after tuning the 4×200 GHz AWG an additional peak rises between two successive orders. Before tuning the FSR was 8.85 nm and after tuning the FSR becomes 4.5 nm. As the power is distributed between the two successive orders the channel loss is increased by 3 dB.

6.3.2.3 Spectral shift

If we heat up the waveguides in such a way that the phase difference between the successive waveguides remains constant the spectrum will redshift. From Fig. 6.11 we can see that the 1515.5 nm wavelength peak shift to 1521 nm. As all the heaters are not identical the phase errors increase, and the side lobe increases. But it is possible to tune the heaters further to optimize the peaks.

Due to fabrication imperfections, limitation of voltage sources and the thermal crosstalk it is not straightforward to optimize the AWG performance. Although there is lot of scope to improve the above performance. In addition a suitable measurement methods like Optical low coherence method [14] is required in order to measure the phase errors accurately and desire corrections.

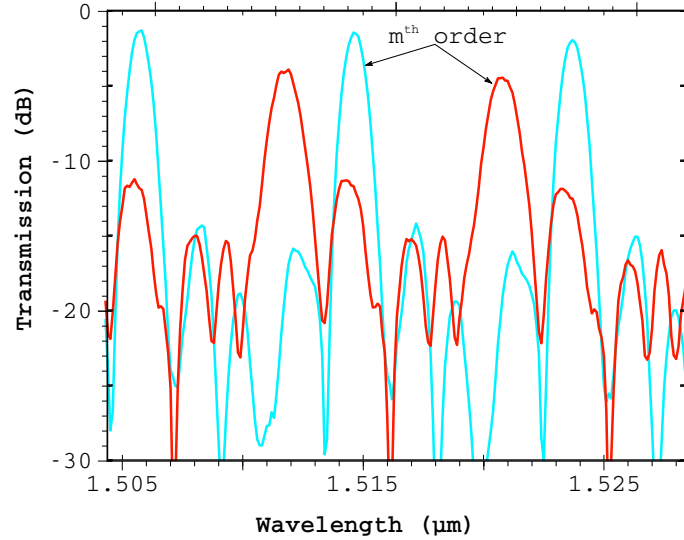


Figure 6.11: Spectral response of the 4×200 GHz AWG for 2^{nd} output (blue line) before tuning by the designed FSR and (red line) after tuning with half of the designed FSR.

6.4 Conclusion

In this section we demonstrated optical switching using a zeroth order AWG and carrier-depletion based silicon modulators. Although we have achieved decent results there is still a lot of room to improve these results. The loss and switching speed will be improved by improving the modulator's performance. Also some very preliminary results on actively tuning the AWG were shown, which indicate possibilities for future work. On this aspect optical vector network analyzer [15] can be useful to correct the phase error of the each arm precisely.

References

- [1] W. Van Berlo, M. Janson, L. Lundgren, A.C. Morner, J. Terlecki, M. Gustavsson, P. Granstrand, and P. Svensson. *Polarization-insensitive, monolithic 4 x 4 InGaAsP-InP laser amplifier gate switch matrix*. IEEE Photonics Technology Letters, 7(11):1291–1293, 1995.
- [2] K.A. Williams, G.F. Roberts, Tao Lin, R.V. Penty, I.H. White, M. Glick, and D. McAuley. *Integrated optical 2x2 switch for wavelength multiplexed interconnects*. Selected Topics in Quantum Electronics, IEEE Journal of, 11(1):78–85, Jan 2005.
- [3] M. Schienle, G. Wenger, S. Eichinger, J. Muller, L. Stoll, and G. Muller. *A 1x8 InP/InGaAsP optical matrix switch with low insertion loss and high crosstalk suppression*. Lightwave Technology, Journal of, 14(5):822–826, 1996.
- [4] G.A. Fish, B. Mason, L.A. Coldren, and Steven P. DenBaars. *Compact, 4x4 InGaAsP-InP optical crossconnect with a scaleable architecture*. Photonics Technology Letters, IEEE, 10(9):1256–1258, 1998.
- [5] R.M. Jenkins, J.M. Heaton, D.R. Wight, J.T. Parker, J.C.H. Birbeck, G.W. Smith, and K.P. Hilton. *Novel 1xN and NxN integrated optical switches using self-imaging multimode GaAs/AlGaAs waveguides*. Applied physics letters, 64(6):684–686, 1994.
- [6] T. Tanemura and Y. Nakano. *Design and scalability analysis of optical phased-array 1xN switch on planar lightwave circuit*. IEICE Electronics Express, 5(16):603–609, 2008.
- [7] T. Tanemura, M. Takenaka, A. Al Amin, K. Takeda, Tomonari Shioda, M. Sugiyama, and Y. Nakano. *InP InGaAsP Integrated 1x5 Optical Switch Using Arrayed Phase Shifters*. Photonics Technology Letters, IEEE, 20(12):1063–1065, 2008.
- [8] T. Tanemura, K. Takeda, and Y. Nakano. *Wavelength-multiplexed optical packet switching using InP phased-array switch*. Opt. Express, 17(11):9454–9459, May 2009.
- [9] H. Yu and W. Bogaerts. *An Equivalent Circuit Model of the Traveling Wave Electrode for Carrier-Depletion-Based Silicon Optical Modulators*. Lightwave Technology, Journal of, 30(11):1602–1609, June 2012.
- [10] H. Yu, M. Pantouvaki, J. Van Campenhout, D. Korn, K. Komorowska, P. Dumon, Y. Li, P. Verheyen, P. Absil, L. Alloatti, , D. Hillerkuss, J. Leuthold,

- R. Baets, and W. Bogaerts. *Performance tradeoff between lateral and interdigitated doping patterns for high speed carrier-depletion based silicon modulators*. Opt. Express, 20(12):12926–12938, Jun 2012.
- [11] A. Masood, M. Pantouvaki, G. Lepage, P. Verheyen, J. Van Campenhout, P. Absil, D. Van Thourhout, and W. Bogaerts. *Comparison of heater architectures for thermal control of silicon photonic circuits*. In Proceedings of IEEE Group IV Photonics, 2013.
- [12] S. Cheung, T. Su, K. Okamoto, and S.J.B. Yoo. *Ultra Compact Silicon Photonic 512x512 25 GHz Arrayed Waveguide Grating Router*. Selected Topics in Quantum Electronics, IEEE Journal of, 20(4):1–7, July 2014.
- [13] S. Pathak, M. Vanslembrouck, P. Dumon, D. Van Thourhout, and W. Bogaerts. *Effect of mask grid on SOI arrayed waveguide grating performance*. In 10th IEEE Int. Conf. Group IV Photonics, 2013.
- [14] K. Takada, H. Yamada, and Y. Inoue. *Optical low coherence method for characterizing silica-based arrayed-waveguide grating multiplexers*. Lightwave Technology, Journal of, 14(7):1677–1689, Jul 1996.
- [15] D. K. Gifford, B. J. Soller, M. S. Wolfe, and M. E. Froggatt. *Optical vector network analyzer for single-scan measurements of loss, group delay, and polarization mode dispersion*. Appl. Opt., 44(34):7282–7286, Dec 2005.

7

AWGs in other material systems

7.1 Introduction

In the previous chapters 4, 5, and 6 we experimentally demonstrated AWGs in the SOI material platform for telecom wavelengths. But the theory, design and simulation of the AWG discussed in chapters 2 and 3 are applicable to many other material systems and wavelength ranges also. To demonstrate this general applicability we adopt the necessary modifications in the design and simulation for different materials and wavelength platforms (discussed in chapter 2). By providing an appropriate index, wavelength and waveguide dimension it is possible to design an AWG for other materials and wavelengths. In this chapter we demonstrate silicon nitride AWGs for visible wavelengths, silicon AWGs for short wave infrared and mid-infrared and germanium AWGs for mid-infrared wavelength.

7.2 Silicon nitride for visible wavelengths

One of the key applications of photonic integrated circuits is on-chip biological sensing and detection [1, 2]. On-chip biological sensing techniques include evanescent field based sensing, fluorescence and Raman spectroscopy [3, 4]. The visible and very near infrared (500 -900 nm) wavelength range is suitable for such applications as these wavelengths cause minimum photodamage to living cells. The other advantage of this wavelength range is low absorption of water and fluorescence. The wide availability of sources and detectors in this wavelength range gives additional advantages.

However, silicon exhibits significant absorption in the visible-NIR wavelength range which makes it necessary to find an alternative material. In this perspective silicon nitride (Si_3N_4) becomes a very suitable material. Other than transparency in the visible-NIR wavelength range Si_3N_4 doesn't suffer from two photon absorption and also it is less temperature sensitive.

In recent years photonics research groups have demonstrated low loss waveguides [5] and fiber grating couplers [6] in Si_3N_4 , and we want to demonstrate de/multiplexers in this wavelength range as the spectrometers for sensing. This work was done in collaboration with Dr. A.Z. Subramanian¹ and Daan Martens²

¹Dr. A.Z. Subramanian is participating in this work as part of his post-doctoral research goal to demonstrate on chip Raman spectroscopy.

²Daan Martens is contributing as a part of his PhD research to use an AWG for biological sensing in the visible-NIR wavelength range.

7.2.1 Design

To design a low loss AWG in Si_3N_4 , the main important component is the waveguide. With 220 nm thick Si_3N_4 on SiO_2 a 700 nm wide waveguide is the optimal choice as single mode waveguide for the central wavelength of 900 nm. To keep the phase error low the delay lines of the rectangularly shaped AWGs are made out of single and multi-mode waveguides like we did for silicon. Therefore 700 nm and 900 nm wide waveguides are used to design the AWG. A 5 μm long linear taper is used between the 700 nm waveguide and the 900 nm waveguide to avoid exciting here order modes inside the 900 nm waveguide. As the Si_3N_4 waveguide has a lower index contrast than silicon waveguides the bend radius needs to be increased significantly. A bend with 30 μm radius is used to design the Si_3N_4 AWG as shown in Fig. 7.1.

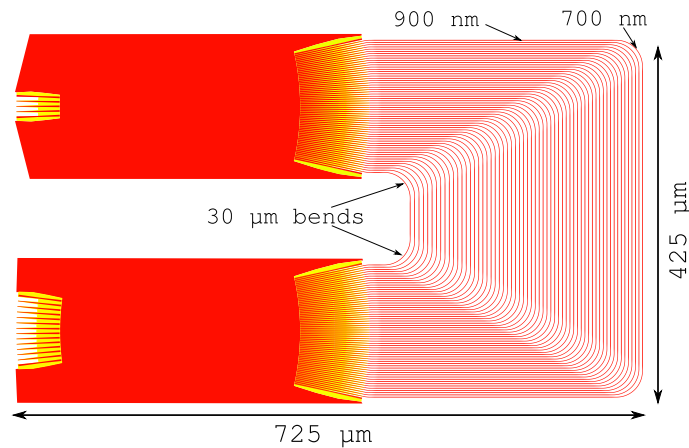


Figure 7.1: Mask layout of $12 \times 2 \text{ nm}$ Si_3N_4 AWG with 60 waveguide in array.

Similar as before, a double etch process is used: 220 nm deep trenches define the Si_3N_4 waveguides, as shown in Fig. 7.2 and a 70 nm etch defines the grating couplers and lower contrast Si_3N_4 waveguides. To reduce reflection, a shallowly etched aperture is used for defining all star coupler apertures. The array waveguides are tapered to 1.8 μm through a 50 μm long adiabatic taper at the star coupler interface and separated by 0.2 μm . All input and output apertures are 2.0 μm wide.

We designed $8 \times 2 \text{ nm}$, $12 \times 1 \text{ nm}$ and $12 \times 0.5 \text{ nm}$ Si_3N_4 AWGs with 60 waveguides in array. The Si_3N_4 has a lower index contrast than the silicon therefore it is obvious that the device will be bigger. The footprints are $425 \times 725 \mu\text{m}^2$, $425 \times 1150 \mu\text{m}^2$ and $425 \times 1940 \mu\text{m}^2$, for $8 \times 2 \text{ nm}$, $12 \times 1 \text{ nm}$ and $12 \times 0.5 \text{ nm}$ Si_3N_4 AWGs respectively.

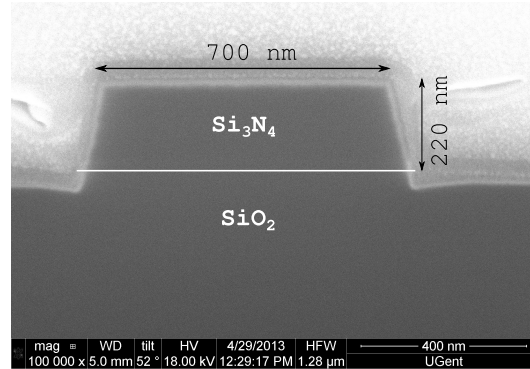


Figure 7.2: Cross-section of a fabricated Si_3N_4 waveguide. The image courtesy by Dr. A.Z. Subramanian.

7.2.2 Experiment

To couple the light into the Si_3N_4 waveguide we used a 70 nm etched fiber grating of 630 nm pitch with 50 % fill factor. The Si_3N_4 grating couplers give a maximum coupling efficiency of - 6.5 dB and a 1 dB bandwidth of 22 nm [6]. For the single mode waveguide the loss is <1 dB/cm, which is essential to achieve low loss AWGs in the Si_3N_4 platform [5]. Figure 7.3, 7.4 and 7.5 show the spec-

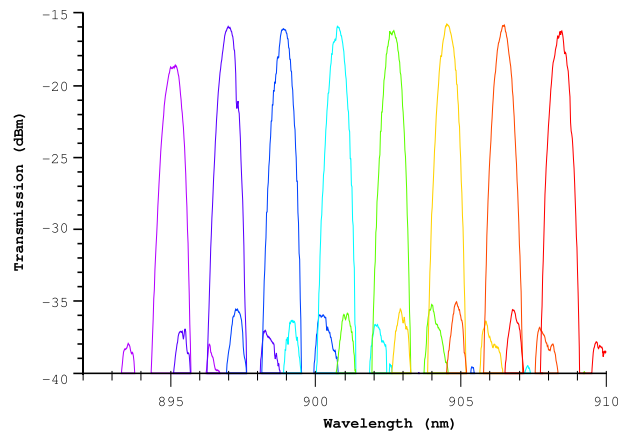


Figure 7.3: Spectral response of the 8×2 nm Si_3N_4 AWG

tral responses of the fabricated 8×2 nm, 12×1 nm and 12×0.5 nm Si_3N_4 AWGs respectively. The spectral responses are fiber-to-fiber and not normalized to the grating coupler's transmission. The estimated on-chip insertion loss is - 1 dB and the crosstalk is -20 dB for the 8×2 nm device. The FSR of the device

is 28 nm. As the FSR decreases to 14 nm for the 12×1 nm device the loss and the crosstalk increase. The center channel loss increases by 0.5 dB for the $12 \times$

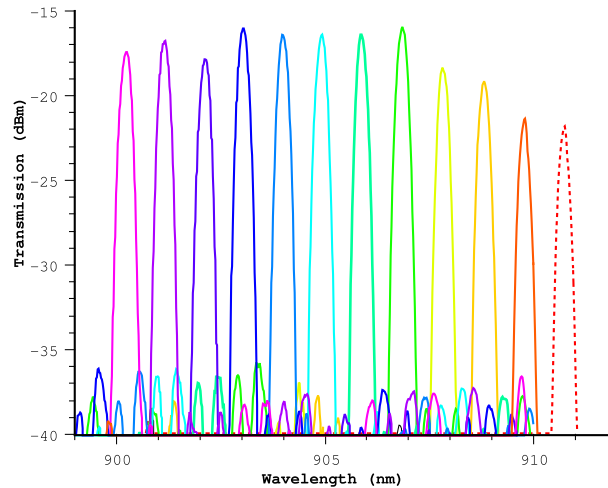


Figure 7.4: Spectral response of the 12×1 nm Si_3N_4 AWG

1 nm AWG compared to the 8×2 nm AWG. The crosstalk of the device is -19 dB. Further decreasing the FSR to 7 nm for the 12×0.5 nm Si_3N_4 AWG the estimated center channel loss becomes -3 dB and the crosstalk becomes 10 dB. This trend is to be expected as the FSR decreases the delay length increases, which increases the loss and the phase error and as a consequence the device performance goes down.

For first generation devices the performance is good. The designs needs to be further optimized to improve the performance. As this is a lower index contrast material, other geometries than the rectangularly shaped waveguide array might give better results, which needs to be tested with next generation devices.

7.3 Silicon for short wave infrared

In the above section we demonstrated Si_3N_4 AWGs for shorter wavelengths. We can also extend the use of AWGs to longer wavelengths in the 2 - 2.5 μm wavelength range [7]. This short wave infrared (SWIR) [8] range will allow probing a wide range of molecules and substances such as glucose and biodiesel [9]. The waveguides are fabricated on the same SOI platform used for telecom wavelengths. A center wavelength of 2.2 μm was chosen for AWG design. 220 nm high and 850 nm wide silicon waveguides are found to be single mode at this

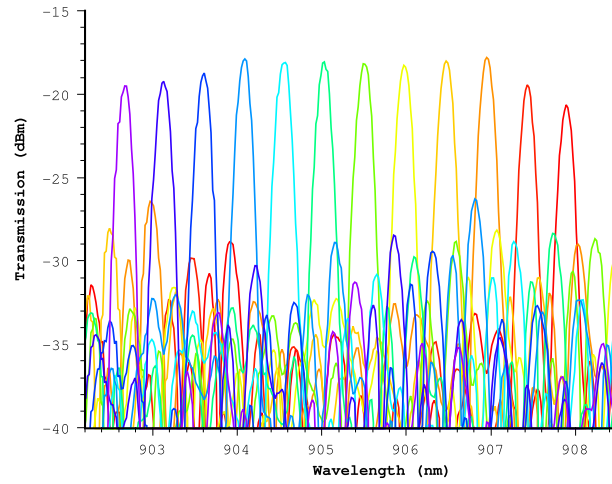


Figure 7.5: Spectral response of the 12×0.5 nm Si_3N_4 AWG

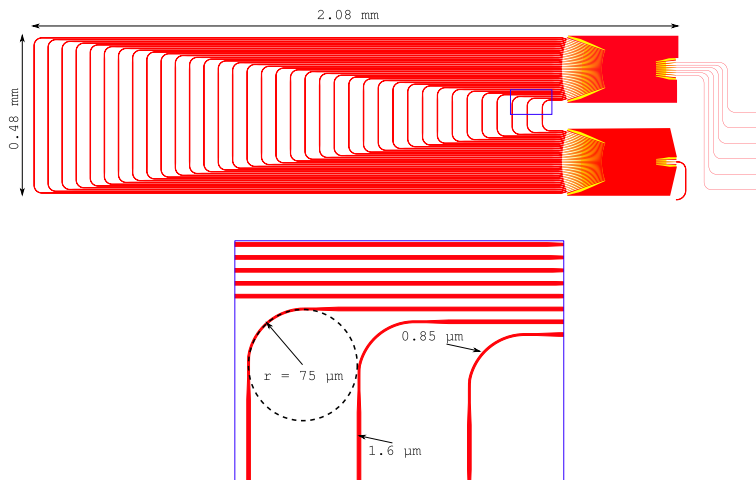


Figure 7.6: Mask layout of the 6×100 GHz AWG for short wave infrared.

wavelength. This work is done in collaboration with Muhammad Muneeb¹

7.3.1 Design

We designed a 6×100 GHz AWG with $2.2 \mu\text{m}$ as the center wavelength. The AWG had 36 waveguides in the array. We used 850 nm as a single mode waveguide and $1.6 \mu\text{m}$ as a multi-mode waveguide. The bend radius was $75 \mu\text{m}$. A $3 \mu\text{m}$

¹This is a part of the PhD research of Muhammad Muneeb.

wide aperture was used for input, output and arm apertures. The device footprint was $2.08 \times 0.48 \text{ mm}^2$. Figure 7.6 shows the mask layout of the $6 \times 100 \text{ GHz}$ AWG.

7.3.2 Experiment

To couple the light from a single mode optical fiber a grating coupler for TE-polarized light is used. The grating coupler consists of 20 deeply etched grating lines to couple the 150 nm thick silicon waveguide [10]. The grating is designed with 1.57 μm pitch and 35 % fill factor for 2.2 μm center wavelength. A linear taper is used to convert the mode from the 150 nm thick waveguide to a standard 220 nm thick silicon waveguide. The 850 nm wide waveguide has 1.15 dB/cm measured loss. Figure 7.7 shows the spectral response of the $6 \times 100 \text{ GHz}$

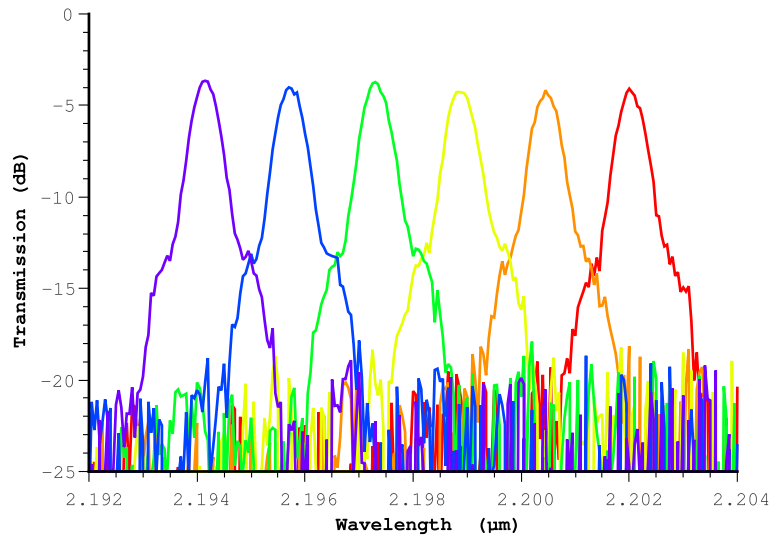


Figure 7.7: Measured spectral response of the $6 \times 100 \text{ GHz}$ AWG for short wave infrared.

AWG for 2.2 μm wavelength [10]. The measured insertion loss is -4 dB and the crosstalk is 16 dB. Although the index contrast is lower than at 1.55 μm , the 2 mm long device experiences significant loss and accumulated phase error. The taper from the 1.6 μm waveguide to the 0.85 μm , the bend radius etc. are not yet fully optimized, which may also have an impact on the performance of the AWG.

7.4 Silicon for Mid-infrared

In the previous section we discussed the AWG for short wave infrared up to $2.2 \mu\text{m}$ in SOI. However silicon is transparent up to $8 \mu\text{m}$ [11], which allows extending the wavelength range as the absorption cross-section of biomolecules is stronger in the mid-infrared from $2.5 \mu\text{m}$ to $8 \mu\text{m}$. This gives a motivation to demonstrate the AWG in the mid-infrared wavelength range [12]. But $3.8 \mu\text{m}$ wavelength is nearly at the edge of the transparency window of the buried SiO_2 [13], which limit the overall transparency window of the SOI material platform. This work is done in collaboration with Muhammad Muneeb¹

The waveguides are fabricated in a 380 nm thick silicon wafer which consists of a 160 nm thick poly-silicon layer on top of a 220 nm thick crystalline silicon layer. For the AWG design $3.8 \mu\text{m}$ is considered to be the center wavelength. A 1350 nm wide shallowly etched waveguide is defined by a 160 nm etching step.

7.4.1 Design

We designed a $6 \times 200 \text{ GHz}$ AWG with 32 waveguides in the array. The single-mode and multi-mode waveguide combination is also used to reduce the phase errors: $1.35 \mu\text{m}$ as single-mode and $2.5 \mu\text{m}$ as multi-mode waveguide. The bend radius is chosen to be $60 \mu\text{m}$. Figure 7.8 shows the mask layout of the $6 \times 200 \text{ GHz}$

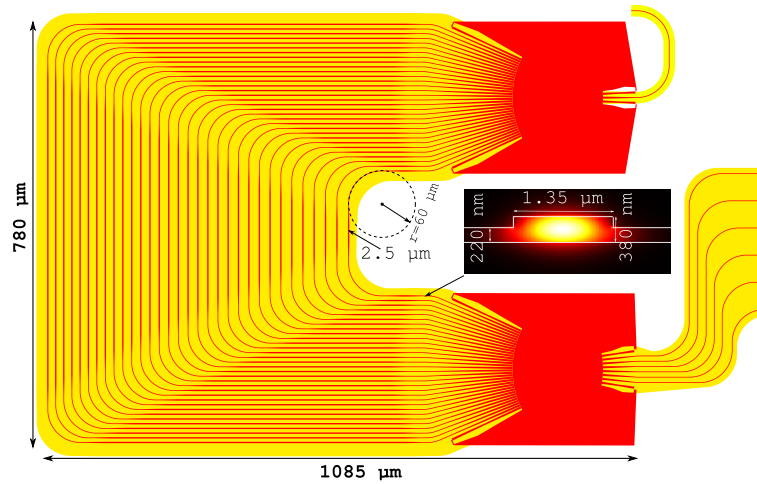


Figure 7.8: Mask layout of the $6 \times 200 \text{ GHz}$ AWG for $3.8 \mu\text{m}$ center wavelength and mode profile of the single-mode waveguide cross sections².

AWG. The footprint of the device is $1085 \times 780 \mu\text{m}^2$.

¹This is a part of the PhD research of Muhammad Muneeb.

²The mode profile is simulated by Muhammad Muneeb.

7.4.2 Experiment

To couple the light from the fiber to the waveguide a fiber grating coupler is fabricated using an etch depth of 230 nm. The grating coupler has a pitch of $2\ \mu\text{m}$ and 50 % fill factor. Figure 7.9 shows the measured spectral response of the $6\times 100\ \text{GHz}$ AWG [14], which is normalized by the reference waveguide to eliminate the grating response. The measured insertion loss and crosstalk of the

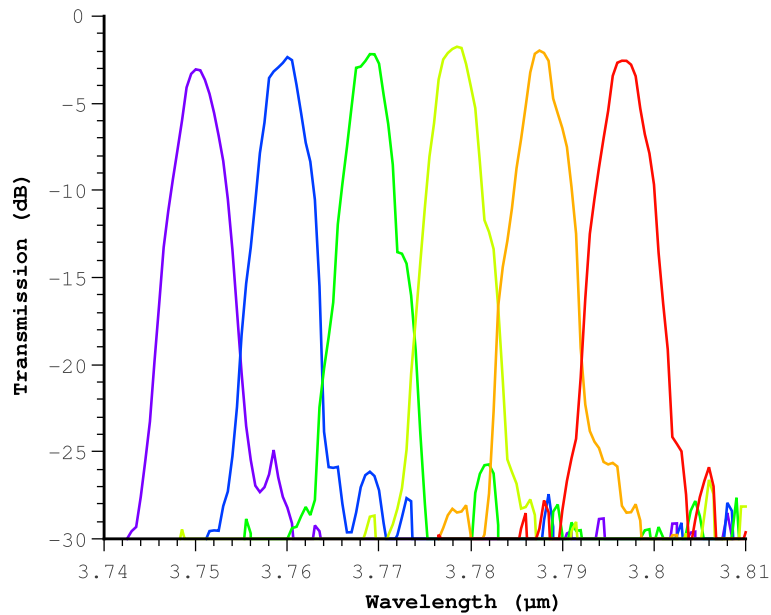


Figure 7.9: Measured spectral response of the $6\times 100\ \text{GHz}$ AWG for short wave infrared.

device are $-1.75\ \text{dB}$ and $-23\ \text{dB}$. The measured wavelength channels are distorted due to the unavailability of a high resolution source in this wavelength range.

7.5 Germanium AWG for Mid-infrared

The mid-infrared (midIR) wavelength range ($3\text{-}12\ \mu\text{m}$) is very suitable for spectroscopic sensing due to the strong absorption of many gases in this region. Over the last half decade the research in this area gained interest due to the availability of compact, cheap coherent light sources: quantum cascade lasers (QCL) [15] and interband cascade lasers (ICLs). These distributed feedback (DFB) based lasers are typically single wavelength but it's possible to thermally tune them over a narrow wavelength range [16]. With a combination of these

lasers array and a multiplexer it is possible to extend the wavelength range. As a multiplexer one of the possible choice is the AWG. The implementation of the AWG in this wavelength range is done in collaboration with Aditya Malik¹

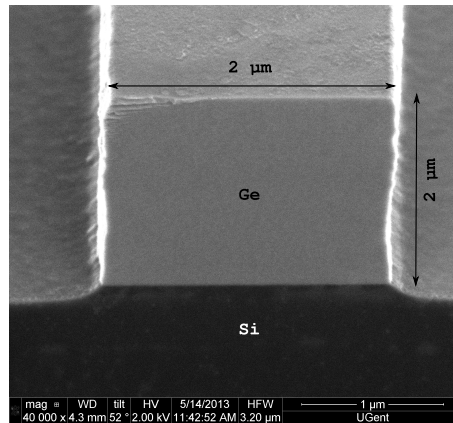


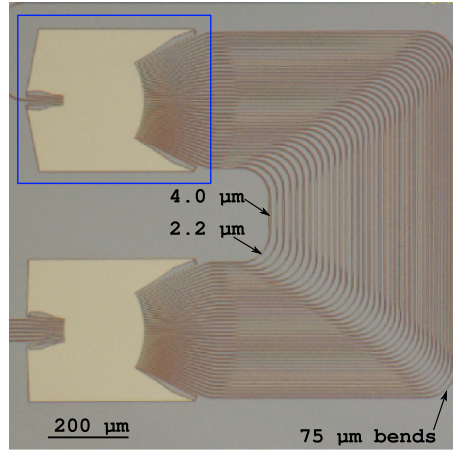
Figure 7.10: Cross-section of a fabricated Ge waveguide. The image courtesy by Aditya Malik.

The buffer layer SiO_2 of the SOI platforms starts absorbing from $3.8 \mu\text{m}$ wavelength. Therefore it is necessary to move to a more suitable waveguide platform such as germanium-on-silicon platform. The main advantage of Ge-on-Si is that it is CMOS-compatible but also transparent for the wavelength up to $14 \mu\text{m}$. A 200 mm Ge-on-Si wafer is used to fabricate the germanium waveguide by a lift-off approach using i-line contact lithography. The 200 mm Ge-on-Si wafer has $2 \mu\text{m}$ thick germanium as a guiding layer on top of the silicon substrate. The lift-off process introduces sidewall roughness as we can see from Fig. 7.10 [17, 18]. This sidewall roughness will increase the crosstalk of the AWG by introducing phase errors.

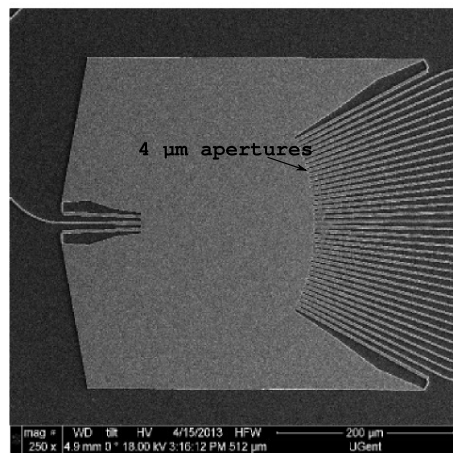
7.5.1 Design

Using a lift-off process and the given facilities of our clean-room it is difficult to achieve a double etch process. So the AWGs were realized with a single etch process. The Ge waveguides were defined by the single $2 \mu\text{m}$ deeply etched trench. We used $2.2 \mu\text{m}$ wide single-mode and $4 \mu\text{m}$ wide multi-mode waveguides to design the Ge AWG at the center wavelength of $5.3 \mu\text{m}$. The AWG has minimal bend radius of $75 \mu\text{m}$. The $4 \mu\text{m}$ wide apertures were used at the interface between the star-coupler and the waveguide array, separated by $1 \mu\text{m}$ gap which

¹Aditya Malik built the waveguide platform and the measurement setup as a part of his PhD research towards the demonstration of an integrated array of QCLs into the waveguides.



(a)



(b)

Figure 7.11: (a) Optical image of the fabricated 5×200 GHz Ge AWG with 36 waveguides (b) SEM image of input star-coupler. Image courtesy of Aditya Malik.

is limited by the i-line lithography. We designed a 5×200 GHz Ge AWG with 36 waveguides in the array. Figure 7.10 shows the optical image of the fabricated device. The device size is $1 \times 1 \text{ mm}^2$.

7.5.2 Experiment

15 μm wide apertures are used to couple the light in the waveguide by means of horizontal coupling¹. The horizontal coupling method couples both TE and TM polarized light into the waveguide. To control the polarization a Babinet-Soleil compensator is used between the source and the fiber. As the waveguide section is nearly square, one can expect polarization independent performances. But due to the cladding variation the device has strong polarization dependence. We tested the device under both TE and TM polarization.

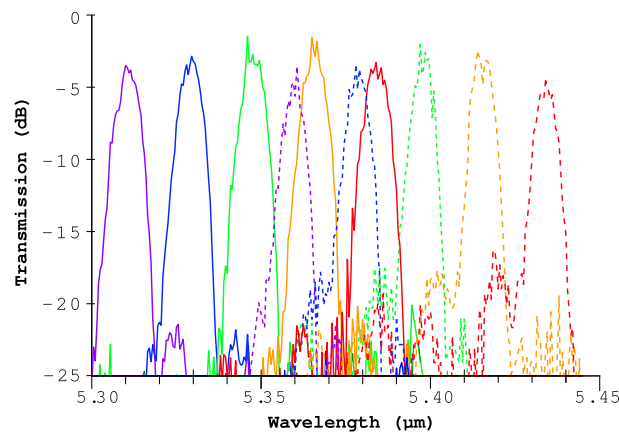


Figure 7.12: Spectral response of the 5×200 GHz Ge AWG (solid line) for TE polarization light (dash line) for TM polarization light.

Figure 7.12 shows the spectral response of the 5×200 GHz Ge AWG for TE and TM polarization light [18]. The spectral responses are normalized with respect to the reference waveguide transmission. The measured insertion losses are -2.5 dB and -3.1 dB and the crosstalk is 20 dB and 16 dB for TE and TM polarization lights respectively. The polarization dependent shift is 51 nm. In this device not only the sidewall roughness is responsible for the phase error but also the TE-TM conversion in the waveguide. By using appropriate side and top claddings it is possible to achieve polarization insensitive de/multiplexing.

This is a very first generation Ge AWG, which needs to be optimized further to improve the performance. As the waveguide width is very large compared to the mask grid the most robust angled waveguide shaped AWG will probably be the best choice for the Ge AWG geometry.

¹The details of the coupling method are described in the PhD thesis of Dr. Wim Bogaerts

7.6 Conclusion

We demonstrated AWGs in different materials and wavelength platforms for various applications, which shows the general applicability of the design method. All the devices presented here are first generation devices of their own kind and have plenty of room for further improvements. This will be implemented in future generation devices by the corresponding collaborators.

References

- [1] X. Fan and I. M. White. *Optofluidic microsystems for chemical and biological analysis*. *Nature photonics*, 5(10):591–597, 2011.
- [2] A. L. Washburn and R. C. Bailey. *Photonics-on-a-chip: recent advances in integrated waveguides as enabling detection elements for real-world, lab-on-a-chip biosensing applications*. *Analyst*, 136(2):227–236, 2011.
- [3] C. L. Arce, D. Witters, R. Puers, J. Lammertyn, and P. Bienstman. *Silicon photonic sensors incorporated in a digital microfluidic system*. *Analytical and bioanalytical chemistry*, 404(10):2887–2894, 2012.
- [4] P. C. Ashok, G. P. Singh, H. A. Rendall, T. F. Krauss, and K. Dholakia. *Waveguide confined Raman spectroscopy for microfluidic interrogation*. *Lab on a Chip*, 11(7):1262–1270, 2011.
- [5] A.Z. Subramanian, P. Neutens, A. Dhakal, R. Jansen, T. Claes, X. Rottenberg, F. Peyskens, S. Selvaraja, P. Helin, B. Dubois, K. Leyssens, S. Severi, P. Deshpande, R. Baets, and P. Van Dorpe. *Low-Loss Singlemode PECVD Silicon Nitride Photonic Wire Waveguides for 532-900 nm Wavelength Window Fabricated Within a CMOS Pilot Line*. *Photonics Journal, IEEE*, 5(6):2202809–2202809, Dec 2013.
- [6] A.Z. Subramanian, S. Selvaraja, P. Verheyen, A. Dhakal, K. Komorowska, and R. Baets. *Near-Infrared Grating Couplers for Silicon Nitride Photonic Wires*. *Photonics Technology Letters, IEEE*, 24(19):1700–1703, 2012.
- [7] G. Roelkens, W. M J Green, B. Kuyken, Xiaoping Liu, N. Hattasan, A. Gassenq, L. Cerutti, Jean-Baptiste Rodriguez, R.M. Osgood, E. Tournie, and R.G. Baets. *III-V/Silicon Photonics for Short-Wave Infrared Spectroscopy*. *Quantum Electronics, IEEE Journal of*, 48(2):292–298, Feb 2012.
- [8] J.G. Crowder, S.D. Smith, A. Vass, and J. Keddie. *Infrared Methods for Gas Detection*. In Anthony Krier, editor, *Mid-infrared Semiconductor Optoelectronics*, volume 118 of *Springer Series in Optical Sciences*, pages 595–613. Springer London, 2006.
- [9] A. K. Amerov, J. Chen, and M. A. Arnold. *Molar Absorptivities of Glucose and Other Biological Molecules in Aqueous Solutions over the First Overtone and Combination Regions of the Near-Infrared Spectrum*. *Appl. Spectrosc.*, 58(10):1195–1204, Oct 2004.

- [10] E. Ryckeboer, A. Gassenq, M. Muneeb, N. Hattasan, S. Pathak, L. Cerutti, J.B. Rodriguez, E. Tournié, W. Bogaerts, R. Baets, and G. Roelkens. *Silicon-on-insulator spectrometers with integrated GaInAsSb photodiodes for wide-band spectroscopy from 1510 to 2300 nm*. Opt. Express, 21(5):6101–6108, Mar 2013.
- [11] R. Soref. *Mid-infrared photonics in silicon and germanium*. Nature Photonics, 4(8):495–497, 2010.
- [12] G. Roelkens, U. Dave, A. Gassenq, N. Hattasan, C. Hu, B. Kuyken, F. Leo, A. Malik, M. Muneeb, E. Ryckeboer, S. Uvin, Z. Hens, R. Baets, Y. Shimura, F. Gencarelli, B. Vincent, R. Loo, J. Van Campenhout, L. Cerutti, J.B. Rodriguez, E. Tournie, X. Chen, M. Nedeljkovic, G. Mashanovich, L. Shen, N. Healy, A. C. Peacock, X. Liu, R. Osgood, and W.Green. *Silicon-based heterogeneous photonic integrated circuits for the mid-infrared*. Opt. Mater. Express, 3(9):1523–1536, Sep 2013.
- [13] R. A. Soref, S. J. Emelett, and W. R. Buchwald. *Silicon waveguided components for the long-wave infrared region*. Journal of Optics A: Pure and Applied Optics, 8(10):840, 2006.
- [14] M. Muneeb, X. Chen, P. Verheyen, G. Lepage, S. Pathak, E. Ryckeboer, A. Malik, B. Kuyken, M. Nedeljkovic, J. Van Campenhout, G. Z. Mashanovich, and G. Roelkens. *Demonstration of Silicon-on-insulator mid-infrared spectrometers operating at 3.8 μ m*. Opt. Express, 21(10):11659–11669, May 2013.
- [15] R. F. Curl, F. Capasso, C. Gmachl, A. A. Kosterev, B. McManus, M. Lewicki, R. and Pusharsky, G. Wsocki, and F.K. Tittel. *Quantum cascade lasers in chemical physics*. Chemical Physics Letters, 487(1):1–18, 2010.
- [16] B. G. Lee, M.A. Belkin, C. Pflugl, L. Diehl, H.A. Zhang, R.M. Audet, J. MacArthur, D.P. Bour, S.W. Corzine, G.E. Huffler, and F. Capasso. *DFB Quantum Cascade Laser Arrays*. Quantum Electronics, IEEE Journal of, 45(5):554–565, May 2009.
- [17] A. Malik, M. Muneeb, Y. Shimura, J. Van Campenhout, and G. Roelkens. *Germanium-on-silicon mid-infrared waveguides and Mach-Zehnder interferometers*. In IEEE Photonics Conference, 2013.
- [18] A. Malik, M. Muneeb, S. Pathak, Y. Shimura, J. Van Campenhout, R. Loo, and G. Roelkens. *Germanium-on-Silicon Mid-Infrared Arrayed Waveguide Grating Multiplexers*. Photonics Technology Letters, IEEE, 25(18):1805–1808, 2013.

8

Conclusion

"A conclusion is the place where you got tired of thinking."

– Steven Wright

8.1 Conclusion

The objective of this work was to improve the performance of the silicon AWGs, with a focus on a 1550 nm center wavelength and WDM-based applications. The devices were fabricated starting from SOI wafers using the CMOS pilot line fabrication process of imec. As a result we achieved compact, highly integrated AWGs not only usable in WDM systems but also as in spectroscopic and sensing applications.

In a first part of this work, we investigated general grating theory and from that derived the necessary theoretical background to understand AWGs operation. We gained better insight in the mechanisms determining its loss and crosstalk, helping us to design improved AWGs and understanding their practical limitations. The goal was to create a generic design tool for AWGs of various geometrical shapes and for different applications. Designing an AWG typically consists of two steps: calculation of the basic parameters from the general AWG theory and generation of the mask layout by using these parameters. Calculation of the AWG parameters changes depending on the material system used, the selected central wavelength and user defined specifications such as channel spacing. All of these then have a direct impact on the mask layout. The parameters calculation and the mask layout were integrated inside a single framework, IPKISS. Understanding the benefits of a particular geometrical shape on the performance of the AWG and how the performance depends on the fabrication process and material platform used, improved AWGs could be designed.

The foremost requirement for a simulation tool to be useful is that it is reliable and predictive. Therefore we developed a semi-analytical model to simulate the AWGs, which is more efficient in terms of calculation time than methods based on FDTD and BPM. To take maximal advantage of the design tool and to save time in the design process by avoiding the need to duplicate the entry of parameters several times (and thereby avoid possible errors in this process), it was fully integrated with the CAD-layout tool, resulting in an integrated, fast and reliable simulation tool.

In the second part of this work the goal was to improve the performance of AWGs fabricated on the SOI waveguide platform (see in the Table 8.1). After having sufficient proofs that the rectangular shaped AWG is the best choice for the this high contrast material system, we mainly used this shape. We experimentally demonstrated silicon AWGs with channel spacings from 50 GHz to 800 GHz. As seen from Table 8.1, it is clear that the silicon AWGs designed and fabricated by us have not only smaller footprint but also higher performance as compared to rest of the world, the performance of which is constantly improving over the years. For channel spacings above 800 GHz, the design needed to be modified to an S-shaped layout to avoid coupling in the waveguide ar-

ray. The performance of these AWGs decreased however because the S-shaped waveguides in the array introduce extra bends and therefore longer waveguides (and hence more phase errors). The two major applications of the AWGs are

AWG Device Type	Channel Spacing (GHz)	Channel Number	Footprint (μm^2)	Crosstalk (dB)
Si Rib [1]	25	50	8000×8000	-7
Si Rib [2]	100	40	2000×2000	-15
Si Rib [3]	200	46	1400×400	-18
Si Wire [4] UGent-imec (2010)	400	8	200×350	-24
Si Wire UGent-imec (2013)	100	8	1630×308	-21
Si Wire [5] UGent-imec (2013)	200	16	920×446	-22.5
Si Wire [5] UGent-imec 2013	400	16	530×435	-26
Si Wire UGent-imec (2013)	800	8	300×307	-27

Table 8.1: State of the art of Silicon AWGs

its use as wavelength de-multiplexers and as a wavelength router. For the de-multiplexers design the AWGs showed improvement in loss and crosstalk with increasing the FSR. As a wavelength router we demonstrated 16×16 200 GHz and 400 GHz AWGs. The 16×16 200 GHz wavelength router shows a good cyclic rotation of the wavelengths. Although due to the dispersion mismatch the cyclic behavior of the AWG breaks down for larger wavelength.

To improve the performance further we analyzed the effect of the mask grid on the width and length of the waveguides used in the array. The best performance is obtained when the waveguide is aligned with the mask grid line and with minimum grid step. We also demonstrated polarization independent de-multiplexing using a polarization diversity scheme. In addition to this we tried to draw a comparison between and determine the relative merits of AWGs and the Echelle grating respectively. Our conclusion was that for high resolution devices the rectangular shaped AWG is the better choice, where for low resolution the Echelle grating is better. In the latter case (low resolution) also the S-shaped AWG can be an attractive alternative.

For some application a flattop spectral response is required. We investigated several approaches to reach this objective: replacing the AWG-input by an MMI or replacing it with an MZI or AWG with FSR equal to the main AWGs channel

spacing. Theoretically the MMI input aperture is more lossy compared to the other two methods but it is easier to design. A good flattop spectral response was obtained using the MMI-AWG approach. We discussed the effect of the MMI length and the number of waveguides in the array on the spectral response in detail. Using the MZI as the input aperture and using the cascaded AWG approach also show promising results in simulation. However so far it seems to be more challenging in their practical implementation on the SOI platform.

The AWG is not only a good wavelength filter but it can also be used in switching applications. We demonstrated for the first time an optical switch in silicon whereby carrier depletion based modulators are integrated in the waveguides of the AWG. The main difference between the wavelength filter design and the switch design is that for the switch the waveguides used in the array are equally long. The performance of a 4×4 switch shows good agreement with simulations. Due to the high loss of the modulators the device has a large loss of -6 dB. Due to the limited number of available electrical sources needed to drive the modulators we used a limited number of waveguides in the array which increased the neighboring channel crosstalk.

From the basic AWG theory we learned that fabrication imperfections in the waveguides are the origin of phase errors and the associated crosstalk. We demonstrated it is possible to compensate for these phase errors by using phase shifters in the waveguides. We demonstrated that for a 4×400 GHz AWG with 14 waveguides having 14 equally long heaters on top a 2 dB improvement in the crosstalk could be obtained. We also demonstrated that we could shift the spectrum and vary the FSR of the device through these adjusting these heaters.

As discussed above, the design and simulation model developed during the first part of the work showed very good results for silicon AWGs operating around the 1550 nm wavelength. But this model is equally applicable for other material systems and wavelengths. To demonstrate this we collaborated with different people. The rectangularly shaped AWG design was used to design first generation devices in silicon nitride for visible wavelengths, in silicon-on-insulator for $2.2 \mu\text{m}$ and $3.8 \mu\text{m}$ wavelengths, and in germanium-on-silicon for $5.2 \mu\text{m}$ wavelengths, for applications in biological sensing, gas spectroscopy etc.

8.2 Future perspectives

We strongly believe Silicon AWGs have a bright future in optical telecommunications. The improvements in their performance reached in this work brings their performance close to that of AWGs fabricated in low index contrast material systems. But we believe that there is still a lot of room to improve the performance. It is obvious that by improving the fabrication process further we can

also improve the performance further. This requires not only that the side wall roughness but also the minimum feature size needs to be improved. In chapter 4 we showed the effect of the mask grid on the waveguide's length, concluding that the waveguides will have a maximal deviation of three times the mask grid step. In the future using a smarter design it should be possible to reduce this length deviation to a single mask grid step. In chapter 2 we defined two formulas for the dispersion angle calculation: one where the refractive index of the slab waveguide is considered to be variable with respect to wavelength and another where it is considered to be constant with respect to wavelength. Simulations showed that the first case shows more deviation from the desired channel spacing while the second case is much more relaxed in this respect. But this remains to be experimentally verified.

In chapter 3 we described the simulation model and showed it reaches a fairly good agreement with the experimental results. But this simulation model makes a few assumptions which need to be refined in order to obtain more accurate results. The simulation does not include coupling between the waveguides. For low resolution AWGs though the gap between the waveguides decreases and the coupling can have a significant impact on the crosstalk. As discussed in chapter 2, the crosstalk originates in the combination of many mechanisms but in simulation we include only the phase error induced by the sidewall roughness. But as we decrease the crosstalk below -26 dB for the above 200 GHz channel spacing AWGs other mechanism like reflections from the facets can have a significant effect on the remaining crosstalk. Therefore it will be interesting to include these reflections in the AWG model, the inclusion of which will also improve the switch simulation where in the real device the edges of the modulators exhibit significant reflections.

Obtaining a flattop spectral response using an MZI-AWG or a cascaded AWG configuration was shown in simulation. However, the proposed design still needs to be experimentally demonstrated. A 1:1 comparison between the three methods proposed to reach a flattop spectral responses will be helpful to allow users to choose the most suitable methods for their application. We tried reflection-typed AWGs but due to the error in the DBR fabrication we didn't get the desired results. We proposed two relatively less fabrication dependent MMI reflectors (shown in appendix A). These devices need to be fabricated in the future. In the switch demonstration the device extinction is limited by neighboring channel crosstalk. By adding more modulators in the array it should be possible to improve the extinction until it is limited by phase errors. This needs to be tested experimentally. By thermally tuning the AWG, we expected to improve the crosstalk by more than 2 dB. There are two issues which need to be solved other than the thermal crosstalk introduced by the heater: first an algorithm to minimize the phase error should be developed before measurement

and second a high resolution voltage source is required.

In chapter 7 we demonstrated the first generation device of silicon nitride for visible wavelength, silicon-on-insulator for 2.2 μm and 3.8 μm wavelength, and germanium-on-silicon for 5.2 μm . In this first try these devices showed promising performance, but they need to be optimized further in order to get best performance within the given fabrication limitations. In chapter 2 and appendix A we show a lot of different geometrical AWG designs which needs to be tested experimentally in silicon and other material platforms to understand the applicability of these designs.

Finally we didn't get chance to test these devices for a particular application like networking or sensing. At this point we believe that the device is ready to be a part of more complex circuits. This will be the next big step determining the future of the silicon AWGs.

References

- [1] P. Cheben, J. H. Schmid, A. Del age, A. Densmore, S. Janz, B. Lamontagne, J. Lapointe, E. Post, P. Waldron, and D.X. Xu. *A high-resolution silicon-on-insulator arrayed waveguide grating microspectrometer with sub-micrometer aperture waveguides*. Optics express, 15(5):2299–306, 2007.
- [2] S. T. Cheung, B. Guan, S. S. Djordjevic, K. Okamoto, and S. J. Ben Yoo. *Low loss and High Contrast Silicon-on-Insulator (SOI) Arrayed Waveguide Grating*. In Conference on Lasers and Electro-Optics 2012, page CM4A.5. OSA, 2012.
- [3] Q. Fang, T.Y. Liow, J. F. Song, K. W. Ang, M. B. Yu, G. Q. Lo, and D.L. Kwong. *WDM multi-channel silicon photonic receiver with 320 Gbps data transmission capability*. Opt. Express, 18(5):5106–5113, Mar 2010.
- [4] W. Bogaerts, S.K. Selvaraja, P. Dumon, J. Brouckaert, K. De Vos, D. Van Thourhout, and R. Baets. *Silicon-on-Insulator Spectral Filters Fabricated With CMOS Technology*. IEEE Journal of Selected Topics in Quantum Electronics, 16(1):33–44, 2010.
- [5] S. Pathak, M. Vanslebrouck, P. Dumon, D. Van Thourhout, P. Verheyen, G. Lepage, P. Absil, and W. Bogaerts. *Effect of Mask Discretization on Performance of Silicon Arrayed Waveguide Gratings*. Photonics Technology Letters, IEEE, 26(7):718–721, April 2014.



Design of AWGs

A.1 Introduction

In chapter 2 we discussed only about the design of the rectangularly shaped AWG as in silicon the rectangularly shaped waveguide array is the best choice. But using the same theory and design tool it is possible to design different geometries which can be useful for other material platforms. Therefore in this appendix we include the other possible designs of the waveguide array.

A.1.1 Circular manhattan

For low contrast waveguide the bend radius increases significantly, which makes the device size large. In the rectangular manhattan configuration the bends are not contributing in the phase calculations (as the same bends are used in all the delay lines) of the AWG but they definitely contribute to the loss of the device. Therefore a circular manhattan configuration is proposed [1],

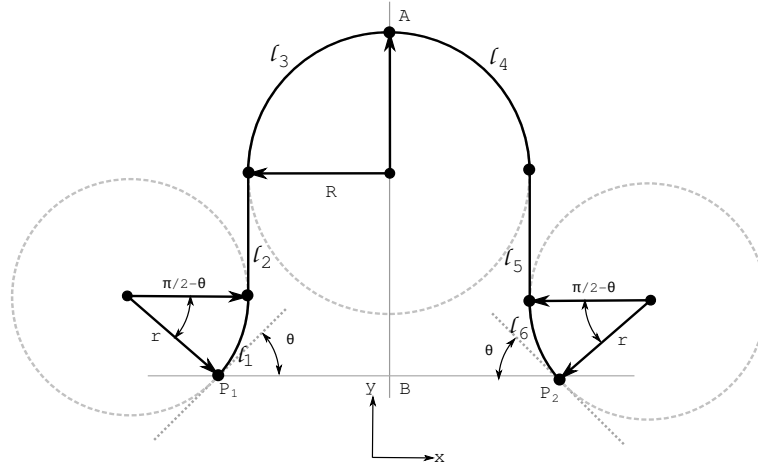


Figure A.1: Geometry of a circular manhattan waveguide paths.

where lengths l_3 , l_4 , l_5 and l_6 of the rectangular manhattan merge to a half circle of radius R as shown in Fig. A.1. The delay line equation will be

$$\pi/2(r + R) - r\theta + l_2 = l/2 \quad (\text{A.1})$$

Where r the minimum bend radius. R depends on the distance between the star-coupler, which is equal to the Q_1B . With the help of Eq. 2.42 (chapter 2) the expression of R can be written as

$$R = L - r(1 - \sin\theta) \quad (\text{A.2})$$

To avoid the loss in the bends R must be greater than or equal to the minimum bend radius (r). l_2 and l_5 are free to adjust in the delay line to keep the waveguide array condition (delay length (ΔL) is constant) fulfilled.

In this configuration it is considered that the bend waveguide has the same effective index of the straight waveguide but often a mismatch between the effective indexes is observed. If the mismatch is large a systematic phase error will be introduced which can be further optimized by adjusting the length of l_2 and l_5 .

A.1.2 Angled waveguide with a constant bend radius

If the mask grid width is very small compared to the waveguide width, sidewall roughness introduced by the mask discretization on the inclined waveguide will be significantly low. This gives freedom to avoid the bends used to keep the waveguide aligned with mask grid line: l_1 and l_8 for the rectangular manhattan and l_1 and l_6 for the circular manhattan. Instead of using those bends the waveguides propagate along the same angles of the output apertures and connected each other by two bends as shown in Fig. A.2. Therefore the grating line

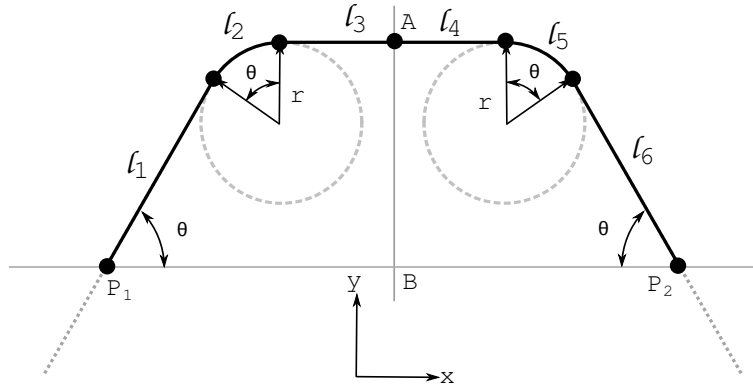


Figure A.2: Geometry of an angled waveguide paths with constant bend radius.

equation will be

$$l_1 + l_3 + r\theta = l/2 \quad (\text{A.3})$$

In this equation there are two variables l_1 and l_3 . We need another equation to calculate these variables which is

$$l_1 \cos\theta + l_3 + r \sin\theta = L/2 \quad (\text{A.4})$$

Now by solving Eq. A.3 and Eq. A.3 we obtain the expressions for l_1 and l_3

$$l_1 = \frac{l - L - 2r\theta + 2r \sin\theta}{2(1 - \cos\theta)} \quad (\text{A.5})$$

and

$$l_3 = \frac{l \cos \theta - L - 2r\theta \cos \theta + 2r \sin \theta}{2(\cos \theta - 1)} \quad (\text{A.6})$$

In Eq. A.5 and Eq. A.6 bend radius r is constant. L and θ are also constant for a set of output apertures. Therefore the delay length (l) will adjust l_1 and l_3 in such a way that the waveguide array condition remains unaltered.

A.1.3 Angled waveguide with variable bend radius

The above design can be modified further by merging l_2 , l_3 , l_4 and l_5 (from Fig.A.2) into one single bend as shown in Fig. A.3. This design [2] is suitable for low contrast waveguides where the bend radius is large. Another advantage of this design method is that it reduces complexity of the design equation. From Fig. A.3 we can write down the grating line equation.

$$l_1 + R\theta = l/2 \quad (\text{A.7})$$

In Eq. A.7 there are two variables l_1 and R . To solve this we need another equa-

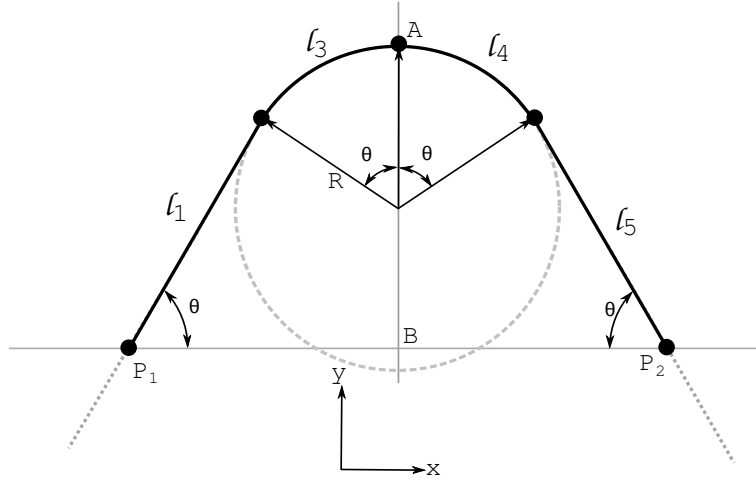


Figure A.3: Geometry of an angled waveguide paths with variable bend radius.

tion which is

$$l_1 \cos \theta + R \sin \theta = L/2 \quad (\text{A.8})$$

Now by solving Eq. A.7 and Eq. A.8 we can have the expressions for R and l_1 .

$$l_1 = \frac{L\theta - l \sin \theta}{2(\theta \cos \theta - \sin \theta)} \quad (\text{A.9})$$

and

$$R = \frac{-L + l \cos \theta}{2(\theta \cos \theta - \sin \theta)} \quad (\text{A.10})$$

The delay length for a set of output apertures will be decided by the bend radius (R) and the length of the straight sections (l_1). Experimental demonstration of the spectral responses of the rectangular and circular AWGs are shown in chapter 5.

A.2 Reflection type AWG

All the geometries of the waveguide array discussed in this appendix and in chapter 2 have a symmetric line AB around which the geometry is mirrored. To reduce the device size to half of its actual size the delay lines can be terminated at the line AB and a reflector can be placed at the waveguide ends as shown in Fig. A.4 (a). The light will travel twice through the same waveguides (once before

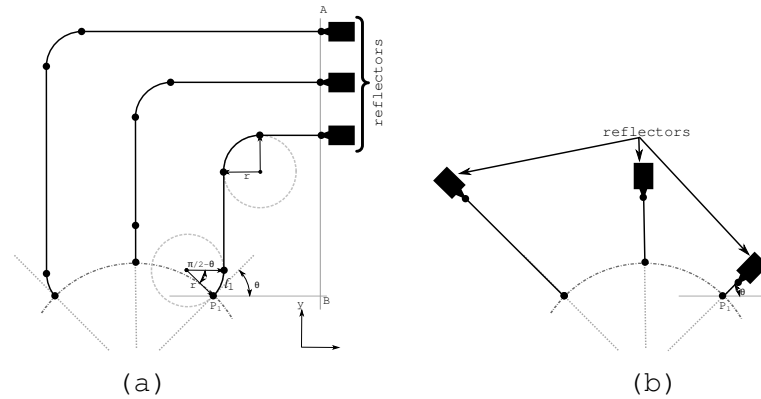


Figure A.4: Geometry of reflection type AWG with (a) rectangular manhattan and (b) angled waveguide paths.

reflection and after reflection from the reflectors) to gain the desired phase difference. The propagation loss will remain the same as light is traveling an equal optical path as compared to the previous case. Theoretically, it is possible to design a reflection type AWG with the length of the smallest delay line equal to zero as shown in Fig. A.4 (b). Therefore, it is possible to decrease the device size further and also the propagation loss. The insertion loss of the device also depends on the loss of the reflectors. For this design, a low loss broadband reflector is needed. Some examples can be a distributed Bragg reflector (DBR) [3], a looped multi-mode interferometer (MMI) or 'Y' branch can be used.

In SOI platform, DBR mirrors have been designed to have low loss but they have a small bandwidth. With a 'Y' branch, it is possible to have a broadband but

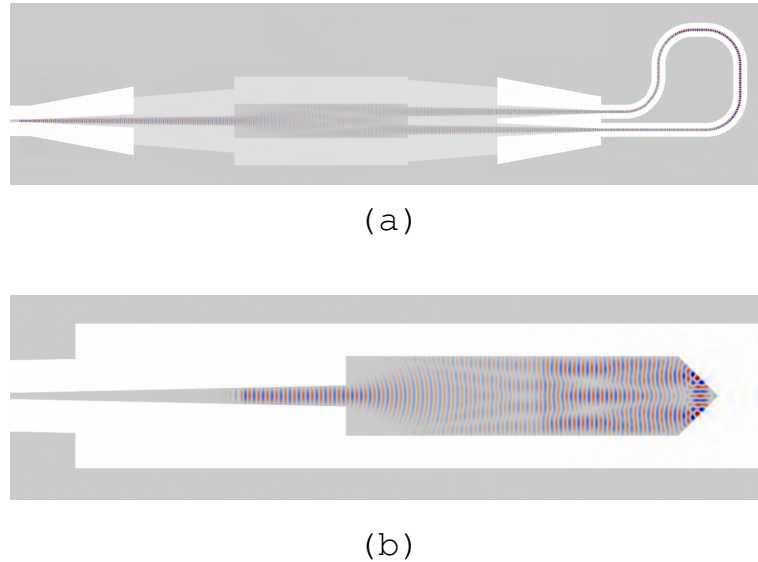


Figure A.5: MMI based reflectors (a) output looped shallowly etched MMI and (b) deep etched MMI with 45° facets.

in general these designs are highly lossy. Therefore we choose an MMI based reflector as they can be designed to have a low insertion loss and broadband reflection. An 1×2 MMI can be made to act as a reflector with two of the following modifications: connect the output of the MMI in a loop (Fig. A.5(a)) and creating a 45° facets at the position where two fold field is generated (Fig. A.5(b)). A shallow etched MMI is used for loop back method. The light will be divided equally into two outputs of the MMI and will reenter the MMI with equal phase which will create a constructive interference at the input of the MMI irrespective of the wavelength. The FDTD simulation result for the same is shown in Fig. A.5 (a). For the other method a deep etch MMI is used as reflections will be strong from a deeply etched mirror. After dividing equally into two images the light will experience total internal reflections by the two 45° angle facets and these two images will create constructive interference at the input of the MMI [4]. The FDTD simulation result is shown in Fig. A.5 (b).

A.3 Low resolution AWG

All the design methods discussed above are for a high resolution AWG i.e. with a large delay length. As we discussed before, the main problem in AWG design is the phase error, which increase with longer delay line. As we increase the chan-

nel spacing the delay length decreases which in turn decreases the phase error contributed by the side wall roughness but at the same time the gap between two successive waveguides will decrease, which will increase the coupling between two waveguides. The coupling between two waveguides also introduce the phase error. Further increment of channel spacing will introduce a waveguide overlap in the above discussed design methods. Therefore for low reso-

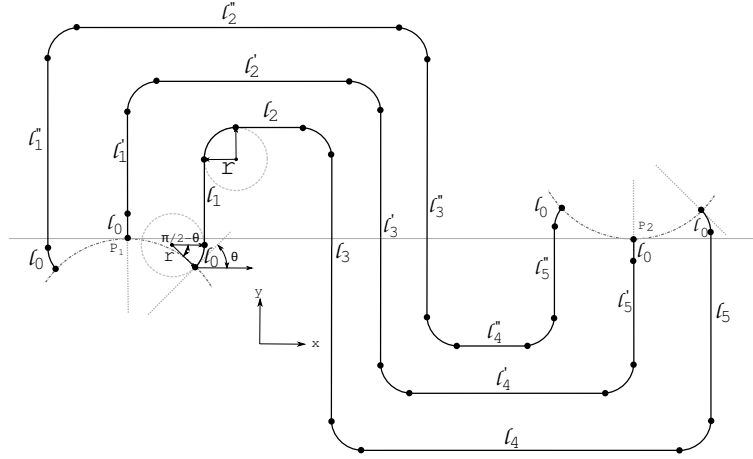


Figure A.6: Geometry of an angled waveguide paths with variable bend radius.

lution AWGs, the best way to connect two star-coupler is with S-shaped waveguides. With S-shaped waveguides it is possible to design a AWG with infinite channel spacing [5] i.e. the two star-couplers are connected with waveguides of equal length as shown in Fig. A.6. To have an equal length for waveguide array the total length along x direction and the total length along y direction must be equal for all the waveguides. Therefore for Fig. A.6 we can say along the y direction

$$l_1 + l_3 + l_5 = l'_1 + l'_3 + l'_5 = l''_1 + l''_3 + l''_5 = \text{constant} \quad (\text{A.11})$$

and along the x direction

$$l_2 + l_4 = l'_2 + l'_4 = l''_2 + l''_4 = \text{constant} \quad (\text{A.12})$$

As the radius of all the bends is equal to r the 90 degree bends are not in the part of the delay length calculations. Although the initial bend l_0 depends on the aperture angle θ , which is balanced by using an equivalent straight sections. In general these design methods can be used for very small channel spacing to very large channel spacing AWGs. But the smallest waveguide of the S-shaped AWG will be longer and contain two extra bends compare to the conventional box-shaped AWGs, which will increase the insertion loss as well as the crosstalk.

Therefore for the small channel spacing AWG this not the best choice. The experimental demonstration of the S-shaped AWGs are shown in chapter 5.

A.4 Conclusions

We developed design methods for various shaped AWGs in IPKISS for different materials and applications with the help of basic knowledge of geometry. For high-contrast waveguides (sharp bends) a rectangular layout will generate a very compact device which is further optimized with the combination of narrow and wide waveguides. With large bend radii the device will be much larger and therefore this design is not very attractive in such materials. Therefore the circular layout is introduced. For low resolution AWGs the S-shaped layout is developed. By knowing the limitation we also designed a reflection-type AWG, which has a footprint half of the original device. All the different shaped AWG shown in this chapter are not completely optimized or experimentally tested. An experimental comparison is needed to conclude the applicability of these design methods.

References

- [1] N. Ismail, F. Sun, G. Sengo, K. Wörhoff, A. Driessen, R. M. de Ridder, and M. Pollnau. *Improved arrayed-waveguide-grating layout avoiding systematic phase errors*. Opt. Express, 19(9):8781–8794, Apr 2011.
- [2] A.R. Vellekoop and M.K. Smit. *Four-channel integrated-optic wavelength demultiplexer with weak polarization dependence*. Lightwave Technology, Journal of, 9(3):310–314, 1991.
- [3] K. Okamoto and K. Ishida. *Fabrication of silicon reflection-type arrayed-waveguide gratings with distributed Bragg reflectors*. Opt. Lett., 38(18):3530–3533, Sep 2013.
- [4] E. Kleijn, M.K. Smit, and X.J.M. Leijtens. *Multimode Interference Reflectors: A New Class of Components for Photonic Integrated Circuits*. Lightwave Technology, Journal of, 31(18):3055–3063, 2013.
- [5] T. Tanemura and Y. Nakano. *Design and scalability analysis of optical phased-array $1 \times N$ switch on planar lightwave circuit*. IEICE Electronics Express, 5(16):603–609, 2008.

